Droplet Production and Transport in Microfluidic Networks with Pressure Driven Flow Control

by

Tomasz Glawdel

A thesis
presented to the University of Waterloo
in fulfillment of the
thesis requirement for the degree of
Doctor of Philosophy
in
Mechanical Engineering

Waterloo, Ontario, Canada, 2012

Author's Declaration

I hereby declare that I am the sole author of this thesis. This is a true copy of the thesis, including any required final revisions, as accepted by my examiners.

I understand that my thesis may be made electronically available to the public.

Abstract

Droplet based microfluidics is a developing technology with great potential towards improving large scale combinatorial studies that require high throughput and accurate metering of reagents. Each droplet can be thought of as a miniature microreactor where complex reactions can be performed on the micro-scale by mixing, splitting and combining droplets. This thesis investigates the operation and control of droplet microfluidic devices operating using constant pressure sources to pump fluids where feedback from the droplets influences the overall performance of the device. For this purpose, a model system consisting of a single T-junction droplet generator and a single network node is used to understand how pressure source control effects droplet generation and transport through microfluidic networks.

The first part of this thesis focuses on the generation of Newtonian liquid-liquid droplets from a microfluidic T-junction operating within the squeezing-to-transition regime with stable flow rates. An experimental study was performed to characterize the effects of geometry (height/width ratio, channel width ratio) and flow parameters (Capillary number, flow rate ratio, viscosity ratio) on the droplet size, spacing and rate of production. Three stages of droplet formation were identified (lag, filling and necking), including the newly defined lag stage that appears at the beginning of the formation cycle once the interface pulls back after a droplet detaches. Based on the experimental observations, a model was developed to describe the formation process which incorporates a detailed geometric description of the drop shape with a force balance in the filling stage and a control volume analysis of the necking stage. The model matches well with the experimental results as data falls within 10% of the predicted values.

Subsequently, the effect of surfactants on the formation process was investigated. Surfactant transport occurs on a timescale comparable to the production rate of droplets resulting in dynamic interfacial tension effects. This causes strong coupling between the mass transport of surfactants and the drop production process. Using the previously defined force balance, the apparent interfacial tension at the end of the filling stage was measured. The results show that there is a significant deviation from the equilibrium interfacial tension at normal operating conditions for the T-junction generators due to the rapid expansion of the interface. A model was developed to calculate the dynamic interfacial tension for pre and post micellar solutions, which was then incorporated into the overall model for droplet formation in T-junction generators.

Next, the behaviour of microfluidic droplet generators operating under pressure source control was investigated. Coupling between the changing interface and hydrodynamic resistance of the droplets and the flow rate of the two phases creates fluctuations in the output of the droplet generator. Oscillations were found to occur over the short term (one droplet formation cycle) and long term (many formation cycles). Two metrics were developed to quantify these oscillations. Short term oscillations were quantified by tracking droplet speed in the output channel and long term oscillation were quantified by measuring changes in droplet spacing. Analysis of experimental and numerical data shows that long term oscillations have a periodicity that matches the residence time of droplets in the system. A simple model is developed to determine the influence of Laplace pressure, droplet resistance, T-junction generator design and network architecture on the magnitude of these oscillations. From the model a set of design rules are developed to improve the overall operation of T-junction generators using pressure driven flow.

The final part of this thesis studies the transport of droplets through a single microchannel junction under various geometric and flow conditions applied to the two outlet channels. Droplets alter the hydrodynamic resistance of the channel they travel within which creates a feedback effect where the decision of preceding droplets influences the trajectory of subsequent droplets. Multifaceted behaviour occurs where sometimes the trajectory of droplets follows a repeatable pattern and other times it is chaotic. As part of this work, a discrete analytical model was developed that predicts droplet transport through the junction including transitions between filtering and sorting, bifurcation in the patterns, composition of the patterns, and an estimation of when patterns will disintegrate into chaos. The model was validated by comparing it to compact numerical simulations and microfluidic experiments with good agreement.The complex behaviour of a simple junction emphasizes the challenge that remains for more highly integrated droplet microfluidic networks operating with pressure driven flow.

Acknowledgements

First and foremost, I would like to thank my advisor, Dr. Carolyn Ren, for giving me the opportunity to work under her guidance. Her expertise and passion for research, as well as her support and encouragement during my study is truly appreciated. She has helped me grow into a capable researcher and a professional.

My whole experience would not have been as rewarding without the help of other members of the Waterloo Microfluidics Lab. My gratitude goes to my fellow colleagues, Zeyad Almutairi , Mostafa Shameli and Bo Yan Yu that have also traversed the long and winding road of graduate studies with me. Many thanks to Dr. Caglar Elbuken, who worked closely with me to initiate the droplet research within our group. His assistance during the initial stages of my thesis was invaluable and his outlook on life and research was truly motivating. Great thanks to Danny Chan, who as an undergraduate researcher tackled any job given to him with exceptional ability. I would also like to thank several other members that attended group meetings and provided valuable input with regards to my work: Dr. Lin Gui, Dr. Said Boybay, Dr. Junjie Ou, and Dr. Tiemen Huang.

I would like to thank the National Sciences and Engineering Research Council for their financial support as part of a three year scholarship. As well, the financial support from Dr. Carolyn Ren is gratefully acknowledged as well.

I am deeply grateful to my friends and family whose support is truly appreciated. I would especially like to thank Leanne Whiteford whose love, support, and company has been one of the greatest sources of strength for me. She has been an encouraging force throughout my graduate studies. I am very grateful to my family, my sister, Joanna, and my parents, Eva and Witold, as well as Leanne's parents, Kevin and Lori, who have been behind me all the way. I would also like to extend thanks to several friends that I met during my time at Waterloo and made life more enjoyable: Cameron Dunning, Brent Forrest, Taylor Hall, Paul Holshoff, Nicole McPhail, Reed Cowper, Duncan Cairns and Brett Campbell.

Table of Contents

Author's Declaration ii
Abstract iii
Acknowledgements v
Table of Contents vi
List of Figures xi
List of Tables xxi

Chapter 1 1
Introduction 1
1.1 Background 1
1.2 Thesis Outline 7

Chapter 2 10
Literature Review of Droplet Microfluidics 10
2.0 Introduction 10
2.1 Forces, Scaling and Dimensionless Numbers 11
2.2 Wettability, Surface Tension, Surfactants and Carrier Fluids 12
2.2.1 Wettability 12
2.2.2 Interfacial Tension 13
2.2.3 Surfactants 14
2.2.4 Carrier Fluids 16
2.3 Droplet Manipulation 16
2.3.1 Droplet Generation 16
2.3.2 Droplet Motion in Microchannels 24
2.3.3 Droplet Breakup 28
2.3.4 Droplet Coalescence 30
2.3.5 Droplet Indexing, Sorting, Storage and Extraction 35
2.4 Droplet Numerical Simulations 40
2.5 Practical Concerns: Visualization, Flow Control, Stability 42
2.5.1 Flow Visualization 42
2.5.2 Flow Control 43
2.5.3 Stable Operation 44

2.6 Applications 45
2.6.1 Fluid and Interfacial Property Measurements 46
2.6.2 Bead and Particle Synthesis 46
2.6.3 Mixing and Chemical Reaction Studies 47
2.6.4 Custom Emulsions 48
2.6.5 Biological Studies 50
2.7 Summary 52

Chapter 3 55
Fabrication Methods and Experimental Techniques 55
3.1 Device Fabrication by Soft Lithography 55
3.2 Fluid and Interfacial Properties 57
3.3 Experimental Setup 58
3.3.1 Flow Sensor Calibration 60
3.6 Safety 61

Chapter 4 63
Modeling of T-junction Droplet Generators in the Squeezing to Transition Regime 63
4.1 Overview of Previous Works 63
4.2 Experimental Design 72
4.2.1 Experimental Setup 74
4.2.2 Experimental Procedure 75
4.2.3 Chip Fabrication 76
4.2.4 Fluid Property Measurements 76
4.2.5 Channel Dimension Measurements 77
4.3 Data Extraction from Videos 78
4.4 Experimental Observations 84
4.4.1 Dynamics of Droplet Formation 85
4.4.2 Parameters Influencing L^*_{lag} 89
4.4.3 Parameters Influencing b^*_{fill} 91
4.4.4 Parameters Influencing b^*_{pinch} 92
4.4.5 Parameters Influencing $2r^*_{pinch}$ 93
4.4.6 Scaling of Operational Parameters 95

4.5 Model of the T-junction Droplet 97
4.5.1 Model Limits and Constraints 97
4.5.2 Geometric Description of the Droplet 98
4.5.3 First Stage: Lag Stage 100
4.5.4 Second Stage: Filling Stage 100
4.5.5 Third Stage: Necking 102
4.5.6 Determine b^* by a Force Balance on the Emerging Droplet 105
4.5.7 Pressure Drop: Extended 3-D Lubrication Analysis 107
4.5.8 Effective Pressure Drop Length 110
4.5.9 Viscosity Contrast Effect 113
4.5.10 Force balance with 3D flow Considerations 115
4.5.11 Calculating the Pinch-off Point $2r_{pinch}$ 117
4.5.12 Calculation of Other Operational Parameters 117
4.5.13 Summary of Model for Droplet Generation 119
4.6 Experimental Validation 124
4.7 Conclusions 128

Chapter 5 131
Effect of Surfactants on Droplet Generation 131
5.1 Introduction 131
5.2 Experimental Methods 134
5.2.1 Surfactant Properties 135
5.3 Experimental Observations 136
5.4 Model of Surfactant Adsorption to Expanding Interfaces 141
5.4.1 Approximation for $A(t)$ for the T-junction 146
5.5 Model Validation with Experimental Data 150
5.5.1 Modification to the Droplet Formation Model 151
5.6 Conclusion 155

Chapter 6 158
Global Design of Droplet Generators with Pressure Driven Flow 158
6.1 Introduction 158
6.2 Metrics for Analyzing Generation Stability 161
6.3 Compact Model of Flow in the T-junction Generator 163

6.3 Experimental Methods 167
6.3.1 Design of Experiment 169
6.3.3 Chip Fabrication 170
6.4 Working Pressure Range 172
6.5 Short Term Velocity Fluctuations 174
6.5.1 Scaling analysis of the Velocity Fluctuations 176
6.6 Long Term Fluctuations in Spacing 180
6.6.1 Analysis of Spacing Fluctuations 181
6.6.2 Numerical Model of Feedback in Droplet Generation 182
6.6.3 Numerical Simulation Results 183
6.7 Reducing Fluctuations through Network Design 187
6.7.1 Design Guidelines 189
6.8 Case Study 191
6.9 Testing of Design Rules 193
6.10 Conclusions 194

Chapter 7 197
Passive Droplet Trafficking at Nodes in a Microfluidic Network 197
7.1 Introduction 197
7.2 Analytical Model: Continuum Based Approximation 204
7.2.1 Conceptual Framework 205
7.2.2 General Model of Sorting 205
7.2.3 Model for Asymmetric Pressures and Branch Lengths 209
7.3 Numerical Simulations of Trafficking 210
7.3.1 Droplet Trafficking Algorithm 211
7.3.2 Idealized Numerical Simulation of Droplet Trafficking 213
7.4 Discrete Model of the Droplet Sorting 214
7.4.1 Selection Rules from Sessoms *et al.* 216
7.4.2 New Set of Selection Rules based on N_T 218
7.4.3 Available Sequences 222
7.4.4 Summary of Discrete Model 224
7.5 Experimental Design 226
7.5.1 Overall Chip Design 227
7.5.2 T-junction Generator Design 228

7.5.3 Diluter Design 229
7.5.4 Sorting Branch Design 230
7.5.5 Experimental Setup to Reduce Noise Contributions 231
7.5.6 Chip Fabrication 233
7.5.7 Video Experimental Setup 233
7.5.8 Data Extraction from Videos 233
7.5.9 Experimental Procedure 234
7.6 Measuring Droplet Resistance Experimentally 235
7.6.1 Loop Based Droplet Resistance Measurements 237
7.6.2 Pressure Method for Droplet Resistance Measurement 238
7.7 Model Validation 240
7.7.1 Ideal-Model General Case Studies 241
7.7.2 Ideal-Model Simplified Case Studies 246
7.7.3 Full-Model Simplified Case Studies 249
7.8 Prediction of Stable and Chaotic Regimes 253
7.8.1 Calculation of the Stability of a Pattern 254
7.9 Additional Non-idealities: Spacing Fluctuations 256
7.10 Effect of Initial Conditions 256
7.11 Experimental Comparison 257
7.12 Suggests for Implementing Sorting in Practice 261
7.13 Conclusions 262

Chapter 8 265
Conclusions and Recommendations. 265
8.1 Contributions of this Thesis 265
8.2 Recommendations for Extension of Work 268

Appendix A 270
Appendix B 271
Appendix C 272

References 273

List of Figures

Figure 1.1 Several examples of commercial LOC products: a) Fluidigm cartridge with integrated membrane valves for performing multiplexed proteomic and genomic studies b) Agilent Technologies 2100 Bioanalyzer chip for performing electrophoresis separations and flow cytometry c) Caliper Life Sciences LabChip 90 for performing electrophoresis separations d) the Endosafe-PTS from Charles Rivers, a portable detection system with loadable cartridges for performing various assays including endotoxin testing, gram negative identification, and a glucan assay. 2

Figure 1.2 Concept of replacing microwell plates conventionally used in biology labs with droplet based microfluidic devices. Each droplet acts like an individual well in the plate where contents can be added or subtracted. Droplets are detected by transporting them past a fixed detector.(Song, Chen *et al.* 2006) 4

Figure 1.3 A simple droplet microfluidic network consisting of one T-junction generator and one node. All inlets and exits are controlled by varying the pressure..... 6

Figure 2.1 (a) Wetting conditions for two-liquid phases in contact with a solid surface. (Left) the two-phases are partially wetting and a three-phase contact line forms, (Right) one phase (2) preferentially wets and a thin absorbed film separates the other phase (1) from the surface. (b) Standard equilibrium wetting condition for two-phase partial wetting with the definition of the contact angle and the three surface tension values (g represents gas but can also be a second liquid).(Squires and Quake 2005; Gunther and Jensen 2006)..... 13

Figure 2.2 Three types of passive microfluidic droplet generators: co-flowing, cross-flowing and flow focusing. Images showing the generators operating in the dripping regime (a,c,e) and jetting (b,f) or squeezing regime (d).(Christopher and Anna 2007) 17

Figure 2.3 Example of microfluidic step emulsification design for producing monodispersed droplets (Priest, Herminghaus et al. 2006) 18

Figure 2.4 Diagram explaining the pressure drop across a slug in a microchannel (a) divided into three main parts the Laplace pressure across the caps, the pressure drop along the body of the droplet and the pressure drop between droplets in the continuous phase. (b) Cross-sectional view illustrating the gutters and thin-film surrounding the droplet in a rectangular channel. (c) Vortices created by the droplet motion in both the continuous and dispersed phases for cases of different viscosities (η).(Fuerstman, Lai et al. 2007; Labrot, Schindler et al. 2009) 24

Figure 2.5 (Left) Slip factor measured for droplets of length l/wc with a viscosity contrast η=0.3 at different capillary numbers. (Right) Slip factor for η=33 against size and capillary number (Jakiela, Makulska et al. 2011)..... 28

Figure 2.6 Droplet breakup at a bifurcation showing the difference of non-breaking droplets (a-e) and breaking droplets (f-i). Breakup is defined by the extension ratio of the droplet prior to it reaching the junction (l_o, w_o) and the velocity v. (k) Shows the phase diagram for breaking (■) and non-breaking

(○) droplets versus Capillary number and the initial extension of the droplets (Link, Anna et al. 2004).....29

Figure 2.7 Examples of passive coalescence techniques. (a) expansion/contraction chamber showing that droplets merge upon decompression at the exit(Bremond, Thiam et al. 2008) (b) pillar design (Niu, Gulati et al. 2008) (c) surface treatment design (gray area is hydrophilic treated segment of the microchannel). (Fidalgo, Abell et al. 2007).....31

Figure 2.8 Examples of active coalescence techniques. (a) Flow rectifying design where the perpendicular (up/down) channels on the right control the film draining time (Tan, Ho et al. 2007) (b) "abacus" design with microfluidic rail showing the streamlines created within the coalescence chamber and the merging of three drops in an experiment.(Um and Park 2009) (c) electrocoalescence of a single pair of droplets (Priest, Herminghaus et al. 2006) (d) thermocapillary merging with a laser (indicated by white dot). (Baroud, de Saint Vincent et al. 2007) 33

Figure 2.9 Extraction technique with second microfluidic two-phase "wall" (on right) where electrodes (black triangles) selectively merge the desired droplet with the continuous stream to create a reaction (c).(Fidalgo, Whyte *et al.* 2008) 39

Figure 2.10 Experimental operation with flow focusing generator operating with flow rate control from dual syringe pumps (a) and pressure driven control from pressure "bombs" (b) over the same flow conditions adjusted for viscosity differences between the oil and water phases. Droplet size in the pressure control varies significantly more than under flow control.(Ward, Faivre et al. 2005).....44

Figure 2.11 Examples of particles fabricated with droplets. (i) different shaped magnetic hydrogel particles including spheres, discs, and rods.(Hwang, Dendukuri et al. 2008) (ii) Janus particles fabricated with two different fluorescence halves.(Shepherd, Conrad et al. 2006).....47

Figure 2.12 (i) Diagram of mixing in droplets through a serpentine showing that the interface between the two fluids is stretched, reorientated and folded as it passes through the curves and straight channels.(Song, Bringer et al. 2003) (ii) Mixing of viscous fluids in a bumpy serpentine channel mixer with fluorescent images showing the striations within the plug.(Liau, Karnik et al. 2005).....48

Figure 2.13 Examples of complex emulsions created with microfluidic droplet generators (i) droplets of different composition and size created by three flow focusing generators outputting to a single microchannel (Hashimoto, Garstecki et al. 2007) (ii) complex foam structure created in low continuous phase flow conditions(Raven and Marmottant 2006) (iii) double emulsions made using a double T-junction design with hydrophobic, and hydrophobic wetting conditions, includes examples of various double emulsions with controlled number and size of core droplets.(Okushima, Nisisako et al. 2004) 50

Figure 2.14 Droplet based study of C. Elegans on a microfluidic chip. (a) array of 24 droplets with arrows pointing to drop containing organisms, drops are fixed in trapped wells. (b) close up of a droplet with the C. Elegan swimming. (Shi, Qin et al. 2008) 51

Figure 3.1 Diagram of the process for fabricating microfluidic chip using soft lithography with multi-level features. (Glawdel 2008) 56

Figure 3.2 a) Microscope experimental setup for performing the T-junction experiments: Eclipse TI microscope, flow sensor, high speed camera, and Fluigent pressure system. b) Close up of the Fluigent system with the MFCS 8 which controls the pressure to 8 outputs and the Fluiwell that contains the fluid reservoirs. 58

Figure 3.3 Calibration curve of "tick" count versus applied flow rate for the SLG 1430 flow sensor. Each data point is the average of three measurements. Linear regression profiles are: -5.23049x + 84.72476 (FC40+10%PFO), -6.07209x + 98.35753 (Hexadecane) and -6.35893x + 103.00735 (Silicone Oil). Goodness of fit is greater than $R^2 > 0.995$ for all three profiles. 61

Figure 4.1 (a) Droplet formation cycle in the T-junction generator consisting of three stages (I) filling period (II) squeezing/necking period and (III) pinch off. Images are actual traces of the interface for n-hexadecane/ 1%Span80 and water, with intersection geometry 1:2 and channel height 50μm, under flow conditions of Ca=0.0087, φ=0.475. All images are equidistant in time. Below the global overview of the T-junction generator is presented with the respective geometric and flow parameters identified. 64

Figure 4.2 A diagram of the overall geometry of the T-junction network with a close up of the local geometry at the junction for the three nominal designs. 74

Figure 4.3 Schematic diagram of the T-junction generator network with the equivalent hydrodynamic circuit for calculating the channel height from the measured flow rate at an applied pressure. 77

Figure 4.4 Sequence of image processes performed to a single frame in the video to isolate only the droplets and to obtain information on the droplets.....79

Figure 4.5 (a) Image with boundary data of the droplets overlaid and the pixel locations transformed into cylindrical co-ordinates, which provides the in-plane droplet shape g(θ). (b) A diagram of the assumed shape of the droplet in three dimensions, where the out of plane curvature is approximated as *h/2*. The volume of the droplet can then be calculated by integrating from the 2-D projection. 80

Figure 4.6 (a) Example of the y-position of the top droplet of an analyzed video. Droplet flashes correspond to a sudden increase in position because a lower droplet becomes the top droplet. A new droplet results in a decrease in position. The line across the image shows the median value of droplet position. (b) The y-position adjusted by the median with the detection events highlighted.....82

Figure 4.7 Results of image analysis used to determine the penetration depth and critical neck thickness at pinch-off as indicated by the markers. The position of the microchannel walls is automatically detected as highlighted by the blue line overlays.....83

Figure 4.8 Images of the drop formation process for four experiments broken down into the three observed stages (i) lag (ii) filling (iii) necking. Silicon oil is the continuous phase and 10%wt glycerol/water the dispersed phase, other experimental data is listed below the images. 85

Figure 4.9 Evolution of droplet shape and volume with time for Case A and B. (a)(c) changes in ● V^*_{drop}, $\Delta 2r^*_n$, □ b^* and (b)(d) in ● V^*_c, ΔV^*_{neck}, □ V^*_{bypass}. Formation is characterized by the lag stage, filling stage and necking stage as indicated by the dashed lines. The dispersed and continuous phase flow remain constant during the entire formation process. Solid lines provide linear fits to the change in volume for the specified regions. 86

Figure 4.10 The continuous phase (green highlighted area) enters further into the side channel of designs with larger channel widths. After detachment this volume of oil is redistributed and contributes to L^*_{lag}. 89

Figure 4.11 Plot of the scaling relationship for L^*_{lag} for three different T-junction geometries including range of viscosity contrasts η=0.12→1.7. Geometries (h^*, Λ^*): □ (*0.5, 35*), ○(*0.4, 1*), ◊ (*0.3, 1*)....91

Figure 4.12 Comparison between experimental measured b^*_{fill} versus the expression by Chrisopher *et al.* (Christopher, Noharuddin et al. 2008) (a) Fluid combination of silicon oil and 10%wt glycerol/water (η=0.12) in different T-junction geometries demonstrating the dependence on h/w_c. (b) Effect of increasing the viscosity of the dispersed phase (10%wt to 70%wt glycerol) for the same T-junction geometry $h/w_c=0.4$. Dashed lines are logarithmic curve fits used to guide the eye, the solid black line correspond to the expression in Chistopher *et al.* (Christopher, Noharuddin et al. 2008). 92

Figure 4.13 Comparison between experimental measured b^*_{pinch} against (a) the flow ratio and (b) the initial penetration depth at the beginning of necking. b^*_{fill}. Geometries (h^*, Λ^*): ● (*0.30, 0.35*), ○ (*0.4, 1*). Dashed lines are used to guide the eye to the linear relation....93

Figure 4.14 Comparison between experimental measured $2r^*_{pinch}$ against penetration depth at the beginning of necking. b^*_{fill}. Geometries (h^*, Λ^*): (*0.4, 1)* and □ (*0.30, 0.35)* open symbols correspond to $\eta=0.12$ and close $\eta=1.7$. Dashed lines are the theoretical limit predicted by Eqn 4.18. 95

Figure 4.15 Plot of the dimensionless droplet volume (a) oil volume (b) frequency of formation (c) and spacing (d) as a function of the flow ratio. Geometries (h^*, Λ^*): □ (*0.4, 1*), ○(*0.30, 0.35*), Δ (*0.6, 0.5*), x (*0.5, 0.5*); silicone oil and 10%wt glycerol/water as the working fluids. 96

Figure 4.16 Geometric reconstruction of the droplet shape as it is being formed in the transition regime. The 2-D view of the droplet shape is used to develop a full 3-D shape of the droplet by assuming that the out of plane curvature is represented by a half circle with a radius of *h/2*. The droplet penetrates a distance of *b* into the main channel. The front of the droplet is described by a half circle of diameter *b*, the back by a quarter circle of radius R_n and the neck thickness by $2r_n$. 99

Figure 4.17 Interface shape immediately after detachment where it recedes back into the dispersed phase inlet. The position of the interface relative to the main channel is defined by the lag length L_{lag} and the volume is defined by $V_{lag.}$ 100

Figure 4.18 Droplet shape at the end of the filling stage for two cases where $w_d \leq b_{fill}$ and $w_d > b_{fill}$. The drops are characterized by extent of protrusion, b, and the neck radius at the filling stage R_{fill}. For the circular segment, the height is given by b and the radius of the circle is w_d. 101

Figure 4.19 (TOP) A sequence of traces showing the boundary of the droplet as it evolves during the necking stage. At first the neck shape follows a quarter circle until it becomes anchored within the dispersed phase channel at a distance w_d. Once it is anchored the shape follows a circular segment until the neck reaches a critical thickness where pinch off occurs. The deformable control volume (CV), and its evolution during the squeezing process is highlighted in green. (BOTTOM) A diagram showing the neck with the relevant variables indicated to describe its shape as a circular segment. A close up of the control volume shows the flow of oil, the boundary which moves with the interface of the neck and the passing of oil around the droplet. 103

Figure 4.20 (a) Diagram indicating the forces acting on the emerging droplet in the filling stage. As the droplet grows it obstructs the continuous phase resulting in a pressure difference across the droplet as wellas shear stress on the interface. These two forces are countered by the interfacial tension force which resists deformation. At some point the droplet reaches a maximum size characterized by the dimension b, where the pressure and shear forces exceed the surface tension force and the neck begins to thin. 105

Figure 4.21 Geometry of the gap where the fluid bypasses the droplet with dimensions indicated for flow fluid flow model of Tchikanda *et al*. Examples of the limits of corner flow and parallel plate flow are also illustrated. 108

Figure 4.22 Dimensionless mean velocity as a function of the gap aspect ratio with the two limits of parallel plate flow and corner flow identified. 110

Figure 4.23 Simulation domain of the 3D numerical model performed in COMSOL Multiphysics 4.1. Calculations were only performed for the continuous phase. Boundary conditions are no-slip at all the channel walls and no-shear at the droplet interface. 111

Figure 4.24 Numerical result for the normalized fluid velocity through the gap region for $h^*=0.2$ and $b^*=0.9$. Shading reads from 0 to 1 by 0.1 from light to dark. 112

Figure 4.25 Effective pressure drop length $\Delta P_{3D}/\Delta P_{asy}$ in the gap region as a function of the gap width-b^*. Data corresponds to ◊ $h^*=0.2$, □ $h^*=0.35$, and ○ $h^*=0.5$. 112

Figure 4.26 Contour plot of the dimensionless velocity profiles in the cross-section of the droplet at the minimum gap height for (a) $h^*=0.3$, $b^*=0.85$, $\eta=1$, and (b) $b^*=0.85$, $\eta=1/100$. Data is non-dimensionalized by the maximum velocity for (a). 114

Figure 4.27 Effect of viscosity contrast on the pressure drop from the 2D numerical simulations. Data corresponds to ◊ $\eta=0.1$, □ $\eta=0.2$,Δ $\eta=0.33$, + $\eta=0.5$, * $\eta=1$, ○ $\eta=2$. 115

Figure 4.28 Plot of b^*_{fill} with respect to h^*/Ca for two different channel aspect ratios and viscosity ratios. 120

Figure 4.29 Calculations of the new critical neck thickness for $h^*=0.2$, 0.35 and 0.5. 120

Figure 4.30 Plot of α with respect to b^*_{fill} for various T-junction geometries with a base value of h^*=0.5, ε^*=0. 121

Figure 4.31 Plot of β with respect to b^*_{fill} for various T-junction geometries with a base value of h^*=0.5, ε^*=0. 121

Figure 4.32 Variation droplet generation for a T-junction geometry of h^*=0.5, Λ^*=0.5 for a fixed flow rate φ=0 against Capillary number. 123

Figure 4.33 Complete set of equations for the modelling of the T-junction droplet generator. 123

Figure 4.34 Parity plot of b^*_{fill} for all experiments. Solid line is perfect parity and the dashed lines are ±10%. 125

Figure 4.35 Parity plot of b^*_{fill} for experiments with L^*_{eff} and $g(\eta, \lambda_{gap})$ ○ silicon oil and ● with a constant L^*_{eff} =0.25 and $g(\eta=1, \lambda_{gap})$. Solid line represents the perfect parity and the dashed lines are ±10%. 125

Figure 4.36 Parity plot of $2r^*_{pinch}$ for all experimental measurements. 126

Figure 4.37 Parity plot of droplet volume for all experimental measurements. 126

Figure 4.38 Parity plot of continuous phase volume for all experimental data points. 127

Figure 4.39 Parity plots for generation frequency for all experimental data. 127

Figure 5.1 Series of micrographs showing the formation of droplets with 1.5% SDS in 1:2 and 1:1 T-junction designs. 137

Figure 5.2 Parity plots of the calculated droplet volume and b^*_{fill} to experimental data using the static interfacial tension. (a)(b) ○ Tween 20 (black) 0.1% (grey) 0.5% (white) 2%. (c)(d) □ SDS (black) 0.5%, 1.5%, and 3%. 137

Figure 5.3 Variation of b^*_{fill} versus incoming dispersed flow rate Q_d. Data corresponds to T-junction with 1:2 0.1% Tween 20 for ○(black) Q_c=1.5-1.9 μL min^{-1}, (grey) Q_c=1.9-2.3 μL min^{-1}, and (white) Q_c=2.3-2.8 μL min^{-1}. 138

Figure 5.4 Plots of the apparent dynamic interfacial tension extracted from video analysis using Eqn. 5.2. (a) Tween 20 experiments with 1:2 T-junction design (black) 0.1%, (grey) 0.5% (white) 2% (b) Tween 20 with 1:1 T-junction design (c) SDS with 1:2 T-junction design (black) 0.5%, (grey) 1.5%, white (3%) (d) SDS with the 1:1 T-junction design. Error bars are associated with the ±1 pixel error for b^*_{fill} measured from the videos. 141

Figure 5.5 Model of surfactant adsorption to an interface with the division of the interface, subsurface and bulk. Schematic adapted from (Eastoe and Dalton 2000) 142

Figure 5.6 Schematic of the effect of interface expansion or contraction on the surfactant transport and interfacial tension. Drawing adapted from (Eastoe and Dalton 2000) 144

Figure 5.7 Schematic of the process of enhanced transport of monomers to an expanding surface by the disintegration of micelles in solution. 145

Figure 5.8 Diagram of the approximated area of the droplet from the projection of the 2D image. 147

Figure 5.9 Area change and dilation rate extracted from video analysis of droplet formation. (a),(b) T-junction Λ^*=0.5 h^*=0.5 with silicone oil and 1.5%SDS water with conditions of □ Ca=0.049 , b^*_{fill}=0.79, f=17.8Hz. ○ Ca=0.015 b^*_{fill}=0.645, f=42.8 Hz. (c)(d) T-junction Λ^*=1 h^*=0.5 with silicone oil and 0.5% SDS water with conditions of □ Ca=0.0048 , b^*_{fill}=0.741, f=9.66 Hz. ○ Ca=0.0149 b^*_{fill} *=0.598, f=20.9Hz. Solid black lines are calculations from Eqn. 5.17 and Eqn. 5.18.....149

Figure 5.10 Plot of combined data from both 1:2 and 1:1 Tjunction designs for the dynamic interfacial tension versus the temporal term in Eqn 3. (a) Tween 20 with (black) 0.1%, (grey) 0.5% and (white) 2% (b) SDS (black) 0.5%, (grey) 1.5% and (white) 3%. Dashed lines are linear fits to the data used to extract the slope. Solid line represents an interfacial tension equal to the static interfacial tension. Error bars are omitted for clarity but are the same scale as those in Figure 3.....150

Figure 5.11 Parity plot of the droplet volume calculated using the dynamic interfacial tension in the amalgamated model. ○ Tween 20 experimental data ● SDS experimental data.....152

Figure 5.12 (TOP) A sequence of traces showing the boundary of the droplet as it evolves during the necking stage when surfactants absent and present in the system. For the surfactant free case the back half of the droplet follows the circular segment approximation (highlighted in blue). With surfactants the neck shape diverges from a circle and appears flatter. The volume missing from the approximation is highlighted in red (BOTTOM) A diagram showing the geometric parameters that can be used to calculate the missing volume. 154

Figure 5.13 Parity plot of the droplet volume calculated using the modifications to the neck volume calculation. ○ Tween 20 experimental data ● SDS experimental data.....155

Figure 6.1 Plot of the deviation in droplet volume (dotted line) and spacing (solid line) against the flow ratio under the conditions of $\alpha=1$, $\beta=1$ and 10% fluctuations of φ. Calculations are made using Eqns.6.1-6.2. 163

Figure 6.2 Schematic of the T-junction generator operating under pressure source control with the relevant parameters indicated. Below is the pressure drop along the main channel without droplets (ΔP_m) and with droplets ($n\Delta P_{drop}$). 164

Figure 6.3 A diagram of the three different chip designs with different channel lengths. Type 1- 1:1:5, Type2- 1:5:2, and Type 3-5:1:2. A close up of the intersection design is also included for the three types of intersections 1:1, 1:2 and 1:3. Outside the intersection area, the channel width is 100 μm and the height is uniform. 168

Figure 6.4 Velocity of a droplet that is downstream of the T-junction generator for n-hexedecane, water, Type 1, 1:2, 35μm. The velocity varies significantly over

a droplet formation cycle, and in this case the standard deviation is >5%. The velocity fluctuations correspond to different stages of the formation cycle, as indicated by the numbered images. The formation cycle is approximately 45ms long and images were taken at 1000fps. Lines that appear to exceed 16 mm/s are a false error that is caused by a new top droplet entering the analysis frame. 174

Figure 6.5 Relative velocity fluctuations observed experimentally compared to that calculated by changes in the interface shape at the inlet and a droplet leaving the channel. Data is shown on a log-log plot in terms of percentages. ● corresponds to experiments using surfactants and ○ to those without 179

Figure 6.6 Example of a typical frame for video analysis of long-term droplet spacing fluctuations. 179

Figure 6.7 Measurement of droplet spacing in a T-junction generator after 10 min of operation. Conditions are R_c:R_d:R_m=1:0.7:5, P_c=800mBar, P_d=790 mBar. The solid black line is the measured values; red line is an 11 point smoothing average. 180

Figure 6.8 Power spectrum of the fast fourier transform of data in Figure 6.7. The strongest peak coincides with the residence time of the droplets. 182

Figure 6.9 Time-trace and FFT analysis of droplet spacing for two numerical simulations (a, b) R_c:R_d:R_m=1:0.1:5, with P_c=500 mBar, γ=50 mN m and (c, d) with R_c:R_d:R_m= 1:0.7:5. 184

Figure 6.10 Measurements of droplet spacing produced by the numerical simulations for conditions similar to the experimental results of Figure 6.7: Rc:Rd:Rm=1:0.7:5, Pc=800mBar, Pd=790 mBar. Noise is added to the simulations as random fluctuations in Pd and Pc. (a) Time-trace of droplet spacing. The solid black line is the measured values; red line is an 11 point smoothing average (b) power spectrum of the FFT analysis with the peak frequency identified. 185

Figure 6.11 Experimental results for the start-up response of a T-junction generator. The channel is initially empty by adjusting the pressure to keep the interface just inside the dispersed channel inlet. The pressure is then increased (P_d=210→250 mBar) and droplets begin to form. Conditions are for silicon oil and water without surfactant with a network design of R_c:R_d:R_m=1:5:2, h=50 μm , and Pc=300 mBar. 186

Figure 6.12 Contour plots of the relative variance in the junction pressure (%) from all three sources versus the global network geometry. Plates correspond to (a) $\Delta P_{Lp}^* = 0.025$, $\Delta P_d^* = 0.0025$, $R_{drop}^* = 0.1$ (b) $\Delta P_{Lp}^* = 0.025$, $\Delta P_d^* = 0.0025$, $R_{drop}^* = 0.5$ (c) $\Delta P_{Lp}^* = 0.1$, $\Delta P_d^* = 0.0025$, $R_{drop}^* = 0.1$ (d) $\Delta P_{Lp}^* = 0.1$, $\Delta P_d^* = 0.0025$, $R_{drop}^* = 0.5$ 188

Figure 6.13 Measured variance in droplet spacing for different network designs as a function of applied pressure Pd. Data corresponds to network geometries of R_d:R_c:R_m (○) 1:4:5, (Δ) 1:0.7:5 and (■) 1:0.1:5. Experimental conditions are provided in Section 4.5. 193

Figure 7.1 Diagram of the two basic designs, (a) branch and (b) loop, used to study droplet trafficking. 198

Figure 7.2 A diagram indicating the main variables relevant to sorting at a T-junction. Asymmetry may exist in the branch lengths, cross-sections, and applied pressures. 205

Figure 7.3 Flow chart of the trafficking algorithm for the numerical simulations. 213

Figure 7.4 Flow chart of the selection rule algorithm for the new discrete model. 221

Figure 7.5 (a) Overall network architecture for the experimental sorting chip which consists of 3 main components: the T-junction generator, diluter and sorting branches. (b) The equivalent hydrodynamic representation of the network used for compact flow modelling. 227

Figure 7.6 Micrographs of the chip near (a) the diluter inlet, (b) the outlet of the branches and (c) the exit of the chip. At each inlet drop of glue was added to the master to create a large reservoir that minimized pressure losses from the inlet tubing to the microchannel. 230

Figure 7.7 Droplet spacing measured over 80 droplets for 4 different cases using the same chip. 232

Figure 7.8 Snapshot from a video of the sorting process with the two interrogation boxes overlaid. 234

Figure 7.9 Chip design for measuring droplet resistance using sorting at an asymmetric loop. Droplets stored upstream in the storage area are transported to the loop sorting into the short branch to equate the resistances of the two branches. The experimental procedure consists of counting the number of droplets that sort to the short branch (grey dots) before the first droplet sorts into the long branch (stripped dot).....237

Figure 7.10 Modified chip design for the droplet measurement using the applied pressure at the diluter (P_{dil}) and the resistance of the measurement channel (dashed line). The flow sensor is connected to Outlet A, while Outlets B and C are plugged during the measurements. Droplet spacing and speed is measured at the bifurcation using the high speed camera.....239

Figure 7.11 Equivalent droplet resistance L_{Rdrop} with respect to droplet length L_d for η=0.1 (♦) and η =1(■). Trend lines are linear fits to the data.....240

Figure 7.12 Idealized numerical simulation results for the pattern length (○). Overlaid are the predictions from the continuum and discrete models. Vertical dashed lines on the left represent the limits for the filtering regime as predicted by the continuum (--) and discrete models (·–). Grey and white regions define the regions where the cycle time is expected to remain unchanged. Black lines are the predictions for T^*_a and T^*_b from the discrete model. The red line corresponds to the selection rules derived in Section 3.3. Each plot corresponds to Case 1(a), Case2 (b), Case 3(c) and Case 4 (d). 242

Figure 7.13 Idealized numerical simulation results for the average number of droplets (○) in the two branches over time and the specific number of droplets at any point in time for branch A (Δ) and B (∇). Red line corresponds to the discrete model prediction for the average number of droplets. Black and blue lines are for the number of droplets in branches A and B respectively. 244

Figure 7.14 Fraction of droplets sorting into channel B ($Prob_b$) from the ideal-model simulations (○). The red line is the prediction by the discrete model and the solid black the continuum model. 245

Figure 7.15 Ideal-model numerical simulation results for the pattern length (○) corresponding to test Case 1 (a), Case 2 (b), Case 6 (c), and Case 9 (d). 247

Figure 7.16 Ideal-model numerical simulation results for the $Prob_b$ (○) corresponding to test Case 1 (a), Case 2 (b), Case 6 (c), and Case 9 (d). 248

Figure 7.17 Full-model numerical simulation results for the T_{cyc}^* (a) and $Prob_b$ (b) for Case 1. 250

Figure 7.18 Full-model numerical simulation results for the T_{cyc}^* (a) and $Prob_b$ (b) for Case 2. 251

Figure 7.19 Full-model numerical simulation results for the T_{cyc}^* (a) and $Prob_b$ (b) for Case 7. 251

Figure 7.20 Full-model numerical simulation results for the T_{cyc}^* (a) and $Prob_b$ (b) for Case 5 and T_{cyc}^* (c) and $Prob_b$ (d) for Case 6. 252

Figure 7.21 Full-model numerical simulation results for the T_{cyc}^* plotted on the left axis with the red line as the prediction and Q_b/Q_a plotted on the right axis as the solid black line. 253

Figure 7.22 Full-model numerical simulation results for the T_{cyc}^* with the prediction for stable (red line) and chaotic regimes (blue line). Lines are offset slightly above the numerical results for clarity. Referring to Table 3.3 results are for (a) Case 1, $\kappa=3/4$, (b) Case 1 with $L_{drop}=0.5$, $\kappa=3/4$, (c) Case 5, $\kappa=1/6$ and (d) Case 7, $\kappa=1/3$. 255

Figure 7.23 Experimental results for the T_{cyc}^* and n_T for (a) symmetric branches and pressures (b) symmetric branches and asymmetric pressures, (c) asymmetric branches and symmetric pressures (c) asymmetric branches and asymmetric pressures. Red line is the discrete model prediction for T_{cyc}^*, the solid black line is the prediction for T_a^* and T_b^* and the dashed line (--) is the continuum model prediction for the total number of droplets. 259

Figure 7.24 Experimental results for the $Prob_b$ for (a) symmetric branches and pressures (b) symmetric branches and asymmetric pressures, (c) asymmetric branches and symmetric pressures (c) asymmetric branches and asymmetric pressures. Red line is the discrete model prediction and the black the continuum model. 260

Figure 7.25 Ideal-model simulations of the effect of adjusting P^* on the distribution of droplets for (a) L=5:5, $L_{drop}=0.5$, and (b) $L=5:4.5$ $L_{drop}=0.5$. Base pattern length is 10. 261

List of Tables

Table 2.1 Summary of relevant dimensionless numbers in micro scale two-phase flow and scaling with respect to the characteristic dimension. 12

Table 4.1 Experimental conditions. Silicone oil was the continuous phase in all cases with various mixtures of glycerol/water as the dispersed phase. Nominal values for the height of the channels and width of the dispersed phase are provided as well as the width ratio (Λ), height ratio (h^*) and viscosity ratio (η). 72

Table 4.2 Pressure conditions used in Case study #2 for silicone oil and water with no surfactant on a type 3 chip, with a 1:2 width ratio, and nominal height of 35μm. P_m is set to 100 mBar and P_d and P_c are set relative to this pressure. 75

Table 4.3 Properties including viscosity, refractive index and interfacial tension for each of the fluids and w/o combinations. Measurements are made at room temperature, 22 ±1˚C. 77

Table 5.1 List of parameters covered in each experiment with surfactants. 134

Table 5.2 Molecular formula, molecular weight (M_w), critical micelle concentration (c_{CMC}) , aggregation number N_A, and diffusion coefficient (D) for the surfactants SDS and Tween 20. 136

Table 5.3 Comparison of slopes extracted from Figure 5.10 and the range calculated from Eqn. 5.19 using surfactant properties found in the literature. 151

Table 6.1 Factors of interest and their levels for studying the T-junction generator. The dispersed phase factor depends on the oil type as surfactant and water type changes as described above. 169

Table 6.2 Table listing the order in which experiments were performed. The five independent factors are listed in columns 2-5. The three right hand side columns are the viscosity (μ_d/μ_c), network channel lengths (L_c:L_d:L_m) and hydrodynamic resistances (R_c:R_d:R_m) ratios. All values shown are nominal. 170

Table 6.3 Experimental results for prediction of $P^*_{d\min}$. Data is presented for 6 different chip designs with various local and global geometries, with and without surfactants. The final two columns present the experimentally measured $P^*_{d\min}$ compared to the calculation from Eqn. 6.12. 172

Table 7.1 List of outcomes from the discrete model for the selection rules. Variables are calculated with respect to the base value. 222

Table 7.2 List of all unique sequences $\left|\Omega_{seq}\right|$ that are possible for T^*_{cyc}= *2 to 9* with the number of D-s in the sequence varying from 1-4. 225

Table 7.3 Dimensions of the final chip design. Data includes the overall length of the channel and the approximate number of droplets for a typical spacing of 600 μm. The cross-sectional area of all the channels was 50x100μm. 228

Table 7.4 Four case studies for the general numerical simulations. Parameters include the length of the two branches (L_1, L_2) [mm], pressures (P_1, P_2) [Pa], droplet equivalent lengths (L_{drop1}, L_{drop2}) [mm], widths and height (w,h) [μm]. The dimensionless variables are the area ratio A^*, droplet resistance ratio R^*_{drop},

branch length ratio Λ and pressure skew P^*. Pressure at the junction was set to 100 Pa. 241

Table 7.5 Nine case studies used to test the simplified conditions. Parameters include the length of the two branches (L_1, L_2) [mm], pressures (P_1, P_2) [Pa], and droplet equivalent lengths (L_{drop1}, L_{drop2}) [mm]. The dimensionless variables branch length ratio Λ and pressure skew P^*. Junction pressure was set to 100 Pa. 247

Table 7.6 Nine case studies used to test the full-model conditions. Parameters include the length of the two branches (L_1, L_2) [mm], pressures (P_1, P_2) [Pa], and droplet equivalent lengths (L_{drop1}, L_{drop2}) [mm]. The dimensionless variables branch length ratio Λ and pressure skew P^*. Simulations were performed including the main channel inlet with the same dimensions as the experimental chip design (100 mm). Pressure at the junction was approximately 228.5 Pa and the applied pressures at the outlet were set to a base of 215 Pa. 249

Chapter 1

Introduction

1.1 Background

The history of Lab-on-a-chip (LOC) devices or micro-Total Analysis Systems (μTAS) traces its roots to the development of ink-jet printers in the 1950s followed by the development of silicon microchannel devices for gas chromatography in the late 1970s, and then by the first chip based electrophoresis separation devices in the1990s.(Manz, Effenhauser *et al.* 1994; Nguyen and Wereley 2006; Whitesides 2006; Haeberle and Zengerle 2007) The development of LOC devices has intensified over the past decade driven by the demand from biomedical researchers for devices that exceed the performance of current macro sized assays. The shift to LOC devices stems from the inherent advantages miniaturization affords including reduced reagent consumption, lower fabrication costs, shorter analysis time, improved sensitivity, portability and higher throughput through massive parallelization.(Beebe, Mensing *et al.* 2002; deMello 2006; El-Ali, Sorger *et al.* 2006; Janasek, Franzke *et al.* 2006) More importantly, scaling down brings the dimension of the device in line with the samples to be analyzed allowing for a level of control over the sample that is simply unattainable with macro scale systems. LOC devices have found a number of applications including drug discovery, clinical diagnostics, genetics research, chemical synthesis, cellular analysis, and bio weapons detection.(Dittrich, Tachikawa *et al.* 2006; Yi, Li *et al.* 2006; Abgrall and Gue 2007; Chin, Linder *et al.* 2007) As the field has matured, several commercial devices have made their way to the marketplace from such companies as Agilent technologies (2100 Bioanalyzer), Caliper Life Sciences (Lab Chip 90), Raindance Technologies (RDT 1000), Fluidigm and Charles River (Endosafe-PTS) (see Figure 1.1).

An LOC device consists of several integrated components such as pumps, mixers, valves, separators, and detectors that are connected by microchannels generally on the order of 10-500 μm. The first LOC devices were fabricated in glass or silicon using well established micro fabrication techniques borrowed from the microelectronics industry. However, the high cost and limited access to fabrication facilities restricted research to a few select groups. The exponential growth of LOC research over the past decade began with the introduction of a novel fabrication process known as soft lithography.(Duffy, McDonald *et al.* 1998; Xia and Whitesides 1998; Duffy, Schueller *et al.* 1999)

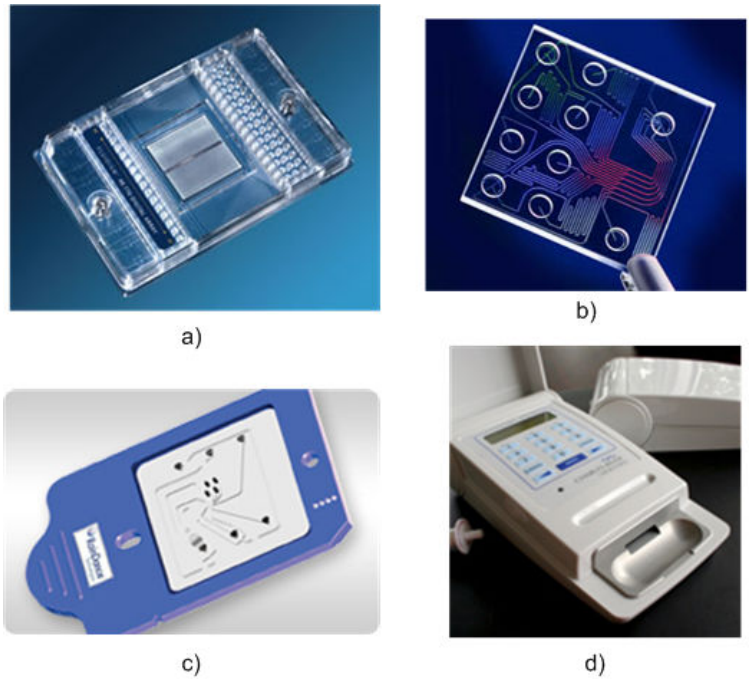

Figure 1.1 Several examples of commercial LOC products: a) Fluidigm cartridge with integrated membrane valves for performing multiplexed proteomic and genomic studies b) Agilent Technologies 2100 Bioanalyzer chip for performing electrophoresis separations and flow cytometry c) Caliper Life Sciences LabChip 90 for performing electrophoresis separations d) the Endosafe-PTS from Charles Rivers, a portable detection system with loadable cartridges for performing various assays including endotoxin testing, gram negative identification, and a glucan assay.

Soft lithography is a micromolding technique, where a polydimethylsiloxane (PDMS) prepolymer mold is cast against a master with raised relief structures representing the fluidic network. To complete the chip the mold is peeled, trimmed, fluidic access holes are punched and the mold is then bonded to another substrate. The wide spread adoption of soft lithography can be largely attributed to the excellent properties PDMS possess for LOC applications. PDMS is optically transparent down to 280 nm, largely inert, and biocompatible, withstands large temperature ranges, and is easily modified by several well established surface treatments.(McDonald, Duffy *et al.* 2000; McDonald and Whitesides 2002; Lee, Park *et al.* 2003; de Jong, Lammertink *et al.* 2006) The natural flexibility of PDMS allows for the integration of active components from membranes such as valves and pumps using pneumatic control.(Unger, Chou *et al.* 2000; Nguyen and Wereley 2006; Melin and Quake 2007) PDMS devices are inexpensive to build in non-clean room conditions and are therefore disposable- a valuable attribute for academic research. However, PDMS has not found its way into many industrial applications due to the higher cost and slower fabrication process than other methods that are more economical at large scale such as microinjection moulding and hot embossing. (Nguyen and Wereley 2006; Abgrall and Gue 2007; Mark, Haeberle *et al.* 2010; Waldbaur, Rapp *et al.* 2011)

Scaling down fluid flow changes the relative importance of various physical phenomena leading to a transformation in how a device operates. The decrease in length scale shifts the physical paradigm from the influence of gravity and inertia forces on the macro scale, to the dominance of viscous and surface forces on the micro scale(Stone, Stroock *et al.* 2004; Squires and Quake 2005; Bruus 2007). For instance, the Reynolds number ($Re=\rho UL/\mu$) in microfluidic devices is typically very small ($Re<<1$) so that flow is strictly laminar and turbulence is absent. The most apt consequence of this fact is that without turbulence there is no chaotic advection, and thus mixing is difficult to achieve since the only means is through diffusion. However, the shift to surface and interfacial dominance also has its advantages. A variety of micro scale phenomena such as capillarity, electrophoresis, electroosmosis, electrohydrodynamics, dielectrophoresis, magnetism and optical forces can be harnessed to perform new functions.(Stone, Stroock *et al.* 2004; Squires and Quake 2005; Nguyen and Wereley 2006; Bruus 2007) The interplay between these forces results in a rich and complex physical system.

The majority of microfluidic devices are based on single phase systems consisting of various miscible aqueous streams. Fluids are controlled within the chip with either syringe pumps, pressure sources at the reservoirs or integrated peristaltic pumps based on the PDMS membrane design.(Pennathur 2008) The well defined nature of laminar flow allows for the formation of novel microenvironments with direct spatial control over concentration fields.(Atencia and Beebe 2005; Squires and Quake 2005) However, single phase flow has several limitations, particularly for large scale combinatorial studies in chemistry, proteomics, genomics, drug screening and biology.

Consider for instance a study that requires the mixing of reagents in reactors with hundreds of samples to be screened against a multitude of conditions. Such a system is plagued with cross-contamination between different fluid streams or between different tests since diffusion can cause unwanted mixing between reagent streams that are in contact with each other. Even if streams are physically isolated by valves, during pressure driven flow Taylor dispersion will smear out sample plugs.(Stone, Stroock *et al.* 2004; Squires and Quake 2005; Nguyen and Wereley 2006; Bruus 2007). If the sample is a protein, contact with the micro channel wall will cause adsorption and further contamination.(Nicolau and Fulga 2003; Lionello, Josserand *et al.* 2005; Roach, Song *et al.* 2005; Boxshall, Wu *et al.* 2006; Toepke and Beebe 2006; Mukhopadhyay 2007) .Such a system also scales up poorly as an approximately linear increase in active components and device footprint is required for each additional reactor.

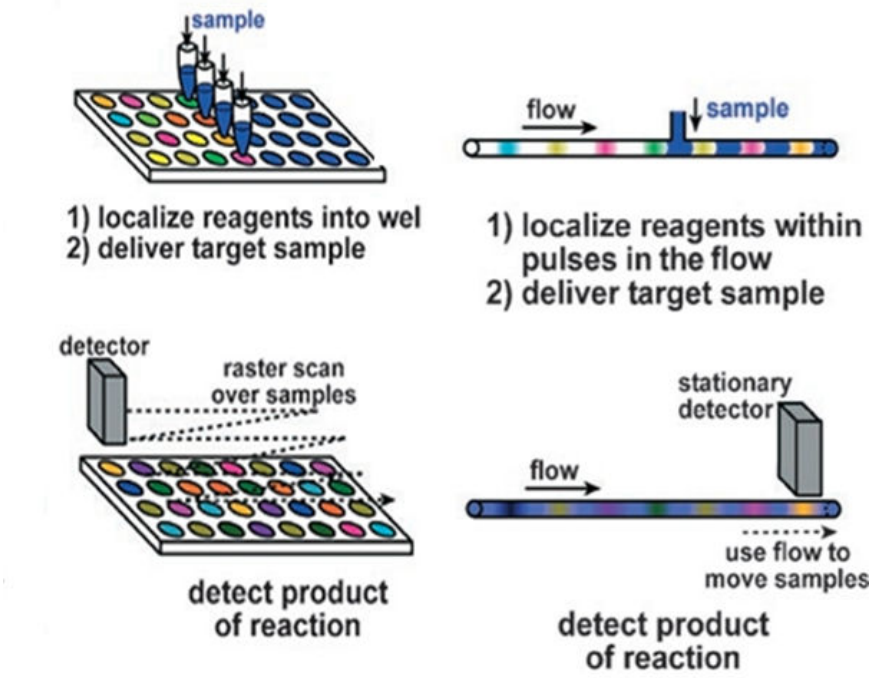

Figure 1.2 Concept of replacing microwell plates conventionally used in biology labs with droplet based microfluidic devices. Each droplet acts like an individual well in the plate where contents can be added or subtracted. Droplets are detected by transporting them past a fixed detector.(Song, Chen *et al.* 2006)

Two-phase droplet microfluidics is a viable alternative for such a study where discrete droplets are formed from immiscible fluids like water and oil. Each droplet is essentially a transportable micro reactor that compartmentalizes reagents preventing them from diffusing away akin to a microwell plate (see Figure 1.2). The small size of the droplets results in minimal consumption of reagents and excellent metering of reactants. Microfluidic droplets can be used in high throughput applications as they can be generated at rates between 1-20 kHz over a range of picolitres to nanolitres with a standard deviation of only 1-3 %. (Christopher and Anna 2007; Shui, Eijkel *et al.* 2007; Teh, Lin *et al.* 2008) Under well defined wetting conditions, droplets are separated from the channel wall by a thin film of carrier fluid which prevents adsorption and cross-contamination between droplets and the channel walls. Mixing is also enhanced due to the formation of counter rotating vortices within moving droplets.(Song, Bringer *et al.* 2003; Song and Ismagilov 2003; Song, Tice *et al.* 2003; Gunther, Jhunjhunwala *et al.* 2005; Muradoglu and Stone 2005; Garstecki, Fuerstman *et al.* 2006) Droplet microfluidics are able to scale up effectively since each individual droplet can be transported to fixed processing stations that perform mixing, splitting, or merging operations. Droplet LOC devices have already found numerous applications in chemical synthesis and biochemical assays.

The difficulty with designing droplet based LOC devices is processing droplets at extremely high rates while maintaining control over each individual droplet. A hypothetical high level device might have the following functions:

- 10 different inlet streams with droplets produced at 1kHz and 100 droplet manipulations per second.
- Precise control over the content and size of each droplet with less than 1% variance.
- Droplets can be split, merged or sorted on demand, and in any combination to perform multi-step reactions.
- Controlled heating and cooling of each droplet.
- The history of each droplet can be tracked from parents through to siblings.
- Content of each droplet can be detected at rates exceeding the rate of production
- Effective transport of each droplet through the network to each processing station at specific times to achieve proper scheduling of events.
- Droplets can be recovered for off chip analysis if needed.

To achieve these ambitious objectives requires a thorough understanding of the phenomena that governs each process. Although several droplet based microfluidic devices have been presented to date, these devices only include one or two operational elements, such as generation and splitting, and only use two inlet streams (water and oil). In many cases, syringe pumps, which produce a constant flow rate output, are used to drive these simple devices because it is easy to know the direction and magnitude of all flow streams. However, the usefulness of syringe pumps is countered by several inherent limitations when considering their application in high level droplet based devices. Syringe pumps can experience severely long settling times when settings are changed, and even at steady state are subject to long-term oscillations due to ratcheting of the stepper motor and imperfections in the drive screw (de Mas, Gunther *et al.* 2005; Korczyk, Cybulski *et al.* 2011). When several syringe pumps are connected to the network, the unique oscillation of each syringe pump will force itself on to the network making the operation of the device unsteady and unpredictable. For example, in a simple microfluidic droplet generator, Korczyk et al showed that using syringe pumps caused oscillation of more than 20% in droplet size and speed, and that these oscillations corresponded exactly with the rate of revolution of the drive screw (Korczyk, Cybulski *et al.* 2011). In addition, as the number of fluid inlet streams increases syringe pumps become less attractive because of their size and cost. Still, given their inherent simplicity there are many situations where syringe pumps are acceptable; however, when

considering the requirements listed above for high-level devices they become unlikely candidates for flow control.

Instead, constant pressure sources offer a more flexible alternative as the atmospheric pressure in several fluid reservoirs can be controlled by a series of regulators, valves with pressure supplied from one source. However, several researchers have noticed that there is a distinct difference in running droplet devices with constant pressure sources rather than constant flow sources. For instance, Ward *et al.* showed that the bubble size changes significantly under pressure driven control but not flow control in a flow focusing generator when the inputs are scaled together. (Ward, Faivre *et al.* 2005). The cause is feedback created by the presence of droplets in the outlet channel and the flow of the two phases which controls the production of droplets. Droplets increase the effective hydrodynamic resistance of the channel they pass through which alters the flow rate of that channel (Baroud, Gallaire *et al.* 2010). In essence, droplets act like discrete resistors that travel through the network altering the pressure field as they go. The resulting pressure and velocity fluctuations influence neighbouring components causing non-linear and erratic behaviour. Understanding the reason for these fluctuations and how to control them is crucial to the development of droplet based devices. The hypothesis that drives this work is that stable and robust control of droplet generation and transport can be achieved with pressure driven flow through effective design of the microfluidic network..

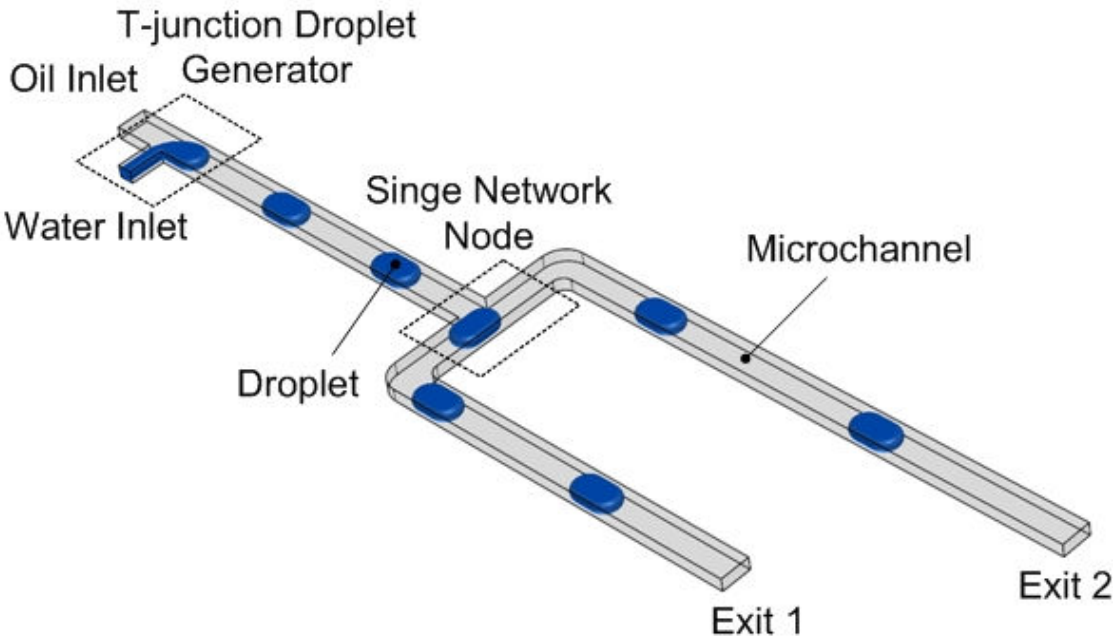

Figure 1.3 A simple droplet microfluidic network consisting of one T-junction generator and one node. All inlets and exits are controlled by varying the pressure.

For this purpose, a simple microfluidic network consisting of a T-junction droplet generator and a single bifurcation is analyzed in detail in this thesis (see Figure 1.3). Droplets are formed at the T-junction generator and then transported along the main channel through the junction and finally to the two exits. All inlets and exits are controlled by varying the atmospheric pressure. First, a systematic study of the droplet generation process at a microfluidic T-junction is performed and an analytical model is developed to describe the influence of channel geometry, fluid properties and flow conditions. The model is able to predict all operational elements including droplet size, spacing and frequency. Next, the model is extended to also include the dynamic interfacial tension effects caused by the presence of surfactants in the system. A global perspective is then taken to analyze the influence of network architecture on the stability of the droplet generator. Finally, the transport of droplets through a simple junction is studied. Transport is regulated by a discrete time-delayed feedback that results in highly periodic behavior where specific patterns of droplet trajectories can form. A model is developed to describe the distribution of droplets in the two branches and the formation of these patterns. The result of this research provides the basis for the development of more complex chips that include multiple generators and nodes that are controlled by pressure sources.

1.2 Thesis Outline

In Chapter 2, an overview of droplet microfluidics is provided discussing the benefits of miniaturizing current chemical and biological systems. The review outlines the fundamentals of two-phase microchannel flow and the various mechanisms used to generate, split, combine, sort and transport droplets through microfluidic networks. This is followed by a brief summary of the various applications that have utilized droplet microfluidics.

In Chapter 3, the experimental setup and procedures used throughout this thesis are summarized. This includes techniques and equipment for performing high-speed visualization of droplets in microchannels, fabricating microfluidic chips, measuring fluid properties and measuring microchannel dimensions.

In Chapter 4, a systematic study of the operation of T-junction microfluidic droplet generators is presented. An experimental study was performed to characterize the effect of flow conditions, fluid properties and geometry on droplet production in the squeezing-to-transition regime. Experiments are performed with water in oil droplets of varying viscosity without surfactants. High speed videos are analyzed to dissect the process of drop formation. Analysis of the videos

shows that a third stage in the formation process, termed the lag stage, should be included. From this analysis a phenomenological model is developed that inherently captures the influence of the intersection geometry, including the channel width ratio and height/width ratio, capillary number and flow ratio on the performance of the generator. The model describes all aspects of formation including droplet size, spacing and frequency of formation.

In Chapter 5, the effect of adding surfactants to the two-phases is investigated. The transport of surfactants occurs on a time scale that is similar to the formation of droplets which leads to coupling between the two processes. As part of this study a model is developed to account for the transport of surfactants to the expanding interface in order to estimate the dynamic interfacial tension. The model is then incorporated into the squeezing-to-transition model developed in Chapter 4 and compared to experimental data.

Chapter 6 looks at the effect of the global network architecture on the performance of a single T-junction generator operating under pressure driven flow. Feedback created by the formed droplets can lead to variation in the flow rates of the two phases which leads to oscillations in droplet generation. Two metrics for quantifying the generator stability are introduced that identify both short term and long term fluctuations in performance. Short term fluctuations are tracked by monitoring droplet velocity and long term fluctuations by the spacing variation between droplets. Spacing variations are shown to be more sensitive and easier to measure than the more commonly used droplet size. Experimental data shows that long-term oscillations have a periodicity that matches the residence time of droplets in the system. A numerical model is built to describe the system and shows that these long-term oscillations are perpetuated by stochastic noise. A simple analytical model is then developed to guide the design of the external microfluidic network in order to improve stability.

In Chapter 7, droplet trafficking at a simple bifurcation consisting of one inlet and two outlets is studied under various asymmetries in channel design and flow conditions. Droplets that enter the junction always sort to the branch with the highest flow rate. Once a droplet enters a branch it alters the division of flow between the two branches, thus influencing the decision of subsequent droplets. Under certain conditions the sequence of decisions can form a pattern that repeats indefinitely, while other times the sequence appears chaotic. The goal of this study is to understand the reason for these patterns and determine if they can be predicted. First, an analytical model is presented that describes the passive trafficking of droplets under all

asymmetries using the mean field approach. Subsequently, a numerical model is developed to describe the sorting process and used to develop a discrete- analytical model of the system that predicts the distribution of droplets in the outlets, the pattern length and composition, and when the system will operate in the chaotic regime. Validation of the discrete model is performed against both numerical and experimental results.

In Chapter 8, a summary of this work is presented and recommendations for further academic studies are suggested. These recommendations focus on complimentary studies that can further enhance the understanding of droplet based microfluidic devices. The knowledge gained in this thesis will improve the understanding of droplet mechanics and will advance the development of droplet based LOC devices. The information obtained during this research will be of interest to researchers in the fields of fluid mechanics, nano engineering, bioengineering and soft matter.

Nomenclature

Acronyms:

PDMS	poly(dimethyl)siloxane
LOC	Lab on a Chip
μTAS	Micro Total Analysis System

Mathematical Symbols:

ρ	density (kg m^{-3})
μ	dynamic viscosity of fluid (Pa s)
L	length scale (m)
Re	Reynold's number (dimensionless)
U	velocity (m s^{-1})

Chapter 2

Literature Review of Droplet Microfluidics

2.0 Introduction

Two-phase flow is a complex phenomena that has a long history in fluid mechanics with several benchmark studies such as Laplace and Young's study of wetting and capillarity in 1804, Rayleigh's study of the instability of a liquid thread in 1879, Taylor's study of droplet break up in shear and elongation flows in 1932 and the study of electrified jets in 1964, and Bretherton's (1961) investigation into segmented flows in capillaries.(Young 1804; Rayleigh 1879; Taylor 1932; Bretherton 1961; Taylor 1964) Covering the entire subject of two-phase flow is unachievable in such a short review, therefore the scope of this review is limited to a narrow division of two-phase flow involving micro scale droplet flows in microchannels.

To begin with, there are two complementary techniques in LOC that also use two-phase flow. The first, known as digital microfluidics, involves the sampling, transport and mixing of droplets on an array of electrodes by electrowetting on a dielectric (EWOD).(Kohler and Henkel 2005; Mugele and Baret 2005; Fair 2007; Miller and Wheeler 2009) The main advantage of these devices is that they are reprogrammable so a single chip can be reused for several different tasks. The second technique involves liquid/gas flows in microchannels, also referred to as bubble microfluidics. Gas/liquid flows have been studied extensively in literature especially in the context of microfluidic heat exchangers and chemical reactors.(Gunther and Jensen 2006; Nguyen and Wereley 2006) However, gas/liquid flows are not ideal for biochemical applications because the liquid is generally the continuous phase so samples are not effectively compartmentalized and gas compressibility causes a delay in controlling the flow field. Therefore, micro-droplet flow is herein defined as liquid/liquid two-phase flows involving incompressible immiscible fluids within microchannels of characteristic dimensions <500 μm and droplet volumes of less than 1μL under low Reynolds number conditions.

The following discussion focuses on current methods developed to manipulate droplets and their subsequent application in a number of fields. Due to the increasing popularity of droplet based flows a number of recent review articles have been published on the general topic of droplets (Atencia and Beebe 2005; Belder 2005; Squires and Quake 2005; Janasek, Franzke et al. 2006;

Haeberle and Zengerle 2007; Shui, Eijkel et al. 2007; Teh, Lin et al. 2008; Guillot, Ajdari et al. 2009; Schaerli and Hollfelder 2009; Baroud, Gallaire et al. 2010; Stone 2010; Zhao and Middelberg 2011), design of droplet generators (Baroud and Willaime 2004; Christopher and Anna 2007; Guillot, Ajdari et al. 2009), reactions in droplets (Gunther and Jensen 2006; Song, Chen et al. 2006), and formation of custom emulsions.(Zhou, Yue et al. 2006) As well, several books on the topics of LOC (Nguyen and Wereley 2006), microfluidics (Bruus 2007), experimental (Faghri and Zhang 2006; Ghiassiaan 2007) and numerical (Prosperetti and Tryggvason 2007) two-phase flow and capillarity(de Gennes, Brochard-Wyart et al. 2003) have been referenced throughout this review. Two-phase flow involves a great deal of non-linearity and instability, and thus emphasis is put towards identifying techniques and operating conditions where the fluid flow is stable and deterministic.

2.1 Forces, Scaling and Dimensionless Numbers

At this point it is appropriate to clearly define the naming convention for the two phases. The phase that carries the droplets is termed the continuous phase, and the droplets themselves the disperse phase. A balance exists in two-phase flow between four primary forces: inertia, viscous shear, interfacial tension and buoyancy. The relative importance of these forces is characterized by a combination of dimensionless numbers including the Reynolds (inertia/viscous), Capillary (viscous/interfacial), Grashoff (buoyancy/viscous), Bond (gravitational/interfacial) and Weber (inertia/interfacial).(Baroud and Willaime 2004; Squires and Quake 2005; Gunther and Jensen 2006; Shui, Eijkel et al. 2007; Teh, Lin et al. 2008; Stone 2010) The scaling of these numbers with size is summarized in Table 2.1. Due to the low flow velocities and high surface to volume ratio in micro flow, inertia and gravity forces become insignificant in comparison to viscous and interfacial forces and therefore Grashoff, Bond and Weber numbers are not usually considered. The Capillary number is the most useful descriptor for analyzing micro scale two-phase phenomena including droplet formation, breakup, coalescence, transport and mixing. It evaluates the competition between viscous stresses, acting to elongate the interface, and surface tension attempting to minimize the surface area. Control over all droplet processes involves manipulating the four independent variables in the capillary number: viscosity μ (Pa·s), flow velocity U (m·s^{-1}), surface tension γ (N·m^{-1}) and g_c the geometric constant. Other important dimensionless parameters that are also used are the ratio of viscosities, $\eta = \mu_d / \mu_c$, and flow rates, $\varphi = Q_d / Q_c$, of the two phases. Typically, the capillary number is calculated from the properties of the continuous phase.

Table 2.1 Summary of relevant dimensionless numbers in micro scale two-phase flow and scaling with respect to the characteristic dimension.

Dimensionless #	Definition	Equation	Scaling
Reynolds	Inertia/viscous	$\frac{\rho UL}{\mu}$	1
Capillary	Viscous/Interfacial	$\frac{\mu U}{g_c \gamma}$	0
Grashoff	Buoyancy/viscous	$\frac{L^3 \rho^2 \beta \Delta T}{\mu^2}$	3
Bond	Gravitational/Interfacial	$\frac{L^2(\rho - \rho_t)g}{g_c \gamma}$	2
Weber	Inertia/Interfacial	$\frac{\rho U^2 L}{\gamma}$	1

The majority of knowledge acquired on two phase flow has been obtained from macro scale studies in the context of unbounded flows where the velocity field away from the interface quickly reaches a bulk value and the droplets have minimal influence on the flow field. This is not true in micro scale flows where the close proximity of the walls strongly influences the fluid dynamics. Confinement helps suppress hydrodynamic instabilities from forming and since the droplets occupy the majority of the microchannel cross-section they also influence the global pressure and flow fields even if their population is low (Guillot, Colin et al. 2007; Guillot, Ajdari et al. 2009; Humphry, Ajdari et al. 2009). To obtain analytical approximations scaling arguments are used based on a balance of drag and viscous forces combined with lubrication theory for fluid flow.

2.2 Wettability, Surface Tension, Surfactants and Carrier Fluids

To obtain stable operation, it is important to match the material properties with the fluids being used. The following section outlines important design parameters that must be first considered during the development of a droplet microfluidic device

2.2.1 Wettability

When two immiscible fluids come in contact with a substrate, two possible conditions can occur: either one liquid preferentially wets the wall and separates the other from the surface, or both liquids are partially wetting and an equilibrium angle is found (see Figure 2.1a). The equilibrium

angle is determined by a force balance on the three-phase contact line: $\gamma_{l_1,l_2}\cos\theta_{eq} = \gamma_{s,l_2} - \gamma_{s,l_1}$, where γ is the surface tension at the liquid/liquid, first solid/liquid, and second solid/liquid interfaces (see Figure 2.1b).(de Gennes, Brochard-Wyart et al. 2003; Darhuber and Troian 2005) Due to the close proximity of the walls to the two phases, the wetting conditions strongly influence the formation and transport of droplets in microchannels. It is essential that the continuous phase preferentially wets the walls to produce stable flow regimes. If this is not the case, then droplets can get stuck as the two phases flip between wetting the walls and device operation is completely irreproducible.(Dreyfus, Tabeling et al. 2003; Tice, Song et al. 2003; Gunther and Jensen 2006; Christopher and Anna 2007; Shui, Eijkel et al. 2007; Teh, Lin et al. 2008) The thin film that forms under preferentially wetting separates the droplets from the microchannel wall which helps lubricate their motion and compartmentalize the contents.

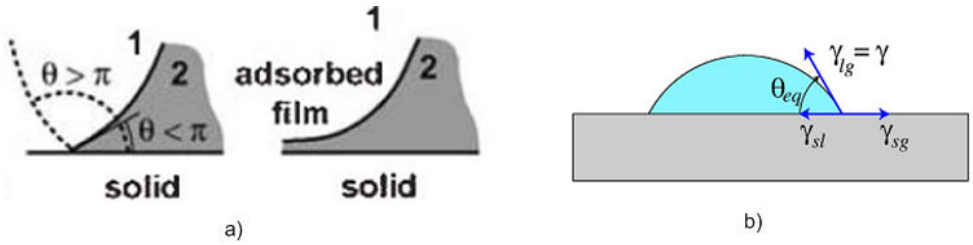

Figure 2.1 (a) Wetting conditions for two-liquid phases in contact with a solid surface. (Left) the two-phases are partially wetting and a three-phase contact line forms, (Right) one phase (2) preferentially wets and a thin absorbed film separates the other phase (1) from the surface. (b) Equilibrium wetting condition for two-phase partial wetting with the definition of the contact angle and the three surface tension values (g represents gas but can also be a second liquid).(Squires and Quake 2005; Gunther and Jensen 2006)

PDMS is naturally hydrophobic so the oil phase wets the walls in water/oil emulsions. However, PDMS can be turned hydrophilic through plasma treatment when bonding it to another substrate during the soft lithography fabrication process. The process is only temporary as the plasma treated surface is unstable in air and reverts back to its natural hydrophobic state in 1-2hrs.(Bhattacharya, Datta et al. 2005) To ensure that the microchannels are hydrophobic, the PDMS can be heat treated after plasma treatment (180°C for 2-4hrs) (Garstecki, Fuerstman et al. 2006) or chemically modified with silanizing agents.(Teh, Lin et al. 2008) Surface treatments can also be used to fabricate heterogeneous wetting conditions which can be used to passively manipulate droplets or created pinned interfaces.

2.2.2 Interfacial Tension

Surface tension arises because of an imbalance of forces on the fluid molecules near the interface when two immiscible phases come in contact. Molecules in the interior are completely

surrounded by molecules of the same type so external forces balance. At the interface the molecules are exposed to both phases and the attractive force of its own molecules creates a net force that draws the molecules inwards. This force is in turn balanced by the fluids resistance to compression. As a consequence of the force balance, the interface attempts to minimize its surface energy by reducing the interfacial area and ends up taking on a spherical shape.(de Gennes, Brochard-Wyart et al. 2003) The curved shape creates a pressure jump across the interface defined by Young-Laplace equation: $\Delta P = \gamma\kappa$, where κ is the curvature of the interface defined from the principal radii, $\kappa = 1/R_1 + 1/R_2$.

The surface tension, γ, is defined as the energy required to increase the surface area by one unit [J m^{-2}] or the force per unit length [N m^{-1}] tangential to the interface.(de Gennes, Brochard-Wyart et al. 2003). The presence of the interface creates a new set of kinematic and dynamic boundary conditions for fluid flow. Since the two fluids cannot mix, the normal component of the velocity at the interface must match in both phases. Tangential fluid velocities at the interface are also equal in both phases. Marangoni stresses as a result of surface tension gradients create a jump in the tangential stress balance at the interface:

$$\mu_c \left.\frac{\partial u_{\parallel}}{\partial r}\right|_c = \mu_d \left.\frac{\partial u_{\parallel}}{\partial r}\right|_d + \nabla_{\parallel}\gamma \tag{2.1}$$

where $\nabla_{\parallel}\gamma$ is the result of spatial variation in surface tension which may be caused surfactant and temperature gradients. Normal to the interface, viscous stresses and pressure changes must also balance (Baroud, Gallaire et al. 2010; Stone 2010) .

2.2.3 Surfactants

Surfactants have both hydrophobic and hydrophilic parts which makes them soluble in both organic and aqueous phases causing them to migrate and become trapped at an interface. The main purpose of adding surfactants is to lower the surface tension at the interface and to stabilize droplets against coalescence. When surfactants are present the physics of two-phase flow changes significantly (Fischer and Erni 2007). Surfactant adsorption is a dynamic mass transfer process that occurs at a time scale similar to the formation and transport of droplets. Surfactants can be transported by the fluid flow (advection) or by diffusion, in the bulk, and along the interface. As such, the interfacial tension varies between the equilibrium values when surfactants are present

and when they are absent. This leads to coupling between the adsorption process and the production rate of droplets in microfluidic droplet generators (Xu, Li et al. 2008; Steegmans, Warmerdam et al. 2009; Wang, Lu et al. 2009; Baret 2011), and the transport of droplets in microchannels (Stebe, Lin et al. 1991; Stebe and Maldarelli 1994; Baret, Kleinschmidt et al. 2009; Martin and Hudson 2009). Under high shear stress conditions surfactants can be stripped from the interface creating surface tension gradients and Marangoni stresses that oppose the direction of flow (Jin, Balasubramaniam et al. 2004; Darhuber and Troian 2005; Baret, Kleinschmidt et al. 2009; Martin and Hudson 2009; Stone 2010; Baret 2011). Large Marangoni stresses can cause the interface between two fluids to act like a solid (no slip) rather than a liquid interface (continuous velocity and stress) which increases the pressure needed to drive droplets through microchannels.

Selecting the appropriate surfactant is important for applications involving biological materials(Stone 2010; Baret 2011). Proteins and enzymes in particular have a high affinity for absorption and in most cases the absorption is irreversible.(Fischer and Erni 2007) Adsorbed proteins not only reduce the surface tension but also impart a "skin" like mechanical property to the droplet. Adsorption can be minimized by utilizing surfactants with neutrally charged hydrophilic head group; however, not many of these surfactants are available commercially so several research groups have synthesized their own. Roach *et al.* developed a perfluoronated surfactant with an oligoethylene glycol (OEG) end group that prevented absorption of bovine serum albumin.(Roach, Song et al. 2005) Along the same lines, Holtze *et al.* also synthesized a perfluoronated surfactant with a neutral polyethylene glycol head group.(Holtze, Rowat et al. 2008) They demonstrated that the surfactant was able to prevent coalescence under severe packing conditions and was biocompatible by growing yeast cells within the droplets.

The interfacial tension for water/oil interfaces is around 50mN/m and can be reduced to 5-15 mN/m with surfactants.(Baroud and Willaime 2004; Link, Anna et al. 2004; Wang, Lu et al. 2009; Baret 2011). The interfacial tension for water/oil interfaces can be measured using a variety of methods, most of which use droplet formation from an orifice to perform the measurements (de Gennes, Brochard-Wyart et al. 2003).

2.2.4 Carrier Fluids

A number of oils have been used in microfluidic devices for the continuous phase including hexadecane, silicone, sunflower, mineral and perfluoronated oils. Hexadecane and mineral oils can swell PDMS microchannels and are not ideal.(Lee, Park et al. 2003; Link, Anna et al. 2004; Adzima and Velankar 2006) For biological applications perfluoronated oils are preferred because they are chemically and biologically inert, swell less in PDMS microchannels and have a high solubility for gases.(Roach, Song et al. 2005; Holtze, Rowat et al. 2008). Furthermore, the viscosity of the continuous phase should be greater than the disperse phase as this helps facilitate the formation of droplets, this condition is met with most water/oil combinations.

2.3 Droplet Manipulation

Droplet generation, breakup and coalescence is a result of a complex interplay between viscous, capillary, Marangoni, electrostatic and van der Walls forces over a wide range of spatial and time scales. Referring back to the discussion on the Capillary number, four independent variables were identified that could alter the flow field: surface tension, viscosity, flow speed and geometry. Each can be used to manipulate droplet flows. The surface tension can be altered by adding surfactants to the fluids or controlling the temperature. The viscosity may also be thermally manipulated or polymers can be added. Tuning the flow speed changes the influence of shear stress on the droplets. Manipulation can be done globally by changing the overall flow rate or locally through geometric design. Through proper management of these variables, passive methods can be developed to induce formation, breakup and coalescence of droplets. Active techniques based on thermocapillary, magnetic, optical trapping, electrophoresis and dielectrophoresis can also be used to control droplets. Below the various passive and active methods for generating, splitting and merging droplets are summarized

2.3.1 Droplet Generation

When two immiscible phases are injected into a channel the fluids can create discrete droplets or stratified flows depending on the wetting properties, flow velocities, fluid viscosity and geometric features. The high degree of control microfluidic droplet generators are able to achieve stems the fact that the length scales of the channels are comparable to the size of the droplets being formed combined with the laminar flow which is highly controllable and stable. Microfluidic droplet

generators may be divided into passive and active types. The following discussion presents the most common types of droplet generators.

Passive Methods

Passive methods rely on the geometry and flow rates of the two phases to generate droplets through instabilities in the flow field. There are three types of common passive droplet generators used in microfluidics (see Figure 2.2): co-flowing, flow focusing and cross-flow designs.

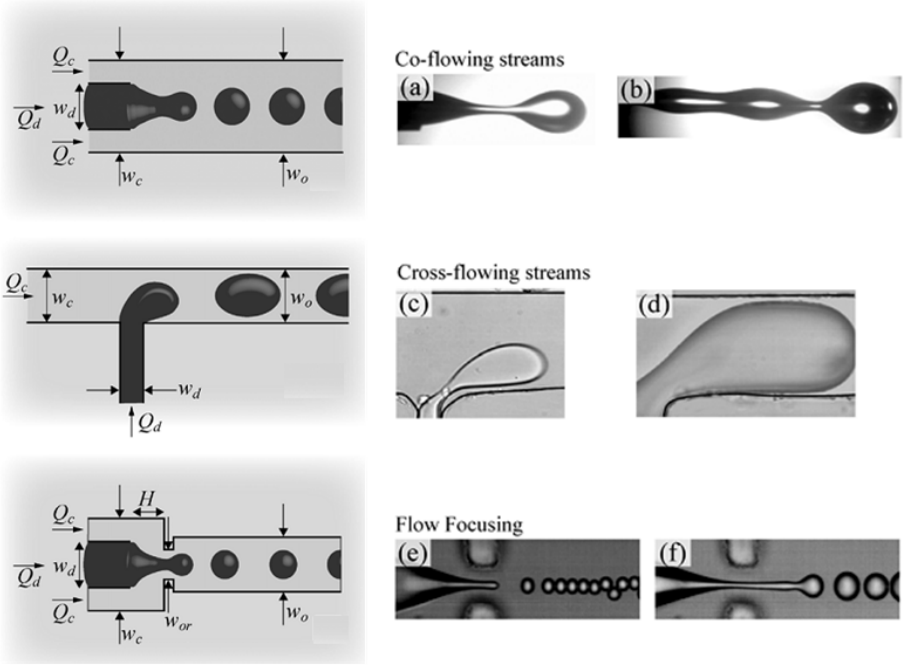

Figure 2.2 Three types of passive microfluidic droplet generators: co-flowing, cross-flowing and flow focusing. Images showing the generators operating in the dripping regime (a,c,e) and jetting (b,f) or squeezing regime (d).(Christopher and Anna 2007)

Co-flowing

The co-flowing design consists of two concentric capillaries with the inner capillary carrying the disperse phase and the outer the continuous.(Umbanhowar, Prasad et al. 2000) As the dispersed phase enters the main channel the viscous stresses created by the continuous phase stretch the interface until it breaks forming a droplet. There are two distinct droplet generating regimes: (a) dripping, where the droplet pinches off near the capillary orifice, or (b) jetting, where droplet breakup occurs at the end of an extended thread. A critical velocity exists that defines the transition between the two regimes.(Cramer, Fischer et al. 2004) Through a detailed stability analysis using lubrication theory, Guillot *et al.* showed that the transition is caused by a change in the breakup mechanism from an absolute instability to a convective instability.(Guillot, Colin et al. 2007; Guillot, Ajdari et al. 2009) At lower velocities the wave created by the Rayleigh-Plateau

instability is able to propagate in both directions resulting in pinch off first near the capillary inlet. While at higher velocities the wave is transported downstream which allows for the stable jet to form before break up. The transition point between the two regimes is a function of the viscosity ratio, Capillary number and the degree of confinement the jet experiences in the outer channel.

The general performance of the co-flowing design is that smaller droplets are formed at higher frequencies when the continuous phase flow rate increases. The flow rate of the inner fluid has less influence on the breakup process. Lowering the surface tension decreases the resistance to breakup resulting in larger droplets. The proximity of the outer capillary walls also influences breakup. Interestingly the viscosity of the disperse phase has no effect on the formation of droplets in the dripping regime.(Cramer, Fischer et al. 2004) The monodispersity, which is the standard deviation of droplet size divided by the average, of co-flowing generated droplets is excellent with typical values around 1%. However, co-flowing design are not often used in planar microfluidic chips since it is difficult to fabricate the concentrically aligned capillaries within the microchannels.

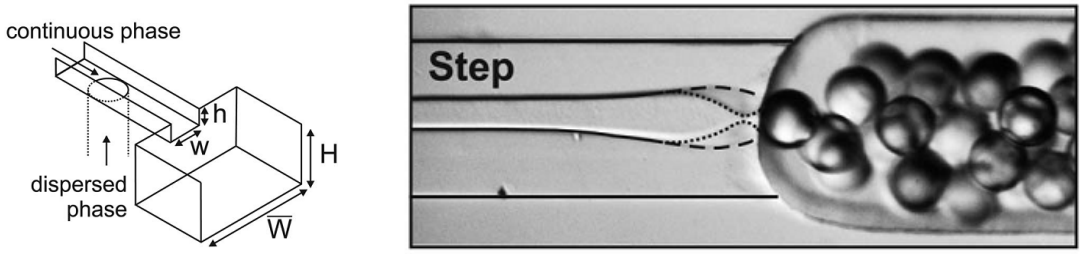

Figure 2.3 Example of microfluidic step emulsification design for producing monodispersed droplets (Priest, Herminghaus et al. 2006)

Co-flowing Step Emulsification

Step emulsification is a modified version of the co-flowing arrangement where a sudden expansion in the microchannel geometry is used to trigger droplet formation as shown in Figure 2.3. Both phases are brought together in a high aspect ratio channel so that they co-flow beside each other. The aspect ratio must be large in order to suppress instabilities from forming before the streams reach the step (Priest, Herminghaus et al. 2006; Saeki, Sugiura et al. 2008; Humphry, Ajdari et al. 2009). The sudden removal of the stabilizing walls at the step destabilizes the thread causing it to break up into droplets.

Operational regimes of the step-emulsification design are similar to the co-flowing case. Depending on the flow conditions (ratio and magnitude of the flow rates), drops can form before the step, or breakup can occur right at the step or jetting can occur past the step. The best conditions for monodispersed droplets to form are when breakup occurs at the step. One of the benefits of the step emulsification design is that highly monodispersed droplets can be produced at extremely high phase fractions (~96%) allowing for foam like emulsions to be made within a microchannel (Surenjav, Herminghaus et al. 2009; Surenjav, Priest et al. 2009).

Flow Focusing

The standard flow focusing geometry in a planar microfluidic chip was first presented by Anna *et al*.(Anna, Bontoux et al. 2003) In this design, the continuous phase and disperse phase flow coaxially at the exit of the inner and outer microchannels, and are then forced through a small orifice. Flowing the continuous phase on either side of the dispersed phase results in more symmetric shearing which improves stability and control over droplet formation. The orifice creates a singular point of high shear stress so breakup consisting occurs at this point.(Tan, Cristini et al. 2006)

The flow focusing design operates in three primary regimes depending on the flow rate ratio (φ): squeezing, dripping and jetting.(Lee, Walker et al. 2009) The squeezing regime appears when the flow rate ratio is very high ($\varphi>1$) so the dispersed phase is the dominant phase in the microchannel. The breakup process is as follows. As the interface enters the orifice it expands and blocks the flow of fluid leading to an increase in upstream pressure which begins to squeeze the neck of the droplet until it pinches off. Droplets that are formed are slightly larger than the size of the orifice and the uniformity is low (~10%). As the continuous phase flow rate is increased the flow focusing generator operates in the dripping regime ($\varphi\sim1$). In this regime, the interface extends just past the orifice and breakup occurs within three orifice diameters. After breakup the remaining interface does not retract but stays fixed within the orifice. Droplets are typically smaller than the orifice but are highly uniform (1-3%). Breakup occurs due to a combination of capillary instabilities combined with viscous drag effects on the emerging droplet. At even higher continuous flow rates ($\varphi<<1$) jetting occurs where the dispersed phase creates a thread that extends at least three orifice diameters downstream. The transition between dripping and jetting is believed to occur when the viscous stresses on the interface are large enough to

advect instabilities downstream before they are formed.(Zhou, Yue et al. 2006) In the jetting regime droplets are typically larger than in the dripping regime and less uniform as breakup is more erratic. The presence of instabilities in the dripping and jetting regime also produces very small (<1μm) satellite droplets behind the larger main droplet.(Tan, Cristini et al. 2006) An additional regime occurs in the presence of surfactants when concentrations are near the CMC at high Capillary numbers known as tip streaming. High viscous stresses advect the surfactant downstream resulting in changes in the surface tension along the interface. A long thread forms that extends far past orifice, which breaks up into very tiny droplets less than a micron in size.(Anna and Mayer 2006)

Several researchers have attempted to model the flow focusing design, but variations in design and use of dimensionless numbers make it difficult to compare results. Recently, Lee *et al.* performed a comprehensive theoretical and experimental analysis attempting to unify previous works .(Lee, Walker et al. 2009) The authors define a Capillary number that incorporates all of the relevant dimensions in the flow focusing design in order to standardize experimental designs. Experiments were performed with nine different designs across a wide number of conditions (flow rate, viscosity ratio). The authors demonstrate that droplet formation can be separated into processes dominated by either the geometry and flow field upstream (squeezing, dripping regimes) or downstream (jetting, tip-streaming) of the orifice. In the upstream operation, performance follows a power law curve of dimensionless diameter versus Capillary number ($d/D_h \propto Ca^{-1/3}$).In the downstream regime, a scaling for the thread length was defined from the centerline velocity of the flow field past the orifice. A critical Capillary number for the cross-over between squeezing and dripping is found at $Ca=1$.

Cross-flow Designs

In cross flow designs, the continuous phase channel and the dispersed phase channel meet at a junction where they are forced through a single exit channel. Several derivations of the design exist where the two inlet channels can be perpendicular (T-junction) (Thorsen, Roberts et al. 2001) or at an angle (Y-junction) (Steegmans, Schroen et al. 2009). Under pressure driven flow the interface is injected into the main channel where shear forces created by the cross-flowing oil phase elongates the interface downstream until eventually a droplet breaks off. First reported by Thorsen et al., the T-junction design has been widely implemented because of its simplicity and the superior control it offers over droplet size. (Thorsen, Roberts et al. 2001)

T-junction generators operate in three regimes: squeezing, dripping and jetting which are a function of the Capillary number and the flow ratio.(Christopher and Anna 2007; De Menech, Garstecki et al. 2008; Gupta, Murshed et al. 2009) Jetting occurs at high Ca numbers where viscous forces overwhelm surface tension. The primary characteristic of jetting is that the interface never recoils back into the dispersed channel and a constant thread extends downstream. Co-flowing is the limit of Jetting where speeds are high enough so that instabilities are convected downstream before they can grow. For monodispersed droplet production the generator is often operated in the dripping or squeezing regimes. The main difference between these two regimes is the degree of confinement that the droplet experiences when it forms.

In the squeezing regime, the strong physical confinement and low Capillary number flow ($\varphi \sim 1$) significantly changes the dynamics of the breakup process. During the formation process droplets grow to a large size where they now begin to influence the local flow field significantly. In the purely squeezing mode, the interface is able to completely penetrate into the main channel and contact the far channel wall before necking occurs. Thus the surface tension forces overwhelm the squeezing pressure during most of the initial penetration period. Drops formed in the squeezing regime are designated as slugs (length greater than the width. Drop formation in this regime is only dependent on the geometry of the T-junction generator and the flow ratio as verified by Garstecki *et al.* and van Steijn *et al* (Garstecki, Fuerstman et al. 2006; van Steijn, Kleijn et al. 2010).

Garstecki *et al.* developed a scaling law that captures the physics of the process: $l/w = \alpha + \beta Q_d/Q_c$, where l is the length of the plug, w the width of the main channel, α is a constant related to the minimum droplet size, and β to the necking time, and Q_d, Q_c are the dispersed and continuous phase flow rates respectively.(Garstecki, Fuerstman et al. 2006) The equation basically states that final droplet size is the volume of the intersection (α) plus the amount of fluid pumped into the droplet as the neck collapses ($\beta Q_d/Q_c$). Note that this equation states that the process is only influenced by the ratio of flow rates and is independent of either the Capillary number or viscosity ratio, which has been verified numerically(De Menech, Garstecki et al. 2008) and experimentally(van Steijn, Kreutzer et al. 2007). Additional studies have shown that the two parameters α and β also depend on the geometry of the generator (Garstecki, Fuerstman et al. 2006; Christopher, Noharuddin et al. 2008; De Menech, Garstecki et al. 2008; Xu, Li et al. 2008; Gupta and Kumar 2010). A recent review by Steegman's *et al*., compared the

validity of several models that have been developed over the past decade and came to the conclusion that the two-stage model best represents the formation process. (Steegmans, Schroen et al. 2009) The problem however is that to date α, β have been treated only as fitting parameters in the development of empirical correlations for a specific T-junction design under study. Consequently, the various correlations performed poorly against external data sets. Recently, van Steijn *et al*. developed a theoretical model for the two parameters in the squeezing regime which combines a geometric description of the shape of the neck during collapse, with continuity arguments for the two phases and a description of the mechanism that leads to droplet pinch-off once the neck reaches a critical thickness. (van Steijn, Kleijn et al. 2009; van Steijn 2010) The model was shown to accurately predict the two scaling parameters across a range of T-junction designs.

Confinement is usually not an issue if the main channel is more than five times wider than the perpendicular channel or if the continuous flow rate is much larger than the dispersed flow rate ($\varphi << 1$). In this regime, also known as the dripping mode, droplet breakup is governed by the balance between the viscous drag on the emerging droplet that penetrates into the main flow and the surface tension resisting deformation. Husny and Cooper-White developed an equation to this effect which was able to predict droplet size with an accuracy of 25% over a wide range of experimental conditions. (Husny and Cooper-White 2006) Droplet size is seen to scale with the inverse of the Capillary number. Xu *et al.* presented a similar analysis using a torque balance and accounted for the extra filling time that occurs as the neck thins.(Xu, Luo et al. 2005) Experiments show that in the dripping regime droplet size depends strongly on the continuous phase flow rate and weakly on the disperse phase flow rate for a given water/oil combination. Recent studies have attempted to build models that bridge the gap between the squeezing and dripping regimes. Xu *et al.* developed a model for all three regimes that combined several previous models with some small modifications.(Xu, Li et al. 2008) The authors propose a modified Capillary number that incorporates the increased velocity around the droplet due to partial blockage of the channel. This collapsed the results of several studies in the dripping regime onto a single line. In the squeezing regime the model of Garstecki *et al.* was used, while in the transient regime an empirical correlation combining both models was proposed. In all cases, the model was able to capture the performance of several T-junction generators in each of the three regimes. Christopher *et al.* developed a transient model with similar arguments and also

included the influence of the viscosity ratio.(Christopher, Noharuddin et al. 2008) Their model agreed reasonably well with experiments, except in the case of high viscosity contrast systems.

Active Methods

Active microfluidic droplet generators are often called "choppers" since they have moving parts that physically break up the fluid stream. Several pneumatic choppers have been developed based on the PDMS valve design. Chen *et al.* developed a device which chopped a hydrodynamically focused stream of water in oil.(Chen and Lee 2006) The chopper consisted of ten pneumatically controlled valves in series. Bransky *et al.* integrated a piezeoelectric actuator that was able to specifically output a single droplet on demand from a reservoir.(Bransky, Korin et al. 2009) Droplet size could be controlled by the pulse strength and time. Pneumatic chambers placed on the sides of a flow focuser can be used to alter the orifice size allowing for greater control over droplet size and the rate of formation.(Abate, Romanowsky et al. 2009)

Electric fields have also been used to form drops. Kim *et al.* used an electric field in a microfluidic flow-focusing device to create a Taylor cone which can generate droplets less than 1μm in size (Kim, Luo et al. 2007). Electrifying the oil phase also helps synchronizes droplet formation in parallel flow-focusing devices.(Link, Grasland-Mongrain et al. 2006) Applying electric fields across a contraction can draw the aqueous phase in and break it off by pulsing the field.(He, Kuo et al. 2006). Formation can also be controlled by adjusting the wettability of the two phases using electrowetting (Malloggi, Vanapalli et al. 2007; Gu, Malloggi et al. 2008). So called "smart fluids" such as giant electrorheological (Niu, Zhang et al. 2009) and magnetorheological fluids (Tan, Nguyen et al. 2010) have been used as the continuous phase to control droplet production and transport. The performance of most passive device can be modulated by using temperature fields using the thermocapillary effect. Tan *et al.* used a local heater right under the flow-focusing point to control droplet size by two orders of magnitude over a temperature range of 20-45°C.(Tan, Murshed et al. 2008) Stan *et al.* instead heated the entire chip using a heat exchanger and was able to achieve similar performance.(Stan, Tang et al. 2009). Baroud *et al.* used pin point lasers and holographic lasers to control droplet performance (Baroud, de Saint Vincent et al. 2007; Baroud, Delville et al. 2007).

2.3.2 Droplet Motion in Microchannels

Historically, much work has been done on the study of gas/liquid flows in capillaries (Bretherton 1961) as well as microchannels.(Wong, Radke et al. 1995; Wong, Radke et al. 1995; Gunther and Jensen 2006; Fuerstman, Lai et al. 2007; van Steijn, Kreutzer et al. 2008) However, there are limited examples of liquid/liquid studies in rectangular microchannels which are more complex due to the asymmetric geometry and the viscous interaction between the fluids. The following discussion focuses on the transport of relatively large droplets which are often termed slugs because they occupy the majority of the cross-sectional area of a microchannel. As such, slugs have a significant influence on the local and global flow fields. The hydrodynamics of slug flow is very rich because of the confined nature of the flow and the interaction with capillary effects which modulate local and global flow fields.

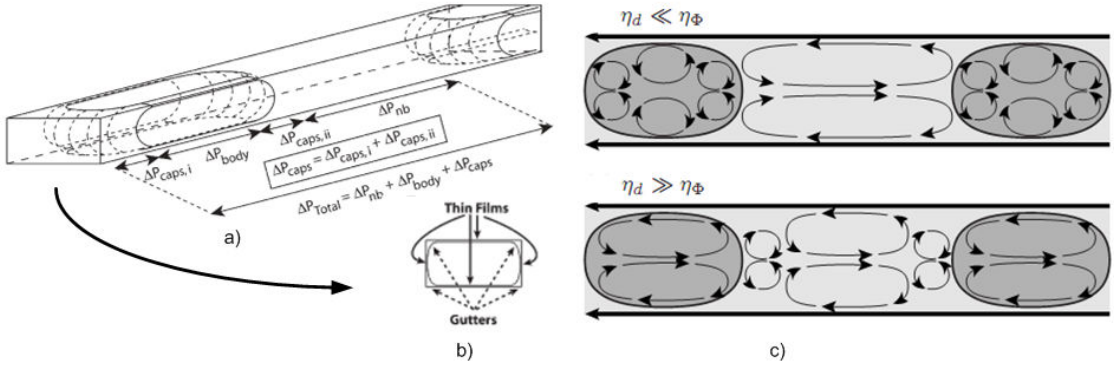

Figure 2.4 Diagram explaining the pressure drop across a slug in a microchannel (a) divided into three main parts the Laplace pressure across the caps, the pressure drop along the body of the droplet and the pressure drop between droplets in the continuous phase. (b) Cross-sectional view illustrating the gutters and thin-film surrounding the droplet in a rectangular channel. (c) Vortices created by the droplet motion in both the continuous and dispersed phases for cases of different viscosities (η).(Fuerstman, Lai et al. 2007; Labrot, Schindler et al. 2009)

The hydrodynamic resistance of a droplet train can be attributed to five different effects (see Figure 2.4): (a) Laplace pressure across the droplet caps (b) viscous dissipation in the thin film around the droplets (c) continuous fluid flow through the corners around the droplets (d) viscous dissipation from counter-rotating eddies in the continuous phase and (e) droplets. The Laplace pressure of a droplet depends on the surface tension and the height/width of the microchannel. For smaller microchannels the Laplace pressure can increase substantially reaching over 500 Pa in 10μm channels. In liquid/liquid two phase flow the two end caps generally have similar shapes so the pressures are balanced. However, under high flow rate conditions the leading and trailing end caps can change shape which changes the pressure balance and increases the apparent

resistance of a droplet. The fluid flow through the thin films can be ignored because of the large size of the gutters.(Wong, Radke et al. 1995) At the interface, the kinematic boundary condition enforces that the tangential fluid velocity is continuous at the interface which creates internal eddies within both the droplets and continuous phase. These eddies have been visualized using u-PIV techniques in straight channels, curves and backsteps, with the flow field even resolved in 3D in some cases (Kinoshita, Kaneda et al. 2007; Malsch, Kielpinski et al. 2008; Timgren, Tragardh et al. 2008).,

Through several experimental studies a number of factors have been identified that influence the droplet hydrodynamic resistance. These are the viscosity ratio between the two fluids, Capillary number (surface tension, droplet velocity) and droplet size and spacing. Adzima and Velankar was the first to study the pressure drop across a train of droplets using pressure taps along a microchannel.(Adzima and Velankar 2006) For water/glycerol droplets in hexadecane the authors found that the hydrodynamic resistance increases with droplet size and decreases with droplet velocity. Vanapalli *et al.* used a highly sensitive microfluidic manometer to study the resistance of a single droplet in a microchannel using water/glycerol droplets in mineral oil.(Vanapalli, Banpurkar et al. 2009) They found that the resistance increases with droplet size up to a maximum at a plug size of approximately $l/w=3$. At lower droplet sizes approaching the dimensions of the microchannel or less the droplets have minimal resistance. Past the peak point, the resistance actually decreases as the lower viscosity of the droplet becomes more influential. The resistance also decreased with higher Capillary number and higher droplet viscosity reaching a minimum when the viscosities of the two fluids are equal. Labrot *et al.* built upon these results and studied the influence of droplet spacing on resistance.(Labrot, Schindler et al. 2009) They found a cooperative effect, where droplets closer together actually decreased the overall resistance of the droplet train. This result suggests that eddies formed in the continuous phase actually help to lower the combined resistance of droplets. In addition, surfactants can influence the droplet motion by inducing additional stresses in the thin film region (Stebe, Lin et al. 1991; Stebe and Maldarelli 1994; Fuerstman, Lai et al. 2007).

In a microfluidic network the distribution of flow depends on the hydrodynamic resistance of the branches in an analogous manner to electric current flow. Since droplets contribute to the hydrodynamic resistance of a channel their presence also has an influence on the global flow field. One of the most interesting examples is the transport of droplets through a simple node or junction with only two outputs. Depending on the relative hydrodynamic resistance of the two

channels droplets may sort into only one branch, or both. This occurs because the trajectory of a droplet entering the junction depend on the history of decisions made by a number of preceding droplets which still populate the two outlet branches. Under certain conditions the sequence of trajectories result in a highly stable and repeatable pattern (Fuerstman, Garstecki *et al.* 2007; Cybulski and Garstecki 2010; Sessoms, Amon *et al.* 2010; Smith and Gaver 2010) These far-field interaction between droplets have been exploited to create interactive elements such as logic gates (Cheow, Yobas *et al.* 2007; Prakash and Gershenfeld 2007), signal encoder/decoders (Fuerstman, Garstecki *et al.* 2007; Behzad, Seyed-allaei *et al.* 2010), sorters (Cristobal, Benoit *et al.* 2006; Yamada, Doi *et al.* 2008; Cybulski and Garstecki 2010), and automated coalescence (Niu, Gulati *et al.* 2008) and storage units (Boukellal, Selimovic *et al.* 2009).

The velocity of the slugs is also of interest to LOC design. Droplets move at a velocity slightly different than the average velocity of fluid flow which is described by a slip factor, β (Schindler and Ajdari 2008; Labrot, Schindler et al. 2009):

$$u_d = \frac{Q_m \beta_{slip}}{wh} \tag{2.2}$$

For circular capillaries, Bretherton showed that the existence of the lubrication films causes long inviscid slugs to move faster than the surrounding fluid as (Bretherton 1961):

$$\frac{u_{slug} - u_{ext}}{u_{slug}} \propto Ca_d^{2/3} \tag{2.3}$$

In polygonal capillaries, such as rectangular microchannels, the contribution of the gutters changes the physics of the problems. Wong *et al.* showed that for inviscid slugs the gutter flux occurs in the direction of the motion of the slug and exceeds the film flow by an order of magnitude (Wong, Radke et al. 1995; Wong, Radke et al. 1995). As such, the slugs move at a speed slower than the surrounding fluid:

$$\frac{u_{slug} - u_{ext}}{u_{slug}} \propto -Ca_d^{1/3} \tag{2.4}$$

For either conditions, the slugs velocity is only slightly different, ~0-10%, than the surrounding fluid for typical flow conditions in microchannels. For viscous slugs, the problem becomes more complicated due to the coupling between flows inside and outside the slug (Hodges, Jensen et al. 2004; Ajaev and Homsy 2006). Furthermore, the presence of surfactants can cause Marangoni

stresses which create local variations in the boundary conditions at the interface further complicating the issue (Stebe, Lin et al. 1991; Stebe and Maldarelli 1994; Ajaev and Homsy 2006; Fuerstman, Lai et al. 2007). Generally the addition of surfactants decreases the velocity of droplets compared to the non-surfactant case because of the retardation created by the Marangoni stresses; however, when conditions exist where the mass transport of surfactants (high concentration, fast adsorption/desorption kinetics) exceeds the depletion created by convective transport the droplet will move as if surfactants were absent (Stebe, Lin et al. 1991; Stebe and Maldarelli 1994) .

Throughout the microfluidic literature a wide range of slip factors have been reported that seem to exceed the estimates put forth by theoretical arguments. Fuerstman *et al.* reported a slip factor of 0.83 for bubbly slugs without surfactants and 0.5 when a minor amount was present (Fuerstman, Lai et al. 2007). Vanapalli *et al.* measured the velocity of viscous slugs and found a constant slip factor of 1.28 regardless of the viscosity contrast, length of the slug or the capillary number (Vanapalli, Banpurkar et al. 2009). Labrot *et al.* reported a slip factor of 1.6 for viscous droplets and Sessoms *et al.* found that the slip factor was $\beta>1$ for droplets less than the width of the channel and $\beta<1$ for droplet greater than the width (Labrot, Schindler et al. 2009; Sessoms, Belloul et al. 2009). The disparity between reported results prompted Jakiela *et al.* to perform a comprehensive study of droplet velocity measurements in rectangular microchannels across a range of droplet sizes, capillary numbers and viscosity contrast ratios (Jakiela, Makulska et al. 2011). The results showed a complex dependency on all three parameters as shown in Figure 2.5. For $\eta<1$ the slip factor is highly sensitive for $1.5<l/w<3$ varying from $\beta\sim0.95$-1.35; and nearly constant at $\beta\sim1$ for $l/w>3$. For moderately viscous droplets, $\eta=3.3$, the droplets were always slower than the oil $0.6<\beta<0.95$ and very sensitive to the Capillary number across all lengths. Then for highly viscous droplets, $\eta=33.3$, the trend between the slip factor and the size of the droplets was linear and insensitive to the capillary number. This complex behaviour has not been explained by any theoretical model to date. Additional work is still required to develop, at the very least, an empirical model for the transport speed of droplets in microchannels.

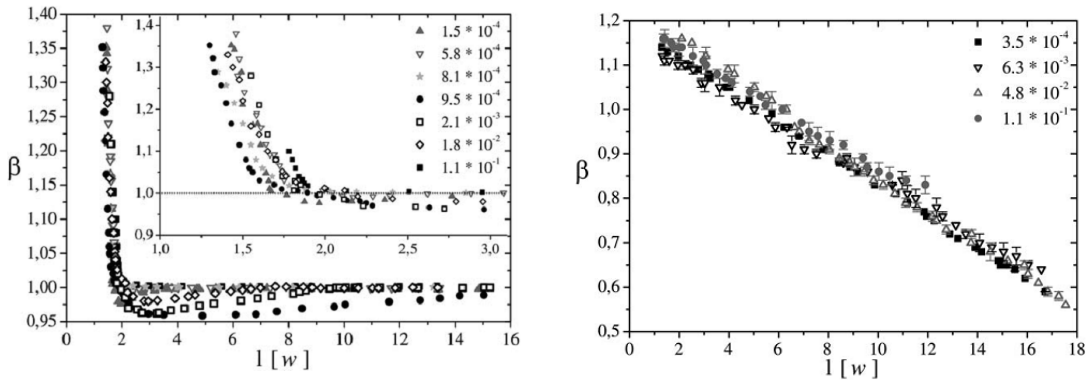

Figure 2.5 (Left) Slip factor measured for droplets of length l/wc with a viscosity contrast η=0.3 at different capillary numbers. (Right) Slip factor for η=33 against size and capillary number (Jakiela, Makulska et al. 2011)

2.3.3 Droplet Breakup

Splitting droplets increases the operational capacity and functionality of a device since these droplets can be processed further by merging with other droplets. Several techniques have been developed to effectively break up a droplet into two or more droplets of predetermined size. The majority of breakup mechanisms in microchannels are based on using shear forces to elongate the droplet past a critical point where breakup occurs (Stone 1994; Cristini, Guido et al. 2003; Cristini and Tan 2004). These methods are passive using geometrical constrictions to split the droplets into precise volumes (Cristini and Tan 2004; Link, Anna et al. 2004; Adamson, Mustafi et al. 2006; Menetrier-Deremble and Tabeling 2006; Yamada, Doi et al. 2008; Leshansky and Pismen 2009).

The most common design is the T-junction bifurcation shown in Figure 2.6. Droplet breakup is controlled by varying the flow rate of the continuous phase and the relative resistances of the two outlet channels(Link, Anna et al. 2004). For each droplet size there is a critical Capillary number where the droplet will breakup. Below this value the droplet will instead be transported down one of the outlet channels. The channel that the droplet chooses depends on which one has the highest local velocity at the moment the droplet reaches the junction.

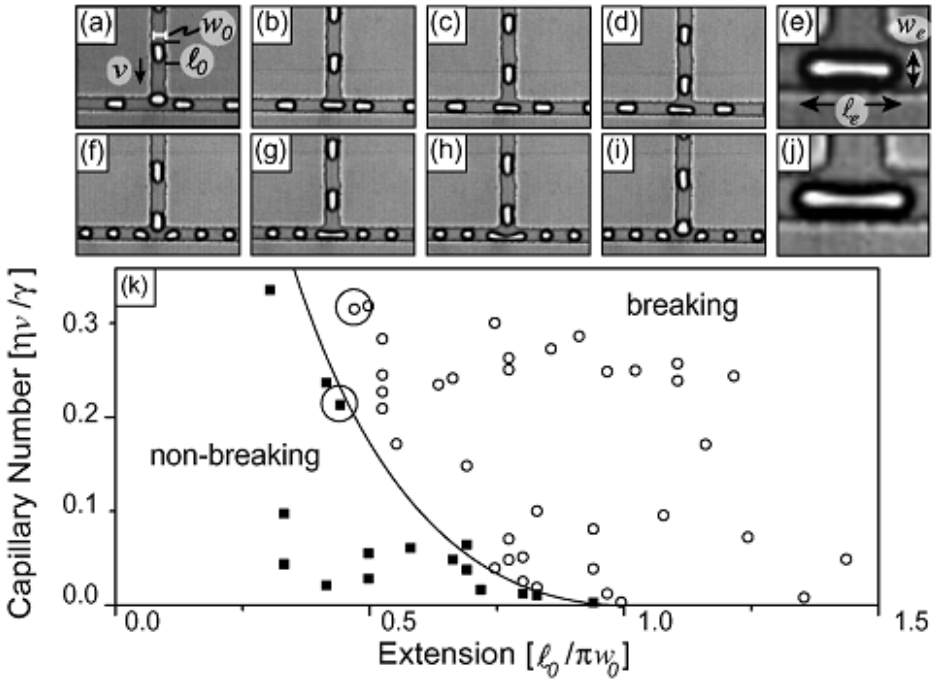

Figure 2.6 Droplet breakup at a bifurcation showing the difference of non-breaking droplets (a-e) and breaking droplets (f-i). Breakup is defined by the extension ratio of the droplet prior to it reaching the junction (l_o, w_o) and the velocity v. (k) Shows the phase diagram for breaking (■) and non-breaking (○) droplets versus Capillary number and the initial extension of the droplets (Link, Anna et al. 2004).

In their original analysis of breakup in a bifurcating channel, Link *et al.* concluded that breakup occurs when the Rayleigh instability forms as the droplet is being stretched at the junction(Link, Anna et al. 2004). Performing studies on slugs of various sizes, defined by their width and length, the group found that droplets being stretched at the junction with characteristic extension criteria $\ell/(w\pi) > 1$ always split. The authors inferred that this coincides with the Rayleigh-Plateau stability limit that a droplet will breakup once the length exceeds the circumference. Based on a scaling analysis of the shear rates, an equation was derived for the critical Capillary that was in excellent agreement with experimental results, $C_r = \alpha\varepsilon_o\left(1/\varepsilon_o^{2/3} - 1\right)^2$, where α is a fitting constant relating the viscosity ratio and geometry, and ε_0 is the extension of the droplet (see Figure 2.6).

In a later work by Leshansky and Pismen (Leshansky and Pismen 2009), they argue that the Rayleigh instability is probably not the cause of the breakup due to the confined nature of the flow and the low Capillary number, as well as evidence from many numerical models. They instead developed a 2D analytical model based on lubrication flow and the pressure build up caused by the droplet blocking the outlet channels as it is being elongated. Essentially the

elongating droplet blocks the flow to the outlet channels increasing the pressure upstream. This causes the droplet to be squeezed at the stagnation point until it is pinched off into two separate droplets. The initial dimensions of the plug are critical, since the plug must be long enough to effectively block the two outlet channels while being stretched. Their resulting analysis also produced an equation that was in good agreement with 2D numerical data and has a similar profile to the curve of Link *et al*.

The size of the two daughter droplets can be controlled by making the two outlet channels asymmetric, either through design of the channels, or through manipulation of the flow rate and pressure (Song, Tice et al. 2003; Link, Anna et al. 2004; Yamada, Doi et al. 2008). However, given that the presence of droplets in the outlet channels changes the resistance of the channel, any deviation from the desired setting can cause erratic droplet breakup(Adamson, Mustafi et al. 2006). This is especially true when multiple splitters are combined serially to repeatedly breakup droplets. Therefore, controlling droplet breakup requires not only reaching the required critical Capillary number for breakup but also limiting the influence of disturbances in the outlet channels. One option is to use constrictions at the breakup junction to locally increase the Capillary number for breakup, and then expand the outlet channels to reduce the hydrodynamic resistance of the droplets. Also, splitting of viscoelastic droplets is less stable due to extensional shear thinning compared to Newtonian droplets of the same viscosity (Christopher and Anna 2009). Limited examples exist of active splitting of droplets in channels, though, electric fields have been used to charge droplets while splitting for further manipulation (Link, Grasland-Mongrain et al. 2006).

2.3.4 Droplet Coalescence

Droplet fusion begins by first draining the fluid between the droplets until they are separated by very thin film. Any disturbance or imbalance on the film will then cause it to rupture and the droplets will fuse. These disturbances can be created by a sudden change in shear stress or by electrical fields. Synchronizing the arrival of merging droplets under high flow rate conditions is the main difficulty with performing fusion (Teh, Lin et al. 2008).

Passive fusion involves proper design of the microchannel geometry to control coalescence (see Figure 2.7). The most common design involves passing the droplets through an expansion region where the droplets slow down, and the continuous phase is allowed to drain around the droplets.

The droplets then exit through a sudden contraction that increases the flow rate and creates the disturbance required to break the film. Several examples of passive designs are shown in Figure 6. Hung *et al.* placed a tapered outlet at the exit of a dual T-junction generator to merge droplets for CdS nanoparticle synthesis.(Hung, Choi et al. 2006) A phase diagram was presented identifying the flow rates and droplet frequencies where coalescence occurred. Bremond *et al.* also studied droplet fusion in an expansion/contraction channel and found that coalescence actually occurs when the droplets decompress.(Bremond, Thiam et al. 2008) The authors demonstrated that the droplets do not coalesce at impact, but at the point where they begin to separate from each other at the exit. Just before fusion two facing nipples can be seen that precede film rupture. It is hypothesized that these nipples form due to the vacuum pressure created between the droplets as they are pulled apart which has been proven analytically (Lai, Bremond et al. 2009) .

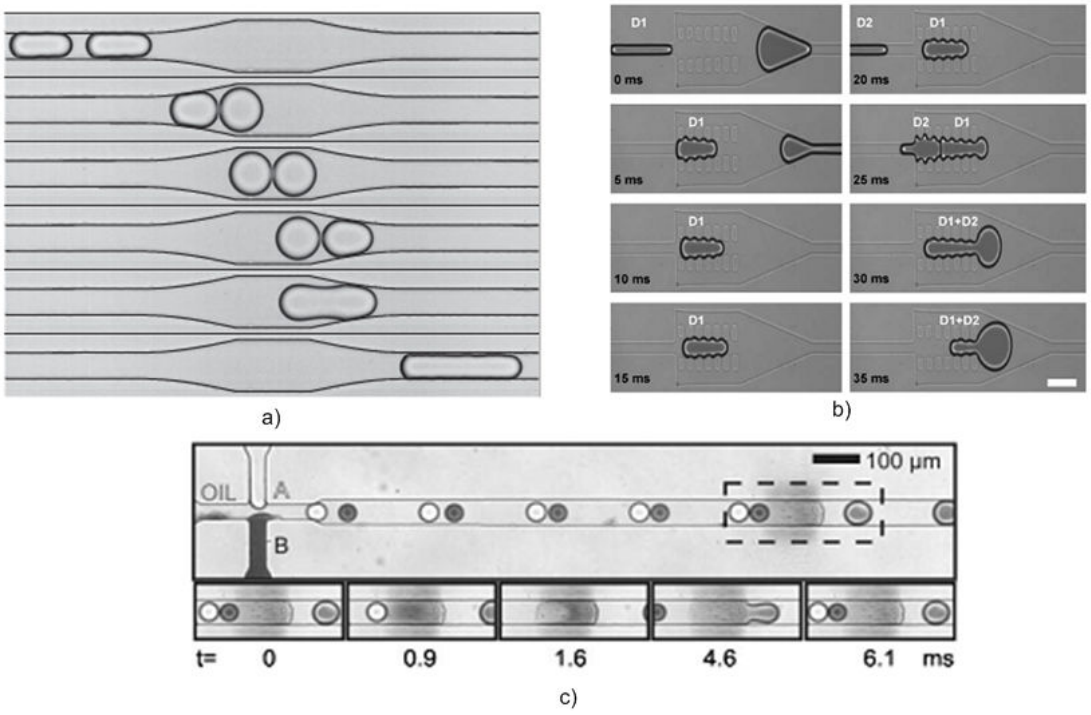

Figure 2.7 Examples of passive coalescence techniques. (a) expansion/contraction chamber showing that droplets merge upon decompression at the exit(Bremond, Thiam et al. 2008) (b) pillar design (Niu, Gulati et al. 2008) (c) surface treatment design (gray area is hydrophilic treated segment of the microchannel). (Fidalgo, Abell et al. 2007).

In a slightly different design, Niu *et al.* used a series of pillars in the expansion region to trap the incoming droplet and hold it in place until the droplet behind merges.(Niu, Gulati et al. 2008) This design allows for greater flexibility in the droplet spacing and timing since the droplet is not

released from the pillars until it merges. The process is governed by a competition between surface tension forces holding the droplet in place, and hydrostatic forces created by the blockage of fluid flow through the pillars. When one droplet is present then only a few pillar channels are blocked so the pressure upstream is low. However, once the second droplet merges, the majority of the pillar gaps are blocked and the pressure upstream builds eventually forcing the merged droplet out.

Christopher *et al.* studied droplet fusion caused by head on collisions at a T-junctions. (Christopher, Bergstein et al. 2009) Droplets from two different streams collided at the junction and either merged, split, or slipped by each other depending on their initial speed. The process of head on collisions is governed by the time the droplets are in contact and the rate of film drainage. Droplets will only coalesce at low speeds and either split or slip at higher speeds. The critical Capillary number above which coalescence will not occur follows a power law dependency that was developed for droplets in unbounded extensional flows. The slipping/splitting process obeyed the critical Capillary equation for breakup at a bifurcating channel developed by Link *et al.*(Link, Anna et al. 2004)

Another passive method involves using selectively fabricated hydrophilic patches in the channel to trap aqueous droplets so they can merge with the droplet behind. Fidalgo *et al.* demonstrated this process by modifying a PDMS channel with poly (acrylic acid) (PAA) using a UV-photopolymerization technique.(Fidalgo, Abell et al. 2007) Cross-contamination at the fusion site is the greatest disadvantage of surface treatment fusion designs. Reagents can also be directly injected into droplets by using a side channel stream that merges with the passing droplet.(Chen and Ismagilov 2006; Song, Li et al. 2006; Li, Boedicker et al. 2007) The volume of fluid inject can be controlled by the flow rate of the side stream. Managing the surface wettability is critical, hydrophilic side channels provide the best control over the process as they prevent the continuous phase from entering the side channels. However, there is still concern with cross contamination between plugs as the merging process can leave behind trace elements in the side channel(Li, Boedicker et al. 2007).

The advantage of passive techniques is that they require no interaction and are easy to implement; their disadvantage is that there is little versatility or control over the coalescence process. Each design has a limited operational range determined by the speed of the droplets (i.e. Capillary number) and there spacing before entering the coalescence chamber.

To improve the viability and control of the droplet process a number of active methods have been developed, which may be categorized by the method used to control the coalescence process: flow control, thermal, and electrical.

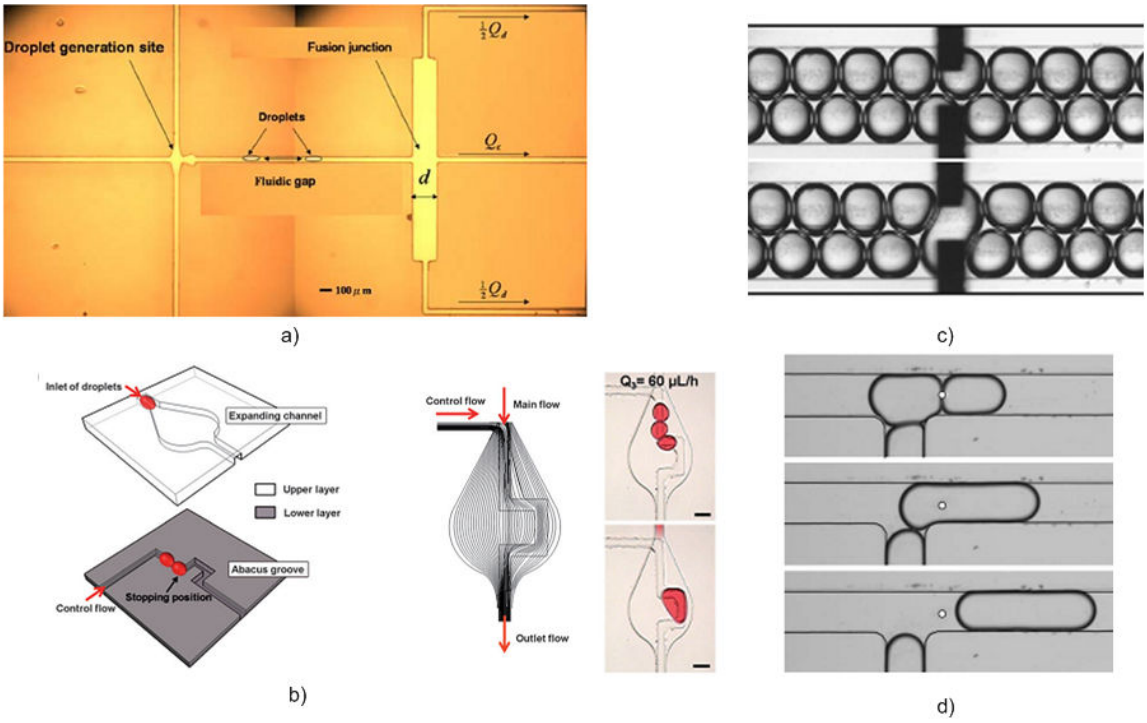

Figure 2.8 Examples of active coalescence techniques. (a) Flow rectifying design where the perpendicular (up/down) channels on the right control the film draining time (Tan, Ho et al. 2007) (b) "abacus" design with microfluidic rail showing the streamlines created within the coalescence chamber and the merging of three drops in an experiment.(Um and Park 2009) (c) electrocoalescence of a single pair of droplets (Priest, Herminghaus et al. 2006) (d) thermocapillary merging with a laser (indicated by white dot). (Baroud, de Saint Vincent et al. 2007)

The flow rectifying design has droplets entering a cross-channel configuration as shown in Figure 2.8.(Tan, Fisher et al. 2004; Tan, Ho et al. 2007) The draining rate and time spent in the fusion chamber is controlled by the flow rates into the perpendicular channels. This allows direct control over the number of droplets that can be merged in a wide range of flow conditions. Um and Park developed a novel microfluidic droplet "abacus" that can accurately add together specific number of droplets (see Figure 2.8b). The designs works by transporting droplets along a microfluidic "rail"-essentially a secondary microchannel on the bottom of the main channel along which the droplets travel.(Um and Park 2009) The droplets enter a chamber where the rail turns abruptly so that the droplet becomes trapped by surface tension at the edge. While the droplet is held in place a second droplet collides and merges. Once the drag force on the merged droplet is high enough the merged droplet is released. The ingenious part of this design is that the drag force can be

controlled by the flow rate of continuous phase to the rail microchannel, and therefore the number of droplets that are merged may be set.

Droplet fusion can be controlled using thermocapillary effects. A laser was used to heat the interface between adjacent droplets until they fused (Baroud, de Saint Vincent et al. 2007; Cordero, Burnham et al. 2008). The temperature gradient created by the laser induces Marangoni stresses due to the temperature dependent surface tension and viscosity of the fluids. Optical tweezers can also be used to selectively force two droplets together until they merge(Lorenz, Edgar et al. 2006; Lorenz, Edgar et al. 2007)

The most common method for actively combining droplets is through electrofusion using either DC or AC fields. A non-uniform electric field created by either spatial or temporal variations can be used to control droplet motion by dielectrophoresis (DEP). DEP can only be implemented if the dielectric properties of the continuous phase and disperse phase are different, which is the case for water in oil emulsions. Since the conductivity of the aqueous droplet is usually much higher than the insulating oil, the electric field vanishes within the droplet and a dipole is created. Two droplets in the electric field align their dipoles and are attracted to each other by a Columbic force. The strength of the force is proportional to the square of the applied electric field.(Eow, Ghadiri et al. 2001) The electrocoalescence process depends on the strength of the applied electric field and the frequency. There exists both an upper and lower limit for the electric field. Typically, the electric field is in the range of 500-1000V/cm. At the upper limit, a repetitive process occurs where the droplets approach each other quickly but are then violently repelled at the last moment, creating many small satellite droplets in between them. The process is caused by an unstable Taylor cone that forms between the droplets (Chabert, Dorfman et al. 2005). At the lower limit, the instability is not strong enough to break the thin film between the droplets.

Several designs based on combined DEP and electrocoalescence have been developed. Wang *et al.* used DEP to move a droplet into a waiting chamber on the side of the main microchannel using DC fields.(Wang, Yang et al. 2009) A secondary droplet also manipulated by DEP was positioned into the chamber and then a high electric field was applied to merge the two droplets. A similar design was also presented by Tan and Takeuchi but the droplets flowed out of the chamber continuously(Tan and Takeuchi 2006). Priest *et al.* used two closely spaced electrodes to induce coalescence of tightly packed droplets in a microchannel (see Figure 2.8c).(Priest, Herminghaus et al. 2006) In a parallel approach that uses electric fields, Link *et al.* created

droplets with a net electric charge by forming them under an applied electric field. (Link, Grasland-Mongrain et al. 2006) Oppositely charged droplets were easily fused simply by bringing them close together.

It is also important to point out that uncontrolled and unwanted coalescence of droplets can occur within microchannels. This problem usually manifests itself when the surface tension is very high (~50mN/m) so that there is a great desire for droplets to merger in order to reduce their combined surface area. Uncontrolled fusion can also occur when droplets are traveling at different speeds in the same microchannel which can occur if the droplets are of different size or viscosity (Jin, Kim et al. 2010). Coalescence can be avoided by using surfactants to stabilize droplets. If surfactants cannot be used to stabilize droplets, then a third mutually immiscible phase can be used to separate them(Khan and Duraiswany 2009). Ismagilov's group has demonstrated this process with both a gas phase (Zheng and Ismagilov 2005) and liquid phase (Chen, Li et al. 2007) placed between reagent plugs. The surface tension of the third phase must be chosen correctly so that it forms a discrete droplet and does not engulf the original droplet.

2.3.5 Droplet Indexing, Sorting, Storage and Extraction

The basic functions of generating, splitting and merging are fine for many simple applications. However, as the size and complexity of an experiment increase new functions are required including the ability to index, sort, store and extract droplets. In the following section, methods that have been developed to perform these tasks are discussed.

Indexing

When many droplets containing different contents are used on the same chip, an indexing system is required to keep track of the droplets. A simple method is to keep the droplets in a specific order once they are formed; however, this becomes impractical once droplets are split, merged or sorted throughout the chip.

Zheng *et al.* presented a method that involves tracking the reagent content of a droplet through matched concentrations of reporter dyes.(Zheng, Tice et al. 2004) The dyes are stored in a secondary droplet that immediately follows the reagent droplet to avoid any possible interference with the reaction. To create alternating droplets, a double-cross injector was used with the reagent and dye streams coupled together. Although this method is useful, it is limited by the need to also

account for the additional dye streams and synchronized transport of both the reaction and indexing droplets.

A more powerful method involves the use of optically barcoded particles that are added to the droplets. Each particle contains a unique sequence of markers that identifies the droplet. Such particles have been fabricated from silica beads encased in layers of different fluorescent material. The optodiversity of the bead can be achieved through four methods: a) control of the fluorescence excitation/emission wavelengths of the dyes b) fluorescence intensity of the dyes c) internal structure of the bead to influence the optical diffraction properties and d) coupled fluorescence energy transfer. In the later case, the excitation/emission of one layer is used to activate another layer with matching fluorescent properties. Up to nine different fluorescent properties and two light scattering properties have been used to distinguish particles, which allows for the encoding of a minimum of 2^9 combinations (assuming only 2 possible set points for each property).(Battersby, Lawrie et al. 2002) A complimentary technique utilizes graphical barcoding rather than spectrographic coding of the particles. Each particle contains an image that can be scanned much like the barcode tags in the grocery store. Pregibon *et al.* demonstrated the fabrication of these particles in a microfluidic device using a continuous flow lithography process.(Pregibon, Toner et al. 2007)

Sorting

Sorting is an essential function of high throughput assays in order to isolate the droplets of interest from the general population and can again be divided into passive and active types. Passive sorting works on the principal of applying a bias to constantly differentiate droplets based on a sorting parameter. Active sorting uses a mechanism to manipulate the motion of the droplets combined with a means to detect the sorting parameter.

Passive methods are limited to sorting droplets based on size. The primary working principal is based on the drag force experienced by different sized droplets. Tan *et al.* developed a number of designs for passively sorting droplets at a bifurcation.(Tan, Fisher et al. 2004; Tan and Lee 2005; Tan, Ho et al. 2008) The branches of the bifurcation are specifically designed so that the streamlines split unevenly. The two exit flows exert a drag force on the droplets in proportion to their projected area and flow rate. Depending on the droplet size there is a shear force imbalance that directs the droplet to the higher flow rate channel. Smaller droplets may experience a force from only one exit channel and will sort accordingly into it. Such designs have been used to

separate smaller satellite droplets from larger droplets for purifying the droplet stream.(Tan and Lee 2005) An improved design demonstrated separation of larger droplets with differences of only 4μm in diameter(Tan, Ho et al. 2008).

Electrical based schemes are the primary method for manipulating droplets in active sorting. Several dielectrophoresis (DEP) based devices have been developed. Wang *et al.* demonstrated sorting into five separate chambers using DEP activation.(Wang, Flanagan et al. 2007) Ahn *et al.* used embedded ITO electrodes to sort droplets at frequencies up to 4 kHz.(Ahn, Kerbage et al. 2006) The electrodes were designed to maximize the electric field gradient for deflecting the droplets. In a complementary technique, Link *et al.* sorted charged droplets using low strength electric fields.(Link, Grasland-Mongrain et al. 2006) In recent years, manipulation has been combined with detection systems for developing fully automated sorting systems. Niu *et al.* used a capacitive sensor integrated in the chip to differentiate droplets by dielectric properties, and sorted them downstream by DEP.(Niu, Zhang et al. 2007) The system was all encompassing, with complete electronics for full automation. An electrochemical sensor was developed by Liu *et al.* to detect the size and speed of passing droplets.(Liu, Gu et al. 2008) Nguyen *et al.* developed an optical detection system with integrated optical fibres for measuring the droplet size.(Nguyen, Lassemono et al. 2006) Finally, Baret *et al.* developed the most complete droplet sorting system based on fluorescence detection and DEP manipulation using a microscope and photomultiplier tube.(Baret, Miller et al. 2009) Sorting reached rates of 2 kHz and was only limited by the shearing of droplets at higher flow rates. The false positive error of the system was only 1 in 10000 at maximum throughput.

It is important to note that several other methods are available for manipulating droplets in microchannels. Optical trapping can be used to individually position droplets(Nagy and Neitzel 2008). Thermocapillary manipulation with lasers has been used to valve, merge and sort droplets through the generation of Marangoni stresses (Baroud, de Saint Vincent et al. 2007; Baroud, Delville et al. 2007; Cordero, Burnham et al. 2008; Delville, de Saint Vincent et al. 2009). Droplets can also be manipulated by using secondary droplets that have controllable rheological properties. Ngyuen *et al.* used magnetic fields combined with ferrofluid droplets to control primary droplets.(Nguyen, Ng et al. 2006) Niu *et al.* controlled droplet traffic with inter droplets of giant electrorheological fluids (GER), whose viscosity can change more than three orders of magnitude under high electric fields.(Niu, Zhang et al. 2009). Capacitive sensing can also be

employed with GER fluids to generate feedback control of sorting and droplet manipulation (Zhang, Wu et al. 2008). A recent review discusses the use of electrorheological fluids for droplet control (Zhang, Gong et al. 2009).In addition, surface acoustic streaming has been used to deflect droplets into sorting channels (Franke, Abate et al. 2009; Yeo and Friend 2009).

Storage

Several applications require long term storage of droplets on the order of 1 minute to several hours or days. Depending on the need, different storage systems can be employed. For short reaction times (<1min), short microchannel delay lines have been used that keep the droplets in order.(Song, Tice et al. 2003) For low volume storage with long reaction times (>1day) droplets can be stored in single file within a long microchannel on-chip or off-chip in a capillary (Laval, Lisai et al. 2007). Zheng *et al.* used the off-chip concept to develop a capillary cartridge that contains a sequence of droplets with different composition (Zheng and Ismagilov 2005) The idea is to use these preformed cartridges to screen a sample against several standard reaction conditions contained within the droplets. Droplets can be re-injected into a microfluidic chip after months of storage without degradation.

As the number of droplets increases, the pressure required to pump the droplets along a microchannel in single file become enormous. Consequently, droplets need to be stored in low hydrodynamic resistance chambers or reservoirs. However, in such designs the order of the droplets is lost so these chambers can only be used when the reaction time is much longer than the reinjection time. For intermediate reaction times (~1min-1hr), delay lines can be implemented that control the order of the droplets to some degree. Frenz *et al.* designed a delay line system with only a10% dispersion in delay times.(Frenz, Blank et al. 2009) The design consists of a chambers connected serially with constrictions in between that redistribute the droplets repeatedly along the delay line.

To acquire time-lapsed information on a large number of droplets it becomes more practical to immobilize the droplets at fixed locations within the chip. Droplets are trapped in an array of wells by either surface tension (Shim, Cristobal et al. 2007; Schmitz, Rowat et al. 2009; Abbyad, Dangla et al. 2011; Dangla, Lee et al. 2011) or shear stress(Huebner, Bratton et al. 2009) and released by a change in flow conditions. One concern with long-term storage in PDMS devices is that the material is permeable to water vapour; therefore, these devices should be stored in saturated environments(Carroll, Rathod et al. 2008; Koster, Angile et al. 2008). In some instance

water can also partition into the oil phase changing the droplet volume.(Huebner, Bratton et al. 2009)

Extraction

In many applications, recovering the contents of the droplets is important for further processing or chemical synthesis. Many analytical techniques such as mass spectrometry, capillary electrophoresis, isoelectric focusing and liquid chromatography are not compatible with droplets and require a continuous flow stream. Thus converting droplet microfluidics into continuous phase microfluidics is essential for expanding the functionality of droplet devices.

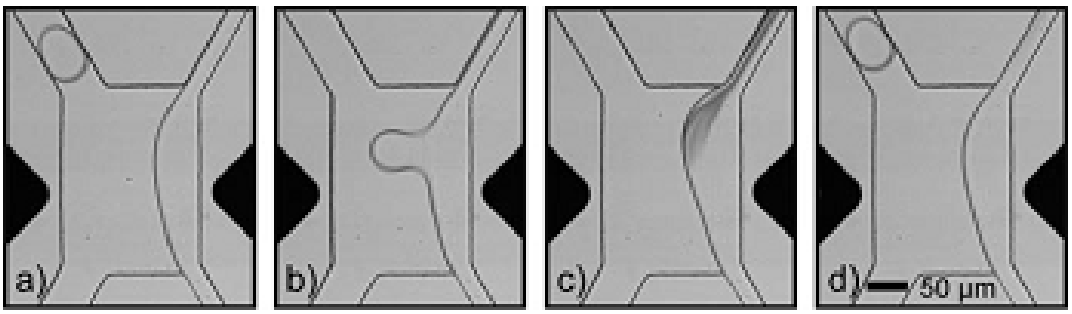

Figure 2.9 Extraction technique with second microfluidic two-phase "wall" (on right) where electrodes (black triangles) selectively merge the desired droplet with the continuous stream to create a reaction (c).(Fidalgo, Whyte *et al.* 2008)

Bulk recovery can be achieved by outputting the droplets to a reservoir and then using a destabilizing agent to disintegrate the droplets (Holtze, Rowat et al. 2008). Though this does not provide control over which droplets are recovered and the two phases still need to be separated. A few examples exist of on-chip droplet extraction. The first example uses a stable liquid/liquid interface that the droplet can pass by and merge with (see Figure 2.9). The interface can be formed through proper surface modification of the microchannel or by operating the system in the stratified regime of two-phase flow. Fidalgo *et al.* developed an extractor with a "virtual" fluid wall and used upstream detection with FACS and DEP actuation to merge selected droplets with a continuous stream.(Fidalgo, Whyte et al. 2008) In a similar design, Roman *et al.* incorporated real-time electrophoresis separation of the droplet contents right after merging.(Roman, Wang et al. 2008)

Another technique uses side channels perpendicular to the main droplet channel to extract the two phases. Gunther *et al.* separated gas droplets from the continuous liquid phase using small side channel capillaries.(Gunther, Khan et al. 2004; Gunther, Jhunjhunwala et al. 2005) The continuous liquid phase can enter the side channels but the gas droplets are held back by the high Laplace pressure created by the shallow channels. Careful control of the pressure drop is required across the side channels or the gas droplets can break through. Liquid/liquid separation can be achieved by using hydrophilic side channels.(Hosokawa, Fujii et al. 1999; Kralj, Sahoo et al. 2007; Castell, Allender et al. 2009) The separation efficiency depends on the time that the droplets are in contact with the side channels which can be controlled by the flow rate and the number of side channels.

2.4 Droplet Numerical Simulations

The quality of information provided by numerical simulations can give great insight into the fundamental physics governing droplet behaviour. Numerical modelling of two phase flow is a vast topic that is well beyond the scope of this review; therefore, only a cursory overview is provided highlighting the most important points.

There are two main types of two-phase flow solvers used for full 3D numerical simulations: moving mesh methods which follow the interface motion, and fixed mesh methods which let the interface evolve through the mesh.(Cristini and Tan 2004; Prosperetti and Tryggvason 2007) Moving mesh methods are efficient and accurate at studying interface deformation but fail when large deformations occur such as in droplet breakup. Fixed mesh methods are better adapted to solving larger problems with multiple interfaces and large deformations like droplet breakup and coalescence.

In fixed based methods an additional function is required to specify the location of the two phases in the computational domain. The most common functions for capturing the interface are the volume of fluid (VOF) and level-set (LS) methods. In the VOF method, the two fluids are specified by volume fractions where the heavier fluid is given a concentration $C=1$ and the lighter fluid $C=0$. An additional scalar convection equation accounts for the motion of the volume fraction ($\frac{\partial C}{\partial t} + u \cdot \nabla C = 0$). Physically this equation means that the mass is always conserved in the heavier phase. In the LS method, the interface between the two phases is represented by a

scalar function which is set to $\Phi=0$ at the interface, $\Phi=1$ in one phase and $\Phi=-1$ in the other. With this formulation both phases are identified as well as the interface. A similar scalar convection equation is used to account for the advection of the interface. In addition, a smoothed Heaviside function is used to interpolate the properties of the two fluids within interface. In both the VOF and LS methods the surface tension is introduced as a body force in the Navier-Stokes equations whose value is determined by the presence of the interface in the computational cell.

The VOF and LS methods are both well characterized techniques that have been used to study several micro scale problems including flow focusing generators (Ong, Hua et al. 2007), mixing in droplets traveling through a serpentine channel (Muradoglu and Stone 2005), and transport of droplets through contractions.(Harvie, Cooper-White et al. 2008) Several commercial CFD packages (Comsol, Fluent, CFX, CFD-ACE, Flow-3D) also include two-phase modules. Glatzel *et al.* reviewed the available packages and compared their performance in modeling micro two phase flow with experimental data.(Glatzel, Litterst et al. 2008) Some packages have a unique set of features such as adaptive meshing and adjustable surface dampening which produced superior computation results. The best packages for two-phase flow were found to be CFD-ACE and Fluent (Comsol was not considered).

Although commercial packages are easily accessible, full 3D numerical models are still very costly to perform and are limited to studying small areas of interest or isolated phenomena. When designing larger networks simplified 1D models are more appropriate since they are able to capture the general physics at a fraction of the computation cost. These models are similar to those used in solving electrical circuits, where flow rate is equivalent to current, pressure to voltage and electrical resistance to hydrodynamic resistance.

Several models have been developed for 1D single phase flow under pressure driven and electroosmotic flow.(Qiao and Aluru 2002; Chatterjee and Aluru 2005; Wang, Lin et al. 2006; Wang, Bedekar et al. 2007; Behzad, Seyed-allaei et al. 2010; Cybulski and Garstecki 2010; Sessoms, Amon et al. 2010; Smith and Gaver 2010). However, two-phase flow models are more complex due to the inherent nonlinear and time dependent nature of the flow. Only a few models have been developed for two-phase flow in recent years. Jousse *et al.* developed a model for bubble flow in a microfluidic Wheatstone bridge.(Jousse, Lian et al. 2005) The model generalized the resistance of the bubbles by using a volume fraction method which provides information on

the global performance of the device but not on the individual droplets. Schindler *et al.* elaborated on this work and developed a model that tracked the individual location of droplets in the network.(Schindler and Ajdari 2008) An important feature of this model is the selection rule used at a junction which specifies that the droplet will enter the channel with the highest instantaneous velocity. The authors applied their model to study several devices presented in literature and were able to explain the unknown operating regimes of these devices. However, their model is still only a basic example of what is required to design complete networks as it incorporates only the limited function of sorting at a bifurcation. Future models will need to incorporate additional functions for generating, breaking up, merging, and trapping droplets.

2.5 Practical Concerns: Visualization, Flow Control, Stability

In this section, several practical concerns are outlined for performing droplet microfluidic studies including methods for visualizing droplets on the micro scale, controlling the overall fluid flow, and conditions for stable operation in highly integrated designs.

2.5.1 Flow Visualization

Characterizing the flow field and droplet motion is essential for evaluating the performance of any microfluidic device (Thoroddsen, Etoh et al. 2008). However, the time dependent nature and small scale of microfluidic two-phase flow requires higher spatial and temporal resolution techniques (Gunther and Jensen 2006). Microscopy is the most common method of visualizing droplets in microchannels. The general setup consists of a microscope coupled with a high speed camera (>2000 fps) using bright-field illumination. With the minimum setup, droplet dynamics can be captured with frequencies around 500Hz and 5μm resolution. For fluorescent detection, the light intensity is too low given the short time the droplet is in the field of view. Pulsed solid state lasers, synchronized with the camera are needed to provide sufficient excitation intensity and low image distortions. Confocal microscopy has also been used to obtain 3D visualization in slice by slice segments.

Flow field data can be obtained with μ-PIV by seeding particles in either the continuous or discrete phase(Santiago, Wereley et al. 1998; Gunther and Jensen 2006). Standard μ-PIV can be used with some small modifications. The temporal nature of two phase flow usually limits the

number of sequential images that can be obtained for averaging the flow field. Areas near the interface are masked off during cross-correlation analysis since refraction/reflection interferes with the fluorescent signal. Flow field measurements in the discrete phase require an additional algorithm for accounting for the translational motion of droplets. Several researchers have applied μ-PIV to study the flow field inside(Wang, Nguyen et al. 2007; Malsch, Kielpinski et al. 2008) and outside (Gunther, Jhunjhunwala et al. 2005; Malsch, Kielpinski et al. 2008) droplets moving in straight and serpentine channels, at low speeds using confocal μ-PV(Kinoshita, Kaneda et al. 2007) and near the intersection of a T-junction generator (van Steijn, Kreutzer et al. 2007).

2.5.2 Flow Control

In the majority of studies (~80% in the reviewer's estimation) syringe pumps are used to control fluid flow. Syringe pumps output a constant flow rate and are analogous to a constant current source in electrical systems. The next most popular means of pumping fluids is using pressure "bombs" to regulate the atmospheric pressure to each reservoir, which is analogous to a constant voltage source in electrical systems. To a lesser extent, on-chip peristaltic pumps have also been integrated using the PDMS valve design; however, these are only useful for low speed applications. Recent studies have promoted the use of constant pressure control over syringe pump control due to the increase in stability if the pressure system is designed properly (Korczyk, Cybulski et al. 2011; Wang, Lin et al. 2011). In theory, syringe pumps are supposed to produce a constant flow, however, in actuality the flow oscillates significantly due to imperfections in the drive screw. The period of these oscillations can be extremely long (~10min~1hr), which means that for proper quantitative measurements data should be averaged over very long periods (3-5 periods) to minimize sampling error.

Furthermore, the type of flow control has a profound influence on the performance of droplet devices because of the coupling between droplets and the hydrodynamic resistance. Droplets have less influence on the global flow field when syringe pumps are used since they automatically adjust for changes in resistance by always outputting a constant flow rate. With syringe pumps it is easy to know the direction and magnitude of all flow streams. The opposite is true for pressure driven flow where the coupling with resistance creates a constantly varying flow field. Ward *et al.* demonstrated the significant effect the two different flow types have on the operation of a flow focusing generator operating in the dripping regime (see Figure 2.10).(Ward, Faivre et al. 2005) Under constant flow rate control the droplets size varied very little over a wide range of flow rate

ratios. However, with pressure driven flow the droplet size varied significantly due to the increased coupling between the droplet formation and flow rate output. In a separate study, Schindler and Ajdari used a 1D model of multiphase flow to analyze droplet traffic in a ladder design which is used to synchronize two droplets in parallel channels by reducing their spacing before they exit. However, the design only worked with constant flow rate but not with constant pressure. These examples demonstrate the importance of recognizing the type of flow control used when evaluating designs in literature.

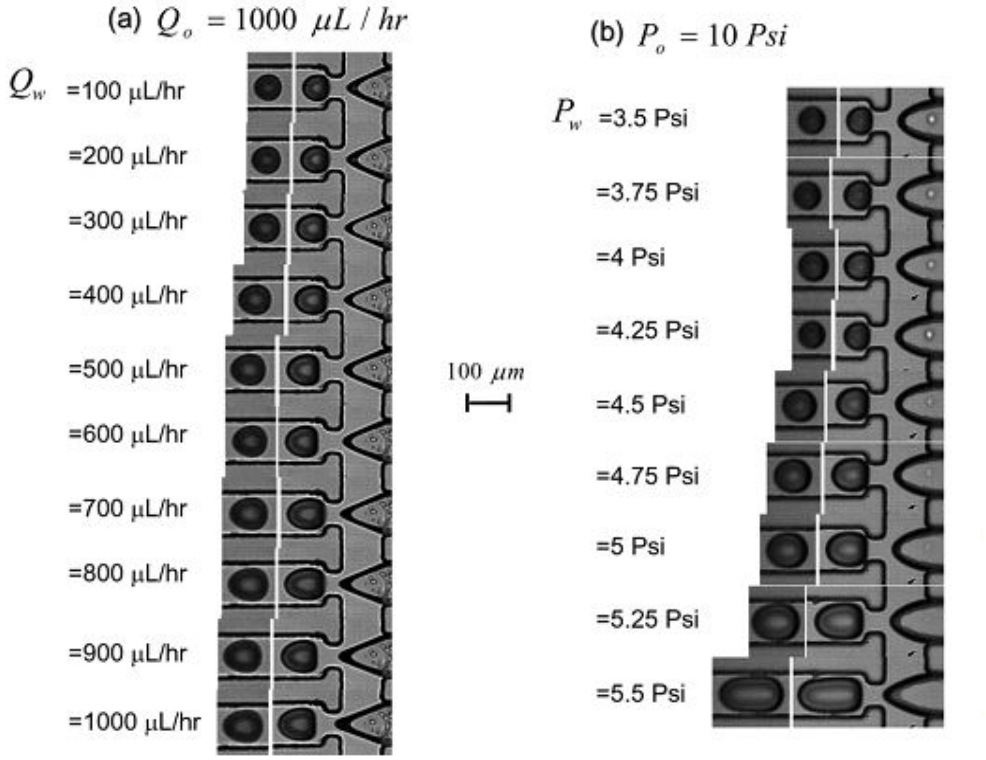

Figure 2.10 Experimental operation with flow focusing generator operating with flow rate control from dual syringe pumps (a) and pressure driven control from pressure "bombs" (b) over the same flow conditions adjusted for viscosity differences between the oil and water phases. Droplet size in the pressure control varies significantly more than under flow control.(Ward, Faivre et al. 2005)

2.5.3 Stable Operation

Although many droplet based microfluidic devices have been presented to date, limited examples exist for large scale integrated devices. The reason is that each component is coupled together through the pressure field with the chip which is influenced by the presence of droplets. Pressure and velocity fluctuations influence neighbouring components causing non-linear and erratic behaviour. For example, splitting(Link, Anna et al. 2004; Adamson, Mustafi et al. 2006;

Menetrier-Deremble and Tabeling 2006; Yamada, Doi et al. 2008) or sorting (Engl, Roche et al. 2005; Jousse, Farr et al. 2006) at a bifurcation can be highly unpredictable if flow conditions are not perfect due to the influence of already split or sorted droplets. Another example of coupled behaviour is the operation of multiple droplet generators in parallel from the same fluid streams.(Barbier, Willaime et al. 2006; Hashimoto, Garstecki et al. 2007; Hashimoto, Shevkoplyas et al. 2008; Li, Young et al. 2008; Tetradis-Meris, Rossetti et al. 2009; Wang, Lu et al. 2009). Several regimes occur where the generators operate in-phase or out of phase. In phase operation results in stable operation with low polydispersity, even if the droplets are not all the same size. Out of phase operation is chaotic with droplets forming at random frequencies and sizes. The source of this behaviour is the feedback caused by the downstream droplets which have already formed.(Sullivan and Stone 2008)

To integrate multiple droplet functions requires an effective means of isolating components from pressure fluctuations (Tetradis-Meris, Rossetti et al. 2009; Kumacheva and Garstecki 2011). This requires designing within a set of parameters which minimizes cross-talk. A number of possible techniques can be incorporated. First, droplets should be smaller than or close to the same size as the microchannels so that their hydrodynamic resistance is minimal. Second, flow restrictions can be incorporated in the inlet streams to increase the overall pressure in the chip.(Gunther and Jensen 2006) Higher pressure drops minimize the importance a single droplet has on the overall resistance leading to more stable flow rates.(van Steijn, Kreutzer et al. 2008) Third, droplet functions should be based on local manipulation that does not affect the global flow field such as DEP for sorting and coalescence.

2.6 Applications

The primary focus of this review was to describe the mechanisms and underlying physics of forming, controlling and transporting droplets in microchannels. The unique functionalities of droplet microfluidics have lead to the development of new applications that were previously not possible with macro scale devices. In the following section, a few interesting applications are briefly highlighted.

2.6.1 Fluid and Interfacial Property Measurements

One of the applications of microfluidic droplets has been to develop systems that measure two-phase flow properties such as viscosity and interfacial tension. The well defined flow profiles of microfluidics can be used to probe the bulk rheological properties of various fluids shear and extensional flow (Pipe and McKinley 2009). Microfluidic rheology is characterized by high Weissenberg numbers (polymer relaxation time to process times) and high shear rates. Geometries include parallel plate flow for shear, extensional flow at a cross-junction with a stagnation point and extensional flow in expanding and contracting constrictions.

One of the advantages of microfluidic rheology is the ability to connect the micro structure of the polymer to the macroscopic properties (Hu, Boukany et al. 2011). For instance, the dynamics of single polymers, such as DNA, can be investigated by fluorescently tagging the DNA in experiments (Hu, Boukany et al. 2011). In addition, small nano-particles or beads can be used with μ-PIV to track flow fields directly, or to measure the viscosity by tracking the Brownian motion of the particles. High throughput measurements can be done on microfluidic chips by automatically mixing samples on-chip and performing rheological measurements simultaneously (Schultz and Furst 2011).

The interfacial tension is one of the controlling parameters that govern droplet formation in microfluidic devices. For this reason, several works have used microfluidic droplet generators to perform micro-tensiometry measurements by correlating droplet size (Steegmans, Warmerdam et al. 2009; Wang, Lu et al. 2009) or rate of production (Xu, Li et al. 2008) to changes in interfacial tension. Interfacial tension has also been measured by analyzing the shape of droplets as they are accelerated and deformed by extensional flow (Hudson, Cabral et al. 2005).

2.6.2 Bead and Particle Synthesis

The flexibility of microfluidics combined with the rapid production and monodispersity of microdroplet generators allows for the fabrication of novel solid particles (Kumacheva and Garstecki 2011)(see Figure 2.11 for examples). The process for making highly uniform particles is straightforward. The primer material is simply mixed on-chip prior to the droplets being formed and then solidified downstream either inside the channel or in a batch reactor outside the chip. Polymerization can occur on-chip via catalyst based reaction, thermal initiation or photoinitiation.(Teh, Lin et al. 2008; Kumacheva and Garstecki 2011)

Synthesis techniques have also been developed to create unique beads with different morphologies and properties. Discs, rods and other shapes have been made by forcing the droplets through confined microchannels and then polymerizing by UV.(Dendukuri, Tsoi et al. 2005; Seo, Nie et al. 2005) Other examples include Janus particles, which contain two distinct parts with different properties (colour, surface wettability, electrical properties) (Quevedo, Steinbacher et al. 2005; Shepherd, Conrad et al. 2006), capsules where polymerization only occurs at the interface (Quevedo, Steinbacher et al. 2005), on-spherical direction dependent magnetic particles by using external magnetic fields to align nanoparticles prior to polymerization (Hwang, Dendukuri et al. 2008) and hydrogels embedded with cells (Kumacheva and Garstecki 2011).

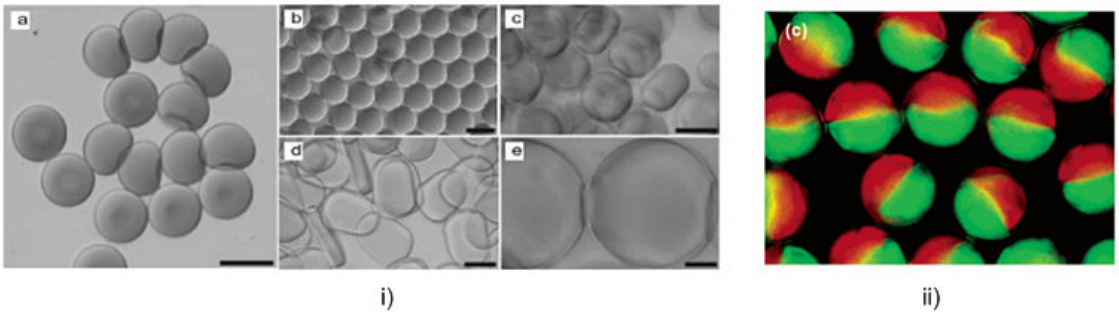

Figure 2.11 Examples of particles fabricated with droplets. (i) different shaped magnetic hydrogel particles including spheres, discs, and rods.(Hwang, Dendukuri et al. 2008) (ii) Janus particles fabricated with two different fluorescence halves.(Shepherd, Conrad et al. 2006)

2.6.3 Mixing and Chemical Reaction Studies

Reactions can occur within two-phase flow in a number of ways. The two fluids can react with each other, the two fluids react in the presence of a catalyst, or the reaction is wholly contained in one of the two fluids. In general, droplets are used in the later situation where they act as ideal micro reactors. Droplets can significantly improve mixing due to the presence of the counter rotating vortices created inside droplets during transport. (Tice, Song et al. 2003) Mixing can be enhanced by passing the droplets through a serpentine channel which changes the orientation of the vortices with time (see Figure 2.12). The parameters influencing the level of mixing are the capillary number, viscosity ratio and the size and shape of the plug traveling in the channel.(Tice, Lyon et al. 2004; Muradoglu and Stone 2005) Using “bumpy” serpentine channels can further improve mixing of very viscous samples with low diffusion coefficients.(Liau, Karnik et al. 2005) Complete mixing in droplets can be achieved in a matter of milliseconds. Therefore, the initial starting point of a reaction can be precisely known. Reaction kinetic studies can be performed by

following the droplet along the length of the microchannel, where position correlates to reaction time if the droplet speed is constant. For example, such techniques have been used to study enzyme kinetics of RNase A (Song and Ismagilov 2003) and the clotting time of blood (Song, Li et al. 2006).

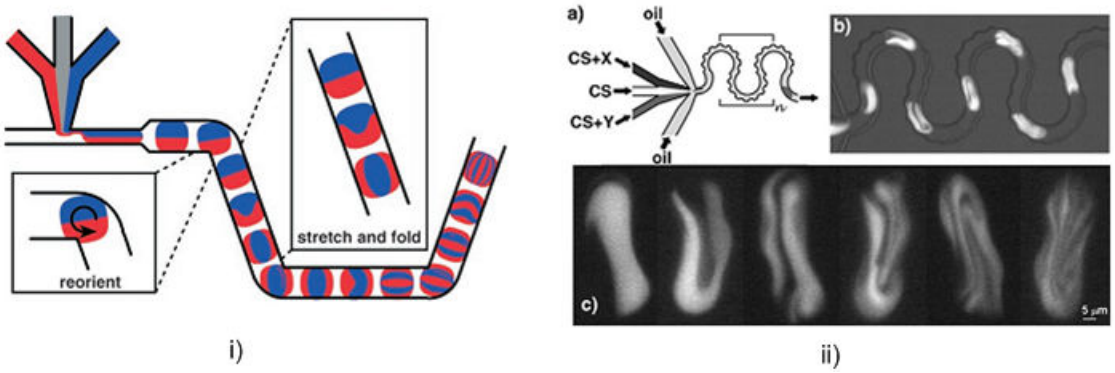

Figure 2.12 (i) Diagram of mixing in droplets through a serpentine showing that the interface between the two fluids is stretched, reorientated and folded as it passes through the curves and straight channels.(Song, Bringer et al. 2003) (ii) Mixing of viscous fluids in a bumpy serpentine channel mixer with fluorescent images showing the striations within the plug.(Liau, Karnik et al. 2005)

Microfluidic droplets can also be used to screen against a number of reaction conditions at high speed. The droplet content can be controlled be either manipulating the ratio of aqueous reagents entering the droplet before it is formed or by merging droplets containing the various reagent. A particularly powerful application of droplet microfluidics has been in developing techniques for protein crystallization (Leng and Salmon 2009). Zheng *et al.* optimized protein crystallization by screening against thousands of reaction conditions in microdroplets.(Zheng, Roach et al. 2003) Droplets have also been used to optimize the synthesis of CdS nanoparticles, where complete mixing results in a more uniform product compared to fabrication with single phase microfluidics.(Shestopalov, Tice et al. 2004) Laval *et al*. studied solubility conditions in a 2D microdroplet array at different concentrations and temperatures.(Laval, Lisai et al. 2007) Solubility curves could be directly read from the chip by monitoring crystallization using cross-polarizers.

2.6.4 Custom Emulsions

Emulsion contains liquid droplets suspended in a second immiscible fluid. Since the droplets are deformable this gives the fluid unique characteristics, including viscosity that changes with shear rate and elasticity rising from surface tension forces. Microfluidic emulsion generators provide the ability of creating custom emulsions of multiple fluids with droplets of different sizes and

compositions as shown in Figure 13. As well, double emulsions can be formed, which are essentially “emulsions of emulsions”, where microdroplets are enclosed within another droplet in the continuous phase.

Hashimoto *et al.* produced complex emulsions of two or three different droplets varying in composition and size using multiple flow focusing generators outputting to a single micro chamber.(Hashimoto, Garstecki et al. 2007) Coupling between the generators limits the structure of the droplet that can be formed. Dense packing of droplets or bubbles can also be used to form specialized foams or flowing crystals. Under disproportionately high dispersed flow rate to continuous flow rate conditions large droplets can be formed with minimum continuous phase separating them. The foams spontaneously organize into highly periodic structures in an attempt to minimize surface energy. The process is of fundamental interest as it represents a self-regulating non-linear system.(Garstecki and Whitesides 2006; Raven and Marmottant 2006; Raven and Marmottant 2009)

Double emulsions can be categorized into different types, as either W/O/W or O/W/O emulsions as well as by the number of droplets contained within the larger droplets. Double emulsions are important in many industries including food sciences, cosmetics, and pharmaceutics.(Nisisako 2008) In 2D microfluidics designs, double emulsions are created by combining two microfluidic generators in series. The most important factor in these designs is that the wettability is controlled by local surface treatments in order to form droplets within the two types of continuous phase. This may be done on one chip with specialized UV-grafting surface treatments, or two separate chips of hydrophobic/hydrophilic materials can be made and connected together. Nisisako *et al.* demonstrated the formation of double emulsions using consecutive T-junction designs.(Nisisako, Okushima et al. 2005) Seo *et al.* also formed double emulsions with consecutive flow focusers.(Seo, Paquet et al. 2007) The size and amount of droplets within the larger droplet can be controlled by varying the flow rates of all the fluids.

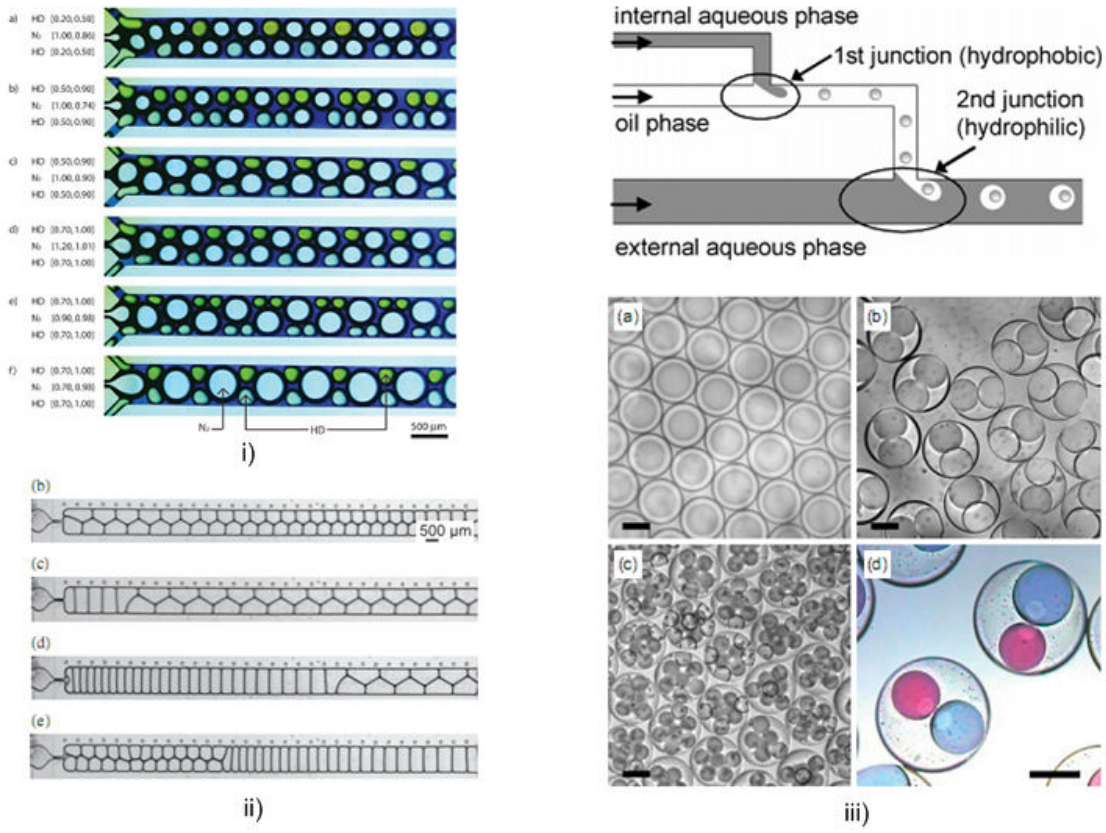

Figure 2.13 Examples of complex emulsions created with microfluidic droplet generators (i) droplets of different composition and size created by three flow focusing generators outputting to a single microchannel (Hashimoto, Garstecki et al. 2007) (ii) complex foam structure created in low continuous phase flow conditions(Raven and Marmottant 2006) (iii) double emulsions made using a double T-junction design with hydrophobic, and hydrophobic wetting conditions, includes examples of various double emulsions with controlled number and size of core droplets.(Okushima, Nisisako et al. 2004)

2.6.5 Biological Studies

One of the most promising applications for droplets is in biological studies both with living cells and other biological materials such as DNA and proteins. These studies are particularly relevant to drug discovery and disease diagnosis. Droplet microfluidics represents a natural progression from the current technology standard of robotic microwell plate systems, to a system that can use even less reagents with higher throughput (Schaerli and Hollfelder 2009).

Microdroplets are ideal vesicles for performing studies on single cells or small groups of cells. Several groups have demonstrated successful cultivation of numerous types of cell in droplets including eukaryotes (Clausell-Tormos, Lieber et al. 2008), embryos (Kohler and Henkel 2005), microbes (Tan, Hettiarachchi et al. 2006; Funfak, Cao et al. 2009) and small organisms such as zebra fish embryos (Funfak, Brosing et al. 2007) and C. Elegans (Shi, Qin et al. 2008) (see Figure

2.14). Clausell-Tormos *et al.* showed that cell proliferation in droplets depends on the droplet size and the number of cells in the droplet as this determines the rate of nutrient consumption (Clausell-Tormos, Lieber et al. 2008) To perform cell studies it is important that all materials are biocompatible. Cells can be stored in PDMS chips or off-chip in PTFE tubing since both are highly permeable to gases. Researchers have also worked on developing new oils and surfactants that promote cell viability and prevent adsorption of proteins at the interface of the droplets.(Roach, Song et al. 2005; Clausell-Tormos, Lieber et al. 2008; Holtze, Rowat et al. 2008)

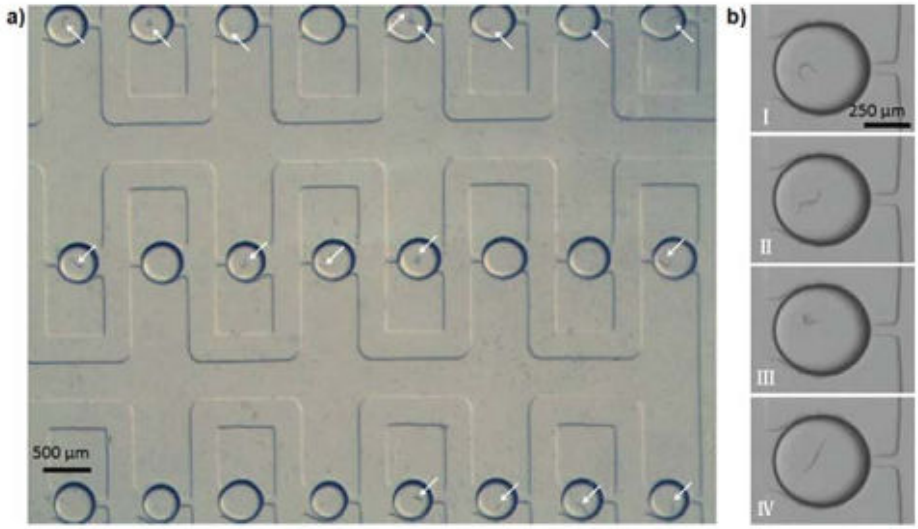

Figure 2.14 Droplet based study of C. Elegans on a microfluidic chip. (a) array of 24 droplets with arrows pointing to drop containing organisms, drops are fixed in trapped wells. (b) close up of a droplet with the C. Elegan swimming. (Shi, Qin et al. 2008)

One difficulty with performing single cell analysis is controlling the number of cells within a droplet. Cell encapsulation from the incoming dispersed stream is purely random and follows a Poisson distribution. The probability of a cell containing only one cell is very low (5-15%) depending on the bulk concentration and size of the droplets. This leaves a lot of cells that contain no cells or multi-cells that must be sorted out. Edd *et al.* developed a technique to improve the efficiency of encapsulation by first passing the cells through a high aspect ratio microchannel where the cells self-organize and are spaced apart equally.(Edd, Di Carlo et al. 2008) Droplet formation matches the cell spacing and encapsulation can reach 95% efficiency; however, the channel must be very long requiring high pressures to pump the fluids.

Since each cell resides in its own isolated picolitre drop, molecules secreted by the cells are contained and can quickly reach detectable levels.(Huebner, Srisa-Art et al. 2007; Huebner, Olguin et al. 2008) Conversely, uptake of molecules can be monitored as they are depleted within

the droplet. After cells are encapsulated they are usually docked into storage compartments to make it easier to monitor them during the experiment.(Shi, Qin et al. 2008; Huebner, Bratton et al. 2009; Schmitz, Rowat et al. 2009) Encapsulation has also been combined with bead polymerization techniques to create hydrogel particles for cell transplantation.(Luo, Pullela et al. 2007; Shintaku, Kuwabara et al. 2007) Cryogenic preservation has been demonstrated by freezing droplet on chip with thermo electric coolers.(Sgro, Allen et al. 2007) In addition to living cell studies, several bioassays have also been demonstrated in droplets. Beer *et al.* demonstrated real-time single copy PCR using a drop based system.(Beer, Hindson et al. 2007) Recently, Kline *et al.* developed a blood typing device using droplet and the standard agglutination assay where antibodies specifically bind to certain types of blood and form a clot.(Kline, Runyon et al. 2008) Clotting was detected by visual inspection of the droplet under a microscope. These examples are only a few of the many applications that have been developed over the past few years.

2.7 Summary

To manipulate and control droplets in microchannels requires an understanding of the underlying physics and forces involved. Methods for generating, transporting, splitting, combining, indexing, sorting, extracting and storing was reviewed. As well, practical concerns such as choosing compatible chip materials and fluids, methods to visualize droplets and control fluid flow within the chip were discussed. Throughout the review an emphasis was put on identifying methods and conditions where droplets can be controlled effectively resulting in stable device operation. Finally, several applications for droplet devices were discussed including particle synthesis, mixing applications, custom emulsions, and biological assays.

Nomenclature

Acronyms:

1D	one dimensional
2D	two dimensional
3D	three dimensional
CFD	computational fluid dynamics
EWOD	electrowetting on a dielectric
DEP	dielectrophoresis
DNA	deoxyribonucleic acid
GER	giant electrorheological fluid
FACS	fluorescence activated cell sorting
LOC	Lab on a Chip
LS	level set
OEG	oligoethylene glycol
O/W	oil/water
PDMS	poly(dimethyl)siloxane
PTFE	polytetrafluoroethylene
μ-PIV	micro particle image velocimetry
UV	ultra violet
VOF	volume of fluid

Mathematical Symbols:

α	fitting factor
β	fitting factor
β_{slip}	slip factor of droplet
γ	interfacial tension (N m^{-1})
ε_o	extension of droplet when splitting
θ	contact angle (rad)
κ	curvature (m^{-1})
μ	dynamic viscosity of fluid (Pa s)
η	ratio of dispersed to continuous phase viscosities
ρ	density (kg m^{-3})
φ	ratio of dispersed to continuous phase flow rates

d	diameter (m)
g_c	geometric constant (dimensionless)
h	height (m)
l,L	length scale (m)
$u,\ U$	velocity (m s^{-1})
w	width (m)
Ca	capillary umber (dimensionless)
D_h	hydraulic diameter (m)
$Q_{d,c,m}$	flow rate of dispersed, continuous or main channel (m^3 s)
Re	Reynold's number (dimensionless)

Chapter 3

Fabrication Methods and Experimental Techniques

The purpose of this chapter is to provide details regarding the experimental aspect of this thesis. The equipment and procedures used throughout this work are concentrated in this chapter. The topics covered include techniques for fabricating chips, visualizing droplet flows in microchannels, and characterizing material properties.

3.1 Device Fabrication by Soft Lithography

Here a brief review is provided for fabricating multi-level polydimethylsiloxane (PDMS) devices via soft-lithography techniques (Xia and Whitesides 1998; Glawdel 2008). The process for fabricating a multi-level PDMS device is summarized in Figure 3.1. with specific instructions for the Waterloo Microfluidics Lab given in (Glawdel 2008). The process begins with designing a photo mask containing the negative image of the microchannel layout. Photo masks are designed in AutoCad and printed commercially on Mylar films with 20k dpi resolution (CAD/Art Services). The minimum microchannel size that can be printed with good clarity is approximately 8 μm. After the photo mask is received the first step is to fabricate a reliable master for molding the PDMS microchannels. Masters are fabricated from the negative photoresist SU-8 on 4-in silicon wafers. Three microscope slide sized designs can fit onto one master.

SU-8 is deposited onto the silicon wafer by spin coating (200 CB, Brewer Science). The thickness of the film defines the height of the microchannel and is controlled by the type of SU-8 and the spin coating process (speed, time). A layer between 0.5-500 μm can be deposited in a single coat. Su-8 is deposited dynamically (as the wafer is spinning) using a precision pneumatic dispensing system (Ultra 1400, Engineered Fluid Dispensing). Afterwards a soft bake is performed at 65°C and 95°C on a set of level hot plates to evaporate the solvent in the photoresist and harden the film. Next, the wafer is placed in a UV exposure system (Newport) and covered with the photo mask containing the design. The assembly is illuminated with UV light (~365nm) where exposed regions undergo photopolymerization and begin to cross-link. A post exposure bake at 65°C and

95° follows to complete the cross linking. The process of spin coating, soft bake, exposure and post exposure bake can be repeated for multiple layers to produce multi-level structures. Once all the layers are completed the master is placed in a large bath of SU-8 developer to dissolve the unexposed SU-8 regions. The wafer is then washed with clean SU-8 developer, isopropyl alcohol and deionized water followed by blow drying with nitrogen. To keep the photoresist from peeling off a small amount of glue (Loctite 3311) is placed around the edge of the wafer and hardened with UV light.

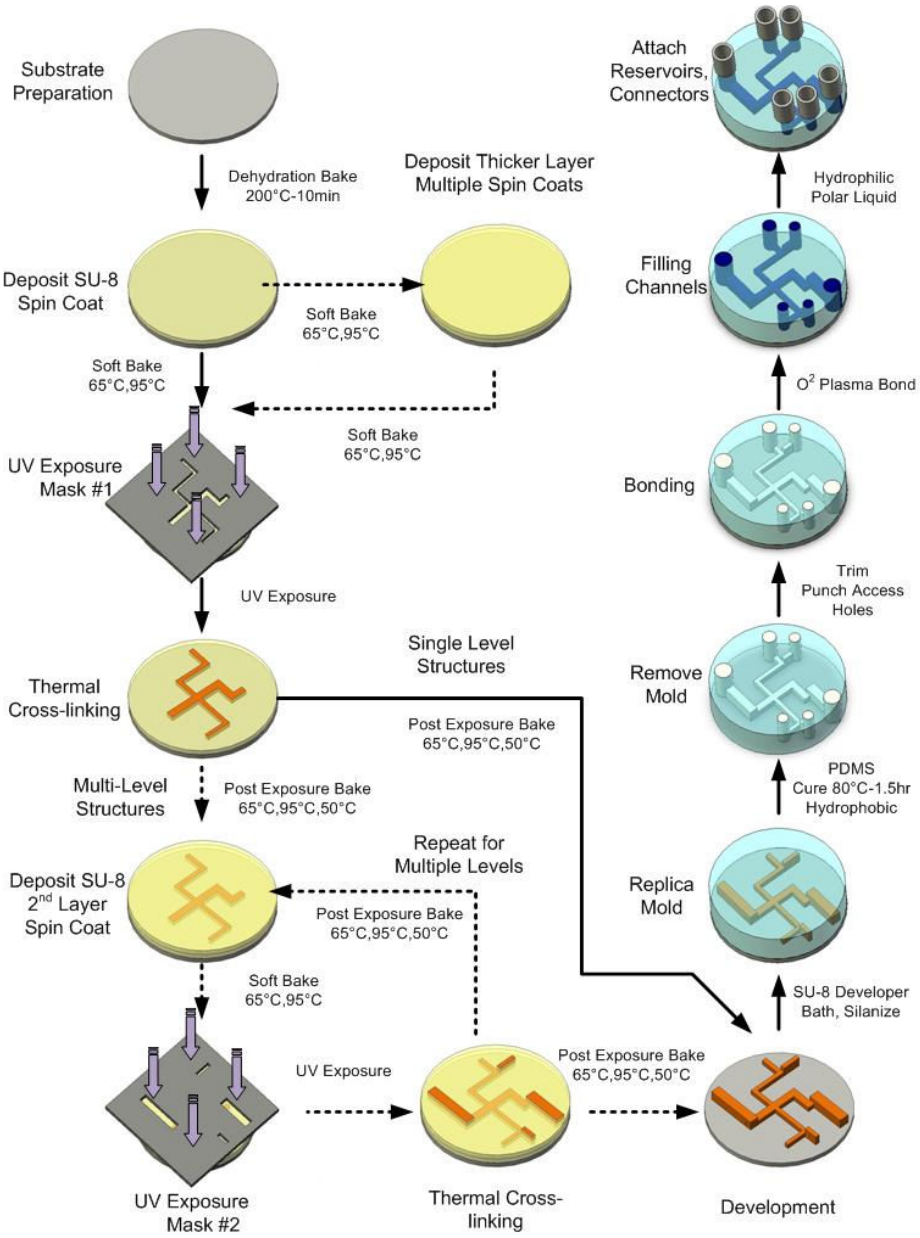

Figure 3.1 Diagram of the process for fabricating microfluidic chip using soft lithography with multi-level features. (Glawdel 2008)

Next, the relief structures on the SU-8 master are molded in PDMS. PDMS is mixed in a ratio of base to curing agent, typically 10:1 by weight, and degassed in a vacuum oven to remove bubbles created when mixing. The master is placed in an aluminum dish and the PDMS is poured over top and cured at 120°C for 2-6 hrs. After the mold cools down, it is cut out, trimmed, and fluidic access holes are punched using a biopsy punch with a diameter that matches the tubing that connects to the chip. To complete the chip, the PDMS mold is bonded to another substrate (glass, PDMS, quartz, silicon) by oxygen plasma treatment. The two substrates are then placed in contact and a permanent bond forms after a few minutes. The plasma treatment also transforms the PDMS from hydrophobic to hydrophilic which makes it easier to fill the microchannels with liquid. To return PDMS back to its natural hydrophobic state the entire chip can be heated at 160°C for 12 hrs. Depending on the oil used additional surface treatments may be required to create the correct wetting conditions to generate water in oil emulsions. Specifics are given when required in subsequent chapters.

Once a master is fabricated the dimensions of the microchannels need to be measured. The width of the channels is measured using the microscope and CCD camera and a calibrated scale that converts the number of pixels into distance on the image. Single line measurements of the dimensions of the channels are measured using a contact profiler (SJ-400, Mitutoyo). For full surface area mapping the relief features on the master are measured using an optical profiler (Wyko NT1100, Veeco).

3.2 Fluid and Interfacial Properties

Measuring the properties of the two working fluids is important for both modelling and experimental design. Specifically, the viscosity and interfacial tension for all the water/oil/surfactant combinations need to be known. Viscosity was measured using a programmable rheometer (LVDV-III Ultra CPE, Brookfield Instruments) with a cone-plate spindle (CPE-40) rated for a measurement range of 0.1-3070 mPas coupled with a cup that contains a thermocouple. Measurements were made over a range of applied shear stresses to verify that each fluid exhibits Newtonian behaviour. The equilibrium interfacial tension for water/oil/surfactant combinations were measured using a Wilhemy plate tensiometer (Data Physics, DCAT 11).

3.3 Experimental Setup

The experimental setup is presented in Figure 3.2. Droplet devices were visualized using an inverted epifluorescence microscope system (Eclipse Ti, Nikon). The system is fully computerized with programmable stage (X,Y,Z), objective nose piece, fluorescence turret and shutters. The properties of the objectives are (NA, working distance): 10x (0.3, 16mm), 20x (0.5, 2.1mm), 40x (0.75, 0.72mm). Filter cubes are provided for Rhodamine B (500-550nm ex, 565nm em) and Fluorescein (495nm ex, 505nm em) dyes. Illumination is provided by a 100 W halogen lamp for bright field applications and phase contrast and a 100W mercury halide lamp (Intensilight C-HGFIE, Nikon) for fluorescence applications. Images are recorded on a Retiga 2000R Fast 1394 monochrome CCD camera coupled to microscope. The digital image quality is 12 bit with a maximum speed of 10 fps at full resolution (1600x1200). With binning the capture speed increases up to 110 fps (8x8 binning). A custom software program comes with the microscope that controls the entire system for taking images at specified times and locations.

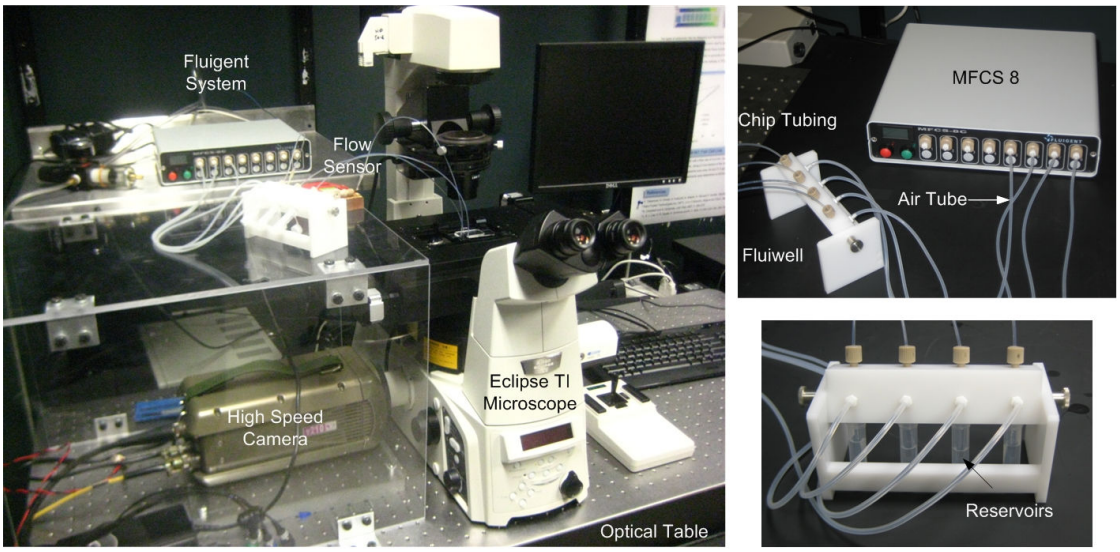

Figure 3.2 a) Microscope experimental setup for performing the T-junction experiments: Eclipse TI microscope, flow sensor, high speed camera, and Fluigent pressure system. b) Close up of the Fluigent system with the MFCS 8 which controls the pressure to 8 outputs and the Fluiwell that contains the fluid reservoirs.

The Retiga camera is excellent for fluorescence imaging due to its high sensitivity, however, is too slow to capture droplet dynamics that occur in the kHz range. An additional high speed CMOS camera (Phantom v210, Vision Research) is also connected to the microscope on the left port using a C-mount adapter (1X DXM, Nikon). At full resolution (1280x800) the camera can take images at 2190 fps, with a 12 bit digital image quality. By lowering the resolution, or

cropping the field of view, the camera can easily exceed 10000 fps. The camera continuously records image to the on device buffer and then downloads them via firewire to the camera once the trigger is activated. The camera may be triggered within the software program or externally through the trigger port (falling edge type).

Fluids are pumped using a high precision microfluidic pressure control system (MSFC 8C, Fluigent). The system pumps fluids by controlling the atmospheric pressure to each reservoir containing fluid up to 1bar with 0.5 mbar accuracy. The system consists of two parts, MSFC 8C which controls the pressure to 8 output channels and two Fluiwells that contain the reservoir system (see Figure 3.1). Each reservoir (CA73960-236, VWR) is connected by an air pressure tube form the MSFC 8C at the top and an outlet tube inserted into the bottom of the reservoir that connects to the chip. The capillary tubing has a large inside diameter (500 μm) in comparison to the microchannels to minimize any pressure loss before the chip inlets. Software is provided for controlling the system as well as Labview drivers for creating new control schemes.

One of the advantages of using a pressure regulation system over a constant flow rate system such as a syringe pump is the time it takes to reach steady state. With the syringe pump it may take over 30 minutes for the system to reach steady state depending on the flow rate and the compliance of the system. However, based on qualitative observation using the Fluigent system, the fluid flow reaches steady state in less than 10s after pressures are applied. This represents a significant advantage when performing the experiments since less time is needed to test various conditions.

Attached between the outlet of the reservoir containing the oil and the chip is an in-line micro flow sensor (SLG 1430-4870, Sensirion). This sensor is able to measure water flow rates up to 40 $\mu L\ min^{-1}$ with updates rates of 100 Hz. The inside diameter of the capillary within the sensor is 480 μm and is therefore not expected to adversely affect the pressure applied to the chip. The sensor is based on thermal anemometry principles to detect the flow rate and is thus sensitive to the physical properties of the fluid being measured. The sensor is initially calibrated for water, but can be recalibrated for other fluids. The procedure used to recalibrate the sensor is given in Section 3.3.2.

The entire system is connected to a computer with a data acquisition card (NI-PCI-6221, National Instruments) and all components are controlled by a custom Labview (National Instruments)

program. The Fluigent system and flow sensor are connected to the computer via USB and RS-232 ports. An output port (USB) from the computer is connected to the trigger on the high speed camera. The program offers both manual and automated control. In manual control, the pressures can be specified while the flow rate and pressures are continuously read. Manual mode is used to prime the chip prior to experiments. In the automated mode, the system runs through a set of steps that apply a series of pressures to the oil and water phases for a given period of time. For each step the camera is automatically triggered and the flow rate and pressure are recorded. When the experiment finishes a data file is output with all of the measured flow rates, pressures and details on the specific case study (fluids used, chip type, ect).

3.3.1 Flow Sensor Calibration

Since the operating principle of the flow sensor (SLG 1430) depends on heat transfer, if thermal properties of the fluid changes the sensor must be recalibrated. The sensor runs in a "raw" mode where direct temperature measurements are outputted as "tick" counts. The typical operational curve for the flow sensor has a sigmoid shape, where the desirable measurement range is in the linear portion of the curve. For water, the measurement range extends from -40 to 40 μL/min; however, for oils which typically have lower thermal conductivities a smaller range is expected. The calibration was performed by connecting the flow sensor via tubing to a 3 mL syringe filled with the appropriate oil. The oil was pumped with a high precision syringe pump (33 Twin, Harvard Apparatus) at various flow rates from 0 to 5 μL/min. The accuracy of the syringe pump is stated to be 0.5% by the manufacturer. At each step, data was average over 1 min (~50 data points) once steady state was reached. Above 6 μL/min the flow sensor exceeded the linear operational regime, and consequently this limit was avoided during experiments. The calibration curves obtained for the 3 types of oils are presented below in Figure 3.3 and show the expected linear dependence. During experiments, the appropriate conversion was inputted into the Labview control program to measure the incoming flow rate of the continuous phase.

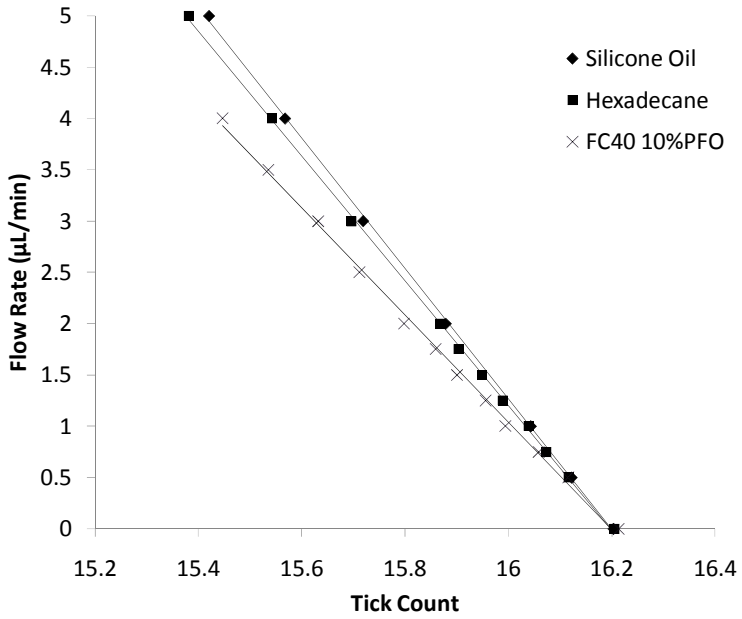

Figure 3.3 Calibration curve of "tick" count versus applied flow rate for the SLG 1430 flow sensor. Each data point is the average of three measurements. Linear regression profiles are: -5.23049x + 84.72476 (FC40+10%PFO), -6.07209x + 98.35753 (Hexadecane) and -6.35893x + 103.00735 (Silicone Oil). Goodness of fit is greater than $R^2 > 0.995$ for all three profiles.

3.6 Safety

Several chemicals mentioned throughout this thesis are especially hazardous to the operator: SU-8 developer (PGMEA), acetone, PDMS curing agent, FC-40, n-Hexedecane, sodium dodecyl sulphate, Tween 20 and Krytox surfactant. All the appropriate safety procedures were followed as described in the respective material safety data sheets. This included the use of fume hoods, goggles, gloves, respiratory devices, face shields and lab coats as was specified. In addition, handling equipment (e.g. bottles, tubing, jars) was checked for compatibility with any chemicals that were used.

Nomenclature

Acronyms:

CAD	computer aided design
CCD	charged coupled device
CMOS	complementary metal–oxide–semiconductor
PDMS	poly(dimethyl)siloxane
UV	ultra violet

Chapter 4

Modeling of T-junction Droplet Generators in the Squeezing to Transition Regime

The work presented in this chapter was published in the following articles:
Glawdel T., Elbuken C., Ren C.L. "Model of Droplet Formation in Microfluidic T-junction Generators Operating in the Squeezing to Transition Regimes: Part 1 Experimental Observations", **Physical Review E**, 85, 016322 (2012)

Glawdel T., Elbuken C., Ren C.L. "Model of Droplet Formation in Microfluidic T-junction Generators Operating in the Squeezing to Transition Regimes: Part 2 Modeling", **Physical Review E**, 85, 016323 (2012)

C. Elbuken (Post Doctoral Fellow in Department of Mechanical Engineer, University of Waterloo) assisted in writing some of the video analysis code for the experiments and the Labview code for running the experimental setup. Danny Chan (Undergraduate Student, Department of Nanoengineering, University of Waterloo) assisted in performing computational fluid dynamic models of flow through the gap surrounding a droplet for results presented in Figures 4.22, 4.23.

4.1 Overview of Previous Works

This chapter focuses on the generation of droplets at a microfluidic T-junction operating in the transition regime where confinement of the droplet creates a large squeezing pressure that influences droplet formation. In this regime, the operation of the T-junction depends on the geometry of the intersection (height/width ratio, inlet width ratio), the capillary number, flow ratio and viscosity ratio of the two phases. A detailed experimental study was performed followed by the development of a theoretical model to understand the formation process. Various parameters are tracked during the formation cycle such as the shape of the droplet (penetration depth and neck), inter droplet spacing, production rate and flow of both phases across several T-junction designs and flow conditions. Historically, the formation process is defined by a two-stage model consisting of an initial filling stage followed by a necking stage. However, video evidence suggests that a third stage should be included at the beginning of the formation process

that accounts for the retraction of the interface back into the injection channel after detachment. Based on the experimental observations a model is developed to describe the formation process. The model incorporates a detailed geometric description of the drop shape during the formation process combined with a force balance and necking criteria to define the droplet size, production rate and spacing. The model inherently captures the influence of the intersection geometry, including the channel width ratio and height/width ratio, Capillary number and flow ratio on the performance of the generator. The model is validated by comparing its predictive ability with data obtained from high speed videos with oil/water combinations in the absence of surfactants.

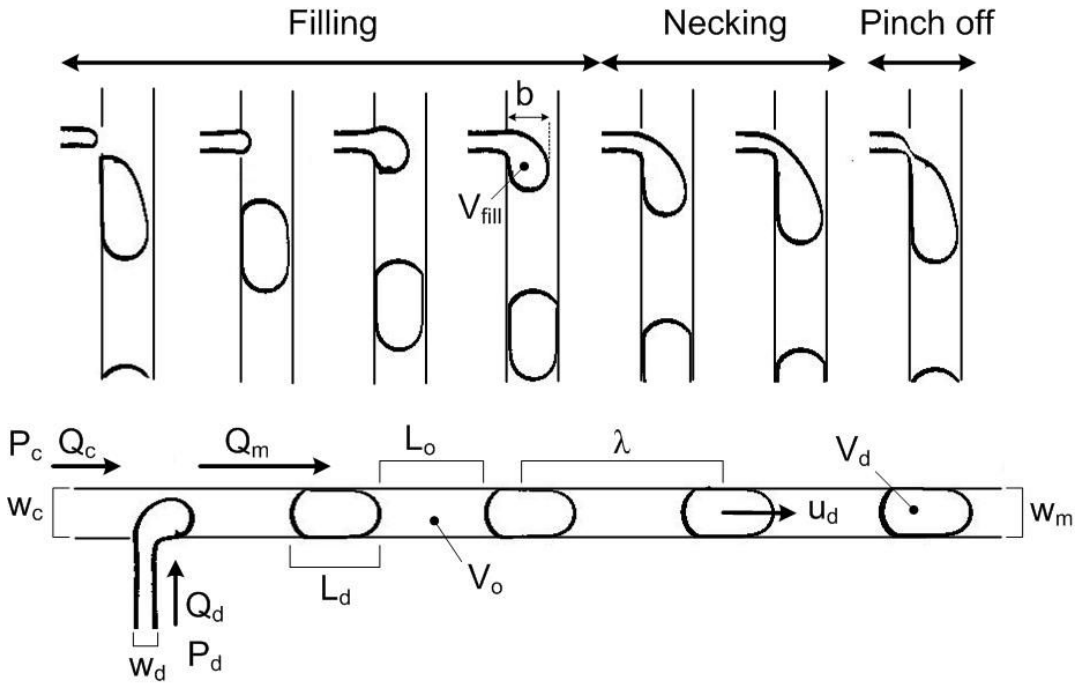

Figure 4.1 (a) Droplet formation cycle in the T-junction generator consisting of three stages (I) filling period (II) squeezing/necking period and (III) pinch off. Images are actual traces of the interface for n-hexadecane/ 1%Span80 and water, with intersection geometry 1:2 and channel height 50μm, under flow conditions of Ca=0.0087, φ=0.475. All images are equidistant in time. Below the global overview of the T-junction generator is presented with the respective geometric and flow parameters identified.

The T-junction design is the most common configuration among the various cross-flow micro fluidic droplet generators. In this configuration, the dispersed phase channel is perpendicular to the continuous phase which is orientated in parallel to the outlet channel. Forces created by the cross-flowing continuous phase break off droplets as the dispersed phase is injected into the main channel (Thorsen, Roberts et al. 2001). Organized by increasing Capillary number, the T-junction generator can operate is several regimes: squeezing, dripping and jetting.(Christopher and Anna 2007; De Menech, Garstecki et al. 2008; Gupta, Murshed et al. 2009). The operational state also depends on the flow ratio and can exhibit hysteretic behaviour (Zagnoni, Anderson et al. 2010).

For the purpose of generating monodispersed droplets, the T-junction generator is typically operated in the squeezing and dripping regimes where droplet size can be accurately controlled by the flow rates of the two phases.

The relevant geometric and flow parameters describing the operation of a T-junction generator are presented in Figure 14. The geometry is defined by the width of the continuous phase inlet, w_c, dispersed phase inlet, w_d , main channel outlet w_m, and channel height, h, which is uniform throughout the network. In this study, the design is restricted to situations where continuous phase inlet and the main channel are the same width, w_c=w_m. The flow rate in the main channel, Q_m, is the sum of the flow rates of the continuous phase, Q_c and dispersed phase, Q_d. These may be controlled by syringe pumps to regulate the flow rate or by pressure regulators. Droplets are formed with a volume, V_d, at a frequency, f, and spacing, λ, and are transported along the channel at a velocity u_d. The space between the droplets occupied by the continuous fluid is L_c and has a volume V_c. Additional relationships can be derived for the droplet flow rate, $Q_d = V_d \cdot f$, droplet velocity, $u_d = \lambda \cdot f$, and number of droplets in the main channel, $n = L_m / \lambda$. Any model developed to describe the operation of the T-junction generator should provide an understanding of the main parameters of interest that defines its performance, namely the droplet volume, frequency and spacing.

The general formation cycle of consists of two stages(van Steijn, Kreutzer et al. 2007) as shown in Figure 4.1. The cycle begins with the filling period (I) where the dispersed phase interface is injected from the side channel and enters into the main flow. The interface continues to grow until it reaches a maximum penetration depth, b, and a neck begins to form. During this time the continuous phase bypasses the droplet and fills the space between the previously formed droplet, increasing the distance between them. (II) The continuous phase then begins to push on the neck causing it to collapse at a linear rate. At the same time the dispersed phase is being pumped into the droplet and it continues to grow.(van Steijn, Kreutzer et al. 2007; Fu, Ma et al. 2010) (III) Eventually the neck filament reaches a critical size where the collapse accelerates and a droplet detaches (Garstecki, Fuerstman et al. 2006; van Steijn, Kleijn et al. 2009). The droplet is pushed downstream as the interface recoils into the dispersed channel and the process repeats.
Thus the final size of the droplet is the volume at the end of the filling stage plus the additional volume pumped in before the neck collapses. The scaling law that captures the physics of the

process has the general form (Garstecki, Fuerstman et al. 2006; Christopher, Noharuddin et al. 2008; Xu, Li et al. 2008):

$$V_{drop}^{*} = \frac{V_{drop}}{w_c^{\,2} h} = \alpha + \beta\varphi \tag{4.1}$$

where V_d^{*} is the dimensionless volume , φ is the flow rate ratio and the variables α and β represent the dimensionless initial fill volume and the rate of droplet growth during the necking phase.

The characteristic difference between the squeezing and dripping regimes is often cited as the degree of confinement experienced by the emerging interface(Christopher and Anna 2007). In the squeezing regime, the interface fills the entire microchannel and contacts the far wall before it is sheared off, while in the dripping regime the droplet is sheared off before it contacts the far wall. The result is two qualitatively different breakup mechanisms that depend primarily on either the geometry of the T-junction (squeezing) or the flow conditions (dripping). The transition regime bridges the gap between the two regimes where both factors influence the formation process. Specifics of the two regimes are discussed below.

Unconfined Droplet Breakup

Unconfined droplet breakup occurs typically in the range of $0.3>Ca>0.02$, in geometries where the outlet channel width is much larger than the dispersed inlet ($w_d/w_c>5$), and the flow ratio is small $Q_d/Q_c \rightarrow 0$ (Christopher, Noharuddin et al. 2008; Xu, Li et al. 2008). In such cases, the emerging droplet does not significantly alter the external flow field as it only penetrates a small distance into the cross-flowing stream ($b/w_c<0.3$) and the final droplet size is smaller than the outlet channel width ($L_{drop}<w_c$). Droplet breakup is governed by a balance of local viscous drag acting on the emerging interface and surface tension resisting deformation. Experiments show that in the dripping regime droplet size depends strongly on the continuous phase flow rate and weakly on the disperse phase flow rate and viscosity ratio (Husny and Cooper-White 2006).This results in an inverse relationship between droplet size and *Ca* (Thorsen, Roberts et al. 2001; Husny and Cooper-White 2006; van der Graaf, Nisisako et al. 2006; Christopher, Noharuddin et al. 2008; Xu, Li et al. 2008; Sang, Hong et al. 2009). Models of the droplet size are adapted from membrane based emulsification studies and are derived from a force balance on the emerging unconfined droplet(Christopher and Anna 2007). The general force balance includes capillary, inertia, lift, drag, and buoyancy (Schroder, Behrend et al. 1998; Nahra and Kamotani 2000; Xu,

Luo et al. 2005; Husny and Cooper-White 2006; Theodorakakos, Ous et al. 2006; Meyer and Crocker 2009; Sang, Hong et al. 2009). However, many of these forces are neglected under typical flow conditions in microchannels and the balance reduces primarily to a competition between surface tension and shear (Garstecki, Fuerstman et al. 2006; Husny and Cooper-White 2006; Christopher, Noharuddin et al. 2008). The final size of the droplet is defined as the point where all the forces reach equilibrium. Often the necking stage is omitted as it is relatively short compared to the fill time, and thus its contribution is to the total volume is small.

Confined Droplet Breakup

In the squeezing regime, the surface tension force exceeds the drag so that the interface is able to extend entirely into the main channel ($b/w_c=1$) (Garstecki, Fuerstman et al. 2006). Once the interface contacts the far wall it obstructs the continuous phase which may only bypass the emerging droplet through the corner gutters (van Steijn, Kreutzer et al. 2007). Pressure begins to build upstream of the droplet and the continuous phase begins to squeeze the neck until the droplet pinches off (De Menech, Garstecki et al. 2008). Droplets formed via this process are often called slugs since they occupy the entire cross-section of the microchannel and their lengths are greater than their widths ($L_{drop}>w_c$). Typically, confined droplet breakup occurs at $Ca<0.002$ in T-junctions where the dispersed and continuous channel widths are comparable ($w_d \approx w_c$). (Garstecki, Fuerstman et al. 2006; Christopher, Noharuddin et al. 2008; Xu, Li et al. 2008).

Garstecki *et al.* demonstrated that the size of the droplets and the rate of necking is largely independent of either the *Ca* or viscosity ratio, a fact that has been supported by several researchers through numerical (De Menech, Garstecki et al. 2008; Gupta, Murshed et al. 2009; Liu and Zhang 2009; Gupta and Kumar 2010) and experimental studies (Garstecki, Fuerstman et al. 2006; van Steijn, Kreutzer et al. 2007; van Steijn 2010). This leads to the fact that the formation process is completely mediated by the geometry of the T-junction and α and β are only a function of w_c, w_d, and h.

Transitional Breakup

The transition regime occurs in the range of $0.02<Ca<0.002$, and is a blend where the formation process is governed both by squeezing pressure and shear stress. The continuous phase is partially obstructed ($0.5<b/w_c<1$) so that it bypasses the emerging interface during the whole formation cycle. Consequently, α and β, depend on both the geometry and the *Ca* which has been observed both experimentally (Christopher, Noharuddin et al. 2008; Xu, Li et al. 2008; Fu, Ma et al. 2010)

and numerically (van der Graaf, Nisisako et al. 2006; De Menech, Garstecki et al. 2008; Liu and Zhang 2009; Gupta and Kumar 2010).

Necking Mechanism

Understanding of the necking mechanism is imperative in developing a model of the formation process; in particular, the moment of pinch-off must be known so that the necking time can be estimated. Detailed μ-PIV studies showed that the neck collapses at a nearly linear rate until it reaches a critical size and then appears to collapse almost instantaneously (van Steijn, Kreutzer et al. 2007). Initially the neck is bound by the upper and bottom walls of the microchannel but it is eventually squeezed to a point where it detaches from the walls and forms a thin circular filament that is connected to the main droplet. In multiphase systems such detached threads are always unstable if they are bounded by an immiscible fluids (Guillot, Ajdari et al. 2009). Analysis of 2D co-flowing streams has shown that drop breakup occurs only when the width of the inner fluid is less than the channel height so that thread is detached and hydrodynamic instabilities may form (Humphry, Ajdari et al. 2009).Similar conditions occur in flow focusing generators where the neck originally collapses at a rate proportional to the continuous flow rate and then collapses rapidly once a detached thread forms (Garstecki, Stone et al. 2005; Dollet, van Hoeve et al. 2008).

The situation for the T-junction generator is slightly different since the thread is compressed against the corner which helps stabilize it against hydrodynamic instabilities (Guillot, Ajdari et al. 2009; van Steijn, Kleijn et al. 2009). Rather than break off when the thread initially detaches, droplet pinch off is actually delayed until the thread reaches a smaller size. Rapid collapse coincides with the additional flow of continuous phase into the necking region from the tip of the droplet. The driving force is the local Laplace pressure difference created by the larger curvature of the thread compared to the tip of the droplet (van der Graaf, Steegmans et al. 2005; Garstecki, Fuerstman et al. 2006; van Steijn, Kleijn et al. 2009). van Steijn *et al.* documented this reversal of flow from the front to back of the droplet using μ-PIV experiments. The authors demonstrated that the entire shape of the droplet defines the moment of collapse and found that the critical neck thickness at the moment of collapse is given by (van Steijn, Kleijn et al. 2009):

$$2r_{pinch} = \frac{hw_c}{w_c + h} \tag{4.2}$$

where h is the height of the channel and w_c the width. This equation suggests that collapse is completely mediated by the geometry of the T-junction.

Breakup Models

The parameters governing droplet formation consist of the geometry of the T-junction and the flow conditions: w_c, w_d, h, Q_c, Q_d, γ, μ_c, μ_d and ρ. Based on the Buckingham Pi theorem, the dimensionless volume can be described by six independent dimensionless groups (De Menech, Garstecki et al. 2008; Gupta and Kumar 2010):

$$\varphi = \frac{Q_d}{Q_c} \quad \eta = \frac{\mu_d}{\mu_c} \quad \Lambda^* = \frac{w_d}{w_c} \quad h^* = \frac{h}{w_c} \quad Ca = \frac{\mu_c Q_c}{\gamma w_c h} \quad \mathrm{Re} = \frac{\rho Q_c}{h \mu_c} \tag{4.3}$$

For typical microchannel flows the Reynolds number is not important (Re<1) and the volume is therefore a function of the five remaining groups:

$$V_d^* = f\left(\varphi, \eta, \Lambda, h^*, Ca\right) \tag{4.4}$$

Assuming the scaling law in Eqn. 4.1 is applicable, α and β by association are also dependent on these dimensionless factors.

A recent review by Steegmans *et al.* compared the validity of several models that have been developed over the past decade and came to the conclusion that the two-stage model consisting of a filling stage and a necking stage best represents the formation process (Steegmans, Schroen et al. 2009). Many of the models to date have treated α and β as fitting parameters in the development of empirical correlations for the specific T-junction design under study (van der Graaf, Nisisako et al. 2006; Xu, Li et al. 2008; Dai, Cai et al. 2009; Fries and von Rohr 2009; Wang, Lu et al. 2009; Zhang and Wang 2009; Fu, Ma et al. 2010).These correlations take the general form of:

$$V_d^* = \alpha^a Ca^b + \beta^c \varphi^d Ca^e \tag{4.5}$$

where a through e are fitting parameters which are may or may not be included in a specific correlation. In the dripping regime many of these models exclude the necking term as well (Husny and Cooper-White 2006; De Menech, Garstecki et al. 2008; Sang, Hong et al. 2009). Differences in the fitting parameters across various studies (Steegmans, Schroen et al. 2009; Fu, Ma et al. 2010) suggests that either some physical phenomena has not been accounted for or that

correlations are not universally applicable and only useful to the unique conditions of a specific study.

There are several notable exceptions to the correlation based models that have attempted to elicit the phenomena governing droplet formation. Models in the dripping regime by Husny *et al.*, Sang *et al.* and Steegmans *et al.* use a detailed force balance to derive the final droplet size. Husny and Cooper-White developed an equation to this effect which was able to predict droplet size with an accuracy of 25% over a wide range of experimental conditions. (Husny and Cooper-White 2006). Sang *et al.* performed a similar analysis but extended it to non-Newtonian power law fluids with good results as well (Sang, Hong et al. 2009). Steegmans *et al.* performed a force balance model on a Y-junction generator and found that the droplet size scales inversely with *Ca* (Steegmans, Schroen et al. 2009). None of these models considered the necking stage in the formation process, and a small degree of empirical fitting is required to achieve good corroboration with experimental results.

In the transition regime, the most notable work is by Christopher *et al.*, who developed a simple force balance to determine the fill volume and incorporated the geometry into the two formation parameters (Christopher, Noharuddin et al. 2008). The force balance includes the surface tension resisting deformation combined with the viscous drag and pressure force created by the blockage of the passing continuous phase such that the droplet volume is given by:

$$V_d^* = b^{*2} + \Lambda^* \varphi \tag{4.6}$$

where b^* is the penetration depth of the emerging droplet in the filling phase, which satisfies the following equation:

$$\left(1 - b^*\right)^3 = b^* Ca \tag{4.7}$$

When compared with experimental results the model captures many of the salient features observed by several researches, namely *Ca* and geometric dependence on the size of the droplets. Christopher *et al.* applied to the model to their own experimental results and found good qualitative agreement. Other researchers have also applied the model to numerical (Gupta, Murshed et al. 2009; Gupta and Kumar 2010)and experimental (Fu, Ma et al. 2010) studies with reasonable agreement, but discrepancies still arise due to the simplest nature of the model.

Recently, van Steijn *et al.* developed a model for the two parameters in the squeezing regime which combines a detailed geometric representation of the droplet with the application of physical principals to describe the formation process (van Steijn 2010). The model represents the best attempt at providing a theoretical foundation for droplet formation and consists of three ingredients: (I) a detailed geometric description of the droplet from the initial fill stage to the necking stage. (II) the application of the continuity equation to derive the evolution of the neck during the squeezing period. (III) the incorporation of the pinch-off mechanism to define the end of the necking stage. The result is a series of equations that describe the two parameters, α and β, entirely based on the geometry of the channel (Λ^*, h^*). It turns out that the most influential parameter is the intersection ratio, Λ^*, followed by the channel height ratio h^*. The authors validated the model by accurately predicting the performance of a variety of T-junction geometries ranging from $\Lambda^*=0.33\rightarrow3$ and $h^*=0.11\rightarrow0.33$. In addition, the authors demonstrate the authority of their model by comparing the evolution of the neck during the squeezing phase with impressive results.

The purpose of this study is to build upon the works of both Christopher *et al.* and van Steijn *et al.* and develop a comprehensive model in the squeezing to transition regime. The model adapts the geometric representation of the formation process from van Steijn *et al.* and includes a more detailed force balance model to determine the initial fill size. Moreover, a new criterion for pinch-off is presented based on our own experimental observations. In addition to the droplet volume, equations are derived for the oil volume and frequency so that the entire operation of the generator is defined. This is the first time that spacing has been considered as part of a comprehensive model.

To validate the model a detailed experimental study is performed that spans the dimensionless parameters discussed above. Silicon oil is used as the continuous phase and various mixtures of glycerol and water as the dispersed phase in the absence of surfactants. The viscosity ratio varies from $\eta=0.12, 0.25, 0.6, 1.7$ and the intersection from $\Lambda^*=0.33, 0.5,$ 1, the height from $h^*=0.35, 0.5, 0.6$ and the Capillary number from $Ca=0.001\rightarrow0.008$. Therefore, our experiments span the typical conditions considered in T-junction generators operating in the squeezing to transition regime (Christopher, Noharuddin et al. 2008; De Menech, Garstecki et al. 2008).
In the following section the experimental protocols are outlined for quantifying the T-junction operation using high speed video analysis. In Section 4.4 the experimental data is assessed to understand the formation process. In Section 4.5 the model is outlined that describes the

performance of the T-junction generator. The new force balance is presented in Section 4.5.10 and the new pinch-off criteria in Section 4.5.11. A comparison between the model and the experimental results are presented in Section 4.6. Finally, conclusions and suggestions for future developments are also outlined.

4.2 Experimental Design

In the preceding discussion, a number of important parameters were identified that were hypothesized to influence the T-junction generator operating in constant pressure mode in the squeezing to transition regime. To evaluate these parameters, and provide quantitative data that can be used to develop a model of the T-junction operation, a comprehensive experimental study was performed. The goal is to test several different conditions by varying the viscosity ratio, local T-junction geometry and Capillary number. Table 4.1 lists the conditions for the experiments that were performed in this study. The specifics of each factor are discussed below.

Table 4.1 Experimental conditions. Silicone oil was the continuous phase in all cases with various mixtures of glycerol/water as the dispersed phase. Nominal values for the height of the channels and width of the dispersed phase are provided as well as the width ratio (Λ), height ratio (h^*) and viscosity ratio (η).

Exp #	D.Ph	h (µm)	w_d (µm)	Λ^*	h^*	η
1-3	Glyc/water 10, 30, 50 % wt	30	30	0.3	0.3	0.12, 0.26, 0.6
4-6	Glyc/water 10, 30, 50 % wt	30	100	1	0.3	0.12, 0.26, 0.6
5-9	Glyc/water 10, 30, 50 % wt	40	30	0.3	0.4	0.12, 0.26, 0.6
10-12	Glyc/water 10, 30, 50 % wt	40	50	0.5	0.4	0.12, 0.26, 0.6
13-16	Glyc/water 10, 30, 50 %, 70% wt	40	100	1	0.5	0.12, 0.26, 0.6, 1.7
17-20	Glyc/water 10, 30, 50 %, 70% wt	50	50	0.5	0.5	0.12, 0.26, 0.6, 1.7
21-22	Glyc/water 10, 30 % wt	50	100	1	0.5	0.12, 0.26

Continuous Phase

For all experiments the continuous phase a low viscosity silicone oil was utilized (DC200, Sigma Aldrich). Silicone oil is actually composed of loose PDMS monomer chains so it naturally wets soft-lithography fabricated PDMS microchannels and does not require any specialized surface treatment. However, silicone oil swells PDMS slightly which changes the dimensions of the channels. Due to this fact, the dimensions of the channels (height and width) are measured carefully before each experiment.

Dispersed Phase

The dispersed phase was a set of glycerol/water mixtures of 10%, 30% 50% and 70% (wt %). Adding glycerol to water increases the viscosity of the dispersed phase without changing the interfacial tension appreciably (~34-37 mN/m). With these combinations the viscosity ratio between the dispersed and continuous phase varies from 0.125 to 1.7.

Surfactants

No surfactant is added to either fluid to eliminate the possibility of mass transport dynamics effecting the interfacial tension. The possibility exists that impurities might still have an effect, but for the purpose of this study, these effects are neglected and a uniform interfacial tension is assumed throughout the formation process.

Width ratio

The cross-sectional shape of the microchannels throughout the network is rectangular with a uniform depth and width. The continuous phase channel and main channel width is kept constant at 100µm, while the width of the dispersed phase inlet is set at 33, 50 and 100µm. This corresponds to width ratios of 1:3, 1:2, and 1:1. Larger width ratios, such as 2:1, are excluded from this study since they are uncommon in literature. As well, a ratio of 1:3 was set as the minimum since Garstecki *et al.* identified that droplets could not be formed in the squeezing regime at ratios of 1:5 (Garstecki, Fuerstman et al. 2006).

Three nominal channel heights were chosen: 30, 50 and 60um. This corresponds to aspect ratios (*h: w*) of 1:3, 1:2 and 1:1.67, which spans a large enough range to study the influence of height on the formation of droplets. The actual height varies from the nominal value because of difference in the SU-8 masters and swelling of the PDMS microchannels by the oils. The specific height for each chip used in a test is measured beforehand as discussed in Section 4.2.5.

Global Network Design

The chip type refers to the global network design of the T-junction generator including the length and relative resistance of the three branches to each other. The global network design can influence the overall performance of the generator by limiting the variation in droplet production. A detailed analysis of the effect of global network geometry on the variability of droplet production is presented in Chapter 3.

In the current experiments the same overall network geometry was used in all cases as shown in Figure 2. The lengths of the inlet channels are 1 cm and the main channel was 5cm. Attached to the inlet of the dispersed phase is a small diameter microchannel (diameter ~25x 100 μm) to increase the hydrodynamic resistance of the dispersed phase branch in order to reduce fluctuations in flow rate according to the analysis provided in Chapter 3.

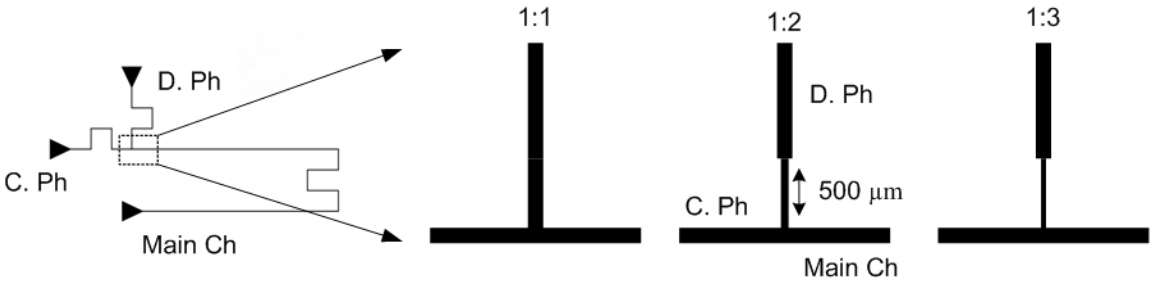

Figure 4.2 A diagram of the overall geometry of the T-junction network with a close up of the local geometry at the junction for the three nominal designs.

4.2.1 Experimental Setup

Each chip was mounted in the microscope setup previously described in Chapter 3. Constant pressure flow was used to control the fluid flow using the Fluigent pressure system. A separate Matlab program is used to design a set of 16 pressure conditions (P_c, P_d) for each experimental case. The program estimates the pressures to be applied using a 1D hydrodynamic model of the network (refer to section 3.14). The conditions are broken down into 4 levels of P_c that attempt to span $0.001<Ca<0.02$. At each P_c level, 4 different P_d are applied to create a range of flow rate ratios and thus droplet sizes. P_d values are calculated so that there is no backflow of oil into the water channel or vice versa. There are also other limits imposed on the pressures. The maximum pressure applied is limited to 1050 mBar by the Fluigent system. The minimum is set to exceed an estimated flow rate of 0.5μL/min in order to get accurate readings from the flow sensor. Due to these limitations, the actual capillary number range for a specific experiment is less than the full range. Each pressure step is applied for a minimum of 120s which corresponds to at least 20 chip volume replacements. An example of a set of experimental conditions used for the case study #2 is provided in Table 4.2.

Table 4.2 Pressure conditions used in Case study #2 for silicone oil and water with no surfactant on a type 3 chip, with a 1:2 width ratio, and nominal height of 35µm. P_m is set to 100 mBar and P_d and P_c are set relative to this pressure.

Step #	1	2	3	4	5	6	7	8	9	10	11	12	13	14	15	16
P_d (mBar)	594	594	594	594	658	658	658	658	722	722	722	722	786	786	786	786
P_c (mBar)	413	432	451	470	448	463	484	528	491	508	533	549	528	555	583	610
P_m (mBar)	100	100	100	100	100	100	100	100	100	100	100	100	100	100	100	100
Time (s)	60	60	60	60	60	60	60	60	60	60	60	60	60	60	60	60

The automated sequence is as follows. The three pressures (P_c, P_d, P_m) are applied for the specified time. When 80% of the time has passed, the high speed camera is triggered and a video is recorded. At the same time the flow sensor begins to continuously record the flow rate until the full time elapses, and the average value is obtained. The system then proceeds to the next pressure step while the video and flow sensor triggers are reset. This is repeated until all of the steps are completed. When the experiment finishes a data file is output with all of the measured flow rates, pressures and details on the specific case study (fluids used, chip type, ect). More details on the overall experimental procedure are provided in the next section.

4.2.2 Experimental Procedure

Below a brief overview of the experimental procedure is provided with references to subsequent sections for more details.

- Before starting a set of experiments with a new oil the entire tubing and flow sensor are cleaned using detergent, water and finally blown dry with high pressure air.
- Next the flow sensor was calibrated for the specific oil using the procedure described in Section 3.3.1.
- Fluid properties are measured beforehand as described in Section 3.2
- For a specific case study several chips of the specified type are fabricated using the procedures describe in Section 4.24
- Next the chip was connected to the pressure system and flushed with oil for 10 minutes. The chip was then inspected carefully for any debris that might block the channels. If the chip was clogged it was thrown away and a new chip was used.
- If the chip was in good shape the channel dimensions were then measured using the protocols described in Section 4.2.5

- Using the dimension of the chip a custom pressure step program was then created for the experiment.
- Pressures to the two phases are manually controlled until consistent droplets are formed. Several different steps in the custom pressure program are checked. The chip is allowed to run for 20 min to stabilize droplet formation.
- The pressure step program is then loaded into the Labview program and run until completion.
- Videos are then edited to a length of 5-10 droplets and saved.
- The custom image analysis program described in Section 4.3 is used to analyze the videos and extract additional experimental data.
- The process is then repeated for the next repetition or new case study.

4.2.3 Chip Fabrication

Different chip designs were fabricated on silicon wafers using standard soft-lithography procedures developed in the lab as previously outlined in Section 3.1. Designs were grouped by the channel height and intersection type, and then by channel layout. Therefore, one master consists of 3 designs (type 1, type 2, and type 3) with the same intersection (ex. 1:1) and same nominal height (ex. 30μm). PDMS molds (Sylgard 184, Dow Corning) in a ratio of 10:1 (base: curing agent) were made and cured at 100˚C for at least 2 hrs. Specific designs were then cut out and fluidic access holes were punched using a 1.5mm biopsy punch (Unicore, Harris).

PDMS molds are bonded to a glass slide coated with PDMS so as to create a homogeneous microchannel. PDMS coated slides are fabricated by spin coating 10:1 PDMS at 3000 rpm for 60s followed by baking for 5 min at 95˚C. The two substrates are exposed to oxygen plasma (PDC-001, Harrick Plasma) under conditions of 29.6W at 500mTorr for 10s. The plasma treatment renders the PDMS hydrophilic, to reverse the process, the chip is heated at 180˚C for 12 hrs. Prior to starting the experiments the chip is primed by pumping silicone oil through the microchannels for 1 hr to guarantee that the channels are fully swollen.

4.2.4 Fluid Property Measurements

Table 4.3 summarizes the various properties that were measured including the viscosity, density, and interfacial tension of the various oil and water/glycerol combinations.

Table 4.3 Properties including viscosity, refractive index and interfacial tension for each of the fluids and w/o combinations. Measurements are made at room temperature, 22 ±1˚C.

Continuous Phase	Dispersed Phase	Viscosity (mPas)		Interfacial Tension (mN/m)
		μ_c	μ_d	γ
Silicone Oil	Glycerol/water 10 wt%	10.2	1.21	37.1
	Glycerol/water 30 wt%		2.61	36.2
	Glycerol/water 50 wt%		6.05	35.2
	Glycerol/water 70 wt%		17.1	34.3

4.2.5 Channel Dimension Measurements

Accurate knowledge of the microchannel dimensions (*w, h*) is critical for calculating the droplet volume from the video image. Most of the oils are slightly soluble in PDMS and this causes the microchannels to swell and the dimensions to shrink. In addition, PDMS is flexible and can bulge under applied pressure driven flow changing the dimensions of the channel (Holden, Kumar et al. 2003). These factors make it difficult to measure the channel dimensions by standard procedures such as using a profilometer to estimate the channel dimensions from the SU-8 master. Instead, measurements of the channel dimensions must be made *in situ* for each specific chip.

To accomplish this we use the current experimental setup consisting of the flow sensor and pressure controller to measure the equivalent hydrodynamic resistance ($R_{hyd}=P/Q$) of the network. From the hydrodynamic resistance the height can be calculated by applying a 1-D hydrodynamic network model for pressure driven flow to the T-junction design (Qiao and Aluru 2002; Chatterjee and Aluru 2005; Jousse, Lian et al. 2005; Bruus 2007). Since the hydrodynamic resistance depends on h^3, the calculation is very sensitive to the measured parameters (*P, Q*) and is therefore an effective means of measuring the channel height. In addition, the value obtained for *h* represents an average or equivalent value over the entire channel network, rather than a point measurement which a profilometer would produce.

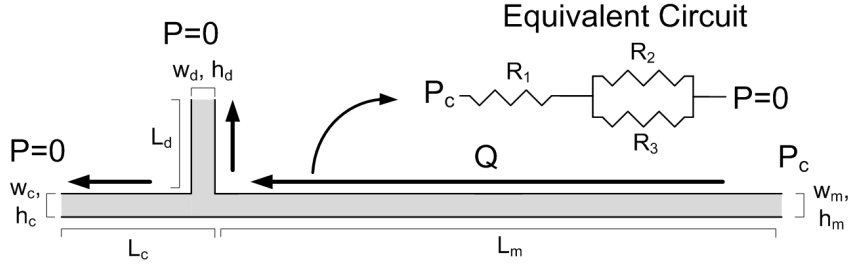

Figure 4.3 Schematic diagram of the T-junction generator network with the equivalent hydrodynamic circuit for calculating the channel height from the measured flow rate at an applied pressure.

Height measurements are performed after the oil has swelled the PDMS sufficiently and just before the droplet experiment starts. The oil inlet from the pressure system is connected to the longest channel in the network (highest resistance), and pipette tips are inserted into the other outlets. To capture any bulging effects, three pressures are applied spanning the range that will be used in the droplet experiment, with the flow rate recorded at each step. The width is measured from a spatially calibrated image of the T-junction intersection and the length (L) is known from the mask print.

Figure 4.3 shows a schematic of the T-junction network and the equivalent hydrodynamic circuit. The equivalent resistance is calculated from the measured values of flow rate and applied pressure:

$$R_{hyd_{eq}} = \frac{P}{Q} \tag{4.8}$$

Applying common circuit analysis methods, the equivalent resistance is equal to one resistor in series with two in parallel:

$$R_{hyd_{eq}} = R_1 + \frac{R_2 R_3}{R_2 + R_3} \tag{4.9}$$

For a rectangular microchannel operating under laminar flow conditions, the hydrodynamic resistance can be calculated from the following equation(Beebe, Mensing et al. 2002; Bruus 2007; Schindler and Ajdari 2008):

$$R_{hyd} = \frac{12\mu L}{wh^3}\left[1 - \frac{h}{w}\left(\frac{192}{\pi^5}\sum_{n=1,3,5}^{\infty}\frac{1}{n^5}\tanh\left(\frac{n\pi w}{2h}\right)\right)\right]^{-1} \tag{4.10}$$

Substituting the measured value on the left hand side of Eqn. 4.8 for the 3 channel resistances, the height can be calculated by iterating until the two sides are equal. A Matlab program was written for this purpose.

4.3 Data Extraction from Videos

Videos captured by the high speed camera are analyzed to extract the breakup parameters including the size, speed, frequency, and spacing of the droplets. Videos were post processed using a custom image analysis program written in Matlab. Since the data obtained from the

videos is important to understanding the operation of the T-junction generator, details about the methods used are discussed below.

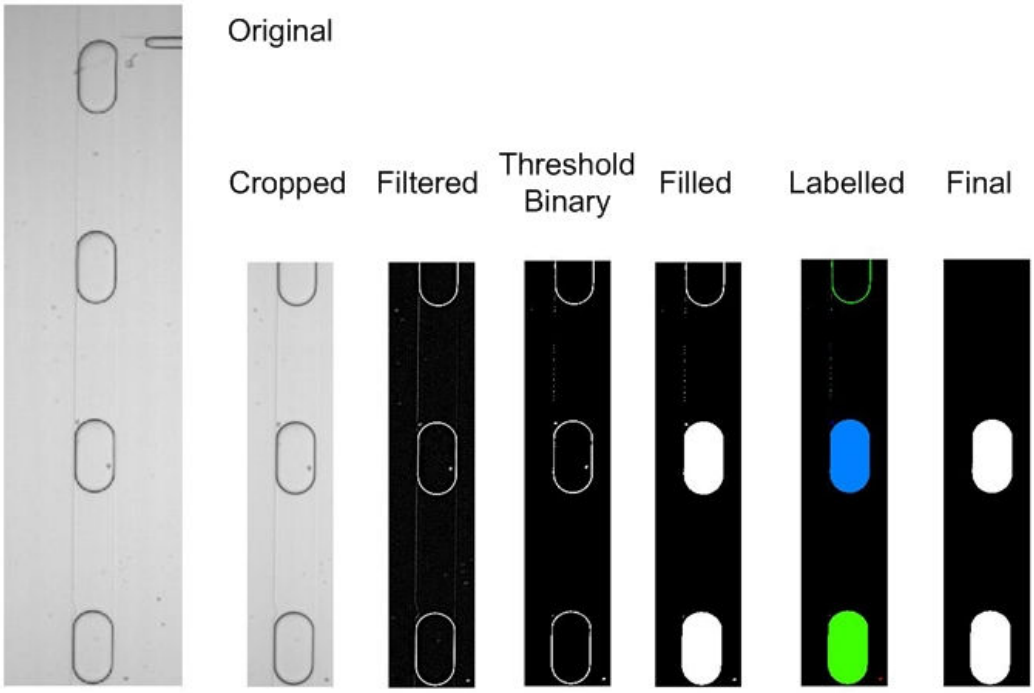

Figure 4.4 Sequence of image processes performed to a single frame in the video to isolate only the droplets and to obtain information on the droplets.

Droplet Identification

The series of steps applied in the droplet identification process is shown in Figure 4.4. For the analysis to work correctly, the droplets must be moving in a downward direction in the same orientation as shown in the figure. Each frame in the video is first cropped to decrease the memory requirement for the subsequent analysis. A logarithmic filter is then applied to enhance the edges of the droplet. Next a threshold binning operation is applied, which identifies all pixels below a critical value, creating a binary image that highlights the edges of the droplets. Areas that are completely enclosed by a boundary are filled. Each "blob" in the image is then identified and labelled. Unwanted regions are eliminated by setting boundaries for the area and location of the centroid. The final product is a binary image of the original with the droplets identified and labelled as shown in Figure 4.4.

Droplet Dimensions, Area, and Volume Calculation

From the final binary image a boundary identification operation is applied to obtain the boundary pixels for each individual drop in the frame. The Cartesian coordinates of the pixels are then

converted into cylindrical coordinates (g,θ) with the origin being the centroid of the drop as shown in Figure 4.5. The length and width of the droplet are calculated by scanning through the diameter at each radial position to find the maximum and minimum distances. The area is calculated by applying a Riemann numerical integration scheme in cylindrical coordinates.

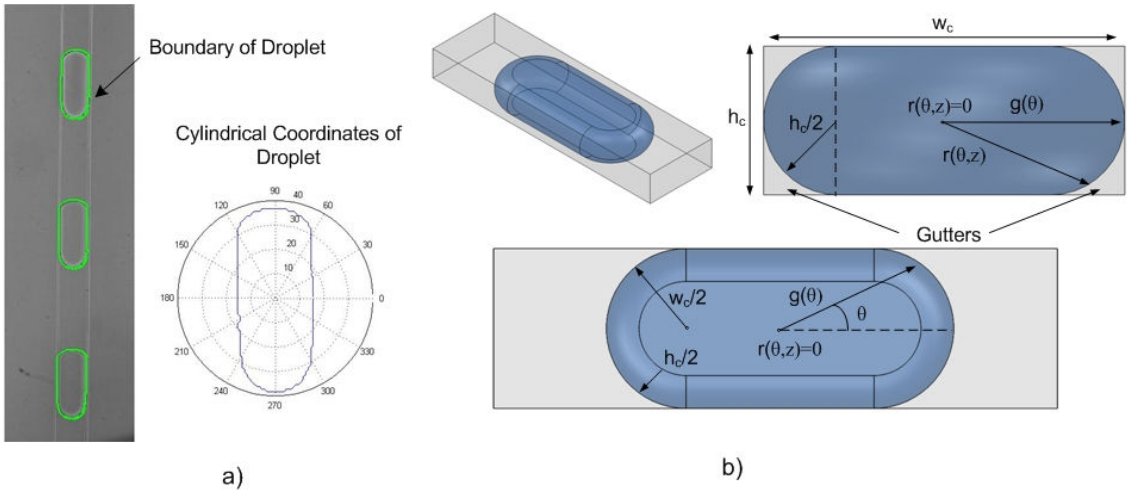

Figure 4.5 (a) Image with boundary data of the droplets overlaid and the pixel locations transformed into cylindrical co-ordinates, which provides the in-plane droplet shape g(θ). (b) A diagram of the assumed shape of the droplet in three dimensions, where the out of plane curvature is approximated as *h/2*. The volume of the droplet can then be calculated by integrating from the 2-D projection.

Originally the volume is estimated from the 2D-image of the droplet using the method described by Christopher and Anna (Christopher, Noharuddin et al. 2008). This method assumes that the droplet is confined by the channel walls and that the edges of the droplet are curved to minimize surface energy as shown in Figure 4.5. The authors approximate the out of plane curvature of the droplet to be equal to half the channel depth ($r_c \approx h/2$), leading to the following expression for the three dimensional shape of the droplet:

$$r(\theta,z)=\left(\frac{h^2}{4}-z^2\right)^{\frac{1}{2}}+g(\theta)-\frac{h}{2} \tag{4.11}$$

where r is the function describing the geometry of the droplet, z is the out of plane co-ordinate, h is the height, and $g(\theta)$ is the function describing the boundary of the droplet in the captured image. This equation is then integrated to obtain the expression for droplet volume:

$$V=\left(\frac{5}{12}-\frac{\pi}{8}\right)\pi h^3+\left(\frac{\pi}{8}-\frac{1}{2}\right)\pi h^2\int_0^{2\pi} g(\theta)\cdot d\theta+\frac{h}{2}\int_0^{2\pi} g(\theta)^2\cdot d\theta \tag{4.12}$$

Since the volume calculation is proportional to the cube of the height, it is important to measure it accurately as described in Section 4.2.5. However, depending on the shape of the droplet this calculation leads to a significant under approximation of the droplet volume. The reason is that the authors assume that the direction of out of plane curvature is in the same plane as the function *g(θ)* which is not true if the droplet is confined by the side walls of the microchannel. Instead, a different method for calculating the volume from the projected area was used that projects the 2D area of the droplet through the height and then subtracts the out of plane curvature around the perimeter (van Steijn 2010) :

$$V_d = h_m A_d - \frac{h_m^{\,2}}{2}\left(1 - \frac{\pi}{4}\right) l_d \tag{4.13}$$

The calculation of the droplet volume is most likely the largest source of error in the experimental measurements. The assumption that the curvature equals half the depth of the droplet may not be valid in some cases. For instance, at high capillary numbers the curvature of the leading edge of droplet increases while the back decreases (Bretherton 1961; Wong, Radke et al. 1995; Wong, Radke et al. 1995; Adzima and Velankar 2006; Fuerstman, Lai et al. 2007; Ody, Baroud et al. 2007; Walsh, Muzychka et al. 2009). In addition, at low surface tensions and large aspect ratios the corner shape may change with the side of the droplet contacting more of the microchannel wall (Ransohoff and Radke 1988; Wong, Morris et al. 1992; Ajaev and Homsy 2006). In this case, the current approximation of the droplet shape would under predict the actual volume. The magnitude of this error is also greater in low aspect ratio channels (*h/w*).

To estimate the error, we consider the lowest aspect ratio design (50μm by 100μm) and compare the cross-sectional area of the approximated shape to the theoretical worst case scenario where the droplet fills the entire cross-section. The difference in volume in these two cases is approximately 10.7%. As this represents a maximum potential error, the actual error is expected to be less and is estimated to be around 2-5%. However, it should be noted that qualitative observations from phase contrast images of the droplets which highlight the corner shape show that the shape matches the approximation. Therefore, calculating the volume of the droplets from the 2D images is considered to be sufficiently accurate for this study.

Droplet Speed, Frequency and Spacing Calculation

Calculating the droplet speed, frequency and spacing requires a robust algorithm given that a multitude of conditions may be encountered when analyzing the videos. For example, the frame

may contain several droplets, or a single droplet, or there are no droplets for several sequential frames. In addition, droplets may "flash" where they appear in one frame and then disappear in the next because the droplet is not properly filled by the identification algorithm. These conditions must be identified and treated when extracting the desired measurements. Details on the algorithm used to calculate the frequency, velocity and spacing are described below.

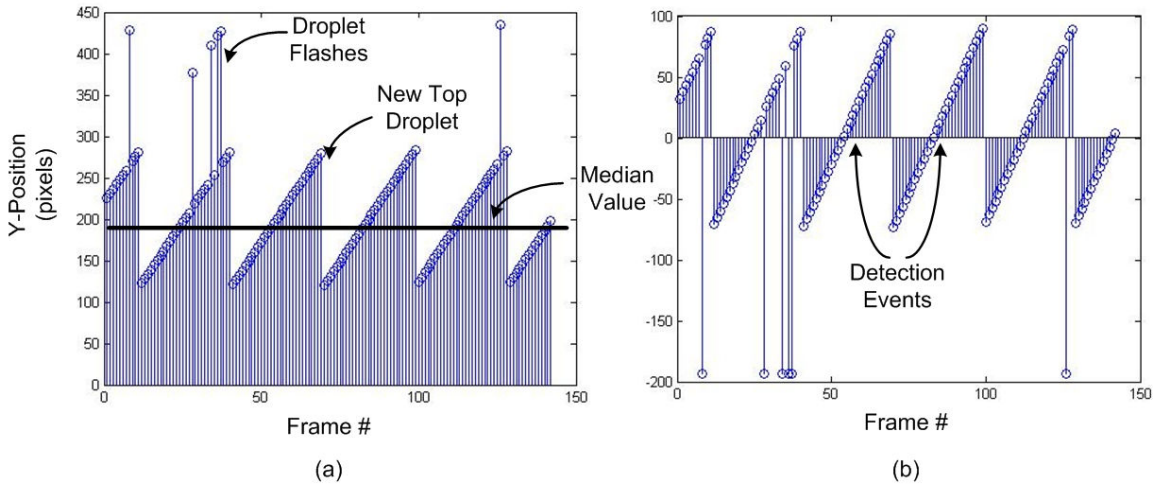

Figure 4.6 (a) Example of the y-position of the top droplet of an analyzed video. Droplet flashes correspond to a sudden increase in position because a lower droplet becomes the top droplet. A new droplet results in a decrease in position. The line across the image shows the median value of droplet position. (b) The y-position adjusted by the median with the detection events highlighted.

Only the droplet closest to the T-junction generator (i.e. top droplet in the frame) is used to calculate the speed, frequency and spacing. First, the position of the top droplet in each frame is recorded for the entire video by tracking its centroid. Next, the displacement from frame to frame is calculated and the median value found. The median value is used in the calculation to remove any erroneous measurements such as when (a) a droplet "flashes" and a lower droplet briefly becomes the top droplet, (b) the current top droplet is replaced by a new droplet entering the frame or (c) there are no droplets in the frame (see Figure 4.6). These conditions are identified by comparing the median value plus a safety factor to the displacement between each frame. Once the conditions are identified they are accounted for in subsequent calculations.

The frequency/period is calculated by measuring the time it takes between droplets passing a specific detection point along the microchannel. The detection point is chosen as the median y-coordinate position of all top droplets, since it guarantees that all droplets pass through the detection point. The median position is then subtracted from the y-coordinate position. Therefore, when a droplet passes the detection point its relative position flips from positive to negative and

this change in sign is used to identify the detection event (refer to Figure 4.6). The specific time is calculated by interpolating between the two frames bracketing the event. Finally, the period (τ) is calculated as the time between events, and the frequency is the inverse of the period ($f=1/\tau$).

The instantaneous speed (u) is calculated by simply dividing the displacement between frames by the frame rate, interpolating between droplet flashes and eliminating cases where a new droplet enters the field of view. The spacing is calculated as the product of the speed and the period ($\lambda=uf$). This method was preferred over actually measuring the distance between droplets in a frame since there are cases where there is one only droplet or no droplets in the field of view. The flow rate of the dispersed phase is calculated as the droplet volume multiplied by the frequency of formation ($Q=Vf$). All data is averaged and the median value and standard deviation outputted. Typical standard deviations are less than 2%.

Measurement of Penetration Depth and Pinch off

In addition to measuring the droplets size, speed and spacing, the depth of penetration of the interface during the filling stage and the size of the neck at pinch off were also extracted from the captured videos. Figure 4.7 shows the tracking of these two parameters for an example case. Penetration depth was calculated by tracking the farthest point on the droplet from the near channel wall. The final penetration depth at the end of the filing stage was calculated depending on the geometry of the T-junction (refer to Figure 4.18for details). The neck was calculated by monitoring the edge of the droplet at a 45° angle to the inner corner of the T-junction. The final point of rapid pinch-off was determined by the sudden increase in rate of collapse of the neck.

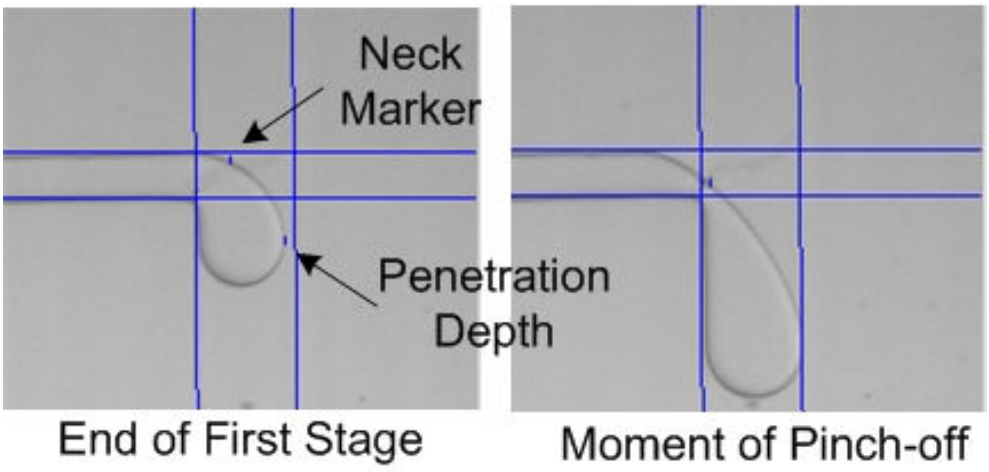

Figure 4.7 Results of image analysis used to determine the penetration depth and critical neck thickness at pinch-off as indicated by the markers. The position of the microchannel walls is automatically detected as highlighted by the blue line overlays.

Video and Data Output

After the analysis, a new video is created of the binary filled images used in the analysis. These videos are checked to verify that there are no errors in the droplet identification process. The data for each experiment is then outputted to a master file that contains all the raw experimental parameters including information on the chip parameters, fluid properties, applied pressures, measured flow rates, droplet dimensions, frequency, period and spacing. This data is then subsequently analyzed to study the operation of the T-junction design. A separate Matlab program takes the data and computes the non-dimensional parameters governing the formation process as well as applies the model to calculate the predicted operational conditions.

4.4 Experimental Observations

Figure 4.8 presents the drop formation process for four different T-junction geometries at specific flow conditions for the same fluid combinations ($\eta=0.12$). Case A and B demonstrate the influence of intersection geometry on droplet production. In both cases the flow conditions (Q_d, Q_c, Ca) are similar but the geometries different. What is first noticeable is the large difference in the rate of droplet production, ~70 Hz for A and ~30 Hz for B and the relative size difference in the droplets. This due to the conservation of mass $Q=Vf$; in order to maintain the same flow rate, larger droplets must be formed at a lower frequency and smaller droplets at a higher frequency. The design of the T-junction is a key factor controlling the formation process including the size and frequency of droplets. Keeping the main channel width (w_c) and flow conditions (Q_d, Q_c, Ca) constant, narrower dispersed channel width (w_d) results in smaller droplets formed at higher rates with smaller inter-droplet spacings (Case A compared to B). Alternatively, keeping the geometry the same and changing the flow conditions, the size, spacing and rate of production can be tuned as shown in C and D. An example of a video of droplet formation is provided in Appendix A.

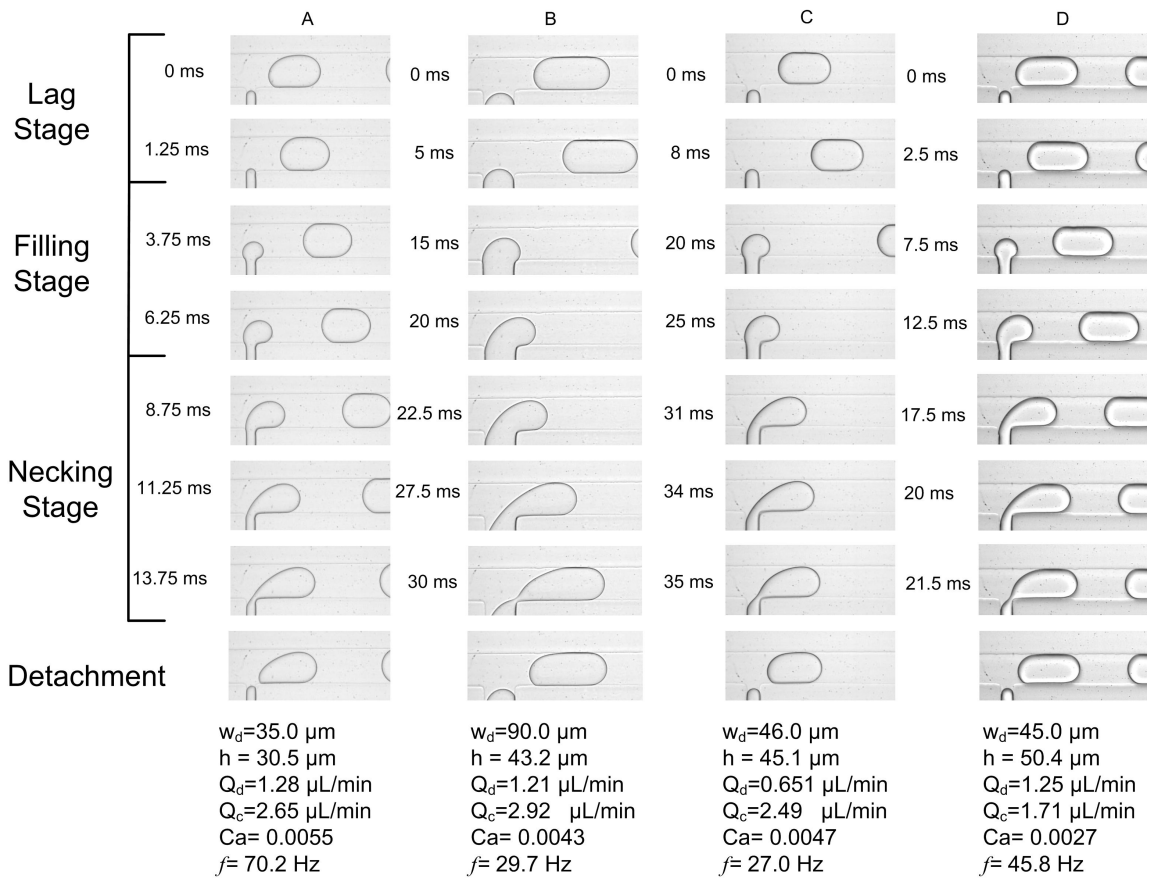

Figure 4.8 Images of the drop formation process for four experiments broken down into the three observed stages (i) lag (ii) filling (iii) necking. Silicon oil is the continuous phase and 10%wt glycerol/water the dispersed phase, other experimental data is listed below the images.

4.4.1 Dynamics of Droplet Formation

To analyze the droplet formation process further, the evolution of the droplet shape-penetration depth b, neck thickness $2r_n$ and droplet volume V_{drop}-was tracked for cases A and B and plotted over the formation cycle t/τ_{drop} (see Figures 4.9 a,c). The corresponding continuous phase volume V_c which was decomposed into the volume surrounding the neck V_{neck} and the volume between the new and old droplet V_{bypass} was also tracked (see Figures 4.9 *b,d*). From these measurements the fraction of the continuous phase flow Q_c collapsing the neck Q_{neck} or bypassing the droplet Q_{bypass} can be measured by tracking the associated change in volumes. Volumes were derived from high speed images of the droplet formation process using Eqn. 4.13. Data is non-dimensionalized, b and $2r_n$ are normalized by w_c and the volumes by $w_c^2 h$.

Based on the analysis of the video evidence, the formation process can be divided into three periods consisting of a short (i) lag stage, followed by the (ii) filling stage and finally the (iii) necking stage. The addition of the lag stage adds another element to the conventional two-stage model of the droplet formation process used by other researchers. Analysis of each stage is provided below.

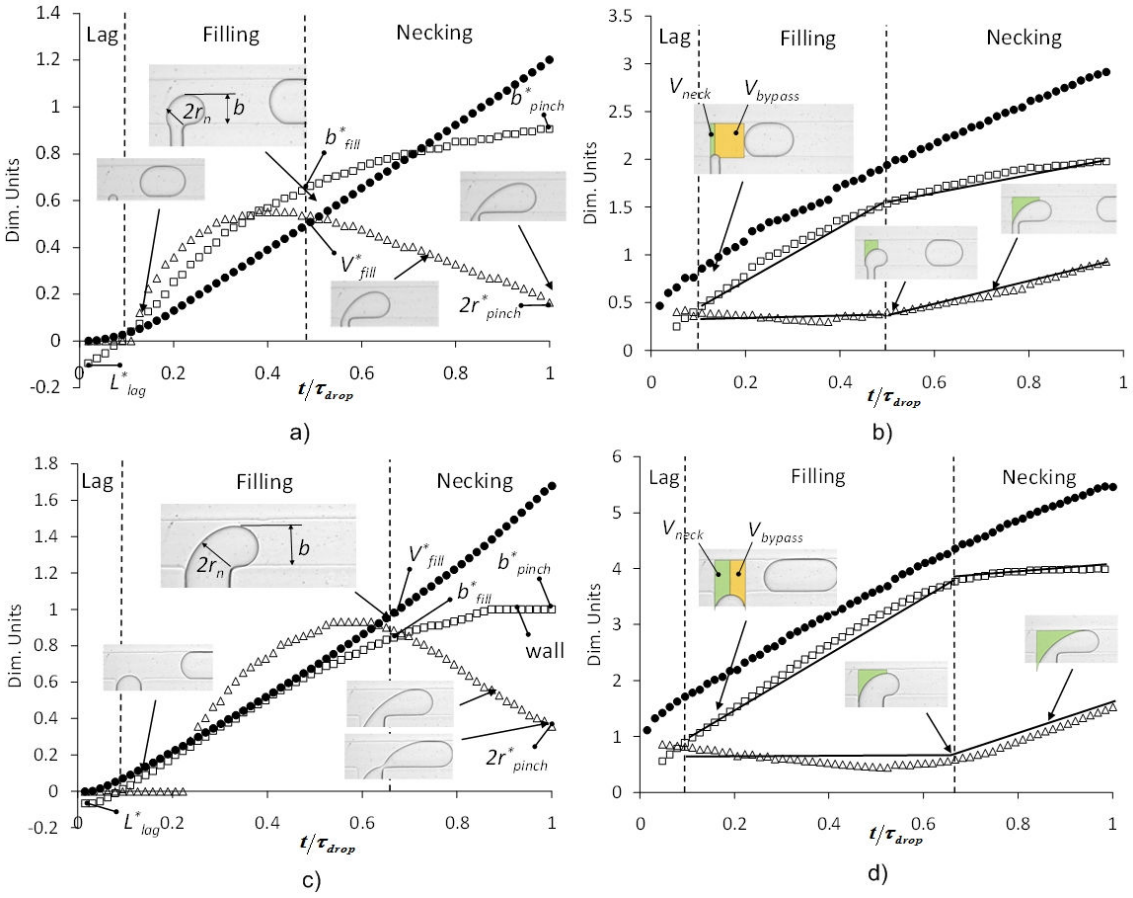

Figure 4.9 Evolution of droplet shape and volume with time for Case A and B. (a)(c) changes in ● V^*_{drop}, Δ $2r^*_n$, □ b^* and (b)(d) in ● V^*_c, Δ V^*_{neck}, □ V^*_{bypass}. Formation is characterized by the lag stage, filling stage and necking stage as indicated by the dashed lines. The dispersed and continuous phase flow remain constant during the entire formation process. Solid lines provide linear fits to the change in volume for the specified regions.

Lag Stage

Immediately after detachment, the interface recedes a small distance L^*_{lag} back into the dispersed phase inlet before it moves forward again and reaches the entrance of the main channel. Almost all of the continuous phase bypasses the interface and fills the space behind the previously generated droplet increasing V^*_{bypass}. The lag stage is typically very short representing 2-10% of

the total formation time and a small portion of the total droplet volume as well (Case A ~4%, B ~2.5%V^*_{drop}); however, the contribution to the spacing, V^*_{cp}, can be significant (Case A ~10%, B~18%) and cannot be ignored if the complete formation process is to be modeled. The duration of the lag stage correlates with the expected value from the flow rate $\Delta t_{lag} = L_{lag} / (Q_d w_d h)$. Therefore, one expects the droplet volume to scale as $V_{drop} \sim L_{lag}$ and the bypass volume as $V_{bypass} \sim \Delta t_{lag} Q_c$ in the lag stage.

Filling Stage

The interface continuous to penetrate into the main channel and the shape of the interface deforms with a small radius at the front of the droplet and a large radius at the back. The neck of the droplet, $2r^*_n$, is the shortest distance between the T-junction corner and the back half of the droplet. In the early filling stage the neck thickness increase sharply, but soon the rate of growth decreases reaching a plateau and then decreases at a linear rate in the necking stage. This transition between the plateau and the subsequent decrease in the neck thickness marks the end of the filling stage. It also marks a point where capillary and drag forces on the droplet balance and the droplet takes on a characteristic shape denoted by b^*_{fill} and a droplet volume of V^*_{fill}. Therefore, one expects the duration of the filling stage to last $\Delta t_{lag} \sim V_{fill} / Q_d$.

During this same period of time the continuous phase keeps bypassing the droplet as V^*_{bypass} increases linearly with time at a rate $dV/dt \sim Q_c$ while V^*_{neck} remains relatively constant. Thus the bypass volume increases by $V_{bypass} \sim \Delta t_{lag} Q_c = V_{fill} Q_c / Q_d$ .As a matter of fact, during the entire formation process the volume of the droplet and the total volume of oil increases at a linear rate confirming that the dynamics of formation has little effect on the global flow rates. For the examples, the penetration depth equals $b^*_{fill} = 0.64$ for case A and $b^*_{fill} = 0.83$ for case B. The smaller b^*_{fill} for Case A results in a comparatively shorter filling stage and smaller droplet fill volumes (Case A V^*_{fill}~40%V^*_{drop}, Case B V^*_{fill}~52%V^*_{drop}).

Necking Stage

The necking stage results in a redistribution of the continuous phase as fraction of the flow is directed to collapsing the neck. The fraction of the flow collapsing the neck seems to correlate well with the portion of the droplet that is blocking the channel $b^*_{fill} = 0.64$, $dV_{neck}/dt \sim 0.55Q_c$ for Case A and $b^*_{fill} = 0.82$, $dV_{neck}/dt \sim 0.80Q_c$ for Case B. The remainder of the continuous phase keeps bypassing the droplet and increases the forward oil volume.

During necking the back half of the droplet takes on different shapes as the radius increases and it is pushed towards the inner corner of the T-junction. This continues until the neck thickness reaches a critical size $2r^*_{pinch}$ where the droplet snaps off suddenly. For Case A this occurs at $2r^*_{pinch} = 0.16$ and case B $2r^*_{pinch} = 0.28$. Both these values are less than the estimate put forth by van Steijn *et al.* in Eqn. 4.2, $2r^*_{pinch} = 0.23$ Case A and $2r^*_{pinch} = 0.31$ Case B(van Steijn, Kleijn et al. 2009) . The smaller $2r^*_{pinch}$ and lower dV_{neck}/dt results in a comparatively longer necking stage for Case A compared to B. However, this is not always the case. If the heights are kept constant, so that $2r^*_{pinch}$ is similar, then design with smaller inlet widths (w_d) will have shorter necking times, as is the situation for Cases B compared to Case C.

During the necking stage the droplet continues to grow at a linear rate, growth is directed more so towards the downstream direction as the length of the droplet increases. Nevertheless the interface still continues to penetrate into the main stream as b^* increases due to a rebalancing of forces on the droplet, though the rate of increase is less than in the filling stage. For Case B the interface actually reaches the far channel wall and b^* plateaus. The value that the interface reaches at the moment of pinch-off is designated by b^*_{pinch}. The duration of the necking stage scales as $\Delta t_{neck} \sim \Delta V_{neck}/Q_c$, and the droplet volume increases as $V_{drop} \sim \Delta t_{neck} Q_d \sim \Delta V_{neck} Q_d / Q_c$, demonstrating the dependence of droplet size on the flow ratio.

In summary, the analysis of the formation process has identified several key parameters that describe droplet generation at the T-junction. These include:

L^*_{lag} - distance that the interface covers during the lag stage.

b^*_{fill} - penetration depth of the interface at the end of the filling stage.

$2r^*_{pinch}, b^*_{pinch}$ - critical thickness of the neck and penetration depth at pinch-off.

The variation of these parameters with geometry, fluid properties and flow conditions is discussed in the following sections.

4.4.2 Parameters Influencing L^*_{lag}

Observations of the droplet formation process showed that the interface tends to pull-back slightly into the side channel once a droplet detaches. The distance that the interface recedes back into the side channel is called the lag distance L^*_{lag}. This effect has not been previously reported most likely because the contribution to the final droplet volume is minimal (~0-5%). However, as the video analysis demonstrated, the lag period contributes significantly to the droplet spacing so it must be included to completely describe the operation of the generator.

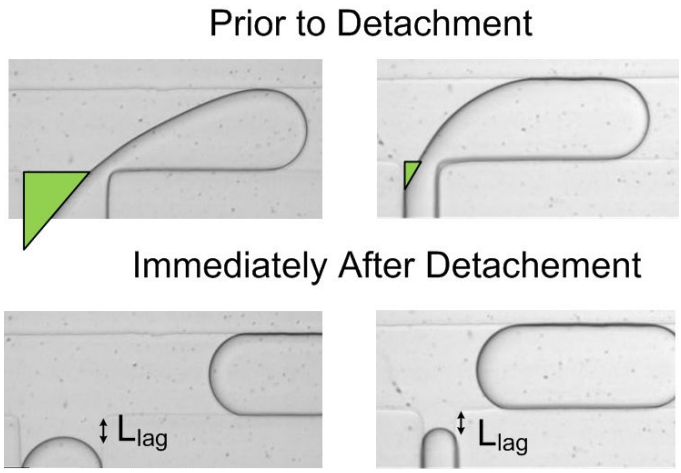

Figure 4.10 The continuous phase (green highlighted area) enters further into the side channel of designs with larger channel widths. After detachment this volume of oil is redistributed and contributes to L^*_{lag}.

Depending on the flow conditions the degree of pullback ranged from nearly 0 to almost 25% of the main channel width. The most obvious trends were that L^*_{lag} decreased with decreasing aspect ratio $h^*\downarrow$ and decreasing dispersed channel width $\Lambda^*\downarrow$. This is mostly attributed to the larger deformations of the back half of the droplet in designs with shallower channels and larger inlet

widths (see Figure 4.10). Therefore, the geometry of the T-junction plays an important role L^*_{lag} purely due to the shape of the neck at detachment.

Another noticeable trend was that for the same generator design L^*_{lag} decreases with increasing dispersed phase flow $Q_d\uparrow$ and increasing dispersed phase viscosity $\mu_d\uparrow$. It is hypothesized that this caused by the competition between the pull-back velocity of the interface right after rupture and the incoming dispersed phase flow.

Pinch-off in the T-junction generator has many similar characteristics to the viscous-capillary pinch-off of two-fluid liquid bridges. The condition consists of the surface tension driven collapse of a thin inner fluid thread of viscosity μ_d surrounded by an external fluid of viscosity μ_c (Lister and Stone 1998; Sierou and Lister 2003).Near the final moments of detachment the inner fluid drains from the thread while the outer fluid creates a viscous drag which slows flow within the thread. Estimates for the two viscous contributions suggest that the velocity within the thread scale as:

$$u_{thread} \sim \frac{\gamma\eta^{1/2}}{\mu_d} \tag{4.14}$$

In estimating the flow dependence of L^*_{lag} we are interested in the pull-back velocity of the tip right after rupture and not the draining flow within the thread. Post-pinching flows are complex and not fully understood, but one can assume that the initial velocity of the receding interface will scale in a similar manner to Eqn. 4.14 (Papageorgiou 1995). If we consider that the receding flow is opposed by the injection of the dispersed phase, it seems reasonable that L^*_{lag} will depend on the relative strength of these two flows:

$$L^*_{lag} \sim \frac{u_{threa}}{u_d} = \frac{\gamma\eta^{1/2}}{\mu_d}\frac{w_d h}{Q_d} = \frac{\eta^{1/2}}{Ca_d} \tag{4.15}$$

where Ca_d is the dispersed phase Capillary number. Figure 4.11 plots the scaling relationship for a few T-junction geometries over a range of flow conditions. For each design the data seems to agree well with the proposed scaling analysis. However, more research is needed to understand the exact influence geometry and flow conditions on L^*_{lag} in order to add its influence to a predictive model. This of course will require a more detailed study of the flow conditions during the final moments of collapse.

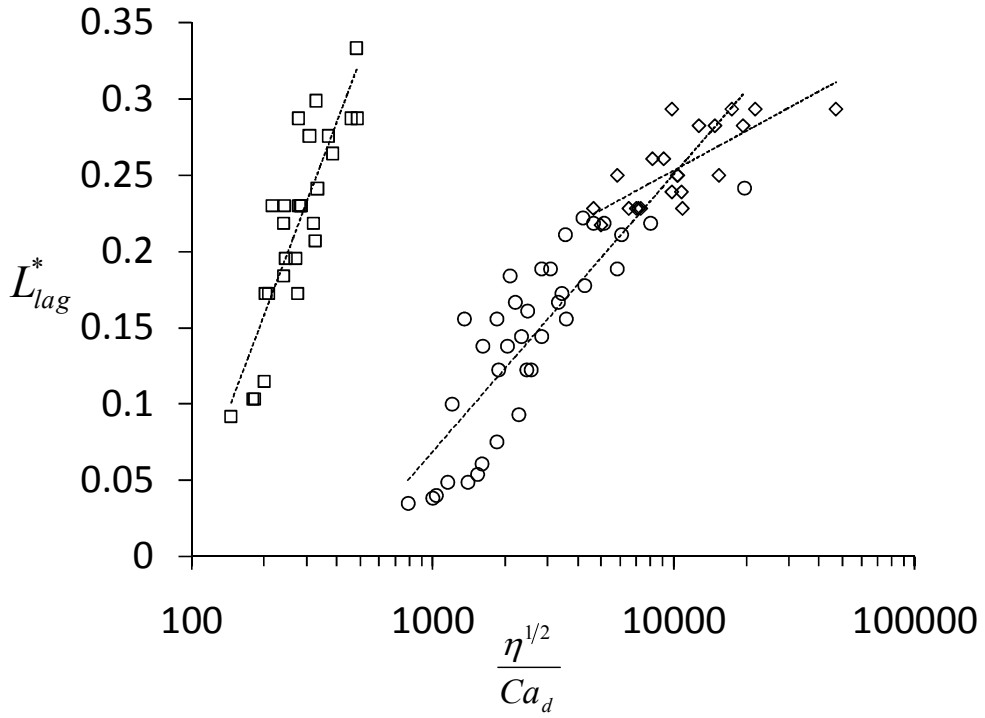

Figure 4.11 Plot of the scaling relationship for L^*_{lag} for three different T-junction geometries including range of viscosity contrasts η=0.12→1.7. Geometries (h^*, Λ^*): □ (*0.5, 35*), ○(*0.4, 1*), ◊ (*0.3, 1*).

4.4.3 Parameters Influencing b^*_{fill}

Previously works have established that b^*_{fill} may be determined by a force balance consisting of competing drag and surface tension forces acting on the interface characterized primarily by the Capillary number (viscous/surface tension). In their forces balance, Christopher *et al.* demonstrated that b^*_{fill} is expected to scale with *1/Ca* as:

$$\frac{b^*}{\left(1-b^*\right)^3} = \frac{1}{Ca} \tag{4.16}$$

However, when this function was compared to experimental data the fit was unsatisfactory as shown in Figure 4.12. First, the expression was unable to capture the influence of the aspect ratio (h/w_c) on b_{fill} as shown in Figure 4.12a where the same fluid combination was used in three different T-junction designs. Second, the expression does not include the relationship between b_{fill} and the viscosity of the dispersed phase as shown in Figure 4.12b. Increasing $\eta=\mu_d/\mu_c$ results in a shift downwards in b_{fill} under the same flow conditions. In fact, it has been previously noted that drop size generally decreases with increasing viscosity due to larger drag forces created on the

interface (Christopher, Noharuddin et al. 2008; Steegmans, Schroen et al. 2009).Therefore, a new model of the formation process requires a more accurate representation of the force balance on the emerging interface that includes these geometric and flow effects.

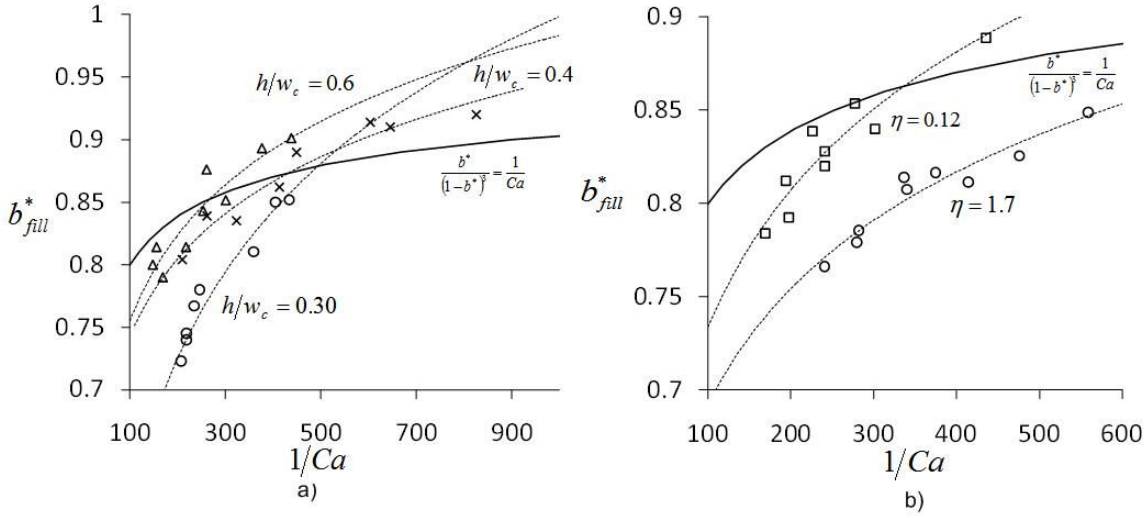

Figure 4.12 Comparison between experimental measured b^*_{fill} versus the expression by Chrisopher *et al.* (Christopher, Noharuddin et al. 2008) (a) Fluid combination of silicon oil and 10%wt glycerol/water (η=0.12) in different T-junction geometries demonstrating the dependence on h/w_c. (b) Effect of increasing the viscosity of the dispersed phase (10%wt to 70%wt glycerol) for the same T-junction geometry $h/w_c=0.4$. Dashed lines are logarithmic curve fits used to guide the eye, the solid black line correspond to the expression in Chistopher *et al.* (Christopher, Noharuddin et al. 2008).

4.4.4 Parameters Influencing b^*_{pinch}

During the necking process the interface continues to penetrate into the cross flowing stream causing b^* to grow. The growth of b^* is a result of the continuous rebalancing of forces as the curvature of the back half of the droplet changes (and the associated Laplace pressure) combined with the increasing volume of the droplet. In addition, the time that b^* has to grow will also depend on the duration of the necking stage which scales with the flow ratio $V_{drop} \sim Q_d/Q_c$, and therefore, one expects to see such a dependency on b^*_{pinch}. Figure 4.13 plots the relationship between b^*_{pinch} and φ for two different geometries, one with a short necking time ($\Lambda^*=0.3$) and the other with a long necking time ($\Lambda^*=1$). For the latter case, larger b^*_{pinch} values occur for the same flow ratio as the necking is longer.

Therefore, a reciprocal relationship exists between the necking time, force balance and b^*_{pinch} which is difficult to predict without some sort of iteration. However, plotting b^*_{pinch} versus

the initial size of the droplet at the beginning of necking b^*_{pinch} shows that a linear relation between the two variables exists. For the two geometries (Λ^*=*0.3, 1)* b^*_{pinch} increases by approximately 15-25% over b^*_{fill} . This simple correlation is used later in the model to avoid the unwanted complexity associated with iteration.

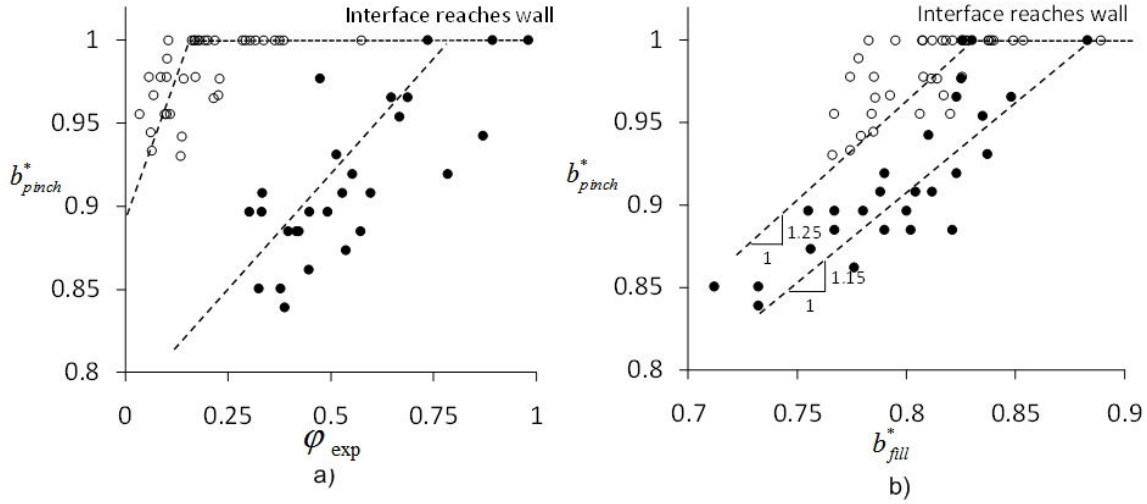

Figure 4.13 Comparison between experimental measured b^*_{pinch} against (a) the flow ratio and (b) the initial penetration depth at the beginning of necking. b^*_{fill}. Geometries (h^*, Λ^*)*:* ● (*0.30, 0.35*), ○ (*0.4, 1*). Dashed lines are used to guide the eye to the linear relation.

4.4.5 Parameters Influencing $2r^*_{pinch}$

Experiments performed by van Steijn *et al.* demonstrated that the neck begins to pinch-off once the difference in Laplace pressure from the tip to the neck of the droplet causes the bypassing continuous phase to reverse direction. The additional influx of oil through the gutters speeds up the rate of collapse and pinch-off occurs almost immediately afterwards. The authors estimated the moment of collapse by considering the pressure difference between the upstream and downstream ends of the drop. Their analysis is repeated here for reference

Using the pressure in the droplet as a reference, the pressure in the oil just outside the drop can be estimated by the Laplace pressure, $P_{Lp} = \gamma\kappa$, where κ is the curvature of the interface. The pressure at the tip of the droplet is given by $P_{tip} = \gamma\left(2/h + 2/w_c\right)$ and at the neck by $P_{neck} = \gamma\left(1/R_n + \min\left(1/r_n, 2/h\right)\right)$, so that the pressure across the drop is:

$$P_{neck} - P_{tip} = \gamma\left(\frac{2}{w_c} + \frac{2}{h}\right) - \gamma\left(\frac{1}{R_n} + \min\left(\frac{1}{r_n}, \frac{2}{h}\right)\right) \tag{4.17}$$

Flow reverses direction when the pressure difference equals zero. This coincides with the neck reaching a critical curvature:

$$2r^*_{pinch} = \frac{h^*}{1 + h^*} \tag{4.18}$$

Note that the smallest term $1/R_n$ is ignored in deriving the previous equation. The expression shows that pinch-off is determined only by the geometry of the generator. The authors validated this result by performing experiments in T-junction generator with ethanol and air as the working fluids and without the use of surfactants. However, when Eqn. 4.18 was applied in this current study, it consistently over predicted the critical thickness that was observed as shown in Figure 4.14. Data is plotted for T-junctions with two different aspect ratios (h/w_c=0.32, 0.47) and two different viscosities contrasts (η=*0.125, 1.7*) against b^*_{fill}, which was chosen because it includes the combine influence of flow conditions (Ca, η) and the shape of the droplet near pinch-off. Such a plot shows that there is indeed a relationship between the flow conditions and $2r^*_{pinch}$ which is not included in the equation by van Steijn *et al.* (van Steijn, Kleijn et al. 2009).

The reason for this discrepancy is that there is a significant difference in the experimental conditions between the current study and those used to validate Eqn. 4.18. In their experiments, van Steijn *et al.*, focused on the squeezing regime where *Ca<0.002*, and the viscosity of the continuous phase is low (1.2 mPas), the viscosity of the dispersed phase is negligible (air) and the surface tension relatively large (~20 mN/m). Comparatively, the viscosity of the continuous phase is 10 times larger (10 mPas), the viscosity of the dispersed phase non-negligible (1-17 mPas) and the surface tension is comparable (~28 mN/m). Since Laplace pressure driven flow around the droplet scales as $Q_{Lp} \sim \gamma / R_{hyd}$ -where R_{hyd} is the hydrodynamic resistance of the gap- the higher viscosity fluids will decrease the significance of Laplace flow and in turn decrease the rate of collapse.

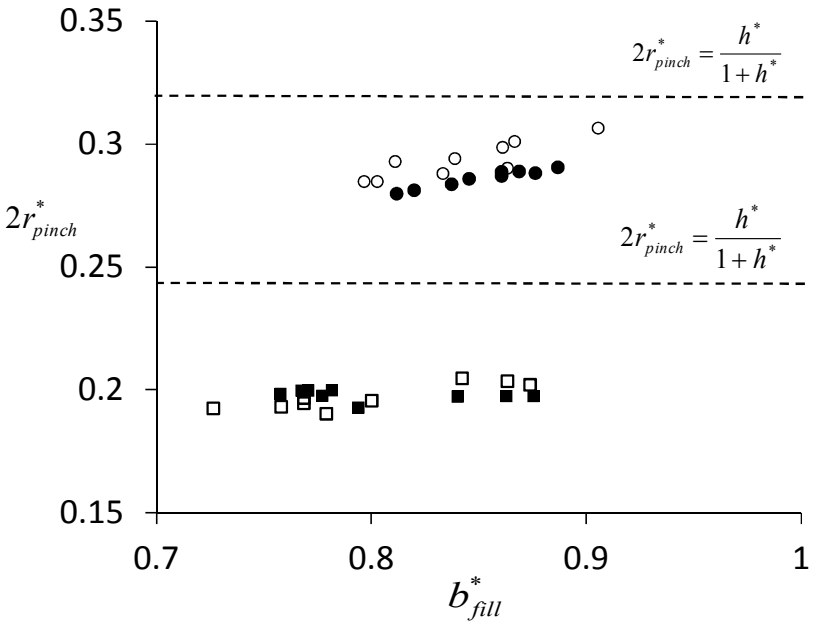

Figure 4.14 Comparison between experimental measured $2r^*_{pinch}$ against penetration depth at the beginning of necking. b^*_{fill}. Geometries (h^*, Λ^*): (*0.4, 1)* and □ (*0.30, 0.35)* open symbols correspond to η*=0.12* and close η*=1.7*. Dashed lines are the theoretical limit predicted by Eqn 4.18.

However, the experimental data shows that $2r^*_{pinch}$ does not vary significantly with the dispersed phase viscosity, which confirms the idea that pinch-off is primarily dictated by the flow of the continuous phase around the drop, and not the internal flow of the dispersed phase. The viscosity of the dispersed phase is expected to come into play during the final pinch-off moments where the rate of thinning of the neck resembles the conditions present in the two-fluid liquid bridge. However, for the purpose of predicting the operation of the T-junction generator (droplet size, spacing, and frequency) the final moments leading to rupture of the neck are not important because of the comparatively short time scale compared to the rest of the formation process. The most important matter is to precisely calculate the moment when the pinch-off process begins which requires a new model for $2r^*_{pinch}$.

4.4.6 Scaling of Operational Parameters

The scaling of operational parameters, (droplet volume, oil volume, spacing and frequency) for the four initial case studies is presented in Figure 4.15. Each generator follows the general scaling law, $V_d^* = \alpha + \beta\varphi$, but with different fitting parameters defining the slope and intercept depending primarily on the T-junction design. Dashed lines in the figure are curve fits to the data.

Scatter around these base lines is caused by experimental variance as well as *Ca* dependence which not included in the plots. According to analysis of the formation process, the continuous phase volume and droplet spacing are expected to vary proportionality with the Q_c and inversely with Q_d. The plots show that both oil volume and droplet spacing scale linearly with the inverse of the flow ratio φ as expected. Frequency is plotted as a dimensionless number scaled by the characteristic residence time of fluid in the channel $t^{-1} = Q_c / w_c^2 h$. Since the formation process is governed by both the flow of the two phases, it is reasonable to expect that frequency will also scale with the flow ratio. As shown in Figure 4c, frequency does in fact scale with φ, but in a non-linear manner.

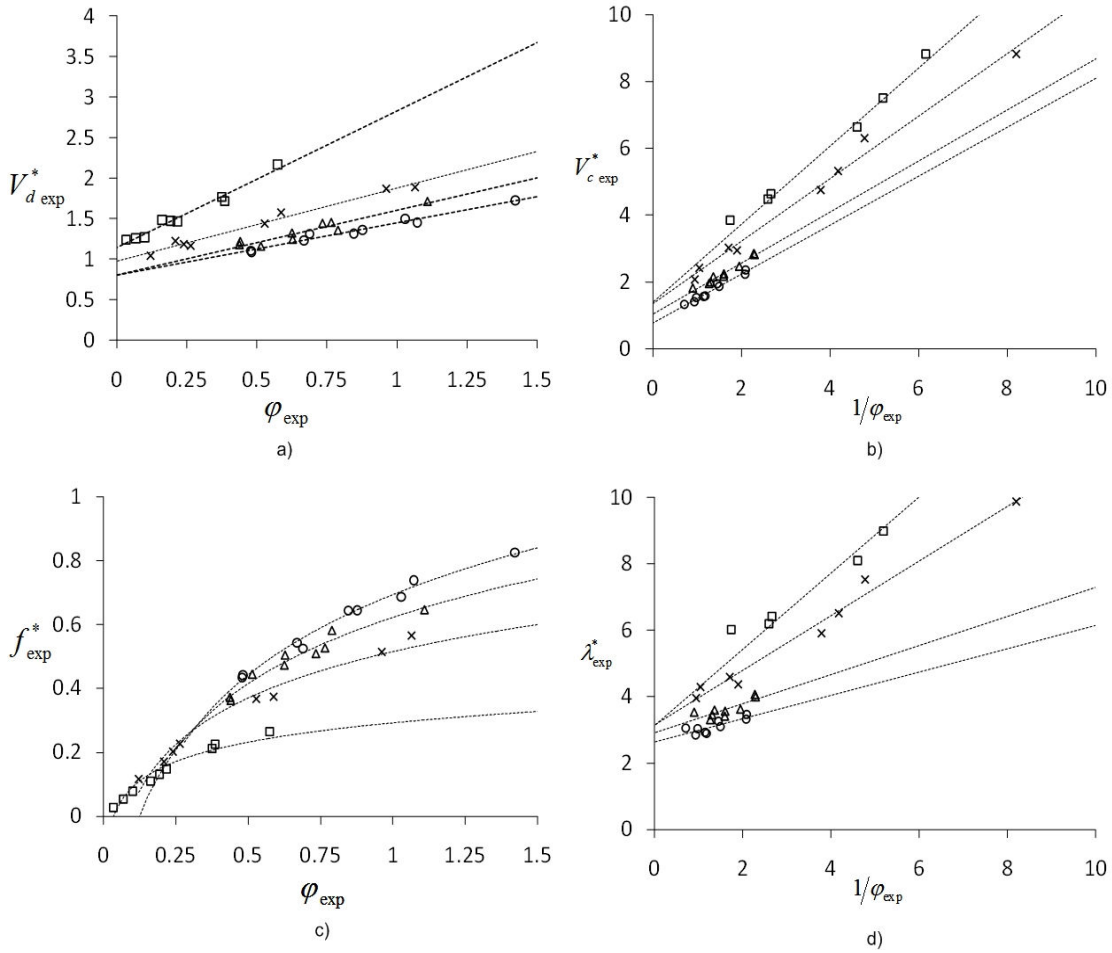

Figure 4.15 Plot of the dimensionless droplet volume (a) oil volume (b) frequency of formation (c) and spacing (d) as a function of the flow ratio. Geometries (h^*, Λ^*): □ (*0.4, 1*), ○(*0.30, 0.35*), Δ (*0.6, 0.5*), x (*0.5, 0.5*); silicone oil and 10%wt glycerol/water as the working fluids.

4.5 Model of the T-junction Droplet

Analysis of high speed videos showed that the droplet formation process can be divided into three sequential stages: (i) a lag stage immediately after detachment of the previous droplet, (ii) a filling stage where the droplet penetrates into the cross-flowing stream and (iii) a necking stage where the droplet begins to detach. The final volume of the droplet is the sum of these three stages and the scaling law that describes this process has the form:

$$\frac{V_{drop}}{w^2 h} = \alpha_{lag} + \alpha_{fill} + \beta\varphi \tag{4.19}$$

In the following discussion a series of expressions are developed to mathematically describe these factors, α_{lag} , α_{fill} and β based on physical principals. The model formulation begins with a general geometric description of the 3D shape of the droplet throughout the formation process. This geometric description is used calculate the evolution of the volume of the droplet during the three stages of the formation process. First, the contribution of the lag stag, α_{lag} , is calculated by the volume added by L^*_{lag} . Second, the volume added at the end stage, α_{fill} , is calculated which includes a new force balance that predicts b^*_{fill} and includes viscosity and geometric influences. Third, necking parameter is calculated using a control volume analysis, which also includes a new method of calculating $2r^*_{pinch}$. Finally, scaling expressions are developed for continuous phase volume, inter-droplet spacing and frequency of formation, thus describing the complete operation of the T-junction generator.

4.5.1 Model Limits and Constraints

The model developed herein applies to droplet formation in the squeezing to transition regime where the breakup process is governed by the squeezing pressure generated as the interface extends into the cross-flowing stream (Garstecki, Fuerstman et al. 2006; Christopher, Noharuddin et al. 2008; De Menech, Garstecki et al. 2008; van Steijn 2010). Fluid flow is laminar and creeping with $Re < 1$ so that inertia forces are negligible and buoyancy forces may also be ignored.

Droplets grow large enough to fill the entire cross section of the channel and form plugs that are longer than the channel width. Droplets are non-wetting and their shape is assumed to be in a state of quasi-equilibrium that attempts to minimize the surface energy throughout the formation

process. Marangoni stresses and dynamic interfacial effects are neglected in the following analysis, so that it is assumed that the interfacial tension remains constant during the formation process and is equal to the equilibrium value. This is valid when surfactants are absent from the system-as is the case for the experiments performed in this study- or when adsorption kinetics are fast compared to the formation process.

The confined geometry stabilizes the neck filament against perturbations, such that the mechanism for pinch-off is not the growth of capillary instabilities as is the case for unconfined geometries(Humphry, Ajdari et al. 2009), but is the reversal of flow around the drop due to Laplace pressure changes as the droplet shape evolves(van der Graaf, Steegmans et al. 2005; van Steijn, Kleijn et al. 2009). Only the condition where the two flow rates are relatively steady during the entire formation process is considered, thus the following model is applicable to both syringe pump and pressure driven flow as long as this condition is met.

4.5.2 Geometric Description of the Droplet

To accurately describe the formation process a geometric description of the droplet shape is necessary. The general shape of the droplet is shown in Figure 4.16 and follows the description provided by van Steijn *et al* but modified into a more general form applicable to the transition regime(van Steijn 2010). The main difference is that van Steijn *et al* studied the squeezing regime where the droplet interface comes in contact with the far wall, while here the transition regime is studied where the droplet only penetrates a certain distance into the main channel.

From the 2-D planar view of the droplet the 3-D shape is reconstructed by assuming that the interface is confined by the upper and bottom walls, and that it takes on a minimum in surface energy, so that the out of plane curvature is half the channel height. The extent that the droplet penetrates into the continuous stream is defined by the characteristic dimension *b*. The difference between the far channel wall and the droplet is the gap width, $w_{gap} = \left(w_c - b\right)$, where the continuous phase bypasses the droplet as it is being formed. A half circle of diameter *b* defines the 2-D shape of the front half of the droplet, while the back and neck is defined by a circle of radius R_n. During the formation process the neck radius changes size as the back of the droplet is pushed towards the corner of the T-junction. The shortest distance from the corner of the T-junction to the back of the droplet is the neck thickness given as $2r_n$.

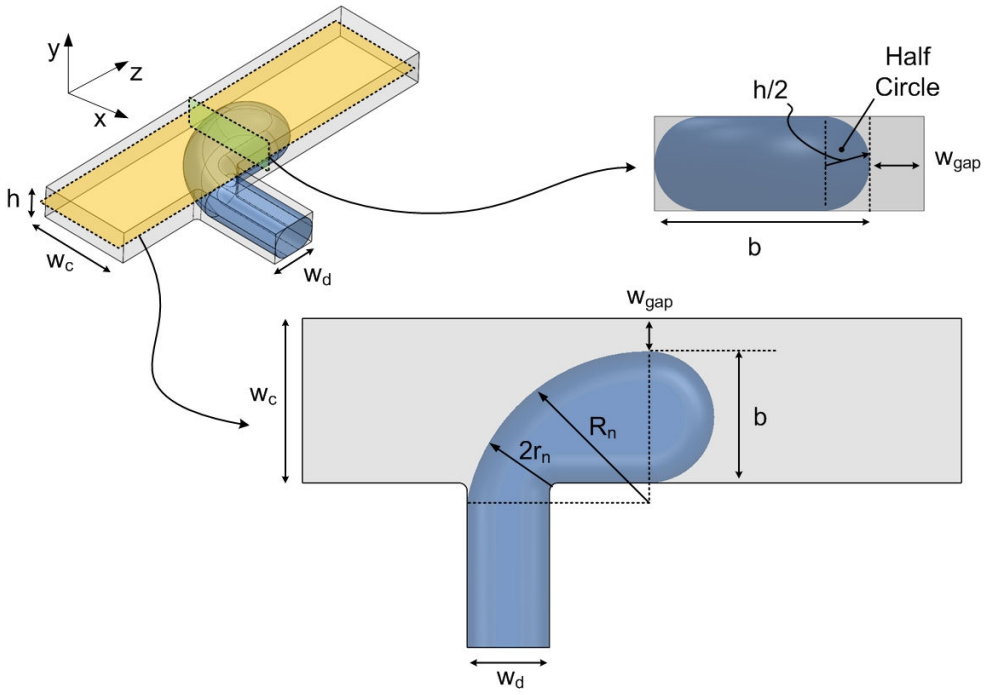

Figure 4.16 Geometric reconstruction of the droplet shape as it is being formed in the transition regime. The 2-D view of the droplet shape is used to develop a full 3-D shape of the droplet by assuming that the out of plane curvature is represented by a half circle with a radius of *h/2*. The droplet penetrates a distance of *b* into the main channel. The front of the droplet is described by a half circle of diameter *b*, the back by a quarter circle of radius R_n and the neck thickness by $2r_n$.

The total volume of the droplet can be estimated from the 2-D shape by projecting the area, A_p, through the channel depth, and then including the contribution from the out of plane curvature along the perimeter, l:

$$V = hA_p \pm 2\left(\frac{h}{2}\right)^2\left(1-\frac{\pi}{4}\right)l \tag{4.20}$$

Dividing by $w_c^2 h$, the dimensionless volume is expressed as:

$$V^* = A_p^* \pm \left(\frac{h^*}{2}\right)\left(1-\frac{\pi}{4}\right)l^* \tag{4.21}$$

A negative sign is used in the second term for the dispersed phase while a positive sign is used for the continuous phase. This geometric description is the basis for deriving expressions for the volume of the droplet and the control volume of the oil surrounding the droplet during the formation process.

4.5.3 First Stage: Lag Stage

Immediately after a drop detaches the interface recedes back into the side channel to a distance L_{lag}. Once the interface recovers it proceeds forward until it reaches the entrance of the channel (see Figure 4.17). The volume of this recovery represents the portion of the total volume that is contributed by the lag stage. Based on the geometric representation presented in Figure 4.17, and the application of Eqn. 4.13, the dimensionless lag volume is given by:

$$V_{lag}^{*} = \alpha_{1ag} = L_{lag}^{*}\Lambda^{*} + \frac{1}{2}\left(1-\frac{\pi}{4}\right)\left(\Lambda^{*2} + \frac{\pi\Lambda^{*}h^{*}}{2}\right) \tag{4.22}$$

Experimental observations showed that L_{lag} is a complicated relationship between the flow conditions (capillary pressure to applied pressure drop) and geometry. An adequate description is not available at the moment for L_{lag}., thus in the model L_{lag} is taken directly from experimental measurements and substituted into Eqn. 4.22.

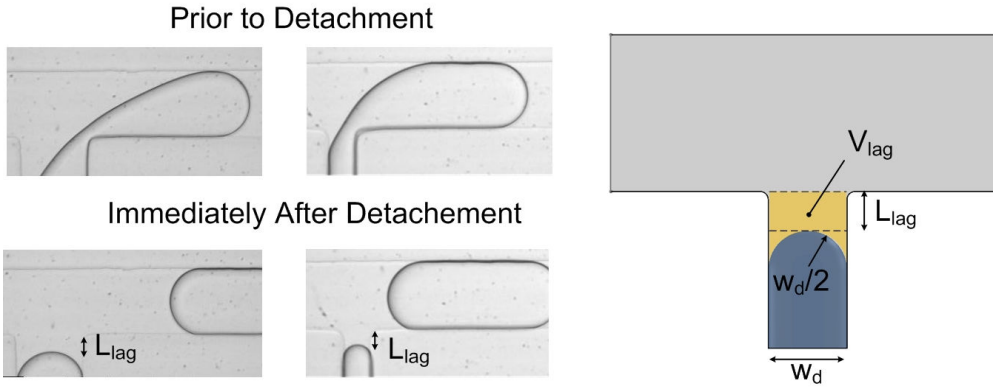

Figure 4.17 Interface shape immediately after detachment where it recedes back into the dispersed phase inlet. The position of the interface relative to the main channel is defined by the lag length L_{lag} and the volume is defined by $V_{lag.}$

4.5.4 Second Stage: Filling Stage

In concurrence with observations made by Christopher *et al.* and van Steijn *et al.*, our own interpretation of the experimental evidence advocates that the droplet takes on a similar shape at the end of the filling stage as shown in Figure 4.18 (Christopher, Noharuddin et al. 2008; van Steijn 2010). The front half of the droplet is defined by a half circle of diameter b_{fill} and the back by a circle of R_{fill}. Two cases exist depending on the geometry of the T-junction, where the neck radius is confined by the virtual channel wall created by the interface at b_{fill} or by the inlet channel $R_{fill} = \max\left(w_d, b_{fill}\right)$.

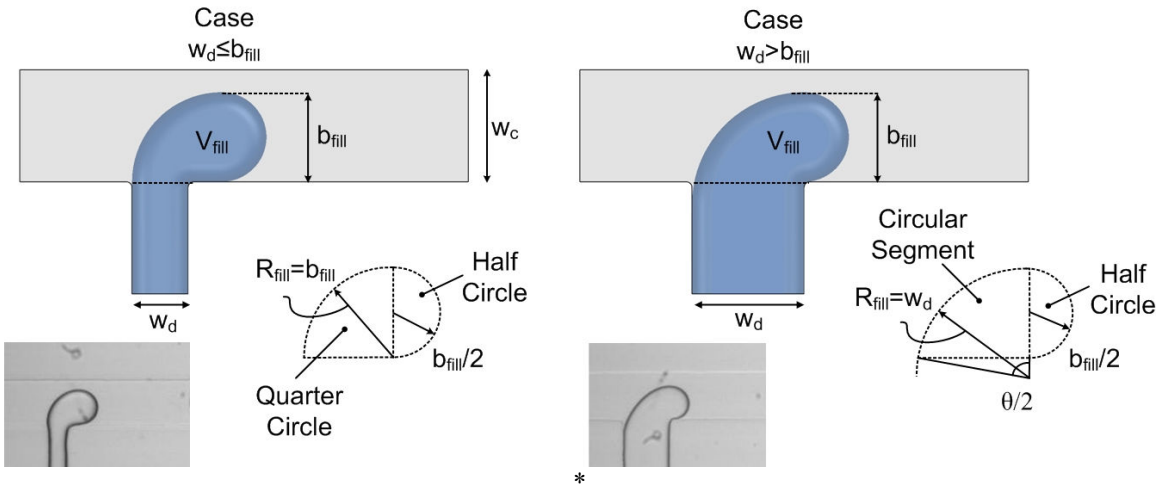

Figure 4.18 Droplet shape at the end of the filling stage for two cases where $w_d \leq b_{fill}$ and $w_d > b_{fill}$. The drops are characterized by extent of protrusion, b, and the neck radius at the filling stage R_{fill}. For the circular segment, the height is given by b and the radius of the circle is w_d.

Applying Eqn. 4.13, to the two shapes the final fill volume, α_{fill} , can be calculated. For the case of $w_d \leq b$ the result is:

$$V_{fill}^* = \alpha_{fill} = \frac{3}{8}\pi b_{fill}^{*\,2} - \frac{h^*}{2}\left(1-\frac{\pi}{4}\right)\left(\pi b_{fill}^* + \left(b_{fill}^* - \Lambda^*\right)\right) \tag{4.23}$$

This is a slightly modified version of the result from van Steijn *et al.*, as the perimeter along the near wall, $\left(b_{fill}^* - \Lambda^*\right)$, is included which was omitted in their work. Note that the perimeter does not include the boundary of the droplet at the intersection of the T-junction (*ie.* the dotted line dividing the droplet in Figure 4.18). For the case of $w_d > b_{fill}$, the calculation is slightly more difficult as the back part of the droplet is defined by half a circular segment. Note that a full circular segment is the area of a circle cut off by a cord (Weisstein 2010). The volume is given as:

$$\begin{aligned} V_{fill}^* &= \alpha_{fill} = \frac{\pi}{8} b_{fill}^{*\,2} + \frac{1}{4}\Lambda^{*2}\left(\theta - \sin\theta\right) - \frac{h^*}{4}\left(1-\frac{\pi}{4}\right)\left(\pi b_{fill}^* + \Lambda^*\theta\right) \\ \theta &= 2\arccos\left(1 - \frac{b_{fill}^*}{\Lambda^*}\right) \end{aligned} \tag{4.24}$$

The remaining unknown in the preceding equations is b_{fill}^* which must be determined by a force balance on the droplet which is presented later. In the following section, the second stage of the droplet formation involving the squeezing of the neck is discussed.

4.5.5 Third Stage: Necking

During the necking stage additional fluid is being pumped into the droplet as the neck collapses. The increase in size of the droplet during this stage is related to the time that the neck remains open and the flow rate of the dispersed phase. The relationship between β and the necking time can be derived as (van Steijn 2010):

$$\beta h w^2 \frac{Q_d}{Q_c} = \Delta t_{neck} Q_d \tag{4.25}$$

where β essentially represents the dimensionless necking time ($\beta = \Delta t^* = \Delta t Q_c / w_c^2 h$). To determine Δt^*_{neck} , van Steijn *et al.* applied conservation of mass to the continuous phase in order to describe the changing shape of the neck in terms of the radius R_n. As the neck collapses the radius becomes larger and the neck interface approaches the inside corner of the T-junction, where once it reaches a critical distance $2r_{pinch}$ it collapses quickly as shown in Figure 24. Therefore, the final shape of the neck at the point of collapse needs to be known in order to calculate β.

To accomplish this conservation of mass is applied to the continuous phase during the squeezing process. Consider the deformable control volume consisting of the continuous phase that surrounds the neck as indicated in Figure 4.19. The change in shape of the control volume during the squeezing process is related to the relative inflow and outflow of the continuous phase across any boundary, which in this case reduces to:

$$\frac{dV_{CV}}{dt} = Q_c \left(1 - \frac{A^*_{bp}}{h^*} \right) \tag{4.26}$$

Here the assumption is made that $\left(1 - A^*_{bp} / h^*\right)$ represents the fraction of the continuous phase flow rate that actually squeezes the droplet neck and does not bypass the droplet through the gap. The dimensionless bypass area is :

$$A^*_{bp} = A^*_{gap} = \left(1 - \bar{b}^*\right) h^* + \left(1 - \frac{\pi}{4}\right) \frac{h^{*2}}{2} \tag{4.27}$$

Where is the average penetration depth during the necking stage: $\bar{b} = \left(b^*_{fill} + b^*_{pinch}\right)$.

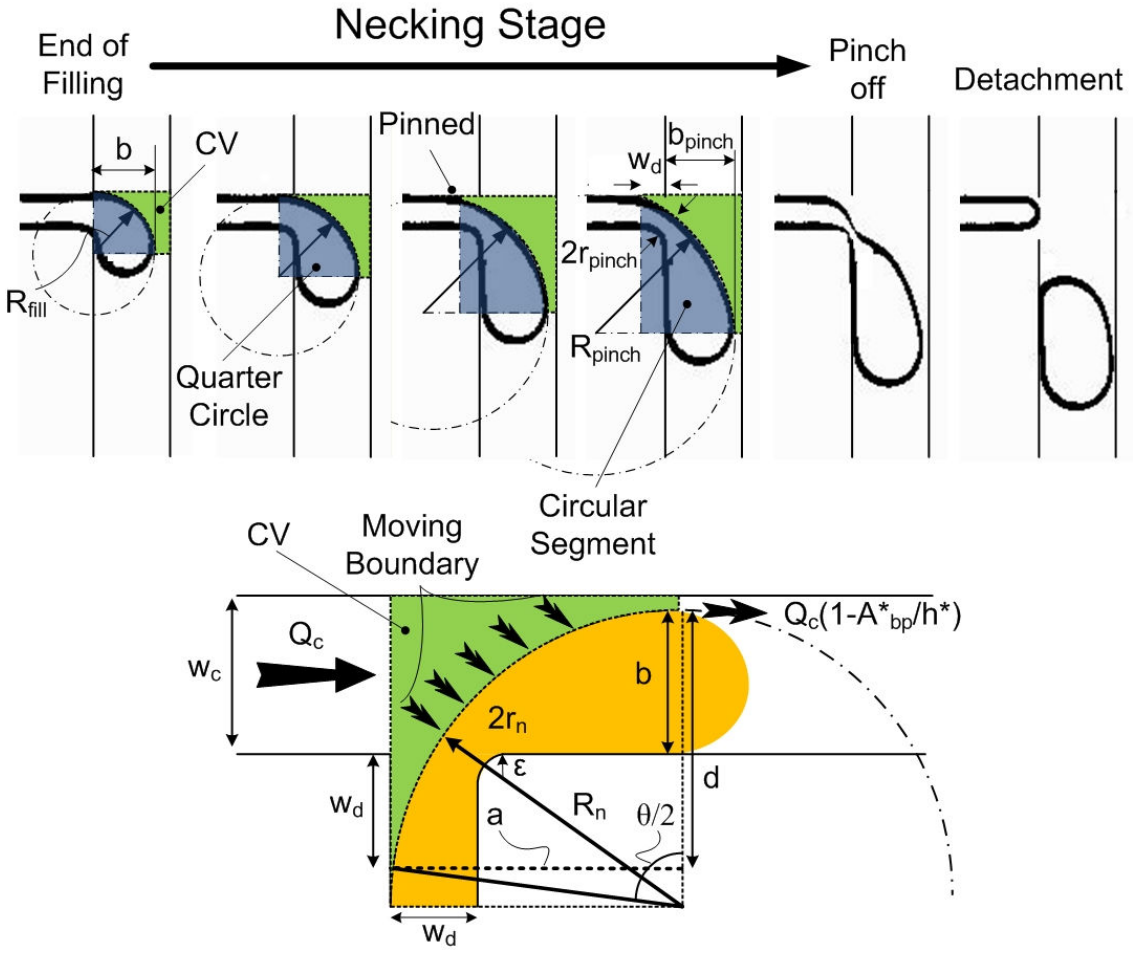

Figure 4.19 (TOP) A sequence of traces showing the boundary of the droplet as it evolves during the necking stage. At first the neck shape follows a quarter circle until it becomes anchored within the dispersed phase channel at a distance w_d. Once it is anchored the shape follows a circular segment until the neck reaches a critical thickness where pinch off occurs. The deformable control volume (CV), and its evolution during the squeezing process is highlighted in green. (BOTTOM) A diagram showing the neck with the relevant variables indicated to describe its shape as a circular segment. A close up of the control volume shows the flow of oil, the boundary which moves with the interface of the neck and the passing of oil around the droplet.

Non-dimensionalizing Eqn. 4.26 and integrating with respect to time from the initial fill volume, $V^*_{c_{fill}}$ to the final pinch volume, $V^*_{c_{pinch}}$, the factor β can be recovered:

$$\beta = \frac{1}{\left(1 - A^*_{bp}/h^*\right)}\left(V^*_{c_{pinch}} - V^*_{c_{fill}}\right) \tag{4.28}$$

After the initial filing period the volume of fluid in the CV is:

$$V^*_{c_{fill}} = \left(1 - b^*_{fill}\right)R^*_{fill} + \left(1 - \frac{\pi}{4}\right)R^{*\,2}_{fill} + \frac{\pi h^*}{4}\left(1 - \frac{\pi}{4}\right)R^*_{fill} \tag{4.29}$$

Determining the final volume at the pinch off point is more difficult. To describe the evolution of neck shape, van Steijn *et al.* used a quarter circle to approximate the neck shape throughout the necking stage. This leads to a final pinch volume of:

$$V^*_{c_{pinch}} = \left(1 - b^*_{pinch}\right)R^*_{pinch} + \left(1 - \frac{\pi}{4}\right)R^{*\,2}_{pinch} + \frac{\pi h^*}{4}\left(1 - \frac{\pi}{4}\right)R^*_{pinch} \tag{4.30}$$

where R^*_{pinch} is related to $2r^*_{pinch}$ through geometric arguments:

$$2r^*_{pinch} - \varepsilon = R^*_{pinch} - \sqrt{\left(R^*_{pinch} - b^*_{pinch}\right)^2 + \left(R^*_{pinch} - \Lambda\right)^2} \tag{4.31}$$

ε is the roundness of the T-junction corner and must be included or it can lead to large errors, R^*_{pinch} can then be calculated by rearranging Eqn. 4.31.

However, in certain circumstances the calculation of the final pinch volume by Eqn. 4.30 was found to be in error when applied to the droplet formation process in the transition regime. The cause was the assumption that the interface adopts a quarter circle shape throughout the entire necking stage as this tends to under predict how long the neck is actually open. Using the quarter-circle approximation causes the continuous phase to penetrate too far into the inlet channel when $2r^*_{pinch}$ is small (refer to Figure 4.19). Based on experimental observations the continuous phase never enters past a distance of w_d into the dispersed phase channel, but remains anchored at this distance although the radius of the neck continues to grow. Consequently, a better approximation to the shape of the interface is half a circular segment as identified in Figure 4.19.

Using the definition of variables in Figure 4.19, the geometric description of the neck shape at pinch off becomes:

$$\begin{aligned}
d^* &= b^*_{pinch} + \Lambda^* \\
a^* &= \sqrt{d^*\left(2R^*_{pinch} - d^*\right)} \\
\theta &= 2\arccos\left(1 - \frac{b^*_{pinch} + \Lambda^*}{R^*_{pinch}}\right) \\
2r^*_{pinch} - \varepsilon &= R^*_{pinch} - \sqrt{\left(R^*_{pinch} - b^*_{pinch}\right)^2 + \left(a^* - \Lambda^*\right)^2}
\end{aligned} \tag{4.32}$$

where R^*_{pinch} is calculated for a specific $2r^*_{pinch}$ by iterating the set of equations above. The final pinch volume is then given as:

$$V^*_{c_{pinch}} = \left(1 - b^*_{pinch}\right)a^* + \left(1 + \Lambda^*\right)a^* - \frac{R^{*\,2}_{pinch}}{4}\left(\theta - \sin\theta\right) + \frac{h^*}{2}\left(1 - \frac{\pi}{4}\right)R^*_{pinch}\frac{\theta}{2} \tag{4.33}$$

Experimental observations showed that for the geometries considered in this study b^*_{pinch} increases by approximately 20% after the filling stage to the end of necking, capped by the far wall ($b^*_{pinch} <= 1$). Therefore, in the following calculations involving the second stage of formation the following expression is used $b^*_{pinch} = \min\left(1.2b^*_{fill}, 1\right)$. Once $V^*_{c_{pinch}}$ is known it is substituted into Eqn. 4.28 to determine the necking factor β. So far definitions for the two factors α and β have been defined; however there are still two unknown quantities, b^*_{fill} and $2r_{pinch}$ that need to be defined.

4.5.6 Determine b^* by a Force Balance on the Emerging Droplet

In cross-flow generator designs, the initial fill size of the droplet is calculated by a force balance in the streamwise direction on the emerging droplet. Following the estimates put forth by Garstecki *et al.* and Christopher *et al.*, three primary forces have been identified which include the interfacial tension, the tangential shear acting on the surface and the squeezing pressure across the droplet(Garstecki, Fuerstman et al. 2006; van Steijn 2010). Necking begins once the stabilizing capillary force is overwhelmed by the shear and pressure forces (refer to Figure 4.20).

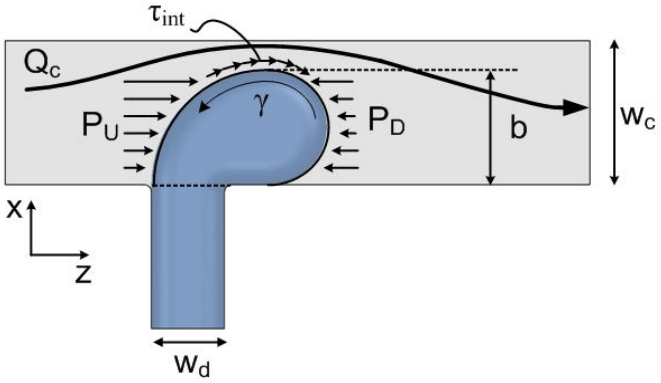

Figure 4.20 (a) Diagram indicating the forces acting on the emerging droplet in the filling stage. As the droplet grows it obstructs the continuous phase resulting in a pressure difference across the droplet as wellas shear stress on the interface. These two forces are countered by the interfacial tension force which resists deformation. At some point the droplet reaches a maximum size characterized by the dimension *b*, where the pressure and shear forces exceed the surface tension force and the neck begins to thin.

The capillary force is associated with the Laplace pressure difference between the upstream and downstream ends of the emerging droplet interface. Based on the droplet shape at the end of the filling phase (refer to Fig 4.18), the upstream interface has a curvature $k=2/b_{fill}+2/h$, while the downstream curvature is $k=1/R_n+2/h$. The sum of these two Laplace pressures, multiplied by the area over which the force is applied, $A\sim b_{fill}h$, gives the resulting capillary force acting on the drop:

$$F_\gamma \approx \left[-\gamma\left(\frac{2}{b_{fill}}+\frac{2}{h}\right)+\gamma\left(\frac{1}{R_n}+\frac{2}{h}\right)\right] b_{fill}h \approx -\gamma h \tag{4.34}$$

Note that the capillary force is negative so it is oriented upstream and thus acts as a stabilizing force preventing droplet detachment. The viscous shear force acting on the droplet may be estimated as the average shear stress on the interface multiplied by the are in the gap, $A\sim b_{fill}h$, and is given as:

$$F_\tau \approx \tau_{\text{int}} b_{fill} h \tag{4.35}$$

The partial blockage of the continuous phase flow by the emerging interface creates a pressure drop across the droplet. The resultant force is the difference between the upstream and downstream pressures multiplied by the exposed area, $A\sim b_{fill}h$:

$$F_P \approx \Delta P_{u-d} b_{fill} h \tag{4.36}$$

The filling stage ends when the three forces sum to zero:

$$F_\tau + F_P + F_\gamma = 0 \tag{4.37}$$

Initial models by Garstecki *et al.* and Christopher *et al.* estimated the pressure drop through a simple scaling analysis based on the Hagen-Poiseuille relation in a thin gap. Here the same approach is taken to quickly estimate the relative magnitude of the shear and pressure forces. Approximating the shear rate on the droplets as the average velocity through the gap $w_{gap}=(w_c-b_{fill})$ divided by the height $\tau_{\text{int}} \approx \mu_c u_{gap} / h$, the resulting shear force becomes:

$$F_\tau \approx \frac{\mu_c b_{fill}}{w_{gap} h} Q_c \tag{4.38}$$

The pressure drop can be approximated using the lubrication analysis for pressure drop between two parallel plates $\Delta P_{u-d} \approx 12 Q_c \mu_c b_{fill} / \left(w_{gap} h\right)^2$ resulting in a pressure force give by:

$$F_P \approx \frac{12\mu_c b_{fill}^2}{w_{gap}^2 h} Q_c \tag{4.39}$$

Taking the ratio of the two forces in order to estimate there importance:

$$\frac{F_\tau}{F_P} \approx \frac{w_{gap}}{12 b_{fill}} = \frac{\left(w_c - b_{fill}\right)}{12 b_{fill}} \tag{4.40}$$

Under typical conditions for droplet generation in the T-junction ($Ca=0.0001 \rightarrow 0.02$, $b^*=0.6 \rightarrow 1$), the shear stress force is only 0 to 5% of the pressure force. Therefore, one can safely neglect the contribution of shear stress from the force balance on the emerging interface so that $F_\gamma = F_P$.

To accurately predict b_{fill} the remaining issue is to develop a model that captures the pressure drop across the droplet correctly. However this is not an easy task as the flow profile through the gap is quite complex since the region is comprised of three walls obeying the no slip conditions and the forth is the interface where shear and velocity between the two phases must be continuous. In addition, the shape of the interface creates a curved boundary in both the out of plane and in plane orientations resulting in a 3D flow profile throughout the gap which does not lend itself to a simple analytical solution. For this reason, a semi-analytical solution was developed based on asymptotic limits to the flow profile using the assistance of numerical simulations.

4.5.7 Pressure Drop: Extended 3-D Lubrication Analysis

Tchikanda *et al.* numerically modeled pressure and shear driven flow in open rectangular microchannels with one boundary being an arbitrary curved interface. Their intended application was the development of evaporative cooling devices with parallel liquid-vapour flows (Tchikanda, Nilson et al. 2004). The authors performed numerical simulations to obtain the flow field for various gap shapes and then developed semi-analytical solutions by blending known asymptotic solutions for the outer limits of channel aspect ratio and interface curvature. For example, when the gap is large and the interface is flat, the flow resembles that between two parallel plates, and when the gap is small it resembles the thin film flow. If the interface is curved and the gap is small then flow is primarily through the two disjoint corners (see Figure 4.21). Tchikanda *et al.* provide separate solutions for shear and pressure driven flow that may be combined together due to the linearity of the Navier-Stokes equations in the lubrication limit. The analytical solutions are easy to apply and are accurate to within a few percent compared to the

full numerical solution. In addition, the pressure driven solution uses a zero shear boundary condition which matches the condition where the viscosity contrast between the two phases approaches zero ($\eta \rightarrow 0$).

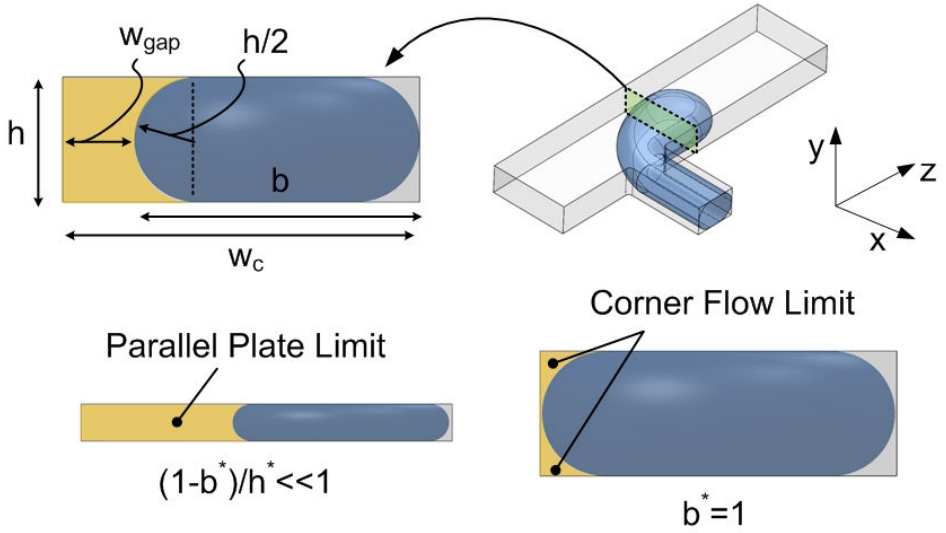

Figure 4.21 Geometry of the gap where the fluid bypasses the droplet with dimensions indicated for flow fluid flow model of Tchikanda *et al*. Examples of the limits of corner flow and parallel plate flow are also illustrated.

The authors provide solutions for the flow in terms of the dimensionless average velocity, $\bar{u}^*$:

$$\bar{u}^* = \frac{Q\mu}{Ah^2\left(-\partial P/\partial z\right)} \tag{4.41}$$

where h is the height of the channel, and A the area of the fluid flows through, μ the viscosity, Q the flow rate and dP/dz the pressure gradient. Integrating the pressure gradient over a uniform conduit of length L, the equation can be rearranged into a format similar to Darcy's Law:

$$\frac{\Delta P}{Q} = R_{hyd} = \frac{L}{\bar{u}^* Ah^2}\mu \tag{4.42}$$

where R_{hyd} is the hydrodynamic resistance and $\frac{L}{\bar{u}^* Ah^2}$ is the geometric component. The average dimensionless velocity is provided as a blend of asymptotic solutions, u_1^* and u_2^*, given by the following expression:

$$\bar{u}^* = \left[\frac{\left(u_1^* u_2^*\right)^{m_1}}{\left(u_1^*\right)^{m_1} + \left(u_2^*\right)^{m_1}}\right]^{1/m_1} \tag{4.43}$$

The expression approaches u_1^* in the limit of $u_1^* >> u_2^*$ and, u_2^* in the opposite limit of $u_1^* << u_2^*$. The shape of the blend is controlled by the fitting parameter m_1. The first asymptote, u_1^*, corresponds to a wide aspect ratio gap, $\lambda_{gap} = h^* / \left(1 - b^*\right)$, or flow between two infinite plates:

$$u_1^* = \frac{1}{12} \tag{4.44}$$

The second asymptote approaches two limits. The first is when the gap is very shallow and the interface is flat, and the second is when the crest of the meniscus is in contact with the wall and flow is only through the corners:

$$u_2^* = \left[\left(\frac{1}{a\lambda_{gap} + 3\lambda_{gap}^{\ 2}} \right)^{m_2} + \left(u_c^*\right)^{m_2} \right]^{1/m_2} \tag{4.45}$$

where u_c^* is the corner asymptotic limit:

$$u_c^* = \left[\frac{\left(u_{co}^*\right)^{m_3}}{1 + \left(u_{co}^*\right)^{m_3} \left[7\left(\lambda_{co} - 2\right)^2\right]^{m_3}} \right]^{1/m_3} \tag{4.46}$$

$$u_{co}^* = 0.0027 \tag{4.47}$$

and λ_{co} is the corner aspect ratio, which is given as $\lambda_{co} = 2$ for the 0˚ contact angle considered in this analysis. For contact angles between 0-30˚ the optimum fitting parameters are: $m_1=1.4$, $m_2=0.83$, $m_3=1.88$ and $a=9.71$. The author`s state that under these conditions the error of the blended set of equations is less than 5% compared to the numerical results.

The curve fits provided by the authors cover a broad range of conditions, many of which are not applicable to the current analysis. For example, in the current study the curvature of the interface is always consider to form a hemi-spherical shape. To improve the curve fits the simulations of Tchinkada *et al.* were repeated for the limited conditions relevant to this study using the commercial finite element software COMSOL 3.5. The results of these simulations reproduced the $\overline{u}^*$ versus λ_{gap} relationship shown in Figure 4.22. Using this data, new optimum fitting parameters were determined based on the asymptotic structure of the model: $m_1=1.4$, $m_2=0.83$, $m_3=1.88$ and $a=7.90$. With this curve fit the average error compared to the numerical results is less than 1.5%.

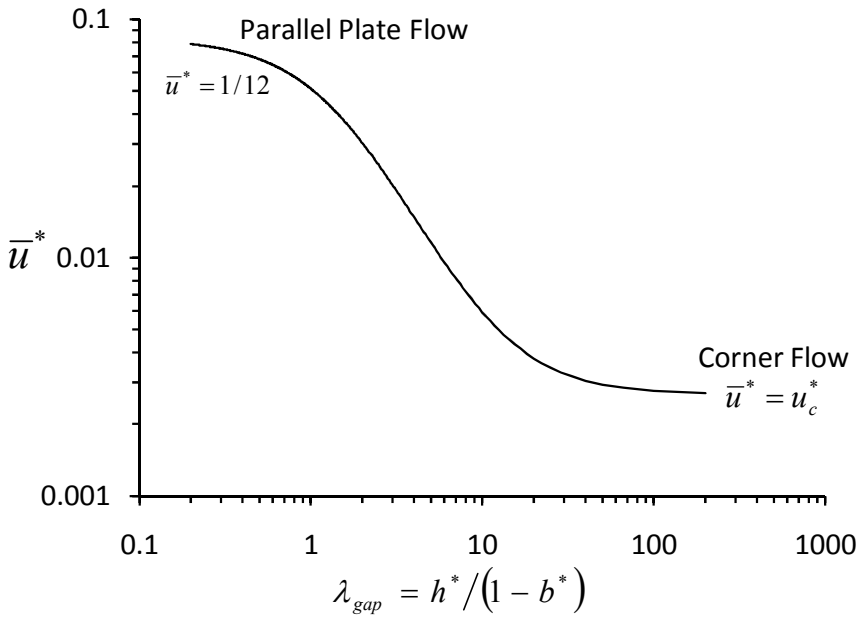

Figure 4.22 Dimensionless mean velocity as a function of the gap aspect ratio with the two limits of parallel plate flow and corner flow identified.

Two additional effects are absent in the approximation by Tchinkada *et al.* which are present in the flow bypassing the droplet. First, the solutions correspond to a conduit with a uniform cross-section along its axis. In the case of the droplet, the gap profile is non uniform due to the curvature in the x-z plane. Secondly, the analysis assumes a zero-shear boundary at the interface which is appropriate for conditions where the continuous phase viscosity is much greater than the dispersed phase viscosity ($\eta \rightarrow 0$). Higher viscosity ratios act to modify the shear stress condition on the interface resulting in an increase in resistance to flow through the gap. These two effects are added to the current asymptotic model as discussed below.

4.5.8 Effective Pressure Drop Length

The interface curvature in the x-z plane creates a constantly varying gap profile along the length of the droplet. Pressure drop generally scales with the cube root of the smallest dimension; therefore, one expects that the effective length over which the majority of the pressure drop occurs in the gap will vary with the penetration depth. Such a dependency was derived by Stone in his study of lubrication flow through shallow curved gaps (Stone 2005).

A numerical study of the flow field through the gap was performed using COMSOL Multiphysics 4.1.Simulations were performed for the same droplet shape as described in Figure 29 for different

droplet sizes $b^*=0.5\rightarrow 1$ and channel heights $h^*=0.2, 0.35, 0.5$. Only one half of the droplet was simulated due to symmetry along the x-z plane as shown in Figure 4.23. Five channel lengths were added before and after the droplet to ensure that the flow field is properly re-aligned at the entrance and exit. Simulations were performed using the Creeping flow module in COMSOL which corresponds to steady-state laminar flow.

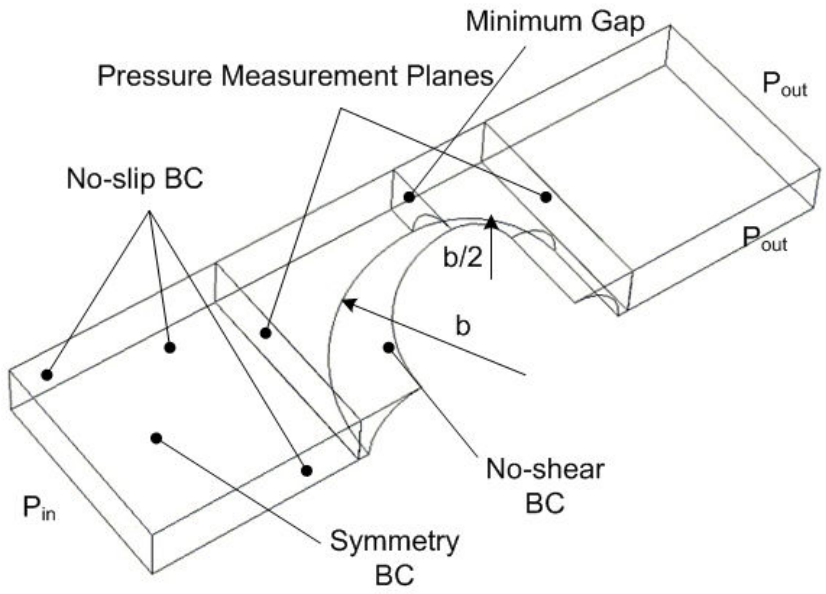

Figure 4.23 Simulation domain of the 3D numerical model performed in COMSOL Multiphysics 4.1. Calculations were only performed for the continuous phase. Boundary conditions are no-slip at all the channel walls and no-shear at the droplet interface.

No-slip conditions were applied to all microchannel walls, and a no-shear condition was applied to the interface of the droplet. A symmetry boundary condition (no-shear) was applied at the plane of symmetry. At the entrance and exit pressures were fixed. Mesh density was increased near the droplet and inside the gap region. Mesh independent studies were performed to confirm that there was a negligible change (~1%) in the results with increasing density. A typical simulation result is presented in Figure 4.24for h^*=0.2 and $b^*=0.9$. For each simulation the pressure drop was measured at two planes just before and after the droplet (total distance between planes is *1.5b*). Additionally, the average velocity in the channel was measured to calculate the total flow rate and determine $\overline{u}^*$.

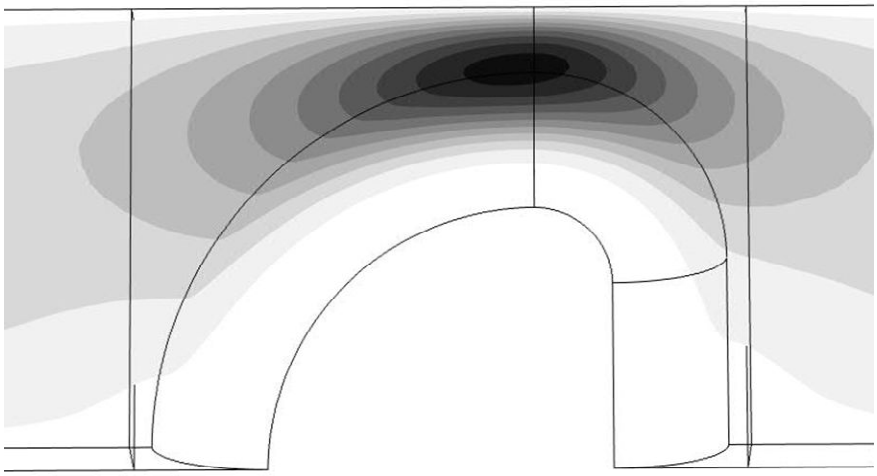

Figure 4.24 Numerical result for the normalized fluid velocity through the gap region for h^*=0.2 and b^*=*0.9*. Shading reads from 0 to 1 by 0.1 from light to dark.

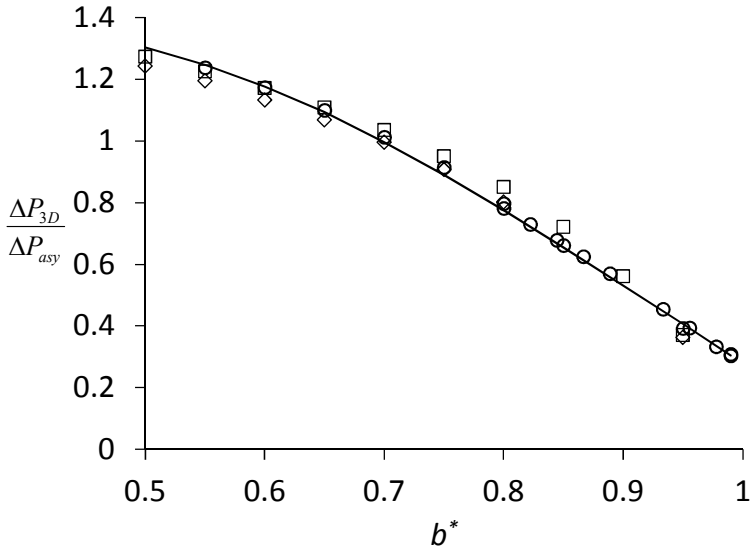

Figure 4.25 Effective pressure drop length $\Delta P_{3D}/\Delta P_{asy}$ in the gap region as a function of the gap width-b^*. Data corresponds to ◊ h^*=0.2, □ h^*=0.35, and ○ h^*=0.5.

The goal here is to still utilize the curve fits provided by Tchiknada *et al.* because of their inherent simplicity and accuracy while adding the influence of the out of plane curvature. This is accomplished by calculating the equivalent length of a channel, with a uniform cross-section at the minimum point of the gap, which produces the same pressure drop as the 3D numerical simulation. Mathematically this relationship is given as the ratio of the pressure drop from the 3D numerical simulations to the pressure drop from the asymptotic model ($L^*_{eff}=L_{eff}/w_c=L^*_{drop}\Delta P_{3D}/\Delta P_{asy}$). Figure 4.25plots the ratio $\Delta P_{3D}/\Delta P_{asy}$ as a function of b^* for a range of h^* for droplets following the shape of $w_d \leq b_{fill}$. Normalizing the 3D result by the

asymptotic model causes all of the data to collapse onto a single curve. The relationship for L^*_{eff} can be described by a blend of limiting solutions consisting of a linear relationship $L^*_1 = Db^* + E$ and an asymptote:

$$L^*_{eff} = L^*_{drop}\left[\frac{\left(L^*_1 L^*_2\right)^k}{\left(L^*_1\right)^k + \left(L^*_2\right)^k}\right]^{1/k} \tag{4.48}$$

For the case $w_d \leq b_{fill}$ then the coefficients are L^*_2=1.3, D= -2.66, E=2.88, k=6 and $L^*_{drop} = 1.5b^*_{fill}$ and for $w_d > b_{fill}$ then L^*_2=*1*, D= -2.66, D=2.88, k=3 and $L^*_{drop} = \Lambda^* + b^*_{fill}$. Therefore, with this modeling the 3D profile of the gap is accounted for and easily integrated with the model of Tchinkada *et al.*

4.5.9 Viscosity Contrast Effect

By increasing the viscosity of the dispersed phase the pressure drop is expected to increase for a given flow rate over the approximation given by Tchinkada *et al.* because of the no-shear condition used at the interface in their analysis. Stones analysis of squeezing flow through a curved gap showed that the pressure drop increases by a factor of 4 when the boundary condition on at the curved interface changes from no-shear (μ_d=*0*) to no-slip (μ_d =∞). This may be contrasted by the case of a sphere translating in an unbound flow at low Reynolds numbers where the drag increases by only 1.5 times from a bubble to a solid (Stone 2005). To estimate this effect, 2D numerical simulations were performed to determine the influence of viscosity contrast on the pressure drop.

Simulations were performed in 2D emulating the cross-sectional view of the microchannel at the minimum gap point. A pressure gradient was applied in the continuous phase while no pressure gradient was applied in the portion of the dispersed phase. Thus flow in the dispersed phase is caused by the drag at the interface created by the bypassing continuous flow. This situation approximates the actual conditions prevalent in the gap during droplet formation. Generally $Q_c > Q_d$ and the continuous phase must flow through a smaller area ~*(1-*b^**)* then the dispersed phase ~b^*. Thus the average velocity in the gap region is typically an order of magnitude higher than the velocity within the droplet, so that as an approximation one can consider the flow in the

drop to be stagnant in comparison. For the boundary conditions, no-slip is applied along all the microchannel walls and continuity at the interface boundary.

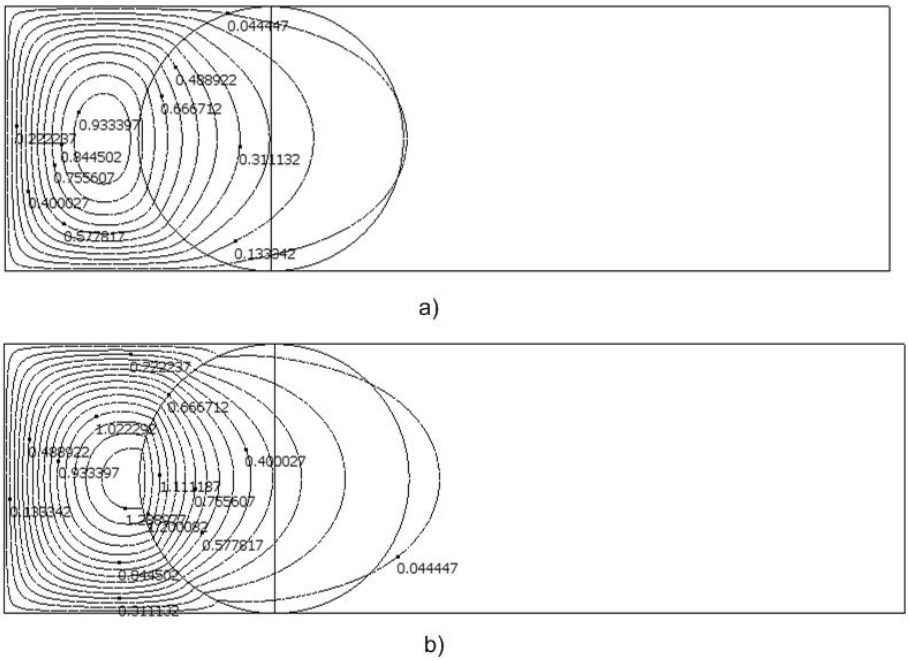

Figure 4.26 Contour plot of the dimensionless velocity profiles in the cross-section of the droplet at the minimum gap height for (a) $h^*=0.3$, $b^*=0.85$, $\eta=1$, and (b) $b^*=0.85$, $\eta=1/100$. Data is non-dimensionalized by the maximum velocity for (a).

Simulations were performed for gaps varying between $b^*=0.6\rightarrow 1$ and viscosity contrasts $\eta=1/100\rightarrow 1$. Figure 4.26 presents the resulting flow field for the case of $b^*=0.8$ and $\eta=1$ and $\eta=1/100$. The solution for flow in gap matches qualitatively with μ-PIV data obtained by van Steijn *et al.* (van Steijn, Kreutzer et al. 2007). The shear on the outer edge of the droplet creates an internal flow inside the droplet that decays exponentially towards the center due to drag from the top and bottom walls. This additional drag retards the flow of the continuous phase increasing the required pressure.

Figure 4.27 plots the relative change in resistance to flow as compared to the no-shear case for different viscosity contrasts. The trend is a non-monotonic function that generally increases as the gap closes ($b^*=0.5\rightarrow 1$). Peculiarly, a small decrease in the relative pressure drop occurs around $b^*=0.95$ presumably due to the unique geometry and competing boundary conditions on the flow within the gap region. A two-step fit is applied to the function approximating the first part $\lambda_{gap} < 2$ with a linear curve fit $g(\eta,\lambda_{gap}) = a(\eta)\lambda_{gap} + 1$ and the second, $\lambda_{gap} \geq 2$ as a constant. The

slope of the linear function scales proportionality with the viscosity contrast and has a form $a(\eta) = 0.1\eta$ (R^2=0.96).

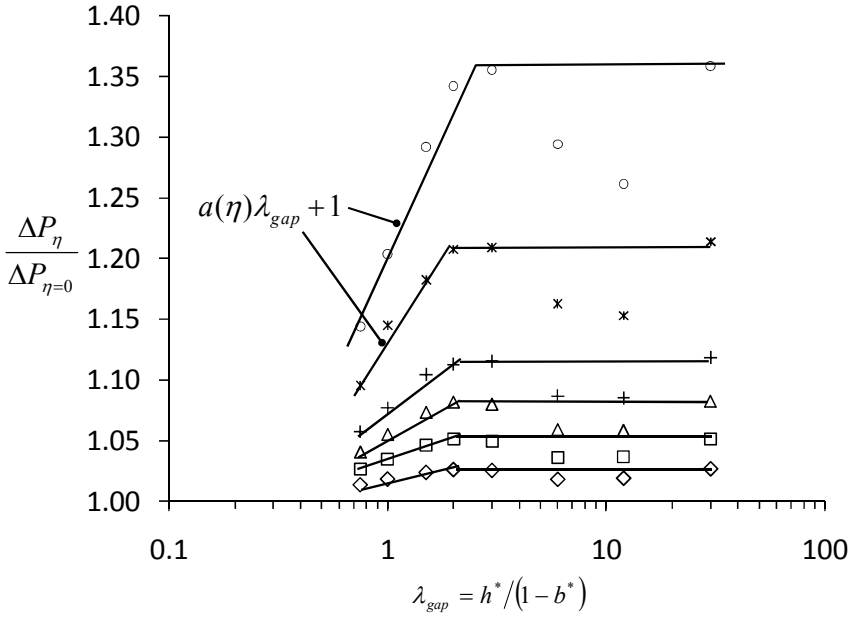

Figure 4.27 Effect of viscosity contrast on the pressure drop from the 2D numerical simulations. Data corresponds to ◊ η=0.1, □ η=0.2,Δ η=0.33, + η=0.5, * η=1, ○ η=2.

The piece-wise function that defines the effect of the viscosity contrast is thus given by:

$$g(\eta, \lambda_{gap}) = \begin{cases} 0.1\eta\lambda_{gap} + 1 & \lambda_{gap} < 2 \\ 0.2\eta + 1 & \lambda_{gap} \geq 2 \end{cases} \tag{4.49}$$

This relationship is used to modify the pressure drop calculation provided by Tchinkada *et al.* and account for the effect of viscosity contrast.

4.5.10 Force balance with 3D flow Considerations

With the new model for the flow through the gap in hand, the force balance on the emerging interface can be revisited. Rearranging Eqn. 4.41, integrating to calculate the pressure drop and including the modification of L_{eff} and $g(\eta, \lambda_{gap})$:

$$\Delta P_{u-d} = \frac{L_{eff} Q_{c_{gap}} \mu_c}{h^2 \left(A_{gap} \bar{u}^*_{gap}\right)} g(\eta, \lambda_{gap}) \tag{4.50}$$

Substituting into the force balance on the emerging droplet Eqn. 4.37, but neglecting the shear stress contribution, the new force balance becomes:

$$-\gamma\left(2-\frac{b_{fill}^{*}}{R_{n}^{*}}\right)h+C\frac{L_{eff}b_{fill}Q_{c_{gap}}\mu_{c}}{\left(A_{gap}\bar{u}_{gap}^{*}\right)h}g\left(\eta,\lambda_{gap}\right)=0 \tag{4.51}$$

where C is a fitting parameter. Non-dimensionalizing the equation results in:

$$\frac{h^{*}}{Ca}=\frac{1}{2}\frac{L_{eff}^{*}g\left(\eta,\lambda_{gap}\right)}{\left(A_{gap}^{*}\bar{u}_{gap}^{*}\right)}\frac{b_{fill}^{*}}{\left(2-b_{fill}^{*}/R_{n}^{*}\right)} \tag{4.52}$$

For the case $w_d \leq b_{fill}$ then $R_n = b_{fill}$ and $w_d > b_{fill}$ then $R_n = w_d$ when calculating the force balance. Because of the complex dependency of several variables on b_{fill}^{*}, the best method for solving Eqn. 4.52 is to iterate until the left and right side converge. Unlike the previous model, a singularity does not exist as the gap closes because of flow through the corners, and therefore, an upper limit must be imposed on Eqn. 4.52 of $b_{fill}^{*} \leq 1$ in the case of divergence.

Comparisons with experiments indicates that the a pre-factor of C=1/2 fits well –a peculiar value as it suggests that the surface tension force is underestimated by a factor of 2 or the pressure force is overestimated by a factor of 2. The cause for this is not quite known but there are several reasons that can be suggested. First is that the force balance in the stream wise direction is not the only contribution to the deformation of the emerging interface as a force in the cross-stream direction also exists. This force is caused by the pressure difference within the droplet and the average pressure in the gap $F_{px} \propto \Delta P_{u-d}/2$ - where the factor of ½ appears. A second explanation is that the continuous phase is also able to bypass the emerging interface through the top and bottom films or the near channel wall which reduces the effective pressure drop. A third explanation is that the surface tension force is underestimated we assumed that the out of plane curvature ~2/h remained the same for the front and back of the droplet. This results in a cancellation of out of plane curvature effects in the surface tension force. It is well known that the curvature of the front cap increases relative to the back cap when droplets travel in microchannels (Gunther and Jensen 2006). If we presume that this effect also occurs during drop formation then it would contribute to an increase in the surface tension force. Most likely, however, it is a combination of these effects that produce the pre-factor of 1/2 and untangling them would require a detailed numerical study which is beyond the scope of this current work. Nevertheless, the penetration depth is well described by Eqn. 4.52 when a pre-factor of 1/2 is used as will be shown later. Once b_{fill}^{*} is calculated it can then be substituted back Eqn. 4.23 or 4.24 to calculate V_{fill}. In

the next section, the flow field equations provided by Tchikanda *et al.* are used again in the derivation of $2r_{pinch}$.

4.5.11 Calculating the Pinch-off Point $2r_{pinch}$

In order to incorporate the observed *Ca* and viscosity dependence on $2r^*_{pinch}$ a new approach was taken which also incorporates the resistance to flow through the gap. The ideas is that pinch-off occurs when the Laplace pressure difference between the front and back of the droplet generates a backwards flow that exceeds some multiple *m* of the bypassing flow $Q_c A^*_{gap}/h^*$. The Laplace pressure driven fluid flow around the drop may be approximated by:

$$\Delta P_{Lp} = \gamma\left(\frac{1}{R_n}+\frac{1}{r_n}\right)-\gamma\left(\frac{2}{b_{pinch}}+\frac{2}{h}\right)=\frac{L_{eff}\,\mu_c\, g\left(\eta,\lambda_{gap}\right)}{h^2\left(A_{gap}\bar{u}^*_{gap}+A_{nw}\bar{u}^*_{nw}\right)}mQ_c\,\frac{A^*_{gap}}{h^*} \tag{4.53}$$

Ignoring the smaller term of $1/R_n$ and rearranging Eqn.4.53, the critical neck thickness is:

$$2r^*_{pinch}=\frac{h^*}{1+\dfrac{h^*}{b^*_{pinch}}+\dfrac{m}{2}\dfrac{Ca}{h^*}\dfrac{L^*_{eff}\,g\left(\eta,\lambda_{gap}\right)}{\bar{u}^*_{gap}}} \tag{4.54}$$

In the case of $Ca\rightarrow 0$, then $b^*\rightarrow 1$ and the limit from van Steijn *et al.* is recovered. Comparisons with experiments show that the optimum fitting parameter is $m=1$ meaning that the sudden collapse of the neck occurs when the back pressure creates a flow that is equal to the bypassing flow. This calculation does not account for the rate of drainage within the neck that occurs after the critical pinch-off point is reached, or the effect of the internal viscosity other than the drag on the reversing Laplace pressure flow. Overall the new model for the neck is more robust since it includes the interfacial tension and viscosity in *Ca* as well as the resistance to fluid flow through the gutters around the drop through $\bar{u}^*$.

4.5.12 Calculation of Other Operational Parameters

In this section the other important operational parameters are calculated including the volume of oil injected between the droplets, droplet spacing and the frequency of formation. The total volume of oil injected can be broken down into three contributions: (a) oil that bypasses the droplet during the lag stage when the interface is inside the dispersed channel (b) oil that bypasses

the emerging interface during the drop filling stage (c) oil that continues to bypass the droplet during the squeezing stage:

$$V_c = V_{c_{lag}} + V_{c_{fill}} + V_{c_{neck}} \tag{4.55}$$

The volume is related to the length of each stage and the oil flow rate which is assumed to remain constant throughout the three stages:

$$V_c = \Delta t_{lag} Q_c + \Delta t_{fill} Q_c + \Delta t_{neck} Q_c \tag{4.56}$$

Note that during the necking stage Q_c is used because all of the flow either collapses the neck or bypasses the droplet and thus contributes to the spacing eventually. The length of each stage is given as $\Delta t_{lag} = \alpha_{lag} w_c^2 h / Q_d$, $\Delta t_{lag} = \alpha_{fill} w_c^2 h / Q_d$ and $\Delta t_{lag} = \beta w_c^2 h / Q_c$. The non-dimensional form becomes:

$$V_c^* = \frac{\alpha_{lag} + \alpha_{fill}}{\varphi} + \beta \tag{4.57}$$

The rate of production and droplet spacing are additional parameters that are important in the design of a droplet generator and can be derived using similar arguments that were employed in the calculation of the droplet volume. The spacing, $\lambda = L_{drop} + L_{oil}$, may be approximated by assuming $V^* \sim L^*$:

$$\lambda^* = \left(\alpha_{lag} + \alpha_{fill}\right)\left(\frac{\varphi + 1}{\varphi}\right) + \beta(\varphi + 1) \tag{4.58}$$

The total time for droplet production is the sum of the three stages:

$$t_{drop} = \Delta t_{lag} + \Delta t_{fill} + \Delta t_{sq} \tag{4.59}$$

In non-dimensional terms the period over which a droplet forms is:

$$t_{drop}^* = \frac{\alpha_{lag} + \alpha_{fill}}{\varphi} + \beta \tag{4.60}$$

The normalized frequency is then the reciprocal of this equation:

$$f^* = \frac{\varphi}{\alpha_{lag} + \alpha_{fill} + \varphi\beta} \tag{4.61}$$

Next, the complete model is summarized so that the reader may access it directly.

4.5.13 Summary of Model for Droplet Generation

Figure 4.33 summarizes the entire calculation procedure that has been outlined in the preceding discussion. Plots for the parameters b^*_{fill}, $2r^*_{pinch}$, α_{fill} and β for various conditions and T-junction designs are provided Figures 4.28-4.31. Analysis shows that the most important parameters governing droplet formation are the T-junction geometry (w_c,w_d, h) and the term h^*/Ca as it governs b^*_{fill} and the necking stage $2r^*_{pinch}$.

Consider Figure 4.28 which shows the calculation for b^*_{fill} for different h^* and two different viscosities η=0 and η=1. The plot shows that the relationship between b^*_{fill} and h^*/Ca is non-linear and depends on h^*. As well, increasing the dispersed phase viscosity decreases b^*_{fill} because of the additional drag on the bypassing fluid. Overall, b^* increases with h^*/Ca until it becomes capped at $b^*=1$. Often this critical point is associated with transition into the "purely squeezing" regime of droplet formation. The model shows that this transition depends on the geometry and viscosity contrast, and can be calculated from Eqn. 4.52 by substituting for $b^*=1$, $A_{bp}{}^*=h^{*2}\cdot(1-\pi/4)$ /2and the corner flow limit of $\overline{u}^* = 0.0027$:

$$Ca_{sq} \le 1.7e^{-3}\frac{h^{*3}}{g(\eta,\lambda_{gap})} \tag{4.62}$$

Therefore, below this Capillary number the interface will always reach the far channel wall in the filling stage and operation will fall into the "purely squeezing" regime. However, for typical conditions (h^*=0.5, η=0) working in this regime requires very low flow rates (Ca_{sq}=4.1e^{-4}) that are generally impractical (typically an order of magnitude lower than the flow rates used in this study ~1 μL/min). This suggests that T-junction generators always operate in the transition regime to some degree and that a model that accounts for the *Ca* dependence is necessary.

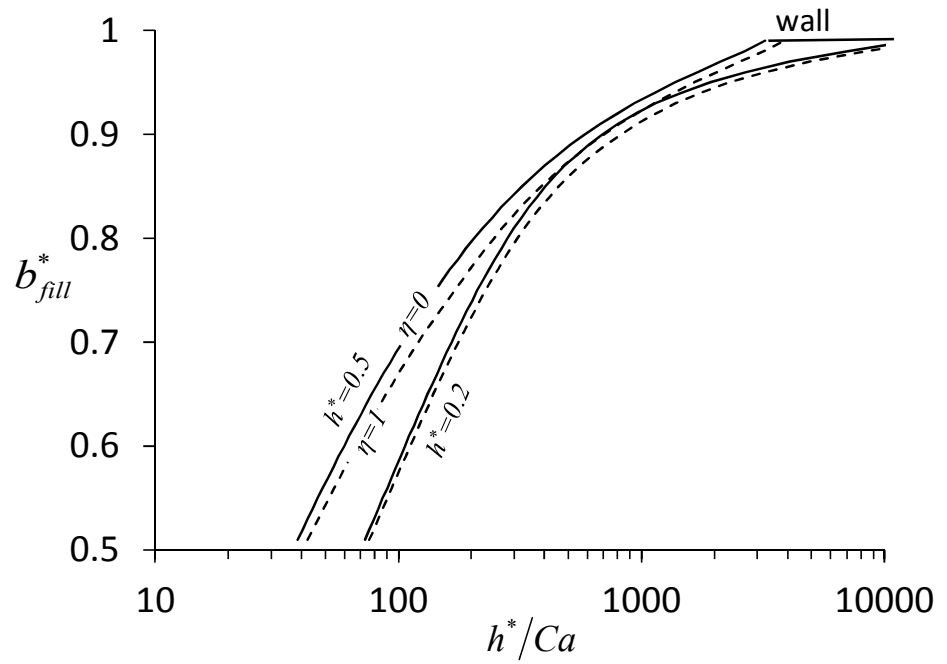

Figure 4.28 Plot of b^*_{fill} with respect to h^*/Ca for two different channel aspect ratios and viscosity ratios.

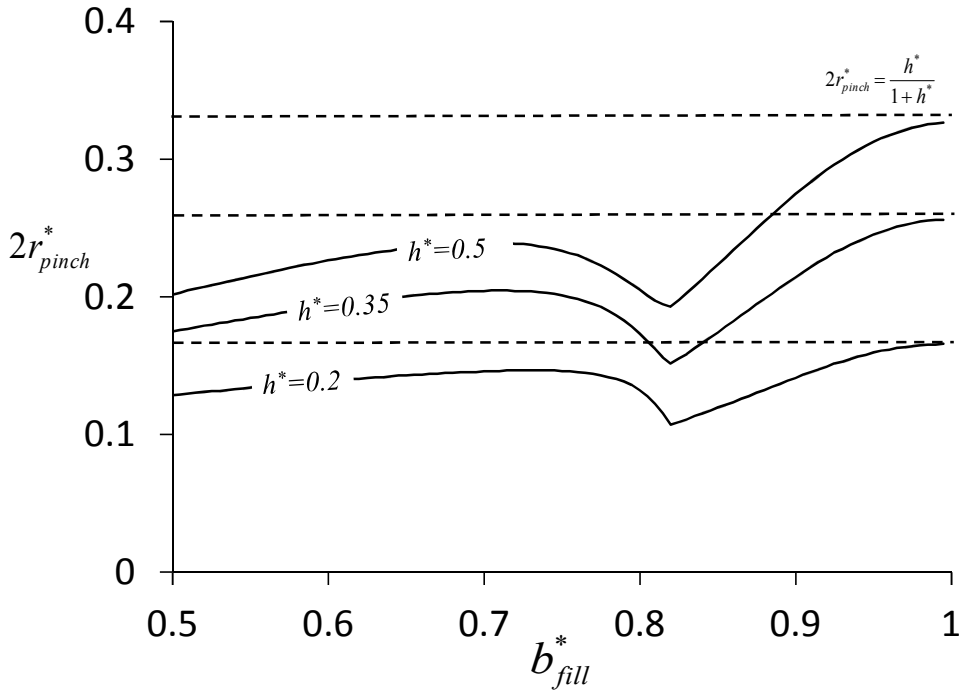

Figure 4.29 Calculations of the new critical neck thickness for h^*=0.2, 0.35 and 0.5.

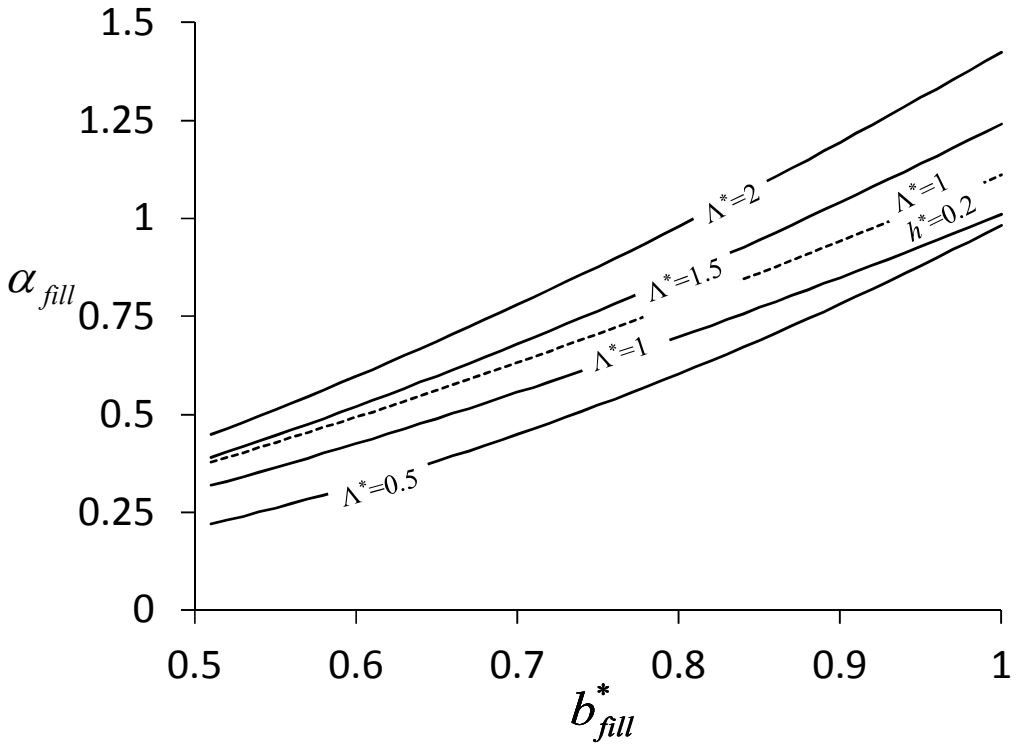

Figure 4.30 Plot of α with respect to b^*_{fill} for various T-junction geometries with a base value of h^*=0.5, ε^*=0.

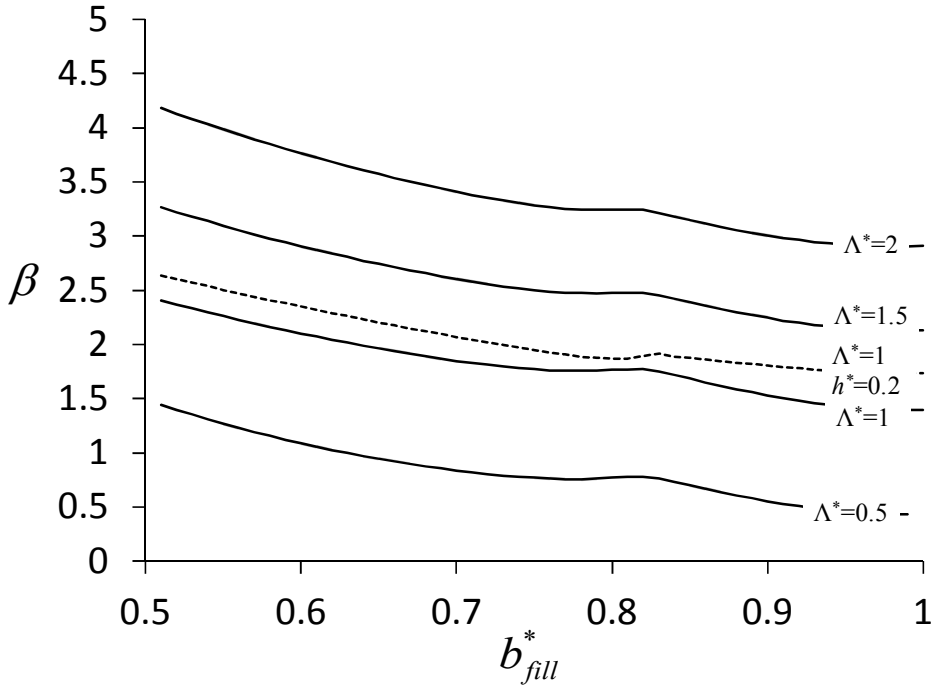

Figure 4.31 Plot of β with respect to b^*_{fill} for various T-junction geometries with a base value of h^*=0.5, ε^*=0.

Fig 4.29 plots the ratio of critical neck thickness against b^*_{fill}. The profile is highly non-linear with an inflection point at b^*_{fill}=0.833 which is caused by the relation $b^*_{pinch} = 1.2b^*_{fill}$ and the limit $b^*_{pinch} \le 1$. To the left of the inflection point b^*_{fill} is still free and the critical neck thickness increases, but then decreases towards the inflection point because the gap closes increasing the resistance to flow around the droplet. To the right of the inflection point b^*_{pinch} is capped at $b^*_{pinch} = 1$ and all of the variables in Eqn. 4.54 are constant, except for the *Ca* term which continues to decrease so that approaches the limit $2r^*_{pinch} \to h^*/(1+h^*)$.

Both α_{fill} and β are primarily governed by the geometry of the T-junction generator, with the width ratio Λ^* having a stronger influence than the height ratio h^* as shown in Figures 4.30 and 4.31. As expected, the fill volume α_{fill} decreases with b^*_{fill} which corresponds to higher *Ca*. What may be a surprise is that the dimensionless necking time β actually increases with higher *Ca* (seen in the plot as decreasing b^*_{fill}). There are two contributions to this effect. First, smaller b^*_{fill} means that the interface blocks a smaller amount of the cross-flow so that of less of the continuous phase is directed to collapsing the neck. Second, higher *Ca* result in lower $2r^*_{pinch}$ values which means the neck is open longer and β increases. The effect of the limit $b^*_{pinch} \le 1$ can also be seen in the small bump at b^*_{fill}=0.83 in the plots.

To illustrate the changing performance of a T-junction generator with higher operational speeds (i.e. higher *Ca*), the variation in V^*_d, V^*_c and f^* is plotted in Figure 4.32 for a standard generator design ($\Lambda^* = 0.5$, $h^* = 0.3$) while keeping the flow ratio constant φ=*0.3*. At lower speeds (*Ca*→0) droplets are larger and spaced further apart which also means that they are produced at comparatively lower rate. As *Ca* increases smaller droplets are formed closer together and the rate of production increases accordingly. This example clearly shows the complex operational behaviour of a T-junction generator within the squeezing-to transitional mode.

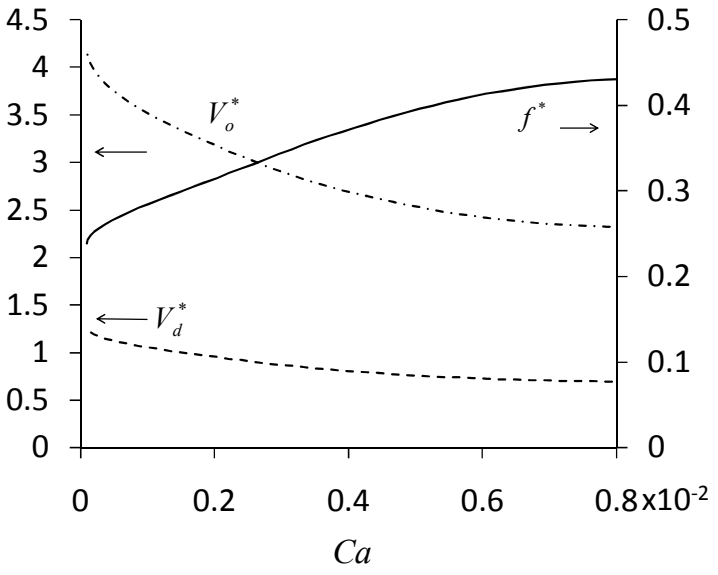

Figure 4.32 Variation droplet generation for a T-junction geometry of $h^*=0.5$, $\Lambda^*=0.5$ for a fixed flow rate φ=0 against Capillary number.

Input Parameters

Q_c, Q_d, h, w_c, w_d, μ_d, μ_c, ε ⟶ Ca, h^*, Λ^*, η, φ

Calculate b^*

$$\frac{h^*}{Ca}=\frac{1}{2}\frac{L_{eff}^*\,g(\eta,\lambda_{gap})}{\left(A_{gap}^*\,\overline{u}_{gap}^*\right)}\frac{b_{fill}^*}{\left(2-b_{fill}^*/R_n^*\right)} \qquad u_c^*=\left[\frac{\left(u_{co}^*\right)^{m_3}}{1+\left(u_{co}^*\right)^{m_3}\left[7\left(\lambda_{co}-2\right)^2\right]^{m_3}}\right]^{1/m_3} \qquad u_{co}^*=0.0027 \qquad g(\eta,\lambda_{gap})=\begin{cases}0.1\eta\lambda_{gap}+1 & \lambda_{gap}<2\\ 0.2\eta+1 & \lambda_{gap}\geq 2\end{cases}$$

$$A_{gap}^*=\left(1-b^*\right)h^*+\frac{1}{2}h^{*2}\left(1-\frac{\pi}{4}\right) \qquad u_2^*=\left[\left(\frac{1}{a\lambda_{gap}+3\lambda_{gap}^2}\right)^{m_2}+\left(u_c^*\right)^{m_2}\right]^{1/m_2} \qquad \lambda_{co}=2 \qquad L_{eff}^*=L_{drop}^*\left[\frac{\left(L_1^*L_2^*\right)^k}{\left(L_1^*\right)^k+\left(L_2^*\right)^k}\right]^{1/k}$$

$$\overline{u}^*=\left[\frac{\left(u_1^*u_2^*\right)^{m_1}}{\left(u_1^*\right)^{m_1}+\left(u_2^*\right)^{m_1}}\right]^{1/m_1} \qquad \lambda_{gap}=h^*/\left(1-b^*\right) \qquad u_1^*=\frac{1}{12} \qquad m_1=1.4 \qquad m_2=0.83 \qquad m_3=1.88$$

$$\Lambda^*\leq b_{fill}^* \quad L_1^*=-2.66b^*+2.88 \quad L_{drop}^*=1.5b_{fill}^* \quad L_2^*=1.3,k=6$$

$$\Lambda^*>b_{fill}^* \quad L_1^*=-2.66b^*+2.88 \quad L_{drop}^*=\Lambda^*+b_{fill}^* \quad L_2^*=1,k=3$$

Calculate α_{lag}, α_{fill}

$$\alpha_{fill}=\begin{cases}\frac{\pi}{8}b_{fill}^{*\,2}+\frac{1}{4}\Lambda^{*2}(\theta-\sin\theta)-\frac{h^*}{4}\left(1-\frac{\pi}{4}\right)\left(\pi b_{fill}^*+\Lambda^*\theta\right) & \theta=2a\cos\left(1-\frac{b_{fill}^*}{\Lambda^*}\right) \quad \Lambda^*>b_{fill}^*\\ \frac{3}{8}\pi b_{fill}^{*\,2}-\frac{h^*}{2}\left(1-\frac{\pi}{4}\right)\left(\pi b_{fill}^*+\left(b_{fill}^*-\Lambda^*\right)\right) & \Lambda^*\leq b_{fill}^*\end{cases} \qquad \alpha_{lag}=L_{lag}^*\Lambda^*+\frac{1}{2}\left(1-\frac{\pi}{4}\right)\left(\Lambda^{*2}+\frac{\pi\Lambda^*h^*}{2}\right)$$

Calculate β

$$\beta=\frac{1}{\left(1-A_{bp}^*/h^*\right)}\left(V_{c_{pinch}}^*-V_{c_{fill}}^*\right) \qquad V_{c_{fill}}^*=\left(1-b^*\right)R_{fill}^*+\left(1-\frac{\pi}{4}\right)R_{fill}^{*\,2}+\frac{\pi h^*}{4}\left(1-\frac{\pi}{4}\right)R_{fill}^*$$

$$V_{c_{pinch}}^*=\left(1-b_{pinch}^*\right)a^*+\left(1+\Lambda^*\right)a^*-\frac{R_{pinch}^{*\,2}}{4}(\theta-\sin\theta)+\frac{h^*}{2}\left(1-\frac{\pi}{4}\right)R_{pinch}^*\frac{\theta}{2}$$

$$d^*=b_{pinch}^*+\Lambda^* \qquad a^*=\sqrt{d^*\left(2R_{pinch}^*-d^*\right)} \qquad \theta=2\arccos\left(1-\frac{b_{pinch}^*+\Lambda^*}{R_{pinch}^*}\right)$$

$$2r_{pinch}^*-\varepsilon=R_{pinch}^*-\sqrt{\left(R_{pinch}^*-b_{pinch}^*\right)^2+\left(a^*-\Lambda^*\right)^2} \qquad 2r_{pinch}^*=\frac{h^*}{1+\frac{h^*}{b_{pinch}^*}+\frac{m}{2}\frac{Ca}{h^*}\frac{L_{eff}^*g(\eta,\lambda_{gap})}{\overline{u}_{gap}^*}}$$

Calculate V_d^*, V_o^*, f^*, λ^*

$$V_d^*=\alpha_{lag}+\alpha_{fill}+\beta\varphi \qquad \lambda^*=\left(\alpha_{lag}+\alpha_{fill}\right)\left(\frac{\varphi+1}{\varphi}\right)+\beta(\varphi+1)$$

$$V_o^*=\frac{\alpha_{lag}+\alpha_{fill}}{\varphi}+\beta \qquad f^*=\frac{\varphi}{\alpha_{lag}+\alpha_{fill}+\varphi\beta}$$

Figure 4.33 Complete set of equations for the modelling of the T-junction droplet generator.

4.6 Experimental Validation

The theoretical model was validated by apply it to the experiments performed for T-junctions with $\Lambda^*=0.34\rightarrow1$, $h^*=0.3\rightarrow0.6$ under conditions ranging from $\eta=0.12\rightarrow1.7$ and $Ca=0.001\rightarrow0.008$. This data covers a wide range of conditions that are typically associated with the transition between squeezing and dripping ($b^*_{fill}=0.65\rightarrow1$). Some data was omitted that did not match the conditions of the model, which include that the flow rates are steady during the formation process (droplet velocity fluctuations <5%), and droplet size variations (which could be artificial from image analysis or real) were less than <3% (refer to discussion in Chapter 6 on oscillations of droplet generator performance). Additional data was omitted if the oil flow rates were too low (<0.5 μL/min) or too high (>5 μL/min) to be accurately measured by the flow sensor. The effectiveness of the model is measured by a series of parity plots that compare the predicted penetration depth, droplet volume, oil volume and production frequency produced by the model to that measured in the experiments. Perfect parity exists when the data falls along the solid black line in the following figures.

Figure 4.34 presents the overall accuracy for the calculation b^*_{fill} from the new force balance for all the experiments. Generally the predictions are very good as most of the data falls within an error range of ±10%, which is deemed acceptable given the potential errors involved in measuring all the parameters from the videos. Figure 4.35demonstrates the importance of including L^*_{eff} and $g(\eta, \lambda_{gap})$ in the force balance. One can see that the omission of these two effects results in a systematic under prediction of the penetration depth. Figure 4.36 presents the comparison between predicted and measured pinch-off. Good agreement is found although there is some scatter due to the difficulties inaccuracy of t he video analysis in measuring the exact moment of collapse. Predictions for V^*_d, V^*_c and $f^*$are provided in Figure 4.37 to 4.39 with excellent correlation between the experimental and model result as all data falls within ±10% of parity. This suggests that the model developed herein is successful in predicting the performance of the T-junction generator in the squeezing-to-transition regime.

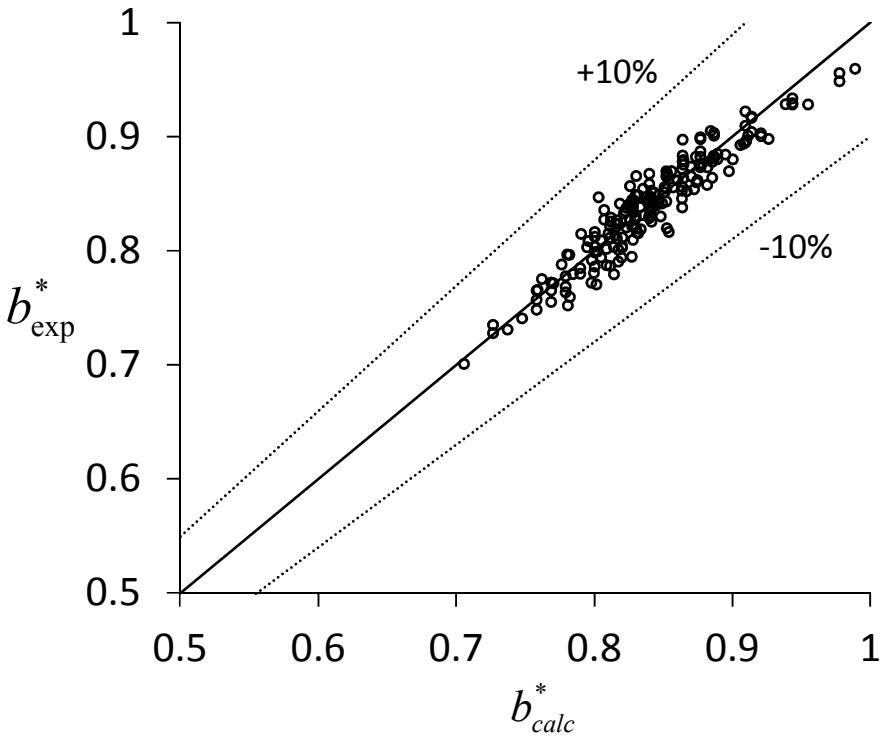

Figure 4.34 Parity plot of b^*_{fill} for all experiments. Solid line is perfect parity and the dashed lines are ±10%.

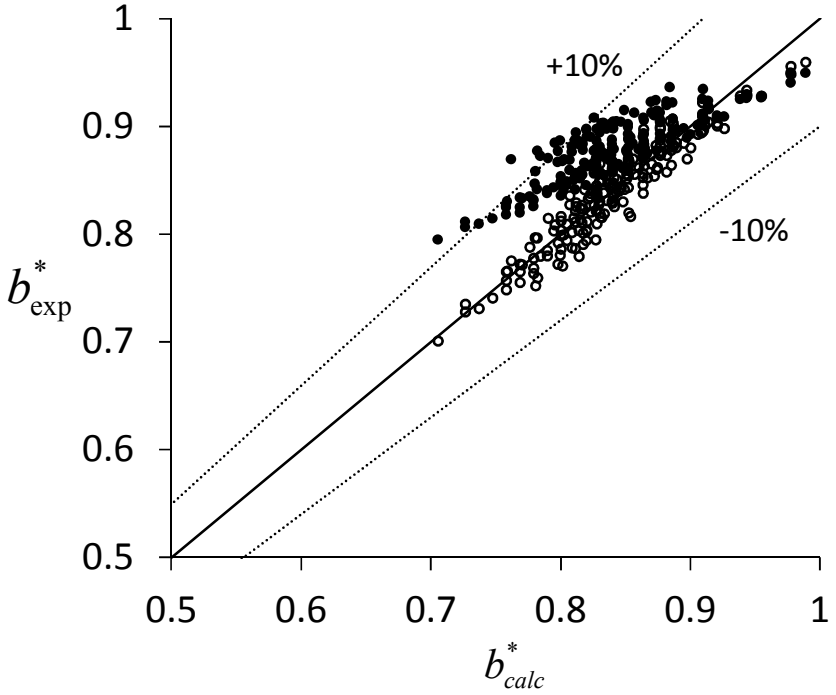

Figure 4.35 Parity plot of b^*_{fill} for experiments with L^*_{eff} and $g(\eta, \lambda_{gap})$ ○ silicon oil and ● with a constant L^*_{eff} =0.25 and $g(\eta=1, \lambda_{gap})$. Solid line represents the perfect parity and the dashed lines are ±10%.

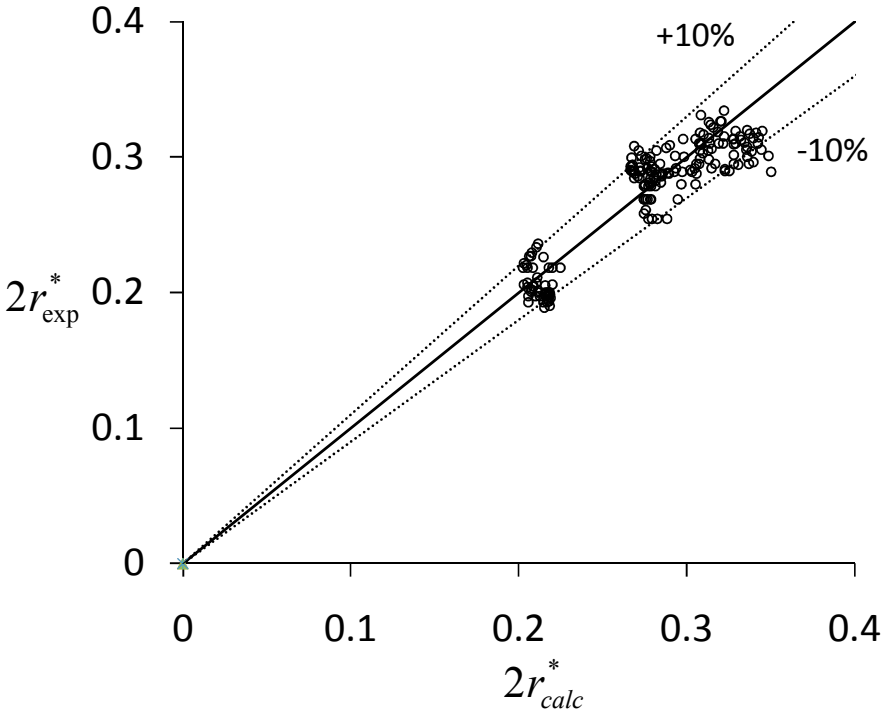

Figure 4.36 Parity plot of $2r^*_{pinch}$ for all experimental measurements.

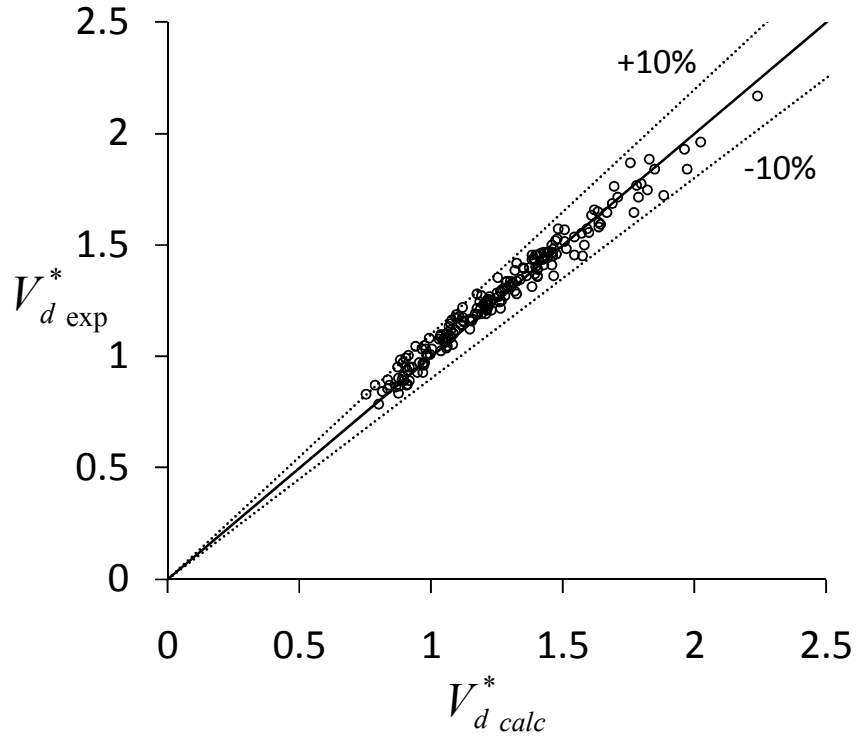

Figure 4.37 Parity plot of droplet volume for all experimental measurements.

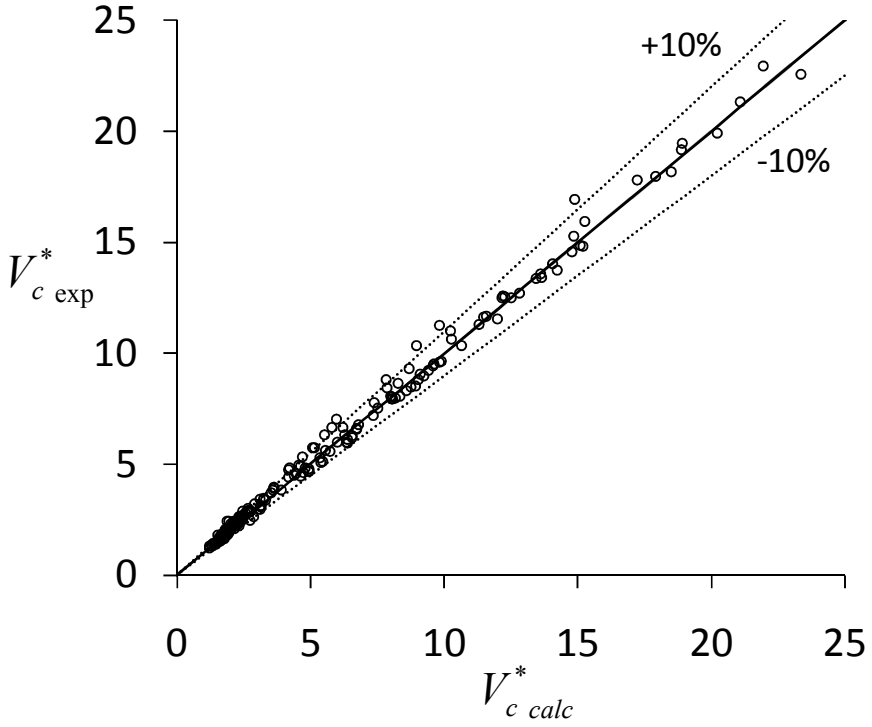

Figure 4.38 Parity plot of continuous phase volume for all experimental data points.

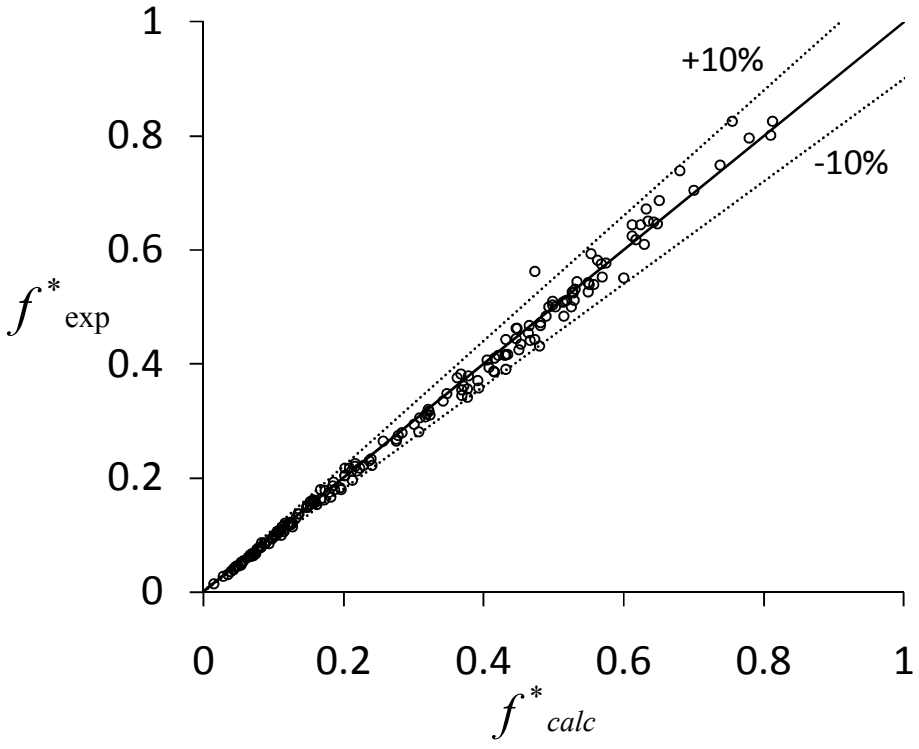

Figure 4.39 Parity plots for generation frequency for all experimental data.

4.7 Conclusions

In this chapter a physical model was presented for the formation of droplets in a microfluidic T-junction generator operating in the squeezing to transition regimes. The model builds upon the work of van Steijn *et al.* and may be decomposed into three main components(van Steijn 2010). First, the geometric description presented by van Steijn *et al.* was adapted to describe the droplet shape and neck in the transition regime. This is followed by a new force balance to calculate the initial fill volume that includes the 3D hydrodynamic resistance of the gap by incorporating the analytical approximations of Tchninkada *et al.*(Tchikanda, Nilson et al. 2004). The new model includes additional factors that account for the 3D curvature of the droplet and the viscosity contrast between the two phases. Finally, a modified pinch-off criteria was developed based on experimental observations that includes the shape of the gap and the strength of the Laplace pressure driven flow in the calculation. The resulting model highlights the strong dependence of flow ratio, *Ca*, and geometry on droplet formation which has been previously documented by several researchers. The model was experimentally validated for a range of T-junction geometry with $\Lambda^* = 0.33,\ 0.5,$ 1, and $h^* = 0.3 \rightarrow 0.6$ for $h^*/Ca = 60 \rightarrow 500$. and $\eta = 0.12 \rightarrow 1.7$. Good agreement was found between the model and experiments for the droplet size, frequency and spacing across all the conditions considered with most data falling within 10% of the predicted value. Additionally, h^*/Ca, was identified as an important parameter for defining the flow in the squeezing-to-transition regime as it determines the degree of squeezing pressure created on the emerging droplet interface.

Despite its success, more testing is required to determine the extent of the models applicability. This includes extending the range of $\Lambda^* > 1$, $h^*/Ca < 50$, and $\eta >> 1$ to determine the limits of the assumptions that were applied as the model was developed. Future extensions of the model into the dripping regime must include the shear stress in the force balance which was omitted in the force balance analysis. Additionally, a model that accounts for the extent of the lag stage is also needed. In its current form the model will still enable the efficient design of T-junction generators, avoiding the ambiguity and frustration of trial and error procedures. As well, the model may be implemented as a subroutine in the larger droplet network trafficking models currently under development (Jousse, Lian et al. 2005; Schindler and Ajdari 2008).

Nomenclature

Acronyms:

2D	two dimensional
3D	three dimensional
CV	control volume
PDMS	poly(dimethyl)siloxane
μ-PIV	micro particle image velocimetry

Mathematical Symbols:

$\alpha_{lag,fill}$	dimensionless lag and fill volumes
β	dimensionless necking time
γ	interfacial tension (N m^{-1})
ε	radius of inner corner in T-junction (m)
θ	angle (rad)
κ	curvature (m^{-1})
λ	inter-droplet spacing (m)
λ_{gap}	gap aspect ratio
μ	dynamic viscosity of fluid (Pa s)
η	ratio of dispersed to continuous phase viscosities
ρ	density (kg m^{-3})
τ_{drop}	drop formation time (s)
φ	ratio of dispersed to continuous phase flow rates
Λ^*	T-junction dispersed to continuous phase widths
a	circular segment cord length (m)
b	interface penetration depth (m)
b_{fill}	interface penetration depth at the end of the filling stage (m)
b_{pinch}	interface penetration depth at pinch-off (m)
d	circular segment height (m)
f	frequency (Hz)
h	height (m)
l	perimeter (m)
n	number of droplets

u_d	droplet velocity (m s^{-1})
u_{thread}	necking thread velocity (m s^{-1})
$\bar{u}^*$	dimensionless average velocity in the gap
r	radial coordinate
r_{neck}	radius of neck during necking (m)
r_{pinch}	radius of neck at the pinch-off point (m)
$w_{c,d,m}$	width of dispersed, continuous and main channels (m)
w_{gap}	width of gap between interface and far channel wall (m)
z	depth coordinate
t	time (s)

A_p	projected area of droplet (m^2)
A_{bp}	area of the bypass around the droplet (m^2)
Ca	capillary number (dimensionless)
$F_{\tau,p,\gamma}$	shear, pressure and interfacial tension force (N)
$L_{c,d,m}$	length of continuous, dispersed and main channels (m)
L_{lag}	distance interface retraces back into the inlet channel after pinch-off (m)
L_{eff}	effective hydrodynamic length of the gap (m)
$P_{d,c,m}$	pressure at continuous, dispersed and main channel exits (Pa)
$Q_{d,c,m}$	flow rate of dispersed, continuous or main channel (m^3 s)
Re	Reynold's number (dimensionless)
R_{hyd}	hydrodynamic resistance (Pa s m^{-3})
R_n	Radius of back half of droplet (m)
V_{drop}	droplet volume (m^3)
V_c	continuous phase volume between droplets (m^3)
V_{neck}	volume of neck during squeezing (m^3)
V_{bypass}	volume of continuous phase bypassing the droplet during formation (m^3)

Chapter 5

Effect of Surfactants on Droplet Generation

The work presented in this chapter was submitted as an article:
Glawdel T., Ren C.L. "Model of Droplet Formation in Microfluidic T-junction Generators Operating in the Squeezing to Transition Regimes: Part 3 Dynamic Surfactant Effects", **Physical Review E**, submitted.

5.1 Introduction

The primary reason for adding surfactants is to reduce the interfacial tension and prevent unwanted coalescence of droplets (Joos 1999; Baret 2011; Erni 2011). A mixture of two immiscible phases is not thermodynamically stable because the minimum system energy occurs when the two phases reduce their interfacial area. This causes the two phases to separate from each other. Surfactants provide an energy barrier that hampers the process of coalescence thereby creating stable (or more correctly meta-stable) mixtures of the two phases. Preventing coalescence is a core requirement in many applications where long-term isolation of droplets is required.

In Chapter 4 a model was developed to describe the formation process of droplets with a T-junction generator operating in the transition regime. Surfactants were purposely omitted from those experiments to isolate the fluid dynamics of the formation process. The presence of surfactants adds additional complexity to the emulsification process. Because surfactants alter the interfacial tension, and the interfacial tension is one of the primary parameters governing drop formation, the transport of surfactant to the interface is an important aspect of the emulsification process. The rate that the interfacial tension changes depends on the characteristics of the surfactant (concentration, diffusion coefficient, micelle kinetics) and the mass transfer process including convection, diffusion, and dilation of the interface. Therefore, during the formation process the interfacial tension changes dynamically within the range bounded by the equilibrium interfacial tension of the pure liquids, and the equilibrium of the system with the added surfactant. In fact several techniques have been developed that utilize droplet formation at a small orifice (usually a capillary tube) to measure the adsorption process through the dynamic interfacial

tension. Examples include the drop volume method (Earnshaw, Johnson et al. 1996; Miller, Zholob et al. 1997; Miller, Bree et al. 1998), maximum bubble pressure method (Bendure 1971; Kloubek 1972; Christov, Danov *et al.* 2006), and growing drop method (Macleod and Radke 1993; Zhang, Harris et al. 1994).Generally, these techniques analyze drop formation at rather large orifices (250-1000 μm) and longer timescales (>0.5s) in comparison to the typical size (20-100 μm) and timescale (0.001-0.5 s) of microfluidic emulsification. In addition, droplets are usually formed via gravitational forces in a quiescent fluid in contrast to the high viscous shear and confined environment of microfluidic emulsification. Thus data obtained with these methods is not immediately transferrable to microfluidic applications

A more apt comparison to microfluidic emulsifications is membrane emulsifications as droplets are generated from tiny pores (5~50 μm) at extremely high rates (~1 kHz) (Joscelyne and Tragardh 2000; Charcosset, Limayem et al. 2004). A considerable amount of work has documented the effects of surfactant dynamics on the production of droplets from membranes including the relationship between dynamic interfacial tension and the size of droplets (Schroder, Behrend et al. 1998; Sugiura, Nakajima et al. 2004; van der Graaf, Schroen et al. 2004), the lag time between consecutive droplets (Geerken, Lammertink et al. 2007), and the number of active pores. An excellent numerical model by Rayner *et al.*, coupled together the evolution of the droplet shape (using Surface Evolver), the flow through the pore, and the adsorption of surfactants to achieve a complete description of the formation process (Rayner, Tragardh et al. 2005). In addition to the influence of the surfactant properties (concentration, diffusion coefficient), these studies revealed that the dispersed phase flux also has an important influence on the dynamic interfacial tension as it determines the degree of surfactant depletion at the interface due to the rate of surface expansion.

A few works have studied dynamic interfacial tension effects in microfluidic droplet generators. Experiments by van der Graaf *et al.* with T-junction generators, demonstrated that under low surfactant concentration droplet formation is comparable to when surfactants are absent indicating that, in most cases, droplet production is faster than surfactant adsorption. Only at high concentration of surfactants was a change in droplet production seen with smaller droplets being produced. Baret *et al.* studied the influence of surfactant kinetics on droplet stabilization by directly monitoring the adsorption of surfactants to the interface in an ingenious manner (Baret, Kleinschmidt et al. 2009). The authors synthesized a specialized oil soluble surfactant with a fluorescent probe attached to the hydrophilic tail of the surfactant. The probe only becomes active

when the tail is within the aqueous phase, such that changes in the fluorescent intensity correlate to surfactant concentration at the interface. Studies were performed with FC40 as the oil and a Krytox based surfactant which are commonly employed for biological applications in droplet microfluidics (Baret 2011). Experiments showed that the interface is nearly bare after the droplet is produced and coverage increases with time as the droplet travels down the microchannel. Coverage across the droplet is also non-uniform as surfactant accumulates near the back end of the droplet where a stagnation point exists. The authors were able to develop a scaling model based on the diffusion limited transport of micelles to the interface to estimate the incubation time needed to prevent coalescence. Good agreement was seen with experimental data, even though convective transport was not included.

The kinetics of adsorption have also been studied through the measurement of droplet production in microfluidic generators (van der Graaf, Steegmans et al. 2005; Nguyen, Lassemono et al. 2007; Steegmans, Warmerdam et al. 2009; Wang, Lu et al. 2009). Wang *et al.* used droplet size, and Nguyen *et al.* used frequency, to quantify the dynamic interfacial tension with microfluidic T-junction generators (Nguyen, Lassemono et al. 2007; Wang, Lu et al. 2009). Both of these studies focused on formation times in the millisecond range. Steegmans *et al.* looked at sub-millisecond effects by analyzing droplet production in a shallow Y-channel design with high flow rates (Steegmans, Warmerdam et al. 2009). These studies all used semi-empirical models to infer the interfacial tension from calibration curves first obtained with pure liquid/liquid combinations. Generally, the measured interfacial tension was far from the equilibrium value, even for small surfactants that were expected to adsorb quickly to the interface.

Having demonstrated the successful modeling of droplet production in microfluidic T-junction generators operating in the transition regime, we now seek to examine the behaviour when surfactants are present in the system. Using the same fluid combination as before (silicone oil, water) droplet formation is studied with the addition of surfactants using high speed video analysis. Two surfactants are studied, one with a small molecular weight that adsorbs quickly, and the other with a large molecular weight that adsorbs slowly. First, the surfactant experimental data is compared to the transition model developed in Chapter 4 to demonstrate the importance of dynamic interfacial tension. Then the dynamic interfacial tension is extracted using the force balance on the emerging droplet in the filling stage. Next, a theoretical model is developed to account for the mass transfer of surfactant to the interface during the formation process. From this

model the dynamic interfacial tension is calculated, which is then substituted back into the operational model of the T-junction generator to predict overall performance.

5.2 Experimental Methods

The same experimental setup was used as described previously in Chapter 4 Section 4.2.1. Homogeneous PDMS microchannnels were fabricated using standard soft lithography methods. Fluid flow was controlled by the Fluigent pressure system and high speed images were taken with the Phantom V210 camera. Experiments were limited to only two T-junction designs: the network layout (L_d:L_c:L_m=5:1:5 cm) and channel height was kept constant (h=45 μm, w_c=100 μm), and the dispersed inlet was varied (w_d=45,100 μm) to test the influence of T-junction design on the dynamic interfacial tension.

Table 5.1 List of parameters covered in each experiment with surfactants.

Exp #	Chip Design (A^*,h)*	Surfactant	Concentration (%w/v)
1-3	0.5, 0.5	SDS	0.5, 1.5, 3
4-6	0.5, 0.5	SDS	0.5, 1.5, 3
5-9	1, 0.5	Tween 20	0.1, 0.5, 2
10-12	1, 0.5	Tween 20	0.1, 0.5, 2

Experiments were performed with silicone oil as the continuous phase and different aqueous solutions of surfactant as the dispersed phase. Two surfactants were chosen for the experiments: sodium dodecyl sulphate (SDS) and Tween 20, both which are soluble in the aqueous phase. In particular, these two surfactants were chosen because they allow for a wide range of adsorption timescales to be investigated (Wang, Lu et al. 2009). SDS is a small anionic surfactant (M_w=288.4 g mol^{-1}) that diffuses quickly and Tween 20 is a relatively large non-ionic surfactant (M_w=1227.2 g mol^{-1}) that diffuses slowly. Three concentrations of each surfactant were tested in both T-junction designs: concentrations of 0.5, 1.5, 3% (w/v) SDS and 0.1%, 0.5%, 2% (w/v) for Tween 20. All of these solutions exceed the CMC by a significant degree: 2-12 x CMC for SDS and 10-200 x CMC for Tween 20. Table 5.1 summarizes the parameters studied in each experiment. For each experiment the flow rates of the two phases was varied to obtain different droplet size and speeds. Data was extracted from high speed videos in the same manner as described in Chapter 4 Section 4.3. Without surfactant the interfacial tension of pure water/ silicone oil was measured as 38.75±0.01 mN m^{-1}. For all Tween 20 combinations the interfacial tension was 9.38±0.1 mN m^{-1} and for all SDS solutions 10.34±0.1 mN m^{-1}. In addition, the

viscosity of each aqueous solution was measured; all solutions exhibited Newtonian behaviour with minimal deviation from pure water (~1 mPas).

5.2.1 Surfactant Properties

For the purpose of analysis it is important to know the properties of the two surfactants. At low concentrations surfactants remain soluble as monomers or dimers in solution. As the surfactant concentration increases, the physical properties abruptly change at a critical concentration known as the critical micelle concentration (CMC). Surfactant monomers arrange themselves into aggregates of tens to hundreds of molecules with their apolar tails oriented toward the center to reduce energy requirements (Joos 1999). Generally, aggregates form spherical structures, however, rod-like structures and other complex structures can form depending on the concentration and environmental conditions (Rosen 1989; Eastoe and Dalton 2000). The specific number of monomers contained in a micelle is called the aggregation number, N_A. Above the CMC, the concentration of monomers remains relatively stable, and only the concentration and structure of micelles changes. In modeling surfactant transport it is important to know the diffusion coefficient of the molecules, the CMC and the aggregation number of the micelles. This data was taken from the literature.

The reported diffusion coefficient for premicellar concentrations of SDS is approximately 8.0 $x10^{-10}$ m^2s^{-1} (Mikati and Wall 1993). Recent studies using the Fourier transform pulsed field gradient NMR method decomposed the average diffusion coefficient into diffusion coefficients of $11.2x10^{-10}$ m^2s^{-1} for monomers and 4.65 $x10^{-11}$ m^2s^{-1} for dimers (Zuev, Kurbanov et al. 2007). A CMC of 2.41 g L^{-1} was reported with an aggregate size between 49.5-100 monomers. Generally, micelle size and polydispersity increase with concentration above the CMC (Bales, Messina et al. 1998). Tween 20, also known as Polysorbate 20, is a non-ionic surfactant consisting of a complex mixture of oglimers with an average molecular weight of 1227.2 g mol^{-1}. Mass spectrometry reveals that the composition consists of approximately 50% polysorbate monolaurates, with the remainder consisting of myristates, palmitates, and stearates (Ayorinde, Gelain et al. 2000). Older studies made 40 years ago measured the CMC of Tween 20 around 0.06 g L^{-1}, however, recent studies place the CMC closer to 0.116 g L^{-1} (Mahler, Printz et al. 2008) and 0.135 g L^{-1}(Nino and Patino 1998; Wu, Xu et al. 2006) and the aggregation number between 24-29 monomers (Tiefenbach, Durchschlag et al. 1999). The discrepancy is possibly due to changes in the manufacturing of the commercial product or batch to batch variation due to the heterogeneous composition (Nino and Patino 1998). Pre-micellar diffusion coefficients for Tween 20 measured

using the surface pressure technique range from 1.9 to 0.3 x10^{-10} m^2s^{-1} for low concentration to concentrations near the CMC. The decrease in diffusion coefficient with concentration even below the CMC may be due to the increasing presence of dimers in the pre-micellar solution. The properties of the two surfactants are summarized in Table 5.2.

Table 5.2 Molecular formula, molecular weight (M_w), critical micelle concentration (c_{CMC}) , aggregation number N_A, and diffusion coefficient (D) for the surfactants SDS and Tween 20.

Surfactant	Molecular Formula	M_w ($g\,mol^{-1}$)	c_{CMC} ($g\,L^{-1}$)	N_A	D (10^{-10} m^2s^{-1})
SDS	$C_{12}H_{25}OSO_3Na$	288.4	2.41[a]	49.5-100[a]	8.0[b]-11.2[c]
Tween 20	$C_{58}H_{114}O_{26}$	1227.2	0.04[d]-0.138[e]	24-29[f]	0.3-1.9[f]

[a] (Bales, Messina *et al.* 1998), [b] (Mikati and Wall 1993), [c] (Zuev, Kurbanov *et al.* 2007), [d] (Wan and Lee 1974), [e] (Mahler, Printz *et al.* 2008), [f] (Tiefenbach, Durchschlag *et al.* 1999)

5.3 Experimental Observations

The experimental study covered Capillary number range of 0.003-0.02 with droplet formation times from 10-200 ms. Within these limits the T-junction generator is expected to operate in the transition regime. Figure 5.1 shows the typical drop formation sequence when surfactants are present for both T-junction designs used in experiments. Based on qualitative observations there is no obvious difference in the evolution of the interface as compared to the case when surfactants are absent (refer to Figure 4.8 in Chapter 4). The only noticeable difference is that the lag stage is extremely short; in fact, it is nearly non-existent for all cases that were studied. This is due to the lower interfacial tension associated with surfactant which weakens the pull-back velocity at pinch-off (refer to Eqn. 4.15).

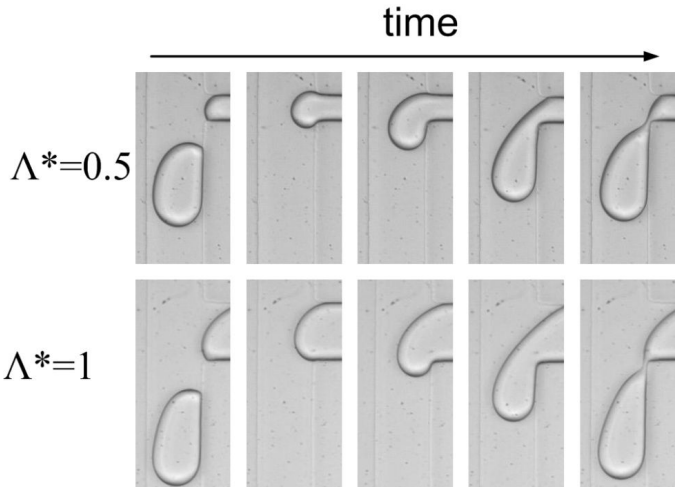

Figure 5.1 Series of micrographs showing the formation of droplets with 1.5% SDS in 1:2 and 1:1 T-junction designs.

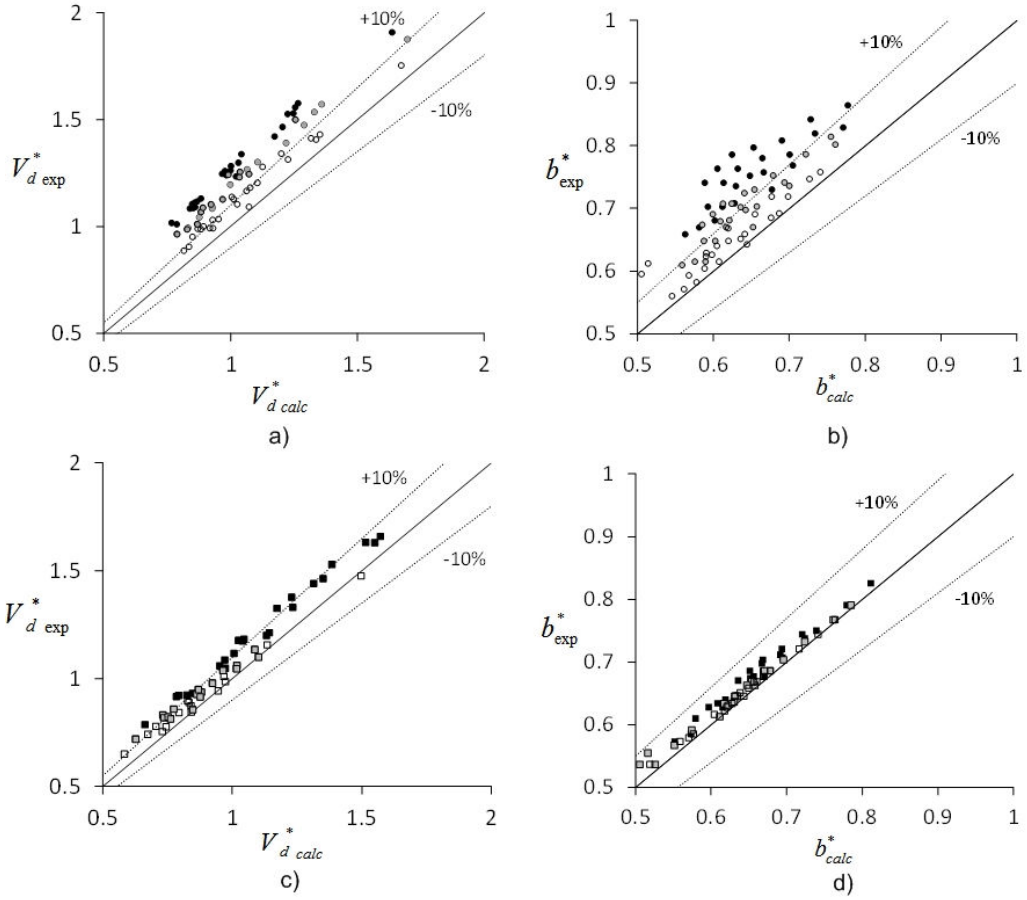

Figure 5.2 Parity plots of the calculated droplet volume and b^*_{fill} to experimental data using the static interfacial tension. (a)(b) ○ Tween 20 (black) 0.1% (grey) 0.5% (white) 2%. (c)(d) □ SDS (black) 0.5%, 1.5%, and 3%.

It is first prudent to quantify the degree to which dynamic interfacial tension influences the droplet formation process. For this reason, experimental data with the surfactants was compared

to the expected values from the operational model developed in Chapter 4 using the equilibrium interfacial tension in the calculations. Parity plots comparing the experimentally measured droplet volume V_d^* and penetration depth b_{fill}^* to the model are presented in Figure 5.2. One can clearly see that the previous model systematically under predicts the operation of the T-junction generator when the equilibrium interfacial tension is used. Essentially, larger droplets are formed than expected which suggests that the interfacial tension during formation is greater than the equilibrium value. Deviations from the model are more pronounce for Tween 20 than SDS because of the lower adsorption rate of the former over the later. In addition, for each surfactant, deviations decrease with increasing surfactant concentration. More importantly, this data shows that dynamic interfacial effects must always be considered when modeling microfluidic droplet generators, even for a small, fast adsorbing surfactant such as SDS (Steegmans, Warmerdam et al. 2009; Wang, Lu et al. 2009).

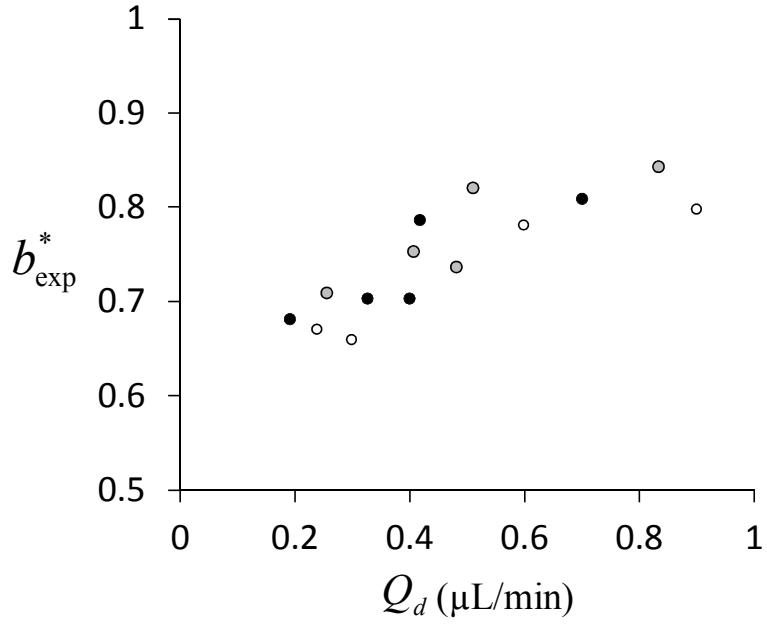

Figure 5.3 Variation of b_{fill}^* versus incoming dispersed flow rate Q_d. Data corresponds to T-junction with 1:2 0.1% Tween 20 for ○(black) Q_c=1.5-1.9 μL min^{-1}, (grey) Q_c=1.9-2.3 μL min^{-1}, and (white) Q_c=2.3-2.8 μL min^{-1}.

Droplet formation is associated with a large change in the shape and area of the emerging interface. For an expanding interface the dynamic interfacial tension depends on the dilation rate; a greater dilation rate results in lower surfactant coverage and thus higher interfacial tensions. In the case of the T-junction generator, the dilation rate is directly proportional to the incoming flow

of the dispersed phase, Q_d. Figure 5.3 plots the variation in b^*_{fill} against Q_d for a constant surfactant concentration of Tween 20 with small ranges of Q_c. One can see that there is a significant correlation between b^*_{fill} and Q_d. Recall that b^*_{fill} is derived from a force balance on the emerging droplet consisting of the pressure force deforming the droplet and the interfacial tension resisting deformation as derived previously in Chapter 4 Section 4.5.10:

$$\frac{h^*}{Ca} = \frac{1}{2}\frac{L^*_{eff}\, g\left(\eta, \lambda_{gap}\right)}{\left(A^*_{gap}\overline{u}^*_{gap}\right)}\frac{b^*_{fill}}{\left(2 - b^*_{fill}/R^*_n\right)} \tag{5.1}$$

Note that within this expression Q_d is not included, and in Chapter 4 comparisons with experiments confirmed the weak dependence on Q_d when surfactants were absent. Therefore, the observed influence of Q_d on the force balance is expected to be caused by the change in the dynamic interfacial tension during the formation process. If b^*_{fill} and the flow conditions are known, then it seems reasonable that Eqn. 5.1 can be rearranged to extract the *apparent* interfacial tension at the end of the filling stage form the experimental data:

$$\frac{\gamma}{\gamma_{eq}} = \frac{1}{2}\frac{L^*_{eff}\, g\left(\eta, \lambda_{gap}\right)}{\left(A^*_{gap}\overline{u}^*_{gap}\right)}\frac{b^*_{fill}}{\left(2 - b^*_{fill}/R^*_n\right)}\frac{Ca}{h^*} \tag{5.2}$$

where *Ca* is calculated using the equilibrium interfacial tension.

Before discussing the results of the dynamic interfacial tension measurement it is sensible to emphasize the use of the word "apparent", as many suppositions are made when using Eqn. 5.2. First, it is important to note that Eqn. 5.2 was derived with the condition that the interface acts as a fully mobile interface (slip boundary condition). However, when surfactant coverage in not uniform, interfacial tension gradients arise which lead to Marangoni stresses that can oppose the direction of flow. Additional gradients may form if the dilation rate is not uniform across the interface or gradients in shear exist along the surface (Erni 2011). Under certain conditions the stresses may cause the interface to act like a solid (no slip condition) (Baret 2011). If this is the case, then Eqn. 5.3 can be reformulated by developing new expressions for $\overline{u}^*_{gap}$ with the no-slip boundary condition on the interface. However, under high surfactant concentrations, and fast adsorption kinetics, gradients are minimal and the interface may remain remobilized (Stebe, Lin et al. 1991; Stebe and Maldarelli 1994; Eggleton and Stebe 1998; Joos 1999; Martin and Hudson 2009).

For the experiments in this study, it is not immediately clear if Marangoni effects are important, as high concentration of surfactants are used (well above the CMC), and surfactants are added to the dispersed phase where strong circulation exists. It also appears that the dilation rate across the interface is non-uniform. Based on observations of the video evidence it appears that the front half experiences a larger expansion rate than the back half of the droplet. If this is the case, then the interfacial tension will be greater at the front than the back of the droplet, which suggests that Marangoni stresses may actually operate *favourably*, in the direction of flow. Analysis of such effects would require a detailed numerical study that couples surfactant transport with interface deformation and flow of the dispersed and continuous phases (Eggleton and Stebe 1998; van der Graaf, Nisisako et al. 2006; van der Sman and van der Graaf 2006). Such an analysis is beyond the scope of this current study, instead, the focus will be on evaluating how far we can extend the operational model to include dynamic interfacial effects.

Figure 5.4 presents the apparent interfacial tension for Tween 20 and SDS solutions for both T-junction designs as function of $t_{fill}^{-1/2}$, where $t_{fill} = V_{fill}/Q_d$. Plotting dynamic interfacial tension data in this manner is standard practice since loading of the interface generally scales with $t_{fill}^{-1/2}$ for both diffusive and convective transport of surfactants (Joos 1999). It should be stated that the error in the extraction of the interfacial tension is quite significant. Because the relation between b_{fill}^{*} and γ is highly non-linear ($\gamma \propto b_{fill}^{*\,-3}$), even small errors in b_{fill}^{*} propagate into larger errors in γ. The error in measuring b_{fill} from videos is estimated to be ±1 pixel; the error bars in Figure 5.4 represent this estimated variance in the calculation of γ from Eqn. 5.2.

As expected, the dynamic effects are more pronounced in the Tween 20 solutions as compared to the SDS solutions and increasing the surfactant concentration reduces the dynamic interfacial tension effects. For the lowest concentration of Tween 20 (0.1%), which is still ten times above the CMC, the apparent interfacial tension is somewhere between 150-300% of the equilibrium value. In fact, the higher end of this range is closer to the bare interface ~38 mN m than to the equilibrium value ~9.3 mN m. Even for the lowest concentration of SDS, which is 2 times the CMC, the apparent interfacial tension is 20% higher than the equilibrium value. Additionally, for

the same surfactant concentration, dynamic interfacial effects are slightly more pronounced in the T-junction design with the smaller inlet (1:2) than the large inlet (1:1). This suggests that the design of the T-junction generator plays an important role in the dynamic interfacial tension as well. Base on these observations, a theoretical model was developed to explain the relationship between the various parameters and the dynamic interfacial tension.

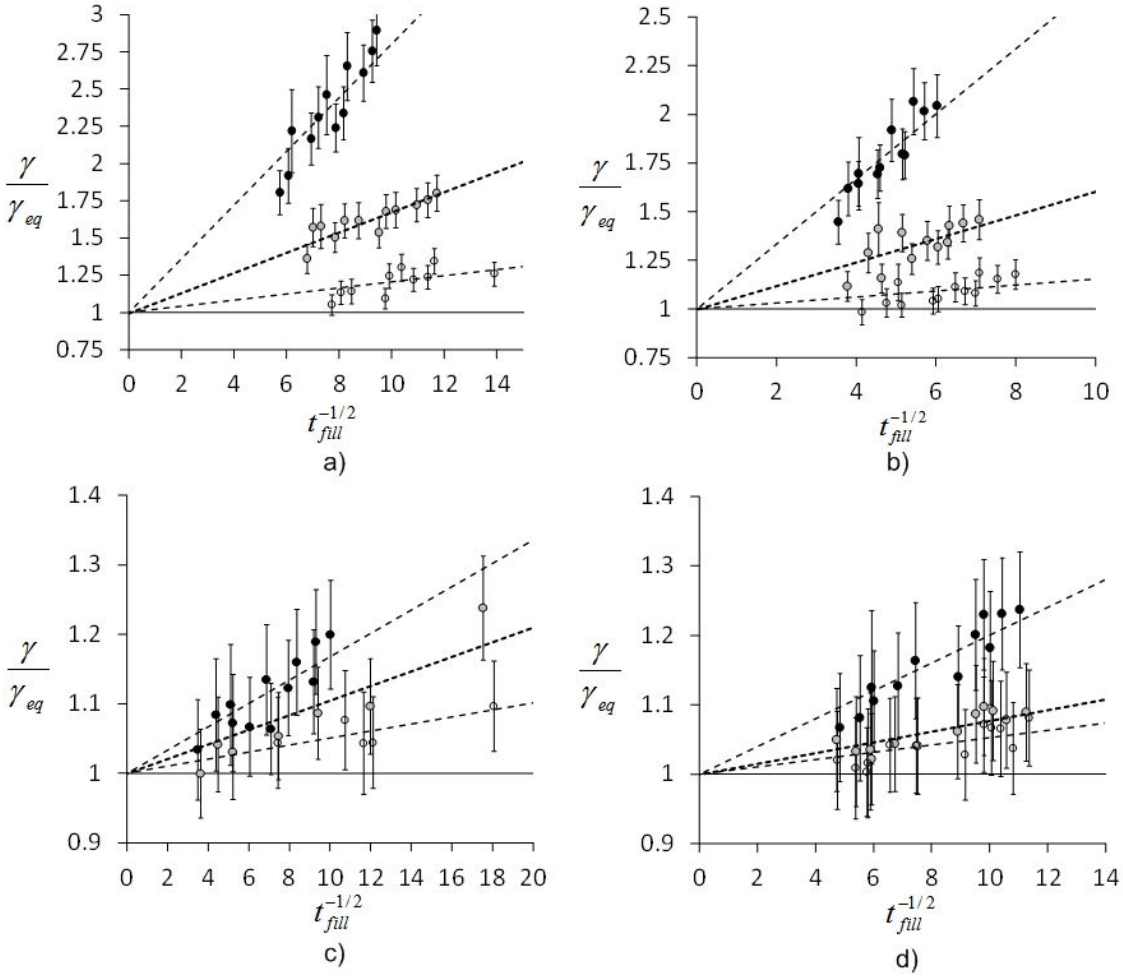

Figure 5.4 Plots of the apparent dynamic interfacial tension extracted from video analysis using Eqn. 5.2. (a) Tween 20 experiments with 1:2 T-junction design (black) 0.1%, (grey) 0.5% (white) 2% (b) Tween 20 with 1:1 T-junction design (c) SDS with 1:2 T-junction design (black) 0.5%, (grey) 1.5%, white (3%) (d) SDS with the 1:1 T-junction design. Error bars are associated with the ±1 pixel error for b_{fill}^{*} measured from the videos.

5.4 Model of Surfactant Adsorption to Expanding Interfaces

When modeling surfactant adsorption, the modeling domain is generally divided into three parts consisting of the interface, the sub surface and the bulk as depicted in Figure 5.5. The subsurface

is an imaginary plane a few molecular diameters above the interface whereby surfactant molecules can adsorb to the interface without further transport. Two mechanisms are often used to describe the adsorption process (Joos 1999; Eastoe and Dalton 2000). In the first case, surfactant molecules that reach the subsurface adsorb instantaneously, such that diffusion is considered the rate controlling step. On the opposite spectrum, in what is termed mixed-kinetic modeling, it is the transfer of molecules from the subsurface to the interface that limiting. Under such conditions, surfactants that reach the subsurface experience a barrier that they must overcome before they can adsorb. A number of factors may contribute to this barrier, and a few examples include the depletion of "vacant" sites as the interface becomes saturated, steric restraints on the molecule, or that a molecule must approach the interface in the correct orientation (Eastoe and Dalton 2000). These processes increase the degree of back-diffusion into the bulk as there is a lower probability that a surfactant molecule will adsorb once it reaches the subsurface.

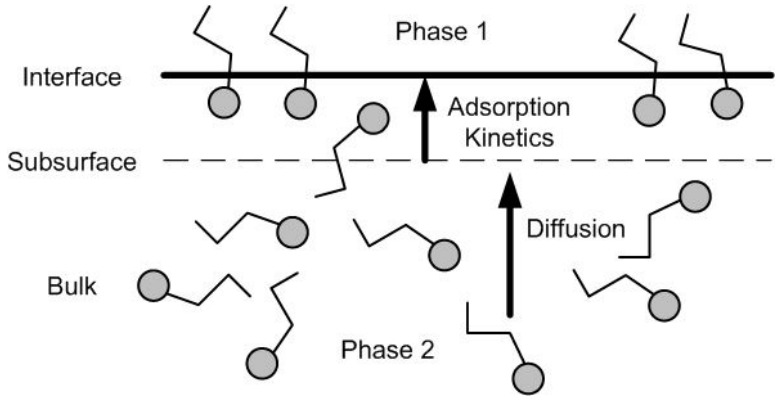

Figure 5.5 Model of surfactant adsorption to an interface with the division of the interface, subsurface and bulk. Schematic adapted from (Eastoe and Dalton 2000)

The decrease in interfacial tension is directly related to the number of surfactant molecules that adsorbed to the interface as defined by the Gibb's isotherm (Joos 1999; Eastoe and Dalton 2000):

$$\Gamma = -\frac{1}{nRT}\frac{\partial\gamma}{\partial \ln c} \tag{5.3}$$

where Γ is the excess surface concentration of surfactant (mol m^{-2}), R is the gas constant (8.314 $J\,K^{-1}\,mol^{-1}$), T the temperature in Kelvin, γ the interfacial tension (N m) and c the concentration of surfactant in the bulk (mol m^{-3}), and $n=1$ for neutral surfactants and $n=2$ for ionic surfactants in the absence of excess electrolytes (Eastoe and Dalton 2000). This equation can be integrated if the relationship between the surface concentration and the bulk concentration are known. For this purpose the Langmuir isotherm is often used, which is based on a Lattice type model with a

maximum number of sites available for adsorption, Γ_∞. Substitution results in the Langmuir-Frumkin equation of state (Eastoe and Dalton 2000):

$$\gamma - \gamma_0 = -nRT\Gamma_\infty \ln\left(1 - \frac{\Gamma}{\Gamma_\infty}\right) \tag{5.4}$$

where γ_o is the interfacial tension for the two phases in the absence of surfactants. For concentrations above the CMC the interfacial tension is constant and the surface coverage approaches Γ_∞. Eqn. 5.4 is only applicable when the interface is at equilibrium, under dynamic conditions the adsorption must be modeled by also including the convective and diffusive transport of surfactant monomers.

Adsorption of surfactants is driven by the concentration gradient created between the subsurface and the bulk as molecules are transferred to the interface (Joos 1999). If diffusion is the rate controlling step, then the boundary condition for the conservation of mass at the interface is:

$$\frac{\partial \Gamma}{\partial t} + \Theta\Gamma = D\left(\frac{\partial c}{\partial z}\right)_o \tag{5.5}$$

where z the co-ordinate normal to the surface, c the concentration in the bulk, D the diffusion coefficient and Θ the dilation rate. Alternatively, Eqn. 5.5 can be reformulated for cylindrical or spherical co-ordinate systems (Joos 1999), however, the process is usually not necessary as the diffusion penetration depth $l_D \sim (\pi Dt)^{1/2}$ is usually much smaller than the radius of curvature. However, this assumption may fail for droplets of small diameter (<70um) with low concentrations of surfactant, as the diffusion boundary layer will approach the size of the droplet (Jin, Balasubramaniam et al. 2004). Under such conditions, the following derivations need to be modified to account for kinetic controlled adsorption (Joos 1999; Baret, Kleinschmidt et al. 2009).

Based on Eqn. 5.5, the difference between the increase in coverage due to surface area changes, Θ, and diffusive transport $D\left(\partial c/\partial z\right)_o$ determines the change in coverage of the interface. For an expanding interface the dilation rate is positive, thus it represents a depletion of surface coverage in the mass transfer process. Figure 5.6 illustrates the two extreme situations that may occur. When the rate of expansion is high, diffusion is not able to supply the interface with enough surfactant, hence the coverage decreases and the interfacial tension approaches that of the natural

oil/water interface. Conversely, at low expansion rates the supply is sufficient and the interfacial tension does not change significantly.

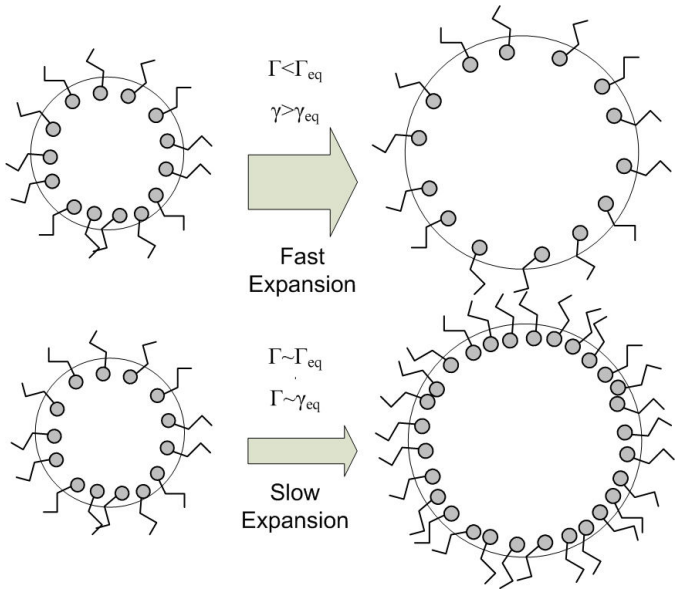

Figure 5.6 Schematic of the effect of interface expansion or contraction on the surfactant transport and interfacial tension. Drawing adapted from (Eastoe and Dalton 2000)

Joos and Vanuffelen demonstrated that Eqn. 5.5 can be integrated using Laplace Transformations and arranged into a form similar to the classical Ward and Tordai (Ward and Tordai 1946) equation for diffusion (Joos and Vanuffelen 1993; Vanuffelen and Joos 1993; Joos 1999):

$$\Gamma(\tau)f(t)=\Gamma_o+2\left(\frac{D\tau}{\pi}\right)^{1/2}c_o-2\left(\frac{D}{\pi}\right)^{1/2}\int_0^{\sqrt{\tau}}c_s(\tau-\lambda)d\sqrt{\lambda} \tag{5.6}$$

where c_o is the bulk concentration and c_s the subsurface concentration, Γ_o the initial surface coverage, λ is an integration variable and $f(t)=A(t)/A_o$ and $\tau=\int_0^t f(t)^2\,dt$ .To achieve the Ward and Tordai equation *f(t)=1*. The difficulty associated with solving Eqn. 5.6 analytically is caused by the convolution integral on the right hand side which accounts for the back diffusion of surfactants from the interface (Eastoe, Dalton et al. 1997). For small deviations from equilibrium, Joos and Vanuffelen linearized Eqn. 5.6 under the assumption of a diffusion limited reaction, and found an equation for the jump in interfacial tension based on the "long time" approximation (i.e. close to equilibrium surface coverage) (Joos and Vanuffelen 1995):

$$\gamma(t)-\gamma_{eq}=\Delta\gamma(t)=[f(t)-1]\left[1+\frac{\zeta}{f(t)-1}\right]\frac{nRT\Gamma^2}{c}\sqrt{\frac{\pi}{4\tau D}} \tag{5.7}$$

where, $\zeta = 1 - \Gamma_o / \Gamma_{eq}$ is the initial surface coverage. If the interface begins at equilibrium then $\Gamma_o = \Gamma_{eq}$, and Eqn. 5.7 reduces to:

$$\Delta\gamma(t) = [f(t) - 1]\frac{nRT\Gamma^2}{c}\sqrt{\frac{\pi}{4\tau D}} \tag{5.8}$$

These equations, however, are only valid for sub-micellar solutions and equations for micellar solutions are needed to compare with experimental conditions in this study. Because of their structure, micelles themselves are not surface active, given that they are unable to straddle the two-phase interface. Only suspended monomers can adsorb to the interface. However, micelles still play an important role in enhancing monomer transport to the interface. At an expanding interface there is a continuous transport of monomers from the bulk to the sub surface as the exposed area increases with time. As a result, there is a local depletion of monomers which breaks the equilibrium between monomers and micelles, causing micelles to break apart, and thereby releasing more monomers into the solution (Joos 1999). In turn, the disintegration of micelles also creates a local depletion of micelles, and therefore micelles will also diffuse from the bulk into this region as well. Consequently, the diffusion of monomers and micelles is coupled, and the process is described by a chemical reaction that includes the diffusion of each component and the micellisation and demicellisation kinetics (Joos 1999) as schematically represented in Figure 5.7.

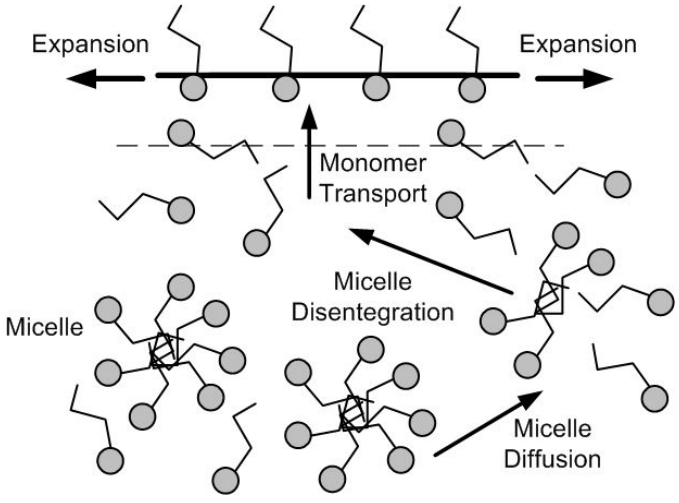

Figure 5.7 Schematic of the process of enhanced transport of monomers to an expanding surface by the disintegration of micelles in solution.

To account for the contribution of micelles in the surfactant transport, an effective diffusion coefficient that replaces the diffusion coefficient in Eqn. 5.8, is often used based on the assumption that micelization kinetics are fast compared to diffusion (Joos 1999):

$$D_{eff} = D(1+\beta)(1+\beta\sigma^2) \tag{5.9}$$

where D is the diffusion coefficient of the monomers, $\beta = c_o / c_{CMC} - 1$ and $\sigma = N_A^{-1/3}$. The result is that the effective diffusion coefficient is much larger than the component monomers and that the diffusion coefficient increases with increasing concentration of surfactant. Actually, Eqn. 5.9 is fairly simplistic representation of the micelization process, more comprehensive models account for the polydispersity of the micelles and the many different pathways of the micelization reaction (Noskov 2002; Christov, Danov et al. 2006; Fainerman, Mys et al. 2006); still, it should serve as an adequate depiction for this first approximation.

Modifications to the interfacial tension jump to include micelles results in:

$$\Delta\gamma(t) = [f(t)-1]\frac{RT\Gamma_{CMC}^2}{c_{CMC}}\sqrt{\frac{\pi}{4\tau D_{eff}}} \tag{5.10}$$

where c_{CMC} is the concentration and Γ_{cmc} the surface coverage at the CMC. For micellar solutions these parameters are constant above the CMC and the only parameter that changes with added concentration of surfactant is the effective diffusion coefficient. Therefore Eqn. 5.10 provides an estimate for the dynamic interfacial tension to an expanding interface. In order to solve Eqn. 5.10 for the T-junction generator, an expression for the temporal evolution of the interfacial area, *A(t)*, is still needed. Such an expression for the T-junction generator is derived next.

5.4.1 Approximation for *A(t)* for the T-junction

The area of the emerging interface during the filling stage is approximated using the definitions provided in Figure 5.8.The shape of the interface is again described by as two parts with the back half defined by a quarter circle of radius *b*, and the front half by a half circle of radius *b/2*. In the following analysis, out of plane curvature effects are neglected for the purpose of simplifying the problem.

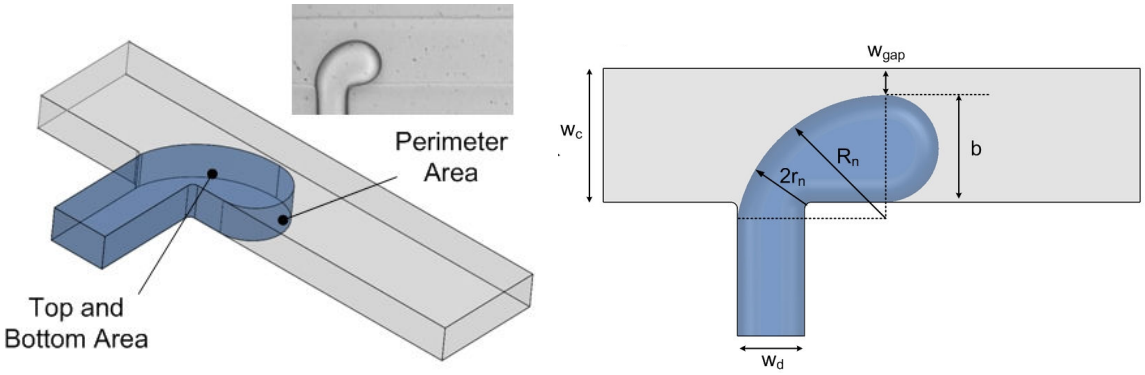

Figure 5.8 Diagram of the approximated area of the droplet from the projection of the 2D image.

Assuming that the flow rate remains constant throughout the formation process, the volume of the emerging droplet is given as:

$$V(t) = \frac{3\pi}{8} b(t)^2 h = Q_d t \tag{5.11}$$

In the representation given in Figure 3, the surface area of the drop consists of the top and bottom surfaces and the area defined by the perimeter:

$$A(t) = 2\frac{3\pi}{8} b(t)^2 + \pi h b(t) + A_o \tag{5.12}$$

where A_o is the initial area of the interface before the onset of expansion which, for T-junction designs, may be approximated as the cross-sectional area of the dispersed channel $A_o = w_d h$. In a previous derivation by van der Graaf *et al*. ,the top and bottom areas were neglected under the assumption that exposure to the surfactant occurs primarily along the perimeter- a reasonable assumption if the surfactant is contained within the continuous phase(van der Graaf, Steegmans et al. 2005). Here the top and bottom surfaces are included because in the current study surfactant was added to the dispersed phase instead. However, it should be noted that even if surfactant is added to the continuous phase, the top and bottom surfaces may still play an important role. Gradients in adsorption correspond to gradients in interfacial tension which are leveled out quickly due to Marangoni effects (Joos 1999). Although the top and bottom surfaces are not exposed to a bulk of the surfactant, readjustment along the surface causes them to still act as a sink , and therefore the following calculations should be an improvement over those of van der Graaf *et al* .(van der Graaf, Steegmans et al. 2005)

Substituting Eqn. 5.11 into Eqn. 5.12 the change in area as a function of time is:

$$A(t) = 2\frac{Q_d t}{h} + \left(\frac{8\pi}{3} Q_d h t\right)^{1/2} + A_o = A_o\left[1 + f_1 t + f_2 t^{1/2}\right] \tag{5.13}$$

With $f_1 = 2\frac{Q_d}{A_o h}$ and $f_2 = \frac{1}{A_o}\left(\frac{8\pi}{3} Q_d h\right)^{1/2}$. The dilation rate is given as $\Theta = \frac{1}{A(t)}\frac{\partial A}{\partial t}$,

where upon substitution of the previous equations:

$$\Theta = \frac{\left(f_1 + \frac{f_2}{2} t^{-1/2}\right)}{1 + f_1 t + f_2 t^{1/2}} \tag{5.14}$$

In the limit $f_1 >> f_2$, or essentially if the top and bottom areas are larger than the perimeter area, the equation reduces to $\theta = \frac{f_1}{1 + f_1 t}$, and a step further, if the initial area is negligible, then $\theta = \frac{1}{t}$.

In the opposite limit of $f_2 >> f_1$, $\theta = \frac{f_2}{2t^{1/2} + 2 f_2 t}$, and if the initial area is negligible $\theta = \frac{1}{2t}$.

However, under most condition in the T-junction design $f_1 \sim f_2$ and so neither of these limits is reached which leaves the more complex function of Eqn. 5.14 for the dilation rate.

To help simplify the problem, the term $f_2 t^{1/2}$ can be linearized using a first order Taylor expansion around time t_o:

$$f_2 t^{1/2} \approx \frac{f_2}{2 t_o^{1/2}} t = \left(\frac{8\pi}{3} Q_d h\right)^{1/2} \frac{t}{2 A_o t_o^{1/2}} \tag{5.15}$$

For convenience, $t_o = 1/f_1$ is chosen as the characteristic time, and upon substitution into Eqn. 5.15 the linearized term becomes:

$$f_2 t^{1/2} \approx f_1\left(\frac{h^2}{A_0}\right)^{1/2} \tag{5.16}$$

Then the area change becomes:

$$A(t) = A_o\left[1 + f_3 t\right] \tag{5.17}$$

where $f_3 = f_1\left(1 + \left(h^2/A_o\right)^{1/2}\right)$, and thus the dilation rate is then simply:

$$\Theta = \frac{f_3}{1 + f_3 t} \tag{5.18}$$

To verify these approximations, Eqn. 5.17 and Eqn. 5.18 are plotted against experimental data as shown in Figure 5.9. This data was obtained by extracting the area change using the approximation presented in Figure 5.8 for each video frame, $A_{\exp} = 2A_{proj} + L_{perm} h$. Data is plotted for high and low Capillary number conditions for both T-junction designs. One can see that the surface area of the droplet increases at a linear rate in the filling stage and then accelerates during the necking stage. Furthermore, the dilation rate decreases quickly during the filling stage decaying to a constant value in the necking stage. The fits provided by Eqn. 5.17 and 5.18 agree well with the experimental data, especially in the filling stage for the dilation rate where we are most interested in capturing the interface expansion effects.

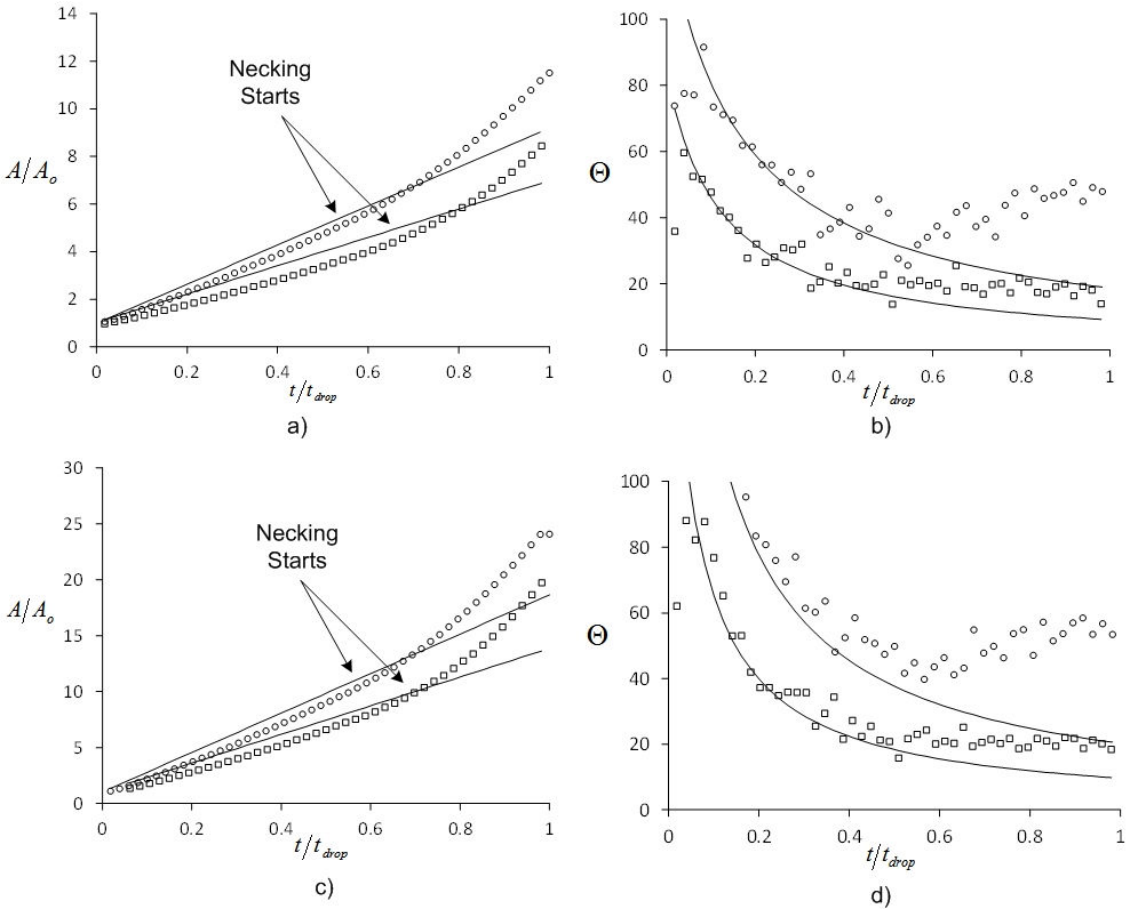

Figure 5.9 Area change and dilation rate extracted from video analysis of droplet formation. (a),(b) T-junction Λ^*=0.5 h^*=0.5 with silicone oil and 1.5%SDS water with conditions of □ *Ca*=0.049 , b^*_{fill}=0.79, *f*=17.8Hz. ○ *Ca*=0.015 b^*_{fill}=0.645, *f*=42.8 Hz. (c)(d) T-junction Λ^*=1 h^*=0.5 with silicone oil and 0.5% SDS water with conditions of □ *Ca*=0.0048 , b^*_{fill}=0.741, *f*=9.66 Hz. ○ *Ca*=0.0149 b^*_{fill}=0.598, *f*=20.9Hz. Solid black lines are calculations from Eqn. 5.17 and Eqn. 5.18.

The interfacial tension jump can then be calculated for a T-junction generator:

$$\Delta\gamma(t) = \frac{nRT\Gamma_{CMC}^2}{c_{CMC}} \sqrt{\frac{3\pi}{4D_{eff}}} \sqrt{\frac{f_3^2 t}{(f_3 t)^2 + 3f_3 t + 3}} \tag{5.19}$$

Eqn. 5.19and Eqns. 5.13-5.18 demonstrate that for a given surfactant (c_{cmc}, D_{eff}, Γ_{cmc}), the dynamic interfacial tension depends on the shape of the T-junction generator (A_o, h) and the flow rate of the dispersed phase (Q_d) in agreement with experimental observations described previously. One should note that in applying Eqn. 5.19 it is assumed that the interface is at equilibrium before expansion starts. In reality, this condition may not be met in a droplet generator when droplets are formed at high rates and the interface does not have time to rest. It should also be stated that the analysis has not included additional transport effects that might enhance adsorption such as internal circulation within the droplet. These two effects are difficult to quantify within an analytical model, but should be recognized as having a potential influence on the dynamic interfacial tension.

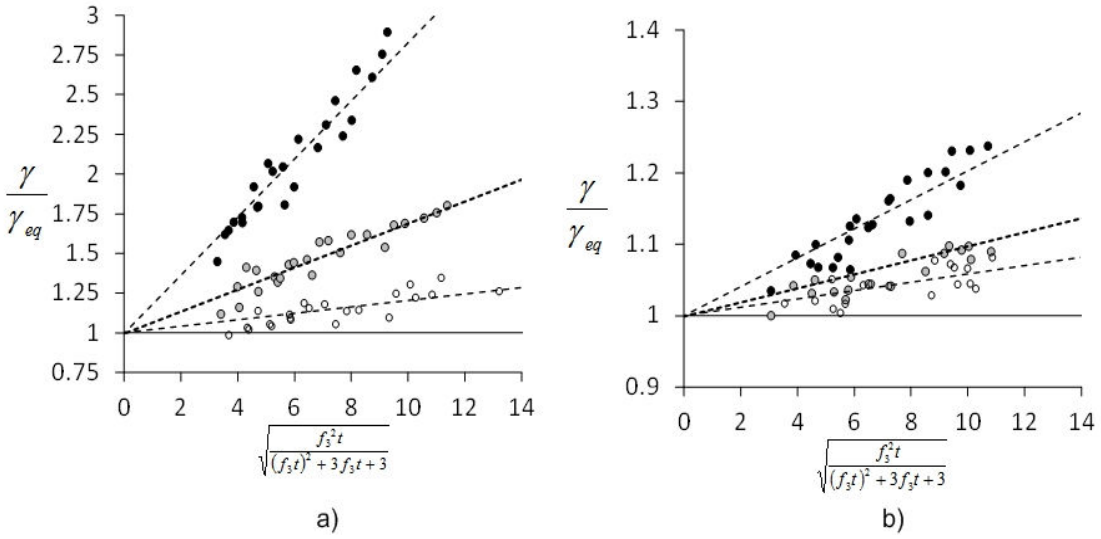

Figure 5.10 Plot of combined data from both 1:2 and 1:1 Tjunction designs for the dynamic interfacial tension versus the temporal term in Eqn 3. (a) Tween 20 with (black) 0.1%, (grey) 0.5% and (white) 2% (b) SDS (black) 0.5%, (grey) 1.5% and (white) 3%. Dashed lines are linear fits to the data used to extract the slope. Solid line represents an interfacial tension equal to the static interfacial tension. Error bars are omitted for clarity but are the same scale as those in Figure 3.

5.5 Model Validation with Experimental Data

The data from both T-junction generators should collapse onto the same curve when plotted against the temporal term in Eqn. 5.19 as the slope is dependent only on the properties of the

surfactant. Figure 5.10 confirms this hypothesis, indicating that the equation developed for *A(t)* is correct. Next the slopes from these curves can be used to compare with the estimated slopes given by the surfactant properties listed previously in Table 5.2. Table 5.3 provides the comparison between the measured and calculated slopes. As part of these calculations a typical surface excesses coverage of Γ_e=3-4x10^{-6} mol m^{-2} was used for SDS and 1.5-2.5x10^{-6} mol m^{-2} for Tween 20 (Fainerman, Mobius et al. 2001). As can be seen, the measured slopes fall within the anticipated range calculated from the surfactant properties, though the calculated range is rather large because of the ambiguity surrounding many of the surfactant properties.

Table 5.3 Comparison of slopes extracted from Figure 5.10 and the range calculated from Eqn. 5.19 using surfactant properties found in the literature.

Surfactant	Tween 20 0.1%	Tween 20 0.5	Tween 20 2%	SDS 0.5%	SDS 1.5%	SDS 3%
Slope	0.2023	0.07310	0.0204	0.0203	0.0098	0.0059
$\frac{nRT\Gamma_{CMC}^2}{\gamma_{eq}c_{CMC}}\sqrt{\frac{3\pi}{4D_{eff}}}$	0.180005-0.500014	0.037945-0.10540	0.009586-0.026629	0.015864-0.028202	0.007869-0.015402	0.006831-0.012144

The analysis has shown that the theory developed herein can be used to predict the influence of dynamic interfacial tension on the droplet formation process. One can understand the influence of surfactant properties, T-junction design and operating conditions on the dynamic interfacial tension. In the following section, this new model for the dynamic interfacial tension is adapted to the model for droplet generation in Chapter 4.

5.5.1 Modification to the Droplet Formation Model

For the calculation of b^*_{fill}, the dynamic interfacial tension is updated at each iteration step until convergence occurs for the force balance. Iteration starts by selecting a low value for b^*_{fill}, and then the volume of the droplet is calculated using the 3D shape calculation for the filling stage in Chapter 4 (Eqns.4.23,4.24). Next, the formation time is calculated as $t=V_d/Q_d$, where Q_d is known, and the dynamic interfacial tension is calculated from Eqn. 5.19. This value is then substituted into the force balance to check if convergence is met. If not, then b^*_{fill} is increased by a small amount and the process repeats.

Calculation of the pinch-off point also includes the interfacial tension as a parameter; however, due to extensive coupling between the final moment of pinch-off, and the ratio of the two-flow rates that determine the necking period it is difficult to predict the dynamic interfacial tension at pinch-off. For simplicity, the dynamic interfacial tension is calculated from Eqn. 5.19 with $t_{neck}=2t_{fill}$ and then this value is substituted into the calculation for the critical pinch-off point. Without further modifications, the amalgamated model was used to predict the complete operation of the T-junction generator using the slopes obtained in Table 5.3.

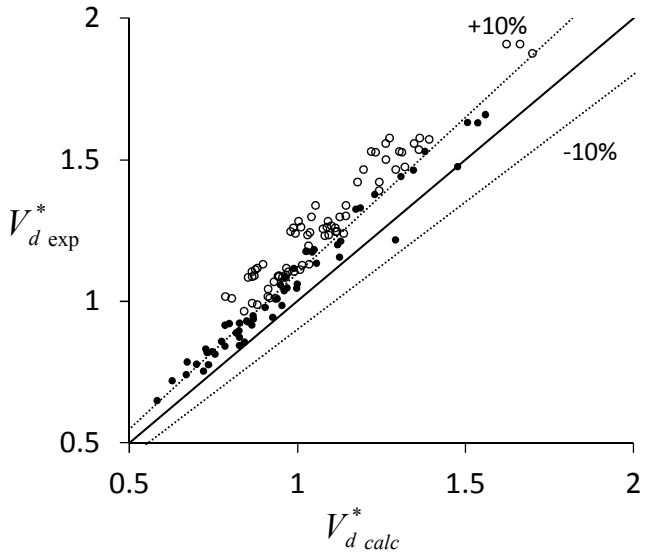

Figure 5.11 Parity plot of the droplet volume calculated using the dynamic interfacial tension in the amalgamated model. ○ Tween 20 experimental data ● SDS experimental data.

Figure 5.11 shows the parity plot for droplet volume predicted using the modified model. Even with the addition of the dynamic interfacial tension the model still under predicts the droplet volume with a large degree of error (~10-20%). A detailed investigation revealed that the filling stage was accurately predicted by the model, and the error was caused by an under prediction of the necking stage due to two reasons.

1. The critical neck thickness for pinch-off, $2r_{pinch}$, was smaller than predicted by Eqn.4.54 in Chapter 4. A smaller neck thickness at pinch off corresponds to longer overall necking periods. In the previous fit to the non-surfactant data, a good fit for the backflow was $m=1$ indicating that oil flow reversed when the Laplace driven flow matched the bypassing oil flow. For surfactants a better fit to the data was $m=2$. This difference may be caused by the difficulty in identifying the pinch-off point with non-surfactant data because the collapse is so sudden. The longer necking time may also be caused by the

depletion of surfactants near the neck which result in Marangoni stresses that retard the drainage of the inner fluid prolonging the necking stage in comparison to when surfactants are absent (Jin, Gupta *et al.* 2006; Lee, Walker *et al.* 2011).

2. The back half of the droplet experiences a greater degree of deformation because the restorative interfacial tension force is lower with the addition of surfactants. As a result, the geometric description that was used in the old model did not accurately describe the shape of the neck during collapse.

Figure 5.12 presents an example of the disagreement between the previous geometric descriptions of the droplet compared to the experimental observations. When surfactants are absent the back half of the droplet follows the circular segment approximation very well (refer to top of Figure 5.12). However, when surfactants are present the neck becomes more elongated and "flattened" as it approaches the inner corner of the T-junction. The corresponding error between the circular segment approximation and the actual neck shape is highlighted in red within Figure 5.12. Similar observations of neck "stretching" have been noted by other researchers when the interfacial tension is very low in T-junction generators (van der Graaf, Steegmans et al. 2005; Steegmans, Warmerdam et al. 2009). It is clear that using the old description to predict the final neck volume will lead to an under prediction of the necking time.

This error may be corrected by including the missing area in the calculation of the neck shape. Figure 5.12 presents the diagram with the geometric parameters that can be used to calculate the missing area. The area is calculated from the difference between the circular segment and the triangle in Figure 5.12:

$$
\begin{aligned}
d_2^* &= b_2^* \\
a_2^* &= \sqrt{d^*\left(2R_{pinch}^* - d^*\right)} \\
\theta_2 &= 2\arccos\left(1 - \frac{b_2^*}{R_{pinch}^*}\right) \\
A_{\mathrm{mod}}^* &= \frac{R_{pinch}^{*2}}{4}(\theta_2 - \sin\theta_2) - \frac{1}{2}a_2^* b_2^*
\end{aligned}
\tag{5.20}
$$

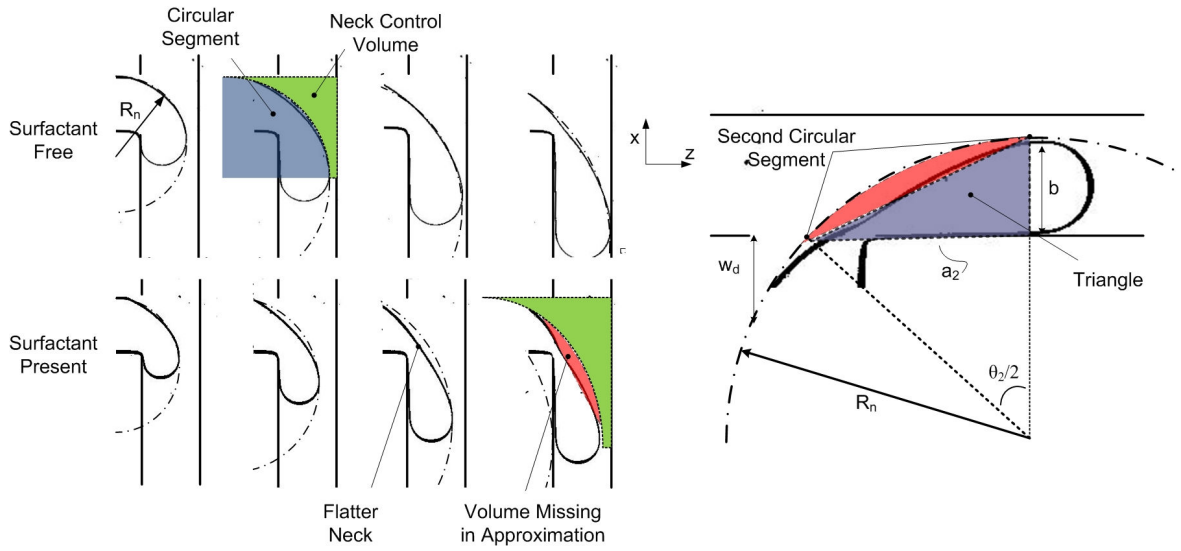

Figure 5.12 (TOP) A sequence of traces showing the boundary of the droplet as it evolves during the necking stage when surfactants absent and present in the system. For the surfactant free case the back half of the droplet follows the circular segment approximation (highlighted in blue). With surfactants the neck shape diverges from a circle and appears flatter. The volume missing from the approximation is highlighted in red (BOTTOM) A diagram showing the geometric parameters that can be used to calculate the missing volume.

The new neck pinch-off volume may be calculated as:

$$V^*_{c_{pinch}} = \left(1 - b_2^*\right)a^* + \left(1 + \Lambda^*\right)a^* - \frac{R^{*\,2}_{pinch}}{4}\left(\theta - \sin\theta\right) + A^*_{\text{mod}} + \frac{h^*}{2}\left(1 - \frac{\pi}{4}\right)R^*_{pinch}\,\frac{\theta}{2} \qquad (5.21)$$

Where $V^*_{c_{pinch}}$ is used to calculate the dimensionless necking parameter:

$$\beta = \frac{1}{\left(1 - \dfrac{A^*_{gap}}{h^*}\right)}\left(V^*_{c_{pinch}} - V^*_{c_{fill}}\right) \qquad (5.22)$$

Figure 5.13 presents the comparison of experimental data to the new model that includes the dynamic interfacial tension, critical neck thickness for pinch-off, and neck volume at pinch-off modifications. The data now falls within ±10% of the predicted values which is deemed to be acceptable considering the estimated uncertainty of the various parameters. Therefore, the original model for the T-junction generator has been successfully extended to include dynamic interfacial tension effects. Revisiting the original comparison between the operational model and the experimental data (Figure 5.2), we saw that the largest error in predicting the droplet size was only 20%. Considering that this data corresponds to 0.1% Tween 20, where the dynamic interfacial tensions increased by 50-300% above equilibrium, it seems reasonable that in a first

approximation the equilibrium interfacial tension can simply be used. The reason for the weak dependence of V_d with γ, is that effects are dampened because V_d scales approximately as $\gamma^{1/3}$. If a more accurate calculation is required then the dynamic interfacial tension effects can be included through the interfacial tension jump approximation.

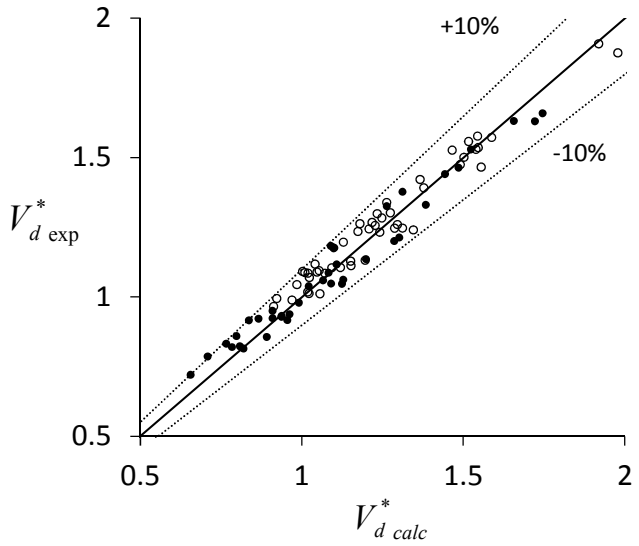

Figure 5.13 Parity plot of the droplet volume calculated using the modifications to the neck volume calculation. ○ Tween 20 experimental data ● SDS experimental data.

5.6 Conclusion

This study examined the influence of surfactants on droplet formation in microfluidic T-junction generators. With microfluidic droplet generators formation times and surfactant adsorption occurs at the same timescale resulting in a dynamic system where the droplet formation process is coupled with surfactant transport through the temporally varying interfacial tension. The importance of these effects was clearly demonstrated in this study. A model was developed to estimate the jump in interfacial tension during the formation process for surfactant solutions above and below the CMC. As part of this model, a new derivation for the relative interface expansion rate in microfluidic T-junctions was also developed. Based on these equations one can understand the relationship between surfactant properties, T-junction design and operating conditions on the dynamic interfacial tension. The adsorption kinetics model was then incorporated into the previous model that describes overall generator performance. Small modifications were needed to the performance model due to deviations in the limit of pinch-off and increased deformation of the droplet neck. Overall, the new model can effectively predict generator performance when surfactants are present and can be used to design and operate T-junction generators.

Nomenclature

Acronyms:

CMC	critical micelle concentration
PDMS	poly(dimethyl)siloxane
SDS	sodium dodecyl sulfate

Mathematical Symbols:

γ	interfacial tension (N m^{-1})
θ	angle (rad)
λ_{gap}	gap aspect ratio
τ_{drop}	drop formation time (s)
φ	ratio of dispersed to continuous phase flow rates
Λ^*	T-junction dispersed to continuous phase widths
Γ	excess surface concentration of surfactant (mol m^{-2})
Γ_o	initial excess surface concentration of surfactant (mol m^{-2})
Γ_{eq}	equilibrium excess surface concentration of surfactant (mol m^{-2})
Θ	dilation rate (s^{-1})
a	circular segment cord length (m)
b_{fill}	interface penetration depth at the end of the filling stage (m)
c_o	concentration of surfactant (mol m^{-3})
c_{CMC}	critical micelle concentration (mol m^{-3})
c_s	sub-surface concentration (mol m^{-3})
d	circular segment height (m)
h	height (m)
$\overline{u}^*$	dimensionless average velocity in the gap
r_{pinch}	radius of neck at the pinch-off point (m)
$w_{c,d,m}$	width of dispersed, continuous and main channels (m)
z	depth coordinate
t	time (s)
A	area of interface (m^2)
A_{gap}	area of the bypass around the droplet (m^2)
Ca	capillary number (dimensionless)

D	diffusion coefficient (m^2s^{-1})
D_{eff}	effective diffusion coefficient accounting for micelles (m^2s^{-1})
L_{eff}	effective hydrodynamic length of the gap (m)
M_w	molecular weight (g mol^{-1})
N_A	aggregation number for micelles
$Q_{d,c,m}$	flow rate of dispersed, continuous or main channel (m^3 s)
R	gas constant (8.314 J K^{-1} mol^{-1}),
R_n	Radius of back half of droplet (m)
T	temperature (K)
V_{drop}	droplet volume (m^3)
V_{fill}	droplet volume at the end fo the filling stage (m^3)
V_{neck}	volume of neck during squeezing (m^3)

Chapter 6

Global Design of Droplet Generators with Pressure Driven Flow

The work presented in this chapter was submitted as an article:
Glawdel T., Ren C.L. "Global Network Design and its Influence on Microfluidic T-junction Performance." **Microfluidics and Nanofluidics,** submitted.

6.1 Introduction

Droplet generators are typically one part of a large system of connected sub-modules that perform specific tasks such as sorting, merging or breaking up droplets. However, the operation of each of these components is coupled together through the pressure field. The droplet generator located at the top of the network diagram; consequently, periodic changes in pressure downstream will coincide with periodic changes in flow rate, and thus erratic motion and production of droplets. These fluctuations are caused by variations in the hydrodynamic resistance of the channels and by the growth and collapse of interfaces. Examples of these conditions are when a droplet enters or leaves the network (Sullivan and Stone 2008; van Steijn, Kreutzer et al. 2008), passes through a constriction/expansion (Liu, Yap et al. 2009), or when a new droplet is formed (Beer, Rose et al. 2009). These oscillations can be highly repeatable because of the linear nature of two-phase flow in microchannels, but in most cases it is desirable to eliminate all potential oscillations in order to simplify operation. This chapter focus on the reduction of such oscillations and on improving the robustness of microfluidic droplet generators operating under pressure driven flow through careful design of the local and global network geometry.

There are several motivations for reducing fluctuations in velocity. Accurate timing of downstream events, such as merging, breakup and sorting, depends on the steady transport of droplets within the network as there is little margin for error due to the high frequency of droplet production (10Hz to 10kHz). Fluctuations in velocity correspond to fluctuations in flow rate. Both the magnitude of flow and the ratio of the dispersed and continuous phase flow rates influence droplet production (Christopher and Anna 2007). Therefore, oscillations in velocity can potentially indicate underlying variation in droplet production (size, spacing and frequency). Obviously reducing these types of variations is a de facto requirement for improving the

robustness of any droplet generator. Furthermore, Beer *et al.* brought up an additional important motivation for reducing velocity fluctuations as it applies to the performance of optical interrogation techniques used to measure the contents of droplets (Beer, Rose et al. 2009). These methods correlate signal strength, such as fluorescence intensity, with the concentration of molecules within the droplets. For quantitative comparison between droplets, the droplet size, read rate and interrogation time needs to be consistent from drop to drop. Erratic fluctuations in droplet velocity will cause interrogation times to vary, thereby introducing systemic errors in the measurements.

For instance, van Stiejn *et al.* observed periodic fluctuations up to 30% from the average velocity in a gas/liquid T-junction generator (van Steijn, Kreutzer et al. 2008). Under their specific experimental conditions, the authors found that oscillations caused by the production of droplets were considerably less than the fluctuation from droplets exiting. This was determined by monitoring velocity fluctuations from start up to steady state. Fluctuations were small from the time that the first droplet was formed until it reached the exit of the main channel. This suggests that the formation of droplets had negligible effect on the flow rates. However, once droplets started continuously exiting the channel large spikes in velocity began to appear. The cause of these fluctuations is the large pressure burst that occurs when a droplet expands uncontrolled into the exit reservoir. Similar results were also observed for oil and water generators by Beer *et al.* (Beer, Rose et al. 2009). The authors applied a fast fourier transform (FFT) analysis to the velocity fluctuations and found that the main power spectrum peak matched the droplet generation frequency. In contrast to the observation of van Steijn *et al.*, the authors found that the periodic spike in velocity occurred at the point of neck rupture rather than when a droplet exited the channel. The reason for this discrepancy is not immediately clear, however, it is presumed that the geometry of the generator and flow conditions played an important role.

Fluctuations in droplet generation may be classified by the time period over which the periodicity occurs. Short-term fluctuations occur on a scale similar to the rate of droplet production as they correspond with the cyclic creation and destruction of the two-phase interface during the formation of a single droplet. Long-term oscillations extend over several droplet cycles. These oscillations can be imposed on the system from outside sources or may occur naturally. Syringe pumps are a common culprit of these external fluctuations if they are used to pump fluids. At low revolutions, racheting of the stepper motor create a pulsate flow; even at higher revolutions imperfections in the drive screw cause slow variations in the flow rate (de Mas, Gunther et al.

2005; Korczyk, Cybulski et al. 2011). Korcyzk *et al.* demonstrated that these oscillations occur with a period $\tau = a\pi D^2/4Q$, where D is the diameter of the syringe piston, a is the pitch of the screw and Q the flow rate (Korczyk, Cybulski et al. 2011). Depending on the syringe used, and the microfluidic device, the period of these oscillations can be surprisingly long, up to 30-60 min. Under such conditions it is necessary to guarantee that data is averaged over several oscillations to correctly assess generator performance.

Naturally occurring oscillations form because of feedback created by the temporally varying channel resistance(Cybulski and Garstecki 2010). As droplets enter and exit the system they dynamically modify the resistance of channels and by association the flow rates. Flow rates determine the size and speed of the droplets which also determines the droplet resistance. This coupling occurs as: flow rate→droplet size, speed→droplet resistance→channel resistance→flow rate. Combined with the fact that droplets are discrete elements, steady state long-term oscillations should be expected.

Droplets have less influence on the global flow field when syringe pumps are used since they automatically adjust for changes in resistance by always outputting a constant flow rate (well, in theory). With syringe pumps it is easy to know the direction and magnitude of all flow streams. However, if highly compliant tubing the system can still experience pulsated flow as the tubing acts like a fluidic capacitor. Malsch *et al.* demonstrated that pressure can build up in the tubing and create a burst of flow when the interface expands from the side channel into the main channel of a T-junction generator (Malsch, Gleichmann et al. 2010).

The feedback effect is more pronounced for systems operating under pressure driven flow. For pressure driven flow coupling with the dynamically changing resistance creates a constantly varying flow field. Ward *et al.* demonstrated the effects that the two different flow types have on the operation of a flow focusing generator operating in the dripping regime (Ward, Faivre et al. 2005). Under constant flow rate control the droplets size varied very little over a wide range of flow rate ratios. However, with pressure driven flow the droplet size varied significantly due to the increased coupling between the droplet formation and flow rate output. Sullivan and Stone performed a theoretical analysis of the feedback effect for a flow focusing bubble generator (Sullivan and Stone 2008). Empirical data was used to relate the droplet size to the added resistance. The model was able to accurately recreate the unsteady production of droplets during start-up.

The effect of feedback is even more prevalent in designs where multiple generators are used in parallel. A single source provides oil and water to all of the generators at the same time. Distribution of oil and water depends on the hydrodynamic resistance of the network which changes with time. Under these conditions, droplet generation can experience several regimes where the generators operate in phase, out of phase, or the generation is completely chaotic (Barbier, Willaime et al. 2006; Hashimoto, Shevkoplyas et al. 2008; Li, Young et al. 2008; Tetradis-Meris, Rossetti et al. 2009). Under these conditions polydispersity of droplets is much larger than for a single generator. Barbier *et al.* studied the simplest parallel system involving two generators, and found that the length of the inlet to the continuous phase and the length of the outlet channel affected the operation of the generators (Barbier, Willaime et al. 2006). The system was modeled as two Van der Pol oscillators, and mathematical derivation confirmed that increasing the lengths of the two channels decrease coupling between the generators. The trend is also seen in massively parallel designs where the architecture of the distribution network has a great influence on the polydispersity of the emulsion (Tetradis-Meris, Rossetti et al. 2009).

In Chapters 4 and 5, the focus was on the effect of local geometry and flow conditions on the droplet generation in terms of the expected size, spacing and frequency. In this chapter, a global perspective is taken where the influence of the global network architecture is considered for a system running entirely on pressure driven flow. The goal here is to improve the performance of pressure driven flow droplet generators by reducing fluctuations in output (droplet size, spacing and speed). The study focuses on the case of a single droplet generator with only one output. The hydrodynamic network is represented by a compact model of the T-junction design. This model is then implemented into a numerical code which couples the simple two-step generation model with the global flow network conditions. Using this model, contributions of various sources to the fluctuations of droplet size, spacing and speed are studied. As part of this analysis a set of "design rules" are developed to help improve overall generator performance using pressure driven flow. A case study is presented to demonstrate the application of these rules. The results of these models are confirmed with experimental data with good overall agreement.

6.2 Metrics for Analyzing Generation Stability

To quantify the stability of generation both short-term and long-term fluctuations need to be considered. Short-term fluctuations can be quantified by analyzing time traces of droplet speed in

the main channel. Droplet speed is directly proportional to the flow rate in the main channel, Q_m, and therefore, monitoring droplet speed indicates the variation in total flow of Q_d and Q_c.

Also of interest is the relative change in the flow of the two phases (Q_d, Q_c). Fluctuations in the flow ratio ($\varphi=Q_d/Q_c$) have a direct consequence as they lead to oscillations in droplet size and spacings. This in turn affects the resistance of the main channel, thus amplifying oscillations even further. Typically, the stability of microfluidic droplet generators is measured by the polydispersity (size variance) of the droplets. Often the exceptional monodispersity of microfluidic droplet generators is quoted to be 1-3% (Christopher and Anna 2007). However, as will be explained soon, spacing rather than size is a far more sensitive metric for quantifying long-term fluctuations in performance.

Droplet formation is often described by a two-step model composed of an initial filling stage followed by a necking stage: $V_d^* = \alpha + \beta\varphi$,where V_d^* is the dimensionless droplet volume ($V_d^* = V_d / w_c^2 h$), and α correlates to the first stage and β to the second (Garstecki, Fuerstman et al. 2006). Generally, these two factors can be considered constant for a specific local generator geometry, as there is only a weak dependence on variations in flow rate (refer to Chapter 5). Spacing is also a function of these two parameters: $\lambda^* = (1+\varphi)(\alpha/\varphi + \beta)$.

Using a first order Taylor expansion, fluctuations in flow ratio propagate into relative fluctuations in droplet size and spacing as:

$$\frac{\Delta V_d^*}{V_d^*} = \frac{1}{V_d}\left(\frac{dV_d^*}{d\varphi}\right)\Delta\varphi = \frac{\beta}{\alpha+\beta\varphi}\Delta\varphi \tag{6.1}$$

$$\frac{\Delta\lambda^*}{\lambda^*} = \frac{1}{\lambda}\left(\frac{d\lambda^*}{d\varphi}\right)\Delta\varphi = \frac{-\frac{\alpha}{\varphi^2}+\beta}{(1+\varphi)\left(\frac{\alpha}{\varphi}+\beta\right)}\Delta\varphi \tag{6.2}$$

Consider a nominal case where $\alpha=1$, $\beta=1$ and a flow ratio of $\varphi=1/10$, then a 10% fluctuation in the flow rate ratio results in a droplet volume change of only ~1% but a spacing fluctuation of ~8%. Figure 6.1 plots the expected variance for different flow conditions assuming a 10% relative fluctuation in the flow ratio. As evidenced in Figure 6.1, when small droplets are formed ($\varphi<0.25$), spacing variations are about 3-4 times larger than droplet size variations. This reverses

above $\varphi=0.5$ where droplets size becomes more sensitive to fluctuations. Therefore, in the range of practical significance (i.e. lower φ), spacing is a far more sensitive indicator to the stability of the system than droplet size. This is because the spacing is largely set during the first stage of the formation process (α/φ), which also tends to be the longer of the two stages ($\alpha>\beta\varphi$) for smaller droplets. Additionally, it is the magnitude of the spacing between droplets is larger than the droplets themselves which makes measuring the spacing an easier and more accurate proposition than droplet size. One can also surmise that a low variance in spacing results in any even lower variance in droplet size. Furthermore, measuring spacing fluctuations compliments measurements of droplet velocity as these fluctuations appear over the short term (1 cycle), while spacing fluctuations appear over the long term (10-1000 cycles). For proper assessment of the system, measurements should be made on both scales to accurately quantify the stability of the formation process.

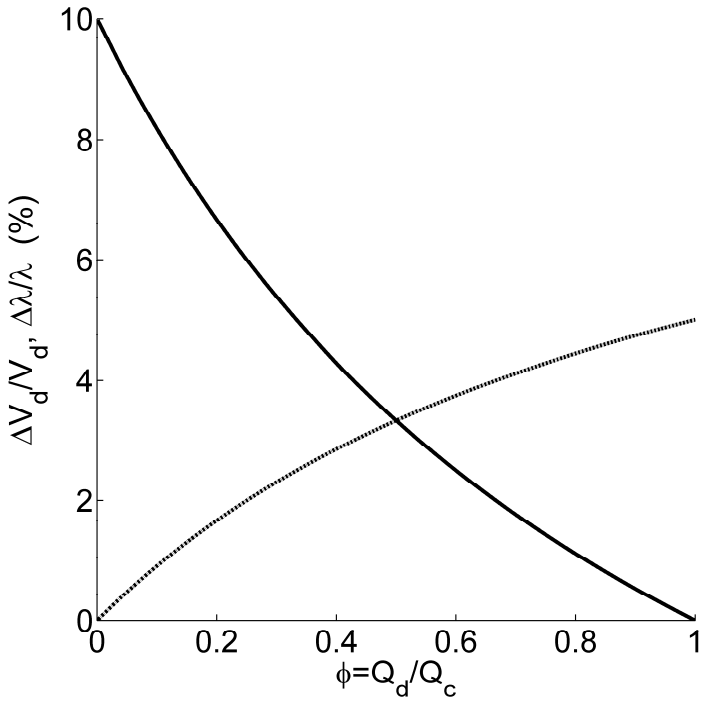

Figure 6.1 Plot of the deviation in droplet volume (dotted line) and spacing (solid line) against the flow ratio under the conditions of $\alpha=1$, $\beta=1$ and 10% fluctuations of φ. Calculations are made using Eqns.6.1-6.2.

6.3 Compact Model of Flow in the T-junction Generator

In this section, a compact model is developed to describe the operation of the T-junction generator. The relevant parameters describing a standard T-junction generator operating under

pressure-driven control are presented in Figure 6.2. All of the geometric dimensions are outlined except for the height, h, which is assumed to be uniform throughout the network. The flow rate in the main channel, Q_m, is the sum of the flow rates of the continuous phase, Q_c and dispersed phase, Q_d. Droplets are formed with a volume, V_d, at a frequency, f, and spacing, λ, and are transported along the channel at a velocity u_d. The space between the droplets occupied by the continuous fluid is L_s. The flow of the two phases is controlled by the applied pressures P_c and P_d. Each droplet increases the resistance of the main channel and contributes an additional pressure drop, ΔP_{drop}, which sums to a total pressure drop of $n\Delta P_{drop}$, where n is the number of droplets in the channel. Additional relationships can be derived for the droplet flow rate, $Q_d = V_d \cdot f$, droplet velocity, $u_d = \lambda \cdot f$, and number of droplets in the main channel, $n = L_m / \lambda$.

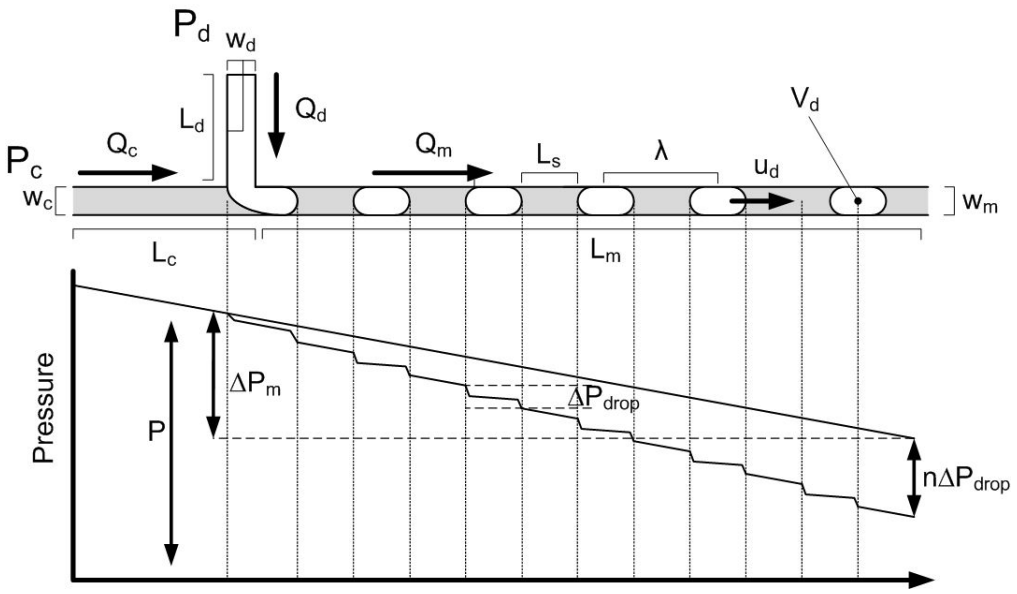

Figure 6.2 Schematic of the T-junction generator operating under pressure source control with the relevant parameters indicated. Below is the pressure drop along the main channel without droplets (ΔP_m) and with droplets ($n\Delta P_{drop}$).

Droplets move along the main channel at a slightly different velocity than the average velocity of fluid flow which can be described by (Schindler and Ajdari 2008; Labrot, Schindler *et al.* 2009; Jakiela, Makulska *et al.* 2011):

$$u_d = \frac{Q_m \beta_{slip}}{A_m} \tag{6.3}$$

where A_m is the cross-sectional area of the main channel and β_{slip} is a proportionality factor that defines the slip between the droplet and the total fluid flow in the channel. The slip factor can be

calculated from known values by substituting parameters (Schindler and Ajdari 2008; Labrot, Schindler et al. 2009):

$$\beta_{slip} = \frac{Q_c + V_d \cdot f}{\lambda \cdot f \cdot A_m} \tag{6.4}$$

A series of non-dimensional factors can also be introduced for the pressure, flow rate ratio, viscosity contrast between the two-phases, and width ratio at the generator:

$$\mathrm{P} = \frac{P_d}{P_c}, \quad \varphi = \frac{Q_d}{Q_c}, \quad \eta = \frac{\mu_d}{\mu_c}, \quad \Lambda = \frac{w_d}{w_c} \tag{6.5}$$

The global flow field within the generator can be described by a compact hydrodynamic model. Due to the low Reynolds numbers conditions ($Re<<1$), pressure driven fluid flow in microchannels is characterized by Stoke's flow conditions. Consequently, fluid flow, Q, and pressure drop, ΔP, can be described by the Hagen-Poiseuille relation, $Q=\Delta P/R_{hyd}$. For a rectangular channel R_{hyd} is given as [Beebe *et al.* (2002)]:

$$R_{hyd} = \frac{12\mu L}{wh^3}\left[1 - \frac{h}{w}\left(\frac{192}{\pi^5}\sum_{n=1,3,5}^{\infty}\frac{1}{n^5}\tanh\left(\frac{n\pi w}{2h}\right)\right)\right]^{-1} \tag{6.6}$$

This equation applies to low-aspect ratio channels ($w \approx h$) and converges quickly after three terms. For high aspect ratio channels ($w>>h$) the equation reduces to:

$$R_{hyd} = \frac{12\mu L}{wh^3} \tag{6.7}$$

When solving for the flow field in large microchannel networks the continuity equation is applied at each intersection in a similar manner to Kirchoff`s law for electric circuits. These compact models are not without limitations and must be applied with some restrictions. The major assumption is that the flow fields are fully developed and uniform which is justified if the channel length is much greater than the channel width ($L>>w$). Regions of 2D or 3D non-uniformity or where complex flow fields exist are not accurately captured by the simplified 1D model. However, since compact models require minimal computation effort they are typically employed to study the general flow field.

The flow rates in each branch are described by the following system of equations:

$$Q_c = \frac{P_c - P_a}{R_c}, \quad Q_d = \frac{P_d - P_{Lp} - P_a}{R_d}, \quad Q_m = \frac{P_a}{R_m}, \quad Q_m = Q_c + Q_d \tag{6.8}$$

where P_a is the pressure at the intersection and P_{Lp} is the Laplace pressure drop across the emerging interface. Here the Laplace pressure is estimated from the curvature of the interface while inside the dispersed channel (Ward, Faivre et al. 2005; Malsch, Gleichmann et al. 2010) :

$$P_{Lp} = \gamma\left(\frac{2}{w_m} + \frac{2}{h_m}\right) \tag{6.9}$$

The resistance of the main channel is the base resistance R_{mo}, plus the contribution from droplets in the channel R_{drop}:

$$R_m = R_{mocp} + nR_{drop} \tag{6.10}$$

For convenience two natural resistances are define for the main channel, the first when it is filled with the continuous phase R_{mocp} and the second when it is filled with the dispersed phase R_{modp}. Additionally, in this analysis the main channel is treated as a single channel, however, if the generator is connected to a network of microchannels than R_m would be replaced with an equivalent overall resistance. Note that droplet resistance is a complex function that depends on several factors including the viscosity ratio, droplet speed, surface tension, channel geometry, size and spacing of the droplets (Fuerstman, Lai et al. 2007; Labrot, Schindler et al. 2009; Vanapalli, Banpurkar et al. 2009). Although several studies have attempted to quantify the influence of these various factors to a certain degree, it still remains difficult to accurately predict droplet resistance for a specific setup without having some empirical data to work with. At the early design stage, however, a suitable rule of thumb to use is that each droplet will increase the resistance of the segment of channel it occupies by 2-5 times. Solving the system of equations and normalizing the resistances by R_c and the pressures by P_c, the junction pressure and three flow rates become:

$$\begin{aligned}
P_j^* &= \frac{P_j}{P_c} = \frac{R_d^* + \left(P_d^* - P_{Lp}^*\right)}{\frac{R_d^*}{R_m^*} + R_d^* + 1} & \qquad Q_d^* &= \frac{Q_d}{P_c / R_c} = \frac{P_d^* - P_{Lp}^* - P_j^*}{R_d^*} \\
Q_c^* &= \frac{Q_c}{P_c / R_c} = 1 - P_j^* & \qquad Q_m^* &= \frac{Q_m}{P_c / R_c} = \frac{P_j^*}{R_m^*}
\end{aligned} \tag{6.11}$$

This model may then be used to study the performance of the generator.

6.3 Experimental Methods

In the preceding discussion, a number of important parameters were identified that are hypothesized to influence the stability of microfluidic droplet generators under pressure driven flow. To evaluate these parameters, and provide quantitative data that can be used to develop a model of the T-junction operation, a comprehensive experimental study was performed. The goal is to test several different conditions by varying the viscosity ratio, interfacial tension, local T-junction geometry and global network design and measure the droplet production variance.

Continuous Phase

Several oils were chosen in order to vary the viscosity of the continuous phase as well as to test different types of surfactants and fabrication methods. These oils, silicone oil 10mPas, n-hexadecane and FC-40, were also utilized in previous microfluidic droplet based studies and therefore provides a direct a means of comparing our experimental results (DC200, H6703, F9755, Sigma Aldrich). Each oil wets the PDMS differently, and in the case of n-hexadecane and FC-40 additional surface treatments are required to achieve ideal wetting conditions (refer to Section 3.3). Silicone oil (DC200, Sigma Aldrich) is actually composed of loose PDMS monomer chains so it naturally wets soft-lithography fabricated PDMS microchannels and does not require any treatment. FC-40 is a perfluorinated oil which is included in this study since it is commonly used in biological application, and data gathered through these experiments may be helpful in the design of future droplet based devices (Clausell-Tormos, Lieber et al. 2008; Holtze, Rowat et al. 2008; Koster, Angile et al. 2008). Finally, n-hexadecane was selected since it has a lower viscosity than the other two oils.

Surfactants/ Dispersed Phase

Each type of oil is paired with a specific surfactant and dispersed phase to vary the interfacial tension and viscosity ratio. The surfactant/dispersed phase are set to two levels, the first is a base solution consisting of only ultra pure water, and the second contains the surfactant. All surfactant concentrations are well over the critical micelle concentration (CMC) so that transport processes at the interface can be ignored.

For silicone oil, 1% (w/v) sodium dodecyl sulphate (SDS) (Sigma Aldrich), which is an anionic surfactant is added to the dispersed phase. While for n-hexadecane, 1% (w/v) of the non- nionic surfactant Span 80 (S6760, Sigma Aldrich) is added. For FC-40 the process is slightly different since it was observed that the right wetting conditions could not be achieved without including a

surfactant. Instead of varying the surfactant, the dispersed phase viscosity was altered by adding glycerol. Thus the base oil solution is 10:1 (v/v) 1H,1H 2H, 2H-Perfluoro-1-octanol (PFO) (370533, Sigma Aldrich) in FC-40, and the dispersed phase is either pure water or a 35% (w/w) mixture of glycerol and water. The glycerol/water ratio was selected so the viscosity ratio between the continuous and dispersed phase was 1:2.

Global Network Design

The chip type refers to the global network design of the T-junction generator. Three designs are chosen which vary the relative length of the inlet/outlet branches too each other as shown in Figure 6.3. The purpose is to test whether the global network design influences the droplet breakup process under constant pressure control. The three designs correspond to relative channel lengths of (a) 1:1:5, (b) 1:5:2, (c) 5:1:2. The minimum length is 1 cm for the inlet oil/water channels. The outlet minimum is 2 cm, as this corresponds to at least 20 droplets in the outlet channel which ensures that the outlet channel resistance does not fluctuate too much as droplets are formed or leave the channel. More important than the length ratio, is the hydrodynamic resistance ratio between the channels as this directly influences the pressure field within the chip. The actual hydrodynamic resistance depends on the viscosities as well as the channel dimensions, and therefore the ratio changes with each chip type and oil/water combination. The relative hydrodynamic resistance for the cases studied is provided in Table 6.2.

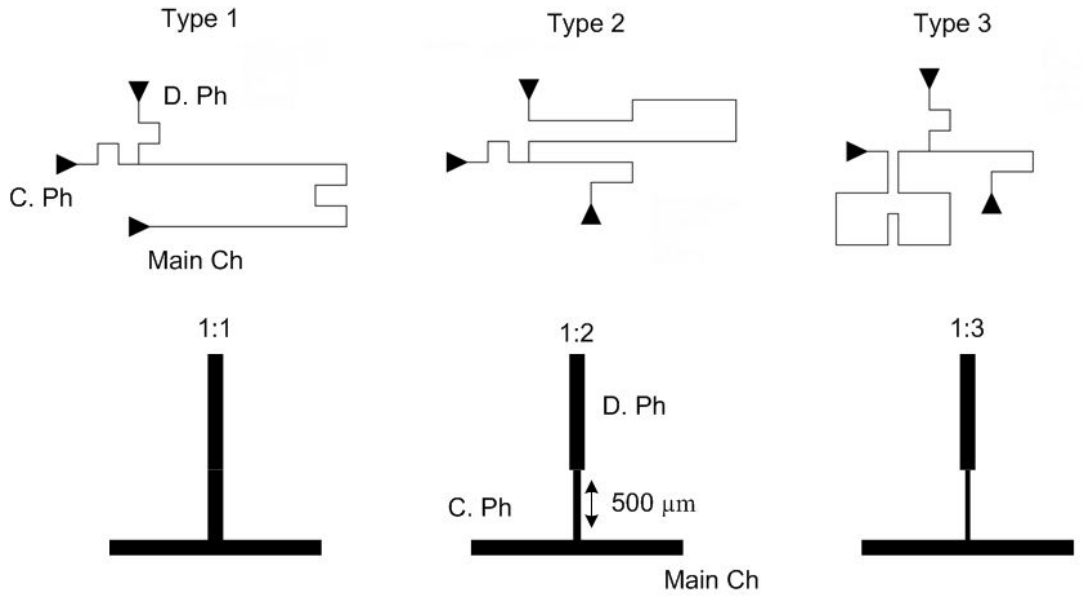

Figure 6.3 A diagram of the three different chip designs with different channel lengths. Type 1- 1:1:5, Type2- 1:5:2, and Type 3-5:1:2. A close up of the intersection design is also included for the three types of intersections 1:1, 1:2 and 1:3. Outside the intersection area, the channel width is 100 μm and the height is uniform.

To summarize, the factors that were selected for experimentation include the continuous phase (C.Ph), dispersed phase/surfactant (D.Ph/Surf), intersection width ratio (W.R), height aspect ratio (H.R) and global chip design (C.Typ). The experimental factors and their levels are presented in Table 6.1.

Table 6.1 Factors of interest and their levels for studying the T-junction generator. The dispersed phase factor depends on the oil type as surfactant and water type changes as described above.

Factors	Process Parameters	Level 1	Level 2	Level 3
C.Ph	Continuous Phase	Silicone Oil	Hexadecane	FC-40
D.Ph/Surf	Dispersed Phase and Surfactant	Y	N	--
C. Typ	Global Chip Design	Type 1	Type 2	Type 3
W.R	Intersection Width Ratio	1:1	1:2	1:3
H.R	Channel Height (nominal)	1:5	1:3	1:2

6.3.1 Design of Experiment

Based on the factors chosen, the total number of potential experiments is 162-not including repetition. Testing all of these combination in a reasonable timeframe is impractical, consequently, Taguchi design of experiment techniques were employed to lower the experimental load and organize the experiments in an efficient manner, (Ross 1995). Taguchi methods provide a means to economically evaluate the significance of several factors by performing only a small portion of the total combinations. The efficiency stems from the use of orthogonal arrays to arrange the factors into a small amount of case studies that vary multiple factors at one time. Typically, Taguchi designs are followed by statistical analysis to determine any interacting effects, however, in this study the orthogonal arrays (OA) are used only as a guide for organizing the experiments effectively.

For the given set of 5 factors that have a mixture of two and three levels, the most appropriate orthogonal array is an L18. This results in a total of 18 case studies. Taguchi methods also insist on randomizing the order in which the case studies are performed to ensure that the experiments are not biased. In these experiments, however, cases with the same type of oil are grouped together to minimize time, since the flow sensor and connecting tubing must be cleaned thoroughly between oil. Table 6.2 shows the L18 OA listing the order in which the case studies were performed. Each case study is repeated 3 times for a total of 54 experiments.

Table 6.2 Table listing the order in which experiments were performed. The five independent factors are listed in columns 2-5. The three right hand side columns are the viscosity (μ_d/μ_c), network channel lengths (L_c:L_d:L_m) and hydrodynamic resistances (R_c:R_d:R_m) ratios. All values shown are nominal.

Exp #	C.Ph	D.Ph/Surf	C. Typ	W.R	H.R	μ_d/μ_c	L_c:L_d:L_m	R_c:R_d:R_m
1	Silicone Oil	Water	Type 2	1:1	1:5	1:10	1:5:2	10:5:20
2	Silicone Oil	Water	Type 3	1:2	1:3	1:10	5:1:2	50:1:20
3	Silicone Oil	Water	Type 1	1:3	1:2	1:10	1:1:5	10:1:50
4	Silicone Oil	Water +1% SDS	Type 1	1:1	1:5	1:10	1:1:5	10:1:50
5	Silicone Oil	Water +1% SDS	Type 2	1:2	1:3	1:10	1:5:2	10:5:20
6	Silicone Oil	Water +1% SDS	Type 3	1:3	1:2	1:10	5:1:2	50:1:20
7	Hexadecane	Water	Type 2	1:3	1:5	1:3	1:5:2	3:5:6
8	Hexadecane	Water	Type 3	1:1	1:3	1:3	5:1:2	15:1:6
9	Hexadecane	Water	Type 1	1:2	1:2	1:3	1:1:5	3:1:15
10	Hexadecane	Water +1% Span 80	Type 3	1:3	1:5	1:3	5:1:2	15:1:6
11	Hexadecane	Water +1% Span 80	Type 1	1:1	1:3	1:3	1:1:5	3:1:15
12	Hexadecane	Water +1% Span 80	Type 2	1:2	1:2	1:3	1:5:2	3:5:6
13	FC-40	Water +10%PFO	Type 3	1:2	1:5	1:5	5:1:2	25:1:10
14	FC-40	Water +10% PFO	Type 1	1:3	1:3	1:5	1:1:5	5:1:25
15	FC-40	Water +10% PFO	Type 2	1:1	1:2	1:5	1:5:2	5:5:10
16	FC-40	35%Gly+10% PFO	Type 1	1:2	1:5	1:2	1:1:5	2:1:10
17	FC-40	35%Gly +10% PFO	Type 2	1:3	1:3	1:2	1:5:2	2:5:4
18	FC-40	35%Gly +10% PFO	Type 3	1:1	1:2	1:2	5:1:2	10:1:4

6.3.3 Chip Fabrication

A total of 27 different chip designs were fabricated on 9 silicon wafers using standard photolithography procedures developed in the lab (Glawdel 2008). Designs were grouped by the channel height and intersection type, and then by channel layout. Therefore, one master consists of 3 designs (type 1, type 2, and type 3) with the same intersection (ex. 1:1) and same nominal height (ex. 35µm). PDMS molds (Sylgard 184, Dow Corning) in a ratio of 10:1 (base: curing agent) were made and cured at 100˚C for at least 2 hrs. Specific designs were then cut out and fluidic access holes were punched using a 1.5mm biopsy punch (Unicore, Harris).

From this point on the fabrication procedure differed depending on the oil type. As mentioned before, it is essential that the continuous phase preferentially wets the walls for stable droplets to form. This requires a unique surface treatment for each type of oil to ensure that the right wetting conditions exist.

Silicone Oil

PDMS molds are bonded to a glass slide coated with PDMS so as to create a homogeneous microchannel. PDMS coated slides are fabricated by spin coating 10:1 PDMS at 3000 rpm for 60s followed by baking for 5 min at 95˚C. The two substrates are exposed to air plasma (PDC-001, Harrick Plasma) under conditions of 29.6W at 600mTorr for 50s. The plasma treatment renders the PDMS hydrophilic, to reverse the process, the chip is heated at 160˚C for 12 hrs. Prior to starting the experiments the chip is primed by pumping silicone oil through the microchannels for 1 hr to guarantee that the channels are fully swollen.

n-Hexadecane

PDMS molds were bonded to PDMS glass coated slides in a similar manner to that of silicone oil. Immediately after plasma treatment a solution of 0.02 mol octadecyltrichlorosilane (OTS) (Sigma Aldrich) in n-hexadecane was pumped through the chip for 20 min. OTS combined with plasma treatment is known to graft OTS chains to PDMS microchannels ensuring consistent hydrophobicity and wetting of n-hexadecane on the walls (Adzima and Velankar 2006). The OTS solution is then flushed with pure hexadecane for 30 min which also swells the microchannels.

FC-40

PDMS molds are oxygen plasma bonded to bare glass microscope slides using the same process specifications as stated previously. After bonding, the device is briefly heated for 2 min on a 95˚C hotplate to solidify the bond. Once the chip cools down, a commercial Teflon based glass surface treatment (Aquapel, PPG Industries) is applied to the microchannels (Holtze, Rowat et al. 2008; Koster, Angile et al. 2008). Aquapel is a rain repellent glass treatment used in the automotive industry that bonds to PDMS and is hydrophilic towards FC-40. The product comes in a custom applicator and is extracted by drilling a small hole in the casing to drain the fluid within. A 5mL gas tight syringe (81520, Hamilton Co.) is used to store the fluid since it reacts with oxygen. To apply the treatment, a small amount of Aquapel is injected into the chip to fill the entire micro channel network and left for 2 min. Afterwards compressed air is blown through the network to remove the residual Aquapel. The chip is then stored in atmosphere for 30 min to complete the surface treatment.

6.4 Working Pressure Range

For a set P_c, the effective range of P_d is limited to the set of conditions where both phases exit through the main channel. The boundaries of this regime are defined by the cases where the flows change direction in the two inlets ($Q_c=0$ or $Q_d=0$):

$$\frac{R^*_{m_{cp}}}{1+R^*_{m_{cp}}} + P^*_{Lp} \le P^*_d \le \frac{R^*_d}{R^*_{m_{dp}}} + 1 + P^*_{Lp} \tag{6.12}$$

Near the lower limit the volume fraction is dominated by the continuous phase (i.e. small droplets with large spacings), while at the upper limit it is dominated by the dispersed phase (i.e. large droplets closely spaced together). The size of this range is of practical significance. If the range is small compared to the resolution of the pressure control system, then droplet production (size, spacing) cannot be finely tuned. For instance, for a pressure regulator with a resolution of 0.5 mbar, and a pressure range of 10mbar, only 20 discrete droplet sizes can be achieved. This of course provides limited tuning of droplet size and spacing; maximizing the number of discrete settings will improve the robustness of the system.

Table 6.3 Experimental results for prediction of $P^*_{d\min}$. Data is presented for 6 different chip designs with various local and global geometries, with and without surfactants. The final two columns present the experimentally measured $P^*_{d\min}$ compared to the calculation from Eqn. 6.12.

Exp #	C.Ph	D.Ph/Surf	w_d (µm)	w_c (µm)	h (µm)	P_{Lp} (mBar)	R_c:R_d:R_m	P_c (mBar)	$P^*_{d\min}$ (exp)	$P^*_{d\min}$ (calc)
1	Si Oil	Water	98	98	42	15.3	10:1:5	400	0.885	0.872
								500	0.884	0.864
2	Si Oil	Water	91	91	31	19.5	2:1:4	400	0.713	0.709
								500	0.700	0.699
3	Si Oil	Water+1%SDS	46	94	43	4.05	10:1:50	400	0.838	0.842
								500	0.830	0.840
4	Si Oil	Water+1%SDS	92	92	41	3.2	1:1:5	400	0.838	0.832
								500	0.830	0.830
5	Si Oil	Water+1%SDS	92	92	41	3.2	1:2:2	400	0.688	0.675
								500	0.660	0.673

Experiments were performed to confirm the validity of Eqn. 6.12 and to quantify the accuracy. Table 6.3 lists the results for six T-junction designs with different intersection and network configurations. Experiments were performed, with and without surfactants, using silicon oil as the

continuous phase and water as the dispersed phase. Measurements were made by fixing P_c and slowly lowering P_d until the interface remained fixed just inside the dispersed channel inlet. This was done at two different levels of P_c. The two columns on the left of Table 6.1 summarize the comparison between Eqn. 6.12 and experimental measurements. Overall, the correlation is good as the prediction is generally within 2% of the measured value.

In reality the available range is often narrower than theoretically predicted by Eqn. 6.12. Usually the pressure is confined to the lower limits because small droplets are often desired rather than long slugs. Furthermore, droplet generation close to the minimum can be very sporadic and uncontrollable. The process is as follows. First, a few droplets are formed and they travel down the main channel. The additional droplets increase the resistance of the main channel shifting the lower limit for P_d upwards. This cuts off the flow of Q_d, resulting in a pause in the production of droplets until the first droplet leaves the system thereby lowering the limit for P_d again. The process repeats with a few droplets being formed, followed by a pause, and followed by more droplets again. Generally, one would like to generate a continuous stream of uniform droplets rather than a pulse of highly dispersed droplets. For this to occur, the system has to run slightly above the lower limit predicted in Eqn. 6.12. The number of additional droplets that would cause the flow to stop can be estimated for a pressure δP_d set above the minimum P_{dmin}:

$$P_{d\,\min}^{*} + \delta P_d^{*} = \frac{R_{mo}^{*} + nR_{drop}^{*}}{1 + R_{mo}^{*} + nR_{drop}^{*}} + P_{Lp}^{*} \tag{6.13}$$

This leads to the following condition which must be met:

$$nR_{drop}^{*} < \frac{\delta P_d^{*}\left(1 + R_{mo}^{*}\right)^2}{1 - \delta P_d^{*}\left(1 + R_{mo}^{*}\right)} \tag{6.14}$$

As long as the number of droplets is less than this limit at the prescribed δP_d , droplets will continuously form without pauses. This calculation is vague without knowing the droplet resistance, which depends in turn on the droplet size, which depends on the flow ratio and thus the pressure applied. However, one can make a reasonable estimate by assuming that, at the lower limit of P_d, droplets that form will be about as long as the channel width ($L_{drop} \sim w_c$). Droplet resistance thus increases the length of channel it occupies by about 2 times. Next, one can also assume that droplet spacing will be large near the lower limit, approximately $\lambda = 20 w_c$, and knowing the main channel length (L_m), the number of droplets in the network can be estimated ($n = L_m/\lambda$). This information can then be used to predict δP_d to generate a continuous stream of

droplets. Although this calculation provides an estimate for the effective range of continuous droplet production, fluctuations in droplet size, spacing and speed can still occur over the formation cycle. These fluctuations are amplified as these parameters are linked to the global flow rates throughout the network.

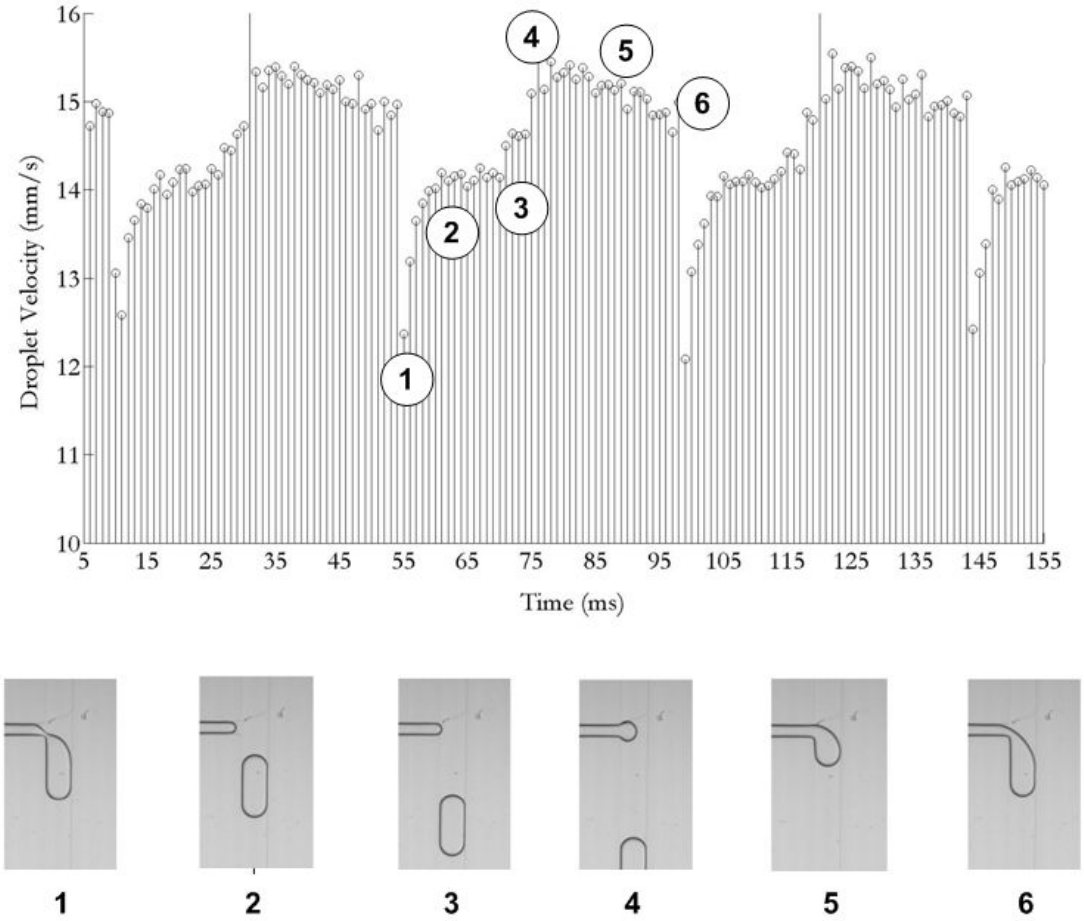

Figure 6.4 Velocity of a droplet that is downstream of the T-junction generator for n-hexedecane, water, Type 1, 1:2, 35µm. The velocity varies significantly over a droplet formation cycle, and in this case the standard deviation is >5%. The velocity fluctuations correspond to different stages of the formation cycle, as indicated by the numbered images. The formation cycle is approximately 45ms long and images were taken at 1000fps. Lines that appear to exceed 16 mm/s are a false error that is caused by a new top droplet entering the analysis frame.

6.5 Short Term Velocity Fluctuations

As mentioned before, short term fluctuations have a period close to the droplet generation frequency. These fluctuations are related to the creation and destruction of the two-phase interface. Figure 6.4 shows an experimental data set with periodic velocity fluctuations up to ~20%. Measurements were made by tracking the displacement of a recently formed droplet just

downstream from the T-junction generator. Velocity fluctuations are highly repeatable over each droplet formation cycle. Recall that velocity fluctuations correlate with fluctuations in Q_m which in turn correlates with fluctuations in the global pressure field. In this example, the source of the velocity fluctuation occurs at the T-junction generator caused by the dynamically changing Laplace pressure drop across the interface as the droplet forms.

Comparing the velocity profile with the formation process occurring upstream, changes in velocity coincide with different stages of the formation process:

1. Droplet pinch-off coincides with a reversal of oil flow from the tip of the droplet into the neck region (van Steijn, Kleijn et al. 2009). This causes a severe drop in velocity as the contribution of Q_c to Q_m decreases. After the droplet detaches the interface retracts into the side channel to a distance of w_d from the intersection.

2. The interface quickly recovers from 1→2, and the velocity increases slightly, however, it is below the maximum velocity seen later when the interface penetrates into the main channel. This is because the curvature of the interface is higher in the side channel which results in a larger Laplace pressure drop across the interface. Generally, the difference between the two plateaus 2→3 and 4→5was more significant when the intersection design was asymmetric (w_d:w_c=*1:2, 1:3*) and less when it was symmetric (1:1).

3. Afterwards (2→3) the interface begins to advance within the dispersed phase channel until it reaches the entrance into the main channel. During the advancement the curvature remains approximately the same ($2/w_d$), and thus Q_m is approximately constant throughout this stage.

4. Once the interface reaches the main channel it begins to expand, decreasing the curvature and the pressure drop across the interface. This causes a sudden increase in the contribution of Q_d to Q_m. The maximum velocity occurs at 4, which may be a surprise, since it happens before the interface expands to its maximum size ($2/w_c$). Presumably this is caused by the fact that the gap between the wall and interface closes, which blocks the flow of the continuous phase thereby decreasing the contribution of Q_c to Q_m.

5. From 4→5→6 the velocity decreases slightly as the pressure drop across the drop changes. Presumably there are two contributions to the decrease. As the droplet increases in length, the amount of Q_c flowing the through the gutters decreases due to the increase in hydrodynamic resistance. Secondly, as the neck is thinning the change in curvature between the front and back of the droplet is causing the pressure drop across the droplet to decrease, lowering the flow of Q_c. This finally culminates in the sudden collapse of the neck at 6 and the sharp decrease in Q_m.

Unlike van Steijn *et al.* the spike in velocity caused by a droplet leaving the channel was not observed in this example (van Steijn, Kreutzer et al. 2008). This is due to the fact that there are many droplets in the main channel, in this example there are 61, and the resistance of a single droplet was found to only increase the main channel resistance by 0.6%. This, however, does not completely eliminate the possibility of fluctuations still occurring at the outlet given that the flexibility of PDMS may attenuate these fluctuations before they reach the generator where observations were made.

6.5.1 Scaling analysis of the Velocity Fluctuations

A scaling analysis may be performed to predict the order of magnitude of velocity fluctuations. This may be accomplished by calculating the relative fluctuation of Q_m due to perturbations in certain variables. Three primary sources for these fluctuations are considered:

1. Laplace pressure fluctuations caused by the evolving interface at the generator. Here only the expansion of the interface from the dispersed phase inlet to the main channel is considered. Not included is the sudden spike during pinch-off because an accurate estimate of the magnitude of this pulse is not currently available.

2. Oscillations in the input pressures P_d and P_c. The main source of these oscillations would be the feedback control in the pressure regulation system. Alternatively, these fluctuations can occur because of processes occurring upstream in the two inlet channels. One example would be the design of a compound droplet generator that is used to produce double emulsions (Nisisako, Okushima et al. 2005). In this setup, an upstream generator creates droplets which are then fed into the dispersed channel inlet of the next

droplet generator. Fluctuations from the upstream generation would thus propagate into the second generator.

3. Oscillations in the resistance of the main channel as droplets enter or leave the network. This is modelled by the addition or subtraction of a single drop $\delta R_m = R_{drop}$. Note that this does not include the sudden pressure pulse created by a droplet expanding uncontrolled into the exit reservoir. This effect may be estimated, if desired, by determining an equivalent droplet resistance when exiting. One can estimate the pressure jump across the rear of the droplet to be on the order of $\delta P = \gamma(2/w_c + 2/h)$. Substituting this into $R_{dropEx} = \delta P / Q_m$, an equivalent "exit" droplet resistance may be calculated. At low flow rates, this equivalent droplet resistance may be 2-5 times higher than the normal in channel droplet resistance (R_{drop}).

Using a first order Taylor expansion, Laplace pressure fluctuations propagate into relative velocity fluctuations as:

$$\left.\frac{\Delta u_d}{u_d}\right|_{P_{Lp}} \propto \frac{1}{Q_m^*}\left(\frac{dQ_m^*}{dP_{Lp}^*}\right)\Delta P_{Lp}^* \tag{6.15}$$

where upon substitution of Eqn. (11) the corresponding non-dimensional equation is:

$$\left.\frac{\Delta u_d}{u_d}\right|_{P_{Lp}} \propto \frac{\Delta P_{Lp}^*}{R_d^* + P_d^* - P_{Lp}^*} \tag{6.16}$$

The Laplace pressure change is calculated by estimating the change in interface curvature from the inlet of the dispersed channel ($\kappa = 2/w_d + 2/h$) into the main channel ($\kappa = 2/h$):

$$\Delta P_{Lp}^* = \frac{1}{P_c}\sigma\left(\frac{2}{w_d}\right) \tag{6.17}$$

Fluctuations in the input pressures can also cause droplet velocity oscillations:

$$\left.\frac{\Delta u_d}{u_d}\right|_{P_d} \propto \frac{\Delta P_d^*}{R_d^* + P_d^* - P_{Lp}^*} \tag{6.18}$$

Similarly, fluctuations caused by a single droplet leaving the channel can be calculated as:

$$\frac{\Delta u_d}{u_d} \propto \frac{1}{Q_m^*}\left(\frac{dQ_m^*}{dR_m^*}\right)R_{drop}^* \tag{6.19}$$

which leads to:

$$\left.\frac{\Delta u_d}{u_d}\right|_{R_m} \propto \frac{R_{drop}^*(1+R_d^*)}{R_d^* + R_d^* R_m^* + R_m^*} = \frac{\frac{R_{drop}^*}{R_m^*}(R_d^*+1)}{\frac{R_d^*}{R_m^*} + R_d^* + 1} \tag{6.20}$$

The magnitude of the total velocity fluctuation may then be estimated by:

$$\frac{\Delta u_d}{u_d} \propto \left(\left(\left.\frac{\Delta u_d}{u_d}\right|_{P_{Lp}}\right)^2 + \left(\left.\frac{\Delta u_d}{u_d}\right|_{R_m}\right)^2 + \left(\left.\frac{\Delta u_d}{u_d}\right|_{P_d}\right)^2\right)^{1/2} \tag{6.21}$$

From the experiments, the standard deviation $\sigma(u_d)/u_d$ is used as a quantifier to compare with Eqn. 6.21. Experimental data obtained during the modelling of the T-junction generator (Chapter 3) was used for the comparison. Note that as part of the calculations the droplet resistance needs to be known so as to substitute in the expected change form one droplet entering or leaving the system Eqn. 6.20. During the experiment Q_c, and Q_d as well as the base values for R_d, R_c and R_{mo} were measured. Droplet resistance was then indirectly estimated by substituting these variables, plus the known number of droplet ($n=L_m/\lambda$), into Eqn. 6.11 and solving for R_{drop}. This was then used as part of the prediction given in Eqns. 6.16, 6.18, 6.20, 6.21.

Figure 6.5 plots the predicted velocity fluctuations of Eqn. 6.21 with the measured values $\sigma(u_d)/u_d$ from experiments. Open circles correspond to experiments without surfactant and filled circles with surfactant. The data shows that the two measures scale together and that the analysis is successful in predicting the order of magnitude of the velocity fluctuations. Generally, the prediction from Eqn. (21) slightly underestimates the real fluctuations; the reason being that several additional sources of fluctuations, namely, droplet pinch-off and uncontrolled droplet expansion were absent from the estimation.

Velocity fluctuations are generally much lower when surfactants are added to the system. Surfactants lower the surface tension which has a twofold effect: (a) it reduces the Laplace drop at the interface near the T-junction nullifying the influence of the expansion and necking pulses

and (b) it reduces the hydrodynamic resistance of a droplet by lowering the contribution of the front and end caps during transport and expansion (van Steijn, Kreutzer et al. 2008). The good agreement between the predictions put forth by the compact model and the experiments provide a certain degree of validation for using compact modelling to describe the overall performance of the generator. This suggests that the simple model can be used to develop guidelines for designing the overall network architecture.

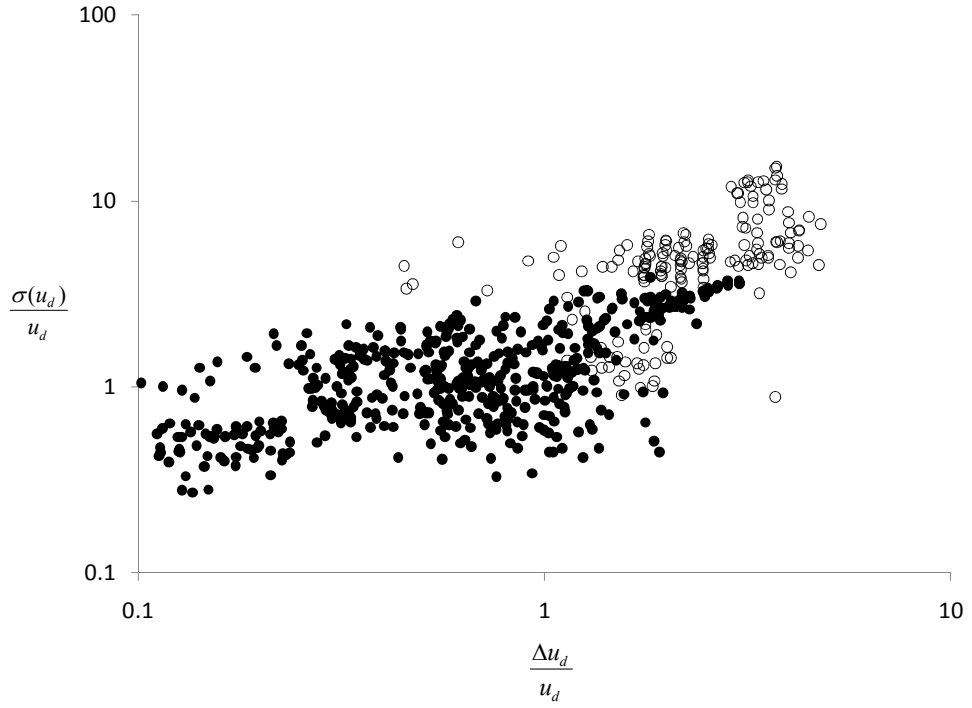

Figure 6.5 Relative velocity fluctuations observed experimentally compared to that calculated by changes in the interface shape at the inlet and a droplet leaving the channel. Data is shown on a log-log plot in terms of percentages. ● corresponds to experiments using surfactants and ○ to those without.

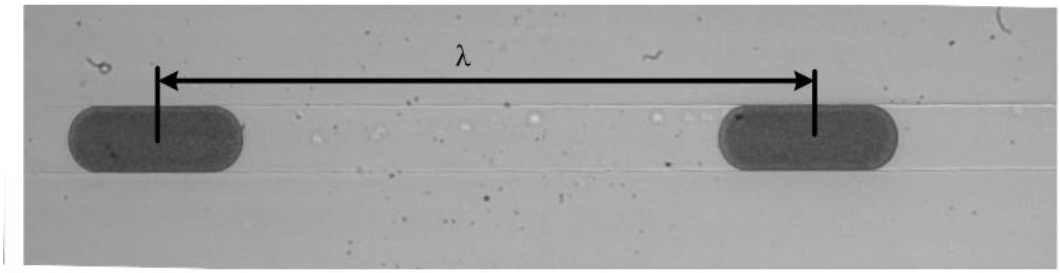

Figure 6.6 Example of a typical frame for video analysis of long-term droplet spacing fluctuations.

6.6 Long Term Fluctuations in Spacing

Experiments were performed with silicon oil/water without surfactant in three different chip designs. A 1:1 intersection was used with a uniform channel width of 100µm and height of 27µm. In the designs, the main channel and the continuous phase channel were kept constant L_m=50mm, L_c=10mm. The resistance of the dispersed phase inlet was varied in 3 levels, first by keeping the cross-section the same and increasing the length L_d=10,70mm, and then by reducing the height of the channel from 27→15µm resulting in an effective length (equivalent in terms of h=27µm) of L_c=400mm. Hence the resulting resistance ratios are R_c:R_d:R_m=1:0.1:5, 1:0.7:5, and 1:4:5. Each chip was run at four different base pressures P_c=350, 500,800, 1000 mbar with three different P_d levels to vary the size and spacing of the droplets. At each setting, a video was taken where approximately 1000-3000 droplet spacings were recorded, which corresponds to at least 20-50 complete system volume replacements. Videos were taken after 10min at the pressure setting to ensure a steady state had been reached. Water soluble black ink (Black Magic, Higgins) was added to the water to enhance the contrast of the droplets during the video analysis. Figure 6.6 shows a typical frame from the videos. Droplet spacing was limited to ~1mm so that two droplets were simultaneously in the field of view.

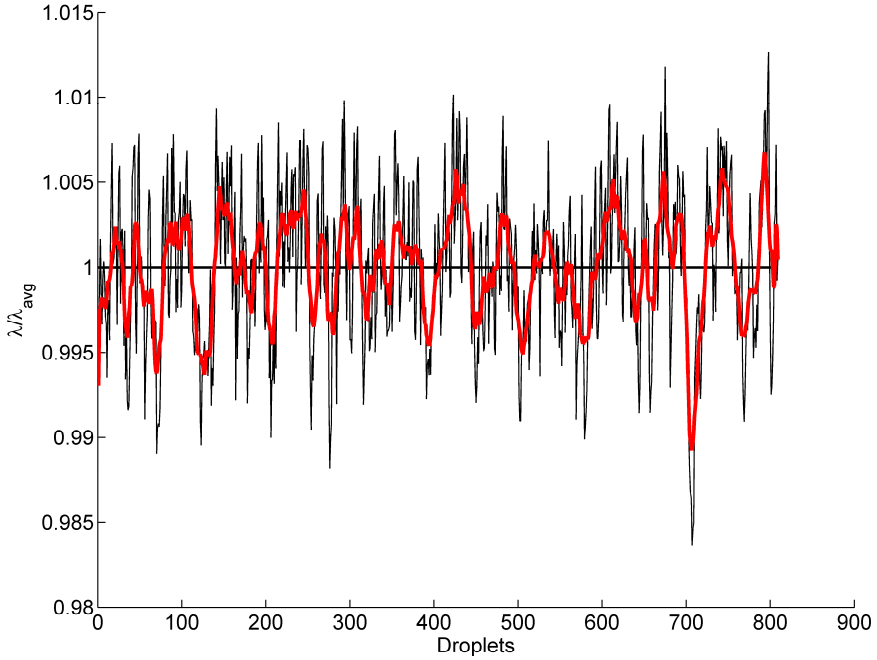

Figure 6.7 Measurement of droplet spacing in a T-junction generator after 10 min of operation. Conditions are R_c:R_d:R_m=1:0.7:5, P_c=800mBar, P_d=790 mBar. The solid black line is the measured values; red line is an 11 point smoothing average.

Data from the videos was extracted using the same blob analysis algorithm as in Chapter 4. Droplet spacing was defined as the distance between the centroids of two sequential droplets. As a pair of droplet travelled through the field of view the spacing was measured for each frame until the lead droplet exited the system. From these measurements a single average value was recorded for the pair. This process was then repeated for the entire video to extract the evolution of droplets spacing over time. A typical result of the time-dependent spacing output is presented in Figure 6.7.

6.6.1 Analysis of Spacing Fluctuations

Examination of the data (Figure 6.7) reveals that droplet spacing experiences both short-term and long-term oscillations. Short term oscillations are created by the stochastic nature of the break up process (and applied pressures) and other sudden pulses such as a droplet exiting a channel. Image artefacts (such as dust) and errors (boundary detection problems) in the video analysis also produce artificial short term fluctuations. However, from within the noise created by the short-term fluctuations, a natural steady and repeatable long-term signal can be seen (smoothed line in Figure 6.7). Analysis shows that these oscillations have a period that coincides with time it takes to completely replace the droplets within the channel, i.e. $\tau=n_{drop}$., where $n_{drop}=L_m/\lambda$. This period may also be interpreted as the average residence time of a droplet in the main channel.

To confirm this observation, the data was analyzed using fast fourier transfer (FFT) analysis in order to extract the strongest frequency (or period) prevalent in the spacing data. Figure 6.8 presents FFT results for the experiment in Figure 6.7. The strongest peak appears at a cycle time $\tau/n_{drop}=1$ indicating that main oscillations have a cycle that equals the channel volume replacement time. Analysis of other experimental results confirm power spectrum peaks near $\tau/n_{drop}=1$. A similar correlation between droplet residence time and cyclic behaviour is also seen in droplet trafficking at a junction as discussed later in Chapter 7. The length of the sorting pattern that forms is determined by the residence time of the droplets in the branch channels. The underlying cause of these long term oscillations is the dynamically changing contribution of droplet resistance to R_m as the flow rates vary slightly. A similar condition appears here for the production of droplets using pressure driven flow.

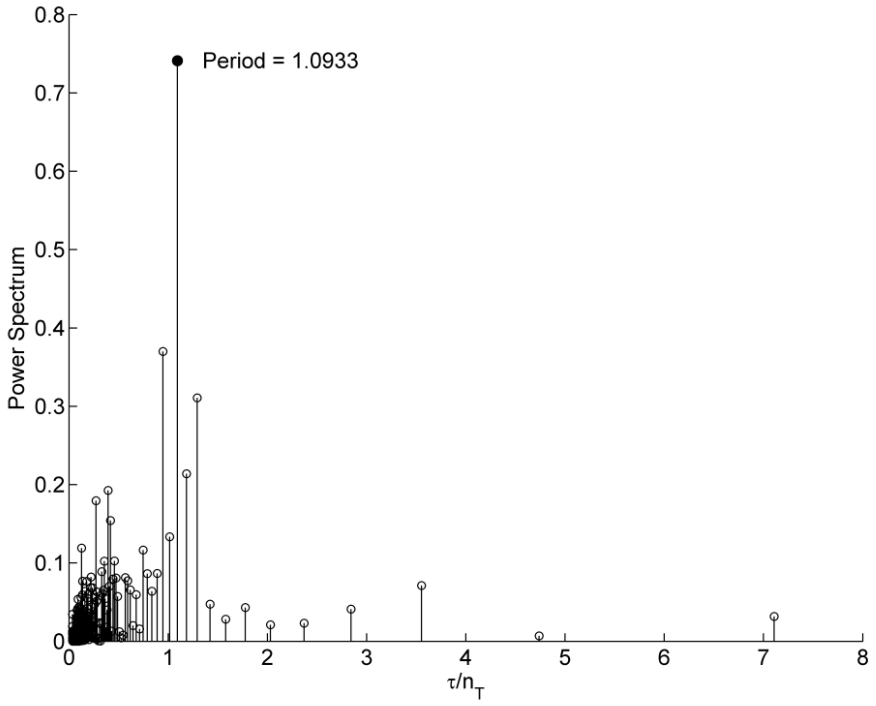

Figure 6.8 Power spectrum of the fast fourier transform of data in Figure 6.7. The strongest peak coincides with the residence time of the droplets.

6.6.2 Numerical Model of Feedback in Droplet Generation

To further investigate this phenomenon a simple compact numerical model was developed of the droplet generation process. At each time step the flow field, and pressure field (Eqn. (11)) was calculated with updates to R_m as the number of droplets in the channel changed. Droplet formation was modelled as a three stage process mimicking the experimental velocity fluctuations of Figure 6.4. The sequence of events is as follows:

1. The interface is contained within the side channel after droplet detachment and must move a distance w_d before entering the counter-flowing continuous stream. Interface curvature is fixed at: $\kappa=2/w_d+2/h$, following the plateau at stage 2→4 in Figure 6.4.
2. The droplet expands to fill an initial size $V_{fill} = \alpha \cdot w_c^2 h$ prior to necking. Interface curvature in this stage is calculated as: $\kappa=2/h$, following the jump to stage 4 in Figure 6.4.
3. The necking begins and the oil replaces a volume of $V_{neck} = \beta \cdot w_c^2 h$. Interface curvature is estimated as: $\kappa=2/h$, following the relatively stable plateau from stage 4→6.

Each newly formed droplet is placed at the entrance of the main channel. The size of the droplet was calculated as the amount of Q_d pumped into the droplet during the latter two stages. Droplet resistance was then correlated to droplet size by $R_{drop}=G_c V_d$, where G_c is a conversion factor. Therefore, each newly formed droplet has a unique volume, resistance and period of formation. At the end of each time step droplets were transported down the channel a distance of $\Delta x = \Delta t Q_m / A$. If a droplet reached the exit it was removed from the system. A highly variable time-stepping algorithm was employed to speed up the simulation. The new time step was calculated as the minimal interval for one of the following events to occur based on the settings in the previous time-step:

1. If in stage 1. The time remaining for the interface to cover the distance wd inside the dispersed channel inlet: $\Delta t = w_d / (Q_d w_d h)$
2. If in stage 2. The time remaining to reach the final fill volume: $\Delta t = \left(V_{fill} - V_d^{(i)}\right) / Q_d$
3. If in stage 3. The time remaining to reach the final neck volume: $\Delta t = \left(V_{neck} - V_o^{(i)}\right) / Q_c$
4. Time remaining for a droplet to reach the exit.

Simulations begin with the main channel empty and run for a specified time. In some instances zero-mean random noise was the applied to P_c, P_d at each time step. Time traces were recorded for all relevant variables including droplet size, spacing and frequency of formation.

6.6.3 Numerical Simulation Results

The goal here is to investigate the effect of the various parameters on the temporal response of the system, particularly the effect of global network geometry. For all of the cases described below, the droplet spacing was fixed (~10wc) by adjusting P_d accordingly. Other parameters that were kept constant are α=1, β=1, G_c=3, w_c=100 μm, L_m=5 cm, and the viscosities μ_d=1 mPas, μ_c=10 mPas.

Figure 6.9 a,b presents the transient droplet spacing, and the correspond FFT analysis, for the case R_c:R_d:R_m=1:0.1:5, with P_c=500 mBar, γ=50 mN m, with the absence of noise in P_c, and P_d. The response follows an exponentially decaying sinusoidal signal. In this example, there are 60 volume replacements and the signal has still not reached a steady state. FFT analysis of the signal confirms that the oscillations in spacing have a period matching closely to the residence time of

droplets in the channel, $\tau/n_{drop}=1$. When the resistance of the dispersed phase channel inlet (R_d)is increased from 0.1→0.7 the decay rate increases and the overall magnitude of the oscillations decreases (see Figure 6.9 c,d). Similarly, the FFT analysis confirms a peak near $\tau/n_{drop}=1$. A strong peak near the residence time was confirmed for every numerical simulation even when n_{drop} and L_m were varied. If the simulation is run for a long-enough time oscillations eventually subside to a constant output in droplet spacing.

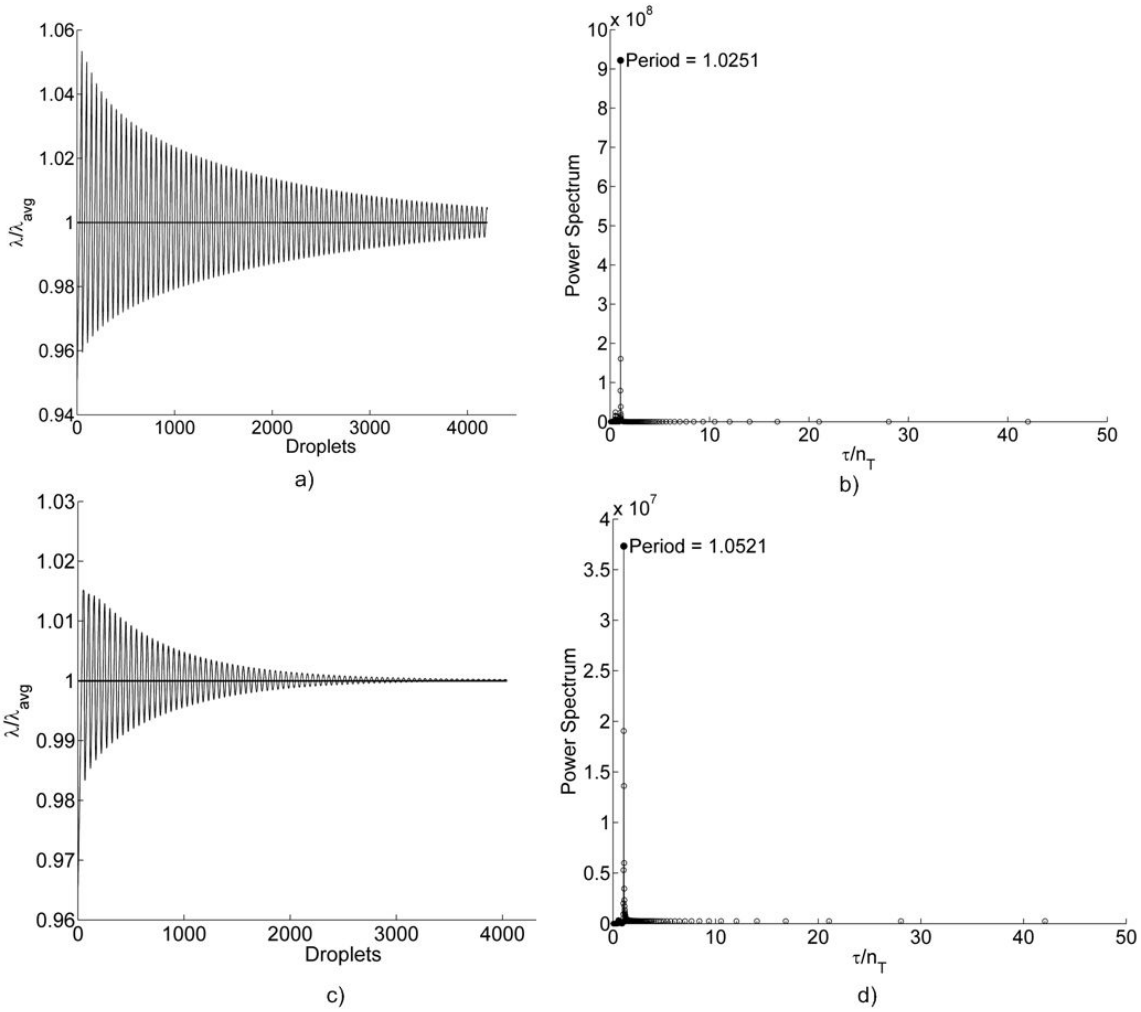

Figure 6.9 Time-trace and FFT analysis of droplet spacing for two numerical simulations (a, b) R_c:R_d:R_m=1:0.1:5, with P_c=500 mBar, γ=50 mN m and (c, d) with R_c:R_d:R_m= 1:0.7:5.

Adding noise ($\sigma(P)$=0.25 mBar) to P_d and P_c further enhances the reproduction of the experimental conditions. Figure 6.10 presents the spacing time-trace with the added noise under the same settings of Figure 6.7 (experimental data). The two signals match quite well in the steady state region of the numerical simulation trace. Both the magnitude and period of the oscillations are qualitatively in agreement. FFT of the numerical results also compares well with

the experimental results (Figure 6.10b). In previous simulations, where noise was absent, the system would always reach a constant output in the long run as oscillations eventually decay (see Figure 6.9c). However, with the addition of noise the system continues to oscillate even after 100 droplet volume replacements. This of course is somewhat expected because of the random perturbations in the inlets (P_d, P_c), what is interesting however, is that $\tau/n_{drop}=1$still remains one of the strongest frequencies in the FFT analysis. This suggests that the small perturbation caused by the randomness of the input conditions perpetuates the slowly varying oscillations in the system. One may thus conclude that long term oscillations are expected to always be part of the response of the pressure controlled droplet generator where feedback is present.

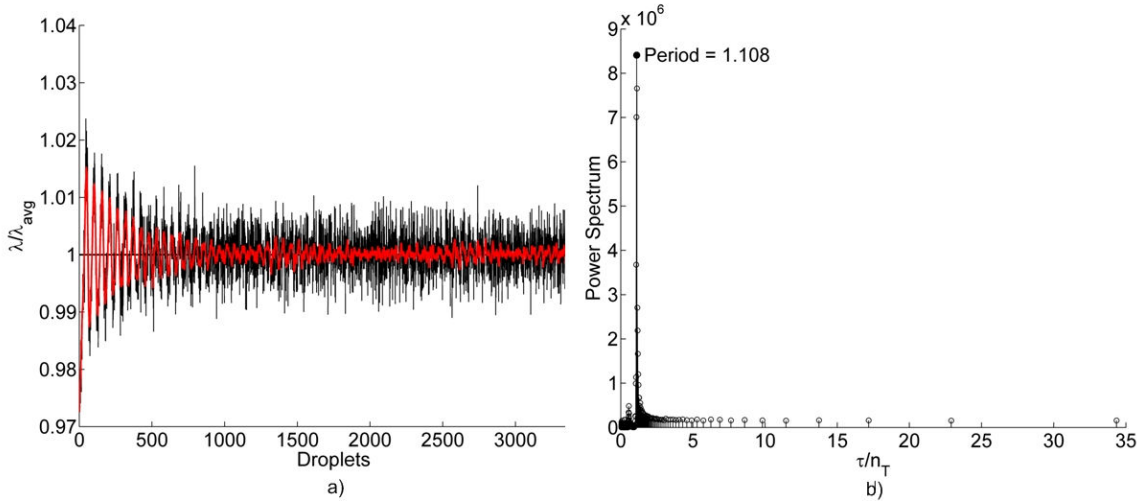

Figure 6.10 Measurements of droplet spacing produced by the numerical simulations for conditions similar to the experimental results of Figure 6.7: Rc:Rd:Rm=1:0.7:5, Pc=800mBar, Pd=790 mBar. Noise is added to the simulations as random fluctuations in Pd and Pc. (a) Time-trace of droplet spacing. The solid black line is the measured values; red line is an 11 point smoothing average (b) power spectrum of the FFT analysis with the peak frequency identified.

Experimental results were also performed to study the transient response during start-up (different than the steady state response in Figure 6.7). Pressures were adjusted so that the interface was just inside the side channel and the main channel was free of droplets. Next, P_d was increased to a new setting and droplets began to form. A video was recorded of the start up. The time-trace of the spacing is shown in Figure 6.11. The results show a similar sinusoidal decaying response as to the numerical results of Figure 6.10. Again the period of these oscillations closely resembles $\tau/n_{drop}=1$. The initial exponential decay takes about 5 cycles before dampening out the large oscillations and reducing to the steady state response.

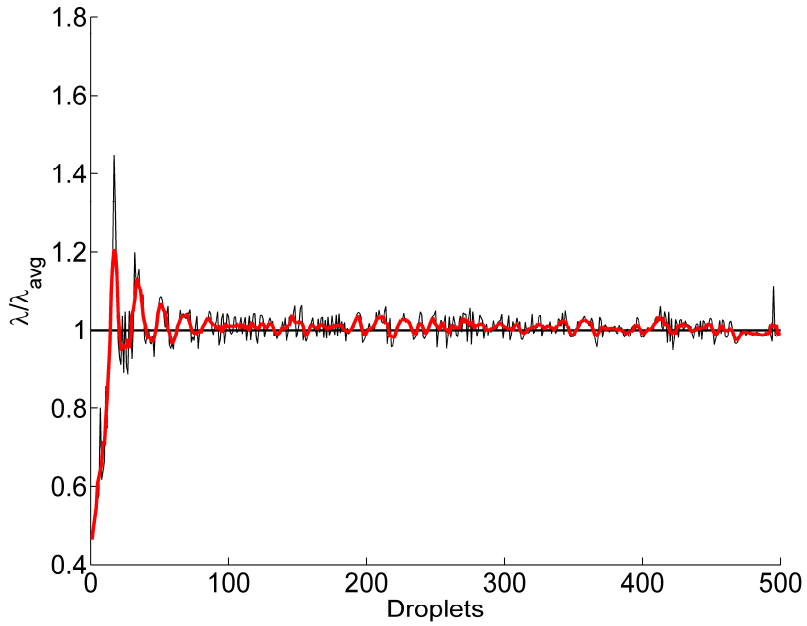

Figure 6.11 Experimental results for the start-up response of a T-junction generator. The channel is initially empty by adjusting the pressure to keep the interface just inside the dispersed channel inlet. The pressure is then increased (P_d=210→250 mBar) and droplets begin to form. Conditions are for silicon oil and water without surfactant with a network design of R_c:R_d:R_m=1:5:2, h=50 μm , and Pc=300 mBar.

Overall, these results are also in agreement with the work of Sullivan and Stone and their analysis of the effect of feedback on a bubble flow focusing generators (Sullivan and Stone 2008). The authors performed a similar numerical simulation and found that the frequency of formation also followed a decaying sinusoidal response. An approximate analytical model developed in conjunction found that the frequency of formation takes the form: $f = f_o + Ae^{(i-\Delta)\omega t}$, where f_o is the steady state solution, A the amplitude of the oscillations and ω the frequency. This sinusoidal response is clearly evident in the numerical and experimental results presented earlier.

Numerical simulations were further utilized to probe methods of improving stability by hastening the decay rate and minimizing the magnitude of spacing fluctuations. Several parameters were varied, and the following trends identified:

- Increasing P_c decreases fluctuations as P_{Lp}, and ΔP_d becomes less influential.
- Similarly, decreasing the surface tension or the curvature decreases fluctuations as this lowers P_{Lp}.
- Decreasing R_{drop} and increasing n_{drop} decrease fluctuations because of lower variance in R_m.
- Increasing R_d relative to R_c decreases the magnitude of the fluctuations.

Although the numerical model developed here is not overly complicated it has proven to be an effective tool for understanding the influence of global network design on droplet generation. In the following section, an approximate analytical analysis is applied to provide a set of guidelines for the design of droplet generators.

6.7 Reducing Fluctuations through Network Design

Here a sensitivity analysis is performed to guide design and provide a quantifiable estimation of expected fluctuations in (i) velocity and (ii) droplet spacing. The single parameter which best captures the combination of these two considerations is the junction pressure (P_j). Following the same logic as before, the relative changes in P_j^* due to the three most prominent sources of variance are:

$$\left.\frac{\Delta P_j^*}{P_j^*}\right|_{P_{Lp}} = \frac{\Delta P_{Lp}^*}{R_d^* + P_d^* - P_{Lp}^*} \qquad \left.\frac{\Delta P_j^*}{P_j^*}\right|_{P_d} = \frac{\Delta P_d^*}{R_d^* + P_d^* - P_{Lp}^*} \qquad \left.\frac{\Delta P_j^*}{P_j^*}\right|_{R_m} = \frac{R_{drop}^*}{R_m^*}\frac{\frac{R_d^*}{R_m^*}}{\frac{R_d^*}{R_m^*} + R_d^* + 1} \tag{6.22}$$

The dependency on many of the variables is similar to the calculation for the variance in droplet speed (Eqns. 6.16-21). The strength of the fluctuations can be controlled by the design of the global network. Figure 6.12 plots the sum of the variance contributions together versus different global network geometries (R_d, R_m) under nominal conditions: P_c=200 mBar, P_{Lp}=5-20 mBar, L_{drop}=100-500 μm and L_c=1 mm. These calculations are made at P_{dmin}, and assuming R_m=R_{mo} where the effects of variance are most severe. Fluctuations are less than 1% to the top right of the thick black line in the figures. The data shows that, in general, increasing R_m and R_d decreases the severity of pressure fluctuations, though with generally diminishing returns for R_d>R_m.

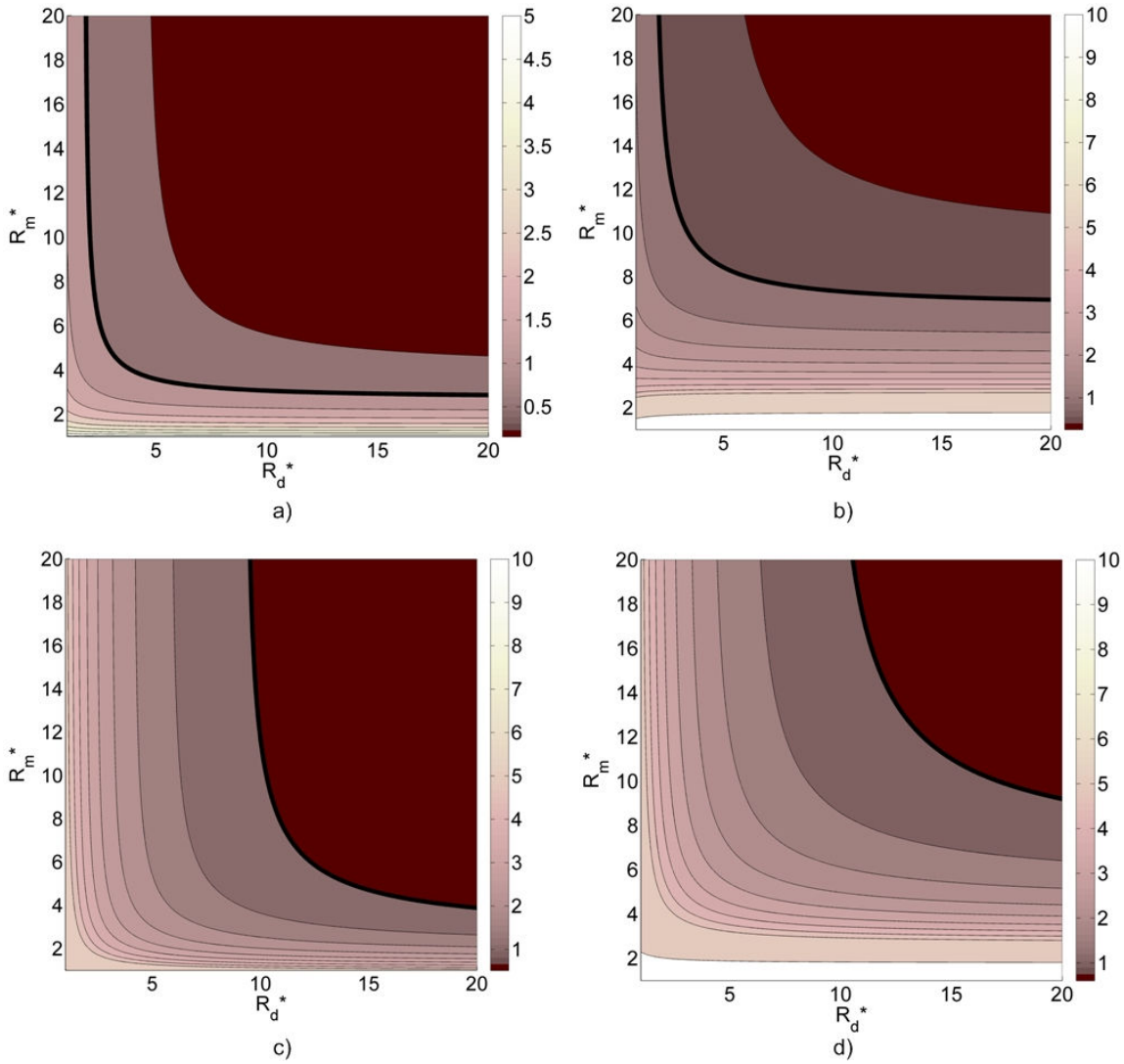

Figure 6.12 Contour plots of the relative variance in the junction pressure (%) from all three sources versus the global network geometry. Plates correspond to (a) $\Delta P_{Lp}^{*} = 0.025, \Delta P_{d}^{*} = 0.0025,\ R_{drop}^{*} = 0.1$ (b) $\Delta P_{Lp}^{*} = 0.025,\ \Delta P_{d}^{*} = 0.0025,\ R_{drop}^{*} = 0.5$ (c) $\Delta P_{Lp}^{*} = 0.1, \Delta P_{d}^{*} = 0.0025,\ R_{drop}^{*} = 0.1$ (d) $\Delta P_{Lp}^{*} = 0.1, \Delta P_{d}^{*} = 0.0025,\ R_{drop}^{*} = 0.5$.

6.7.1 Design Guidelines

From the analysis presented above, a set of design rules can be devised with the focus of (i) minimizing fluctuations in droplet velocity, size and spacing (ii) maximizing the working range to increase the control over droplet generation. Comments are provided in point form below:

Surfactants

- Surfactants should be used whenever possible as they combine to reduce P_{Lp}, R_{drop}, and any effect involving distortion of droplet shape (exit expansion). Adding surfactants is the most effective means of reducing variance in droplet production.
- Surfactant concentration should be kept above the CMC so as to reduce surfactant transport effects (Marangoni stresses). Droplet resistance, for example, actually increases in intermediate concentration of surfactants (<CMC but >0) over surfactant-free conditions or saturated conditions (Stebe, Lin et al. 1991; Stebe and Maldarelli 1994).

Local Geometry

- If surfactants cannot be added than, the generator intersection should be designed to minimize expansion of the interface. For T-junction generators this means using a 1:1 (w_d:w_c) designs.
- The exit should be tapered gently or constructed in some way to reduce pressure spikes that are associated with droplet shape distortion. Controlled exit of droplets, next to the addition of surfactants, is probably the most useful means of improving stability.
- For a fixed pressure P_c, increasing the height of the channels reduces fluctuations because the Laplace pressure drop decreases.

Global Network Configuration

- The number of droplets should be large and the resistance of one droplet compared to the main channel resistance, R_{drop}/R_m, should be small to minimize the influence of a single droplet leaving the channel, $R_d << R_{mo}+nR_{drop}$. A reasonable suggestion is that the main channel should hold at least 50 droplets with a spacing $\lambda=10w_c$, so that fluctuations in R_m will be around 1%.
- To minimize Eqn. (22) the following condition should be met $R_m > R_d >> R_c$. This means a relatively short inlet for the continuous phase and a very long inlet for the dispersed phase.

- The other option is to make the two inlet channels very resistive compared to the outlet (R_c and $R_d >> R_m$) . However, this option is less favourable as it limits the production rate of droplets. Generally the flow of the continuous phase is 5 to 10 times greater than the dispersed phase. A long inlet for the continuous phase means that excessively high pressures are needed to generate a significant amount of flow since most of the pressure drop is contained in the long inlet channel. Higher pressures require more bulky equipment and increase the chance of leakage.
- A reasonable design criteria is that $R_m = R_c$ since improvements are marginal for $R_d > R_m$. Remember the hydrodynamic resistance depends on the viscosity of the fluid. For most water/oil combination s $\mu_d/\mu_c = 1/3 \rightarrow 1/10$. For a design with uniform cross-sectional longer than main channel to match $R_d = R_m$. For bubbles generation where air is the dispersed phase, this means excessively long inlet channels, in the range of several meters, to compensate for the low viscosity. The necessity of these long channels for stable bubble generation has been known for quite some time (de Mas, Gunther et al. 2005).

Pressure System

- For the condition where $R_d = R_c$, the effective pressure range is $P_c < P_d < 2P_c$.
- A highly stable and reliable source of air pressure is required to eliminate transients in the air supply. As part of this system, high resolution pressure regulators are needed to fine tune the flow of the two fluids.
- For a given P_c and pressure resolution, one should verify that the resolution available for controlling droplet size and spacing is sufficient for the application by calculating the number of discrete operating points available.
- Overall, higher applied pressures (P_c) improve stability by (i) reducing the relative importance of Laplace pressure drop (P_{Lp}) compared to hydrodynamic pressure drop (ii) reducing droplet resistance as $R_{drop} \propto u_{drop}^{-1/3}$ and droplet speed is proportional to the applied pressure (Bretherton 1961) (iii) wider dynamic range for the P_d when compared to the resolution of the pressure regulator and (iv) reducing the effect of external pressure fluctuations that may occur such as changes in head between reservoirs as fluid levels rise and fall during operation.

- Running the system away from P_{dmin} also reduces fluctuations as the majority of the pressure drop in the dispersed channel (P_d- P_{Lp} -P_j) is from hydrodynamic losses and not pressure jump across the interface P_{Lp}.

A case study is presented below to afford some context for these rules, and to attach tangible values to the variables which have been introduced.

6.8 Case Study

Consider an application that uses a T-junction generator with silicon oil (μ_c=10 mPas) and water (μ_d=1 mPas) as the two phases without a surfactant (γ~50 mN/m). All channels have the same cross-sectional dimension of w_c=100 μm and h=35 μm. The pressure system in use has an available range from 0-1000 mBar with a resolution of 0.5 mBar.

Calculations are based on using the midpoint of the pressure system P_c=500 mBar. Because surfactants are not used and the surface tension is relatively high, a 1:1 inlet geometry is chosen to limit interface shape distortion during the formation process. A gradual taper can be added to the end of the channel to reduce pressure pulses as the droplets exit. The pressure drop across the interface as it resides in the dispersed channel is P_{Lp}=20 mBar and $P_{Lp}^* = 0.04$. Assuming a maximum droplet spacing of $10w_c$=1 mm, with a minimum of 50 droplets, the main channel length should be design to be L_m=50 mm.

Generally, L_c should be as small as possible, however, for practical reasons it is better to make the length slightly larger. During start up sometimes the two phases may reverse flow and the dispersed phase may enter into the continuous phase channel. If this happens, then we do not want dispersed phase to reach all the way into the reservoir of R_c causing it to be trapped and ejected later during operation. A reasonable length to help reduce the probability of this happening is L_c=10 mm, and thus $R_m^* = 5$.

The next step is to make an assumption on the droplet resistance R_{drop}. For this example, it is assumed that droplets will have a real length of L_{drop}~$1.5w_c$ and a hydrodynamic resistance of L_{hdrop}~$3L_{drop}$., thus $R_{drop}^* = 0.045$. Hence at maximum spacing, the contribution to the total resistance of R_m from the droplets is 31% (nR_{drop}/R_m), and the change in R_m for one droplet leaving is ~0.6%. Following the suggested design of R_m=R_d, the length of dispersed inlet L_d

would need to be 50 cm when considering the viscosity contrast. This is an extremely long channel to fit on a chip. Typically, a long capillary with a small inner diameter would be attached to the inlet to increase the channel length. The best way to achieve the same effect without the long capillary is to create a two-level microchannel design where a portion of the dispersed inlet is much shallower than the rest of the network. Channel resistance scales with h^{-3}, and therefore reducing the height by half will require a channel only 1/8th the length (L_d~60mm), a size far more manageable to fit directly on the chip. Smaller channels are more favourable than a long capillary because they also reduce the dead volume in the system thereby decreasing the time it takes to reach steady state.

Based on this setup the pressure range for P_d^* is 0.87→2.04 or in real terms 436→1020 mbar. The offset from the minimum pressure δP_d^* needed to generate a continuous stream of droplets is approximately 10 mBar, so that the lower limit is now 446mbar. Assuming that 1/3rd of the pressure range is actually used since only smaller droplets are desired, then there are (1020-446)/(3·0.5)=382 discrete system points that can be used to tune droplet generation. Additionally, the flow rates can also be estimated using Eqn. 6.11. For a pressure setup of P_c=500 mBar and P_d=600 mBar, flow rates are estimated (without consideration of R_{drop}) to be Q_d=0.6 µl min^{-1} and Q_c=1.20 µL min^{-1} for a flow ratio of approximately φ=0.5.

For this geometry and setup, calculations for the expected fluctuations in P_j are only 0.75%, and u_{drop} only 0.81%. If P_c is increased to 800 mBar, these fluctuations reduce to 0.48% and 0.51% respectively. If the same system setup is used, but surfactant is added (γ=10 mN m^{-1}), the fluctuations are reduced to 0.14% and 0.16%. In this case, the original dispersed channel $R_d^* = 5$ can be replaced with a shorter channel $R_m^* = 0.5$ still with good performance (0.65%, 0.71% respectively). This example demonstrates the application of the design rules to a specific T-junction generator design. In the following section the design rules are put to the test by comparing the predictions with experimental measurements.

6.9 Testing of Design Rules

Figure 6.13 plots $\sigma(\lambda)/\lambda$ against the dispersed pressure P_d for three network designs (R_d:R_c:R_m), 1:0.1:5, 1:0.7:5, 1:4:5. The data confirms many of the conclusions drawn from the analysis of reducing fluctuations in P_j^* (Eqn. 6.22). As expected, spacing fluctuations decrease with increasing P_c as the effects of P_{Lp} diminishes. On average, fluctuations decreased in accordance with the design rules outlined for the global network ($\uparrow R_d$ causes $\downarrow \sigma(\lambda)/\lambda$). From the figure, the stability (lowest to highest variance) of the three designs can be ordered as (○) 1:4:5, (Δ) 1:0.7:5 and (■) 1:0.1:5, in agreement with theory. Furthermore, moving the system away from P_{dmin}, by increasing P_d, also increases the stability of the system as highlighted by the arrow in Figure 6.13, again in agreement with theory. These results also demonstrate the impressive performance which can be achieved by following the design rules. Less than 0.5% variance in spacing was achieved for the 1:4:5 design and less than 1% variance for the 1:0.7:5 design at the upper end of P_d.

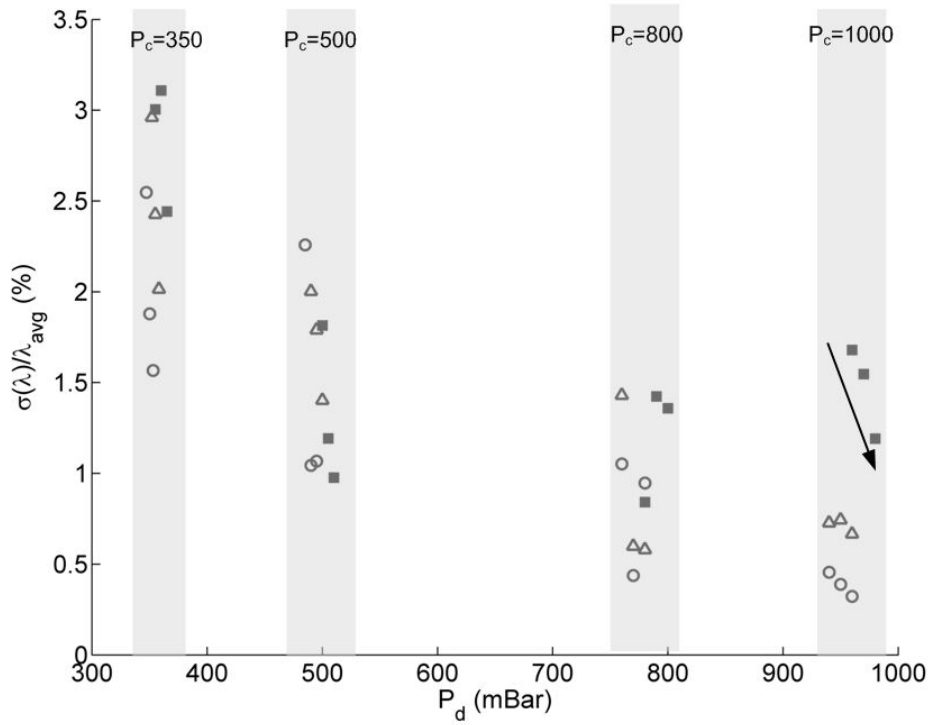

Figure 6.13 Measured variance in droplet spacing for different network designs as a function of applied pressure Pd. Data corresponds to network geometries of R_d:R_c:R_m (○) 1:4:5, (Δ) 1:0.7:5 and (■) 1:0.1:5. Experimental conditions are provided in Section 4.5.

6.10 Conclusions

This work has furthered the understanding of the influence of global network design on the behaviour of pressure driven microfluidic droplet generators. Periodic oscillations in the flow conditions, through changes in the droplet resistance and interface shape, create fluctuations in generator performance. These fluctuations can be characterized by two time scales. Short-term fluctuations which occur over a period equal to, or less than, the droplet generation period; and long-term fluctuations which extend over several droplet generation cycles. The effect of these two fluctuations can be quantified by monitoring the droplet velocity (short-term) and droplet spacing (long-term).

Both types of fluctuations can be minimized through effective design of the droplet generator. Short-term fluctuations are typically prevalent when there are significant changes in interface curvature and large surface tension. Minimizing deviations in interface shape by using a 1:1 design and taper outlet is an effective means of reducing fluctuations. Long-term fluctuations occur because of the feedback effect between the flow-field and the production of droplets. These fluctuations tend to have a periodicity that is associated with the life-time of a droplet in the system, i.e. the residence time. Long-term fluctuations cannot be entirely eliminated, but their influence can be subdued through proper design of the global network as identified by the theoretical model which was developed as part of this study.

Nomenclature

Acronyms:

1D	one dimensional
2D	two dimensional
3D	three dimensional
CMC	critical micelle concentration
OTS	octadecyltrichlorosilane
PDMS	poly(dimethyl)siloxane
PFO	1H,1H 2H, 2H-Perfluoro-1-octanol
SDS	sodium dodecyl sulfate

Mathematical Symbols:

$\alpha_{lag,fill}$	dimensionless lag and fill volumes
β	dimensionless necking time
β_{slip}	slip factor of droplet
γ	interfacial tension (N m^{-1})
κ	curvature (m^{-1})
λ	inter-droplet spacing (m)
μ	dynamic viscosity of fluid (Pa s)
η	ratio of dispersed to continuous phase viscosities
τ	time (s)
φ	ratio of dispersed to continuous phase flow rates
Λ^*	T-junction dispersed to continuous phase widths
a	thread pitch of screw (turn m^{-1})
f	frequency (Hz)
h	height (m)
n	number of droplets
u_d	droplet velocity (m s^{-1})
$w_{c,d,m}$	width of dispersed, continuous and main channels (m)
t	time (s)

D	diameter of screw in syringe pump (m)
$L_{c,d,m}$	length of continuous, dispersed and main channels (m)
$P_{c,d,m,j}$	pressure at continuous, dispersed, main channel exits and junction (Pa)
P_{Lp}	Laplace pressure jump across the interface (Pa)
$Q_{d,c,m}$	flow rate of dispersed, continuous or main channel (m^3 s)
Re	Reynold's number (dimensionless)
$R_{c,d,m}$	hydrodynamic resistance of continuous, dispersed and main channel(Pa s m^{-3})
R_{drop}	hydrodynamic resistance of droplet (m)
V_{drop}	droplet volume (m^3)
V_{fiill}	droplet volume at the end of the filling stage (m^3)

Chapter 7

Passive Droplet Trafficking at Nodes in a Microfluidic Network

The work presented in this chapter was published in the following articles:

Glawdel T., Elbuken C., Ren C.L., "Passive Sorting of Droplets at Microfluidic Junctions under Geometric and Flow Asymmetries", **Lab on a Chip**, 11 (2011) 3774-3778.

C. Elbuken (Post Doctoral Fellow in Department of Mechanical Engineer, University of Waterloo) assisted in writing the Matlab code for performing automated video analysis of the droplet sorting during experiments. He also developed part of the numerical code used to study droplet sorting.

7.1 Introduction

Once droplets are generated they must travel along a series of conduits that compose the microfluidic network. For the trivial case of one exit, droplets simply move along the outlet at a fixed speed and spacing. However, when junctions are added, droplets can choose more than one path, and the trafficking of droplets increases in complexity. The increasing complexity lies in the fact that droplets alter the hydrodynamic resistance of the channel they travel within which influences the global flow field. This creates a feedback effect, whereby the decision made by a preceding droplet influences the decision of subsequent droplets that enter a bifurcation. In some cases, the sequence of decisions can form a pattern of droplet trajectories that repeats indefinitely; while under other circumstances the system can be entirely chaotic (Cybulski and Garstecki 2010; Sessoms, Amon et al. 2010; Smith and Gaver 2010)

Droplet trafficking is thus an example of the transport of discrete elements or signals through networks consisting of nodes that impart a non-linear behaviour; analogous to transport of cars on roads (Nagel 1996), blood cells through capillaries (Carr and Lacoin 2000) and many other biological systems (Angeli, Ferrell et al. 2004). The long-distance interaction between droplets through the global flow field has been exploited to create interactive elements such as logic gates (Cheow, Yobas et al. 2007; Prakash and Gershenfeld 2007), signal encoder/decoders (Fuerstman, Garstecki et al. 2007), sorters (Cristobal, Benoit et al. 2006; Yamada, Doi et al. 2008; Cybulski

and Garstecki 2010), automated coalescence (Niu, Gulati et al. 2008) and storage units (Boukellal, Selimovic et al. 2009). Understanding the motion of droplets in networks is critical to the development of droplet microfluidics; particularly, for combinatorial studies involving multiple reagents and conditions, where achieving high throughput through multiplexing and massive parallelization will require effective trafficking of droplets to their intended destination (Shui, Eijkel et al. 2007; Teh, Lin et al. 2008; Baroud, Gallaire et al. 2010). Active methods (Ahn, Kerbage et al. 2006; Link, Grasland-Mongrain et al. 2006; Niu, Zhang et al. 2007; Wang, Flanagan et al. 2007; Cordero, Burnham et al. 2008; Niu, Zhang et al. 2009; Yap, Tan et al. 2009) can be used to force droplets to follow specific paths; however, these methods must always overcome the natural response of the system.

Past studies have focused on the simplest microfluidic network consisting of (1) a single incoming channel that splits into two outlets or (2) a loop where the two channels recombine into a single outlet (refer to Figure 7.1). Both T-shaped and Y-shaped junctions have been investigated. Droplets that enter the junction may either split into two daughter droplets, or sort into one of the outlet channels. These two modes serve as an effective means for classifying the operational regime of a junction.

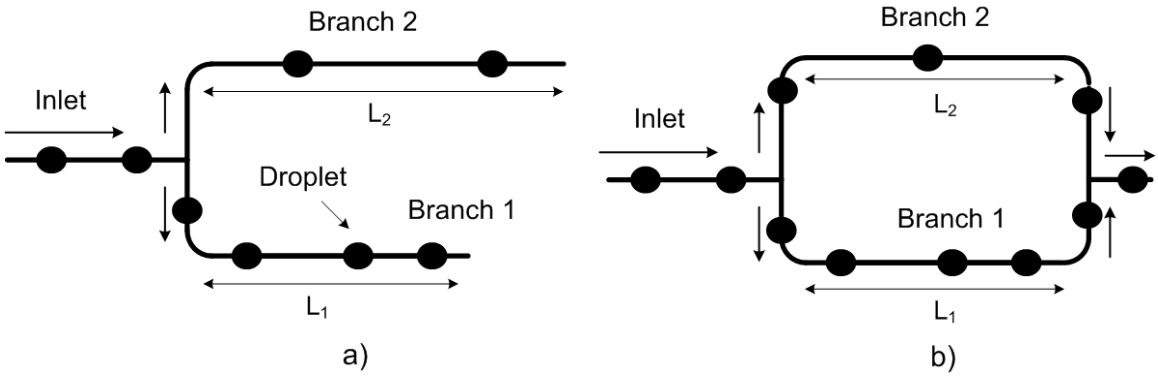

Figure 7.1 Diagram of the two basic designs, (a) branch and (b) loop, used to study droplet trafficking**.**

Splitting

Using a junction to split droplets is one of the most common passive methods of geometrically controlled droplet breakup (Link, Anna et al. 2004). Breakup is typically restricted to relatively high Capillary numbers (*Ca*) and large droplets. Link *et al.* found that a critical Capillary number exists for each droplet size above which breakup will occur: $Ca_r = \alpha\varepsilon_o\left(1/\varepsilon_o^{2/3} - 1\right)^2$, where α is a fitting constant relating the viscosity ratio and geometry, and ε_0 is the extension of the droplet related to the size of the droplet (Link, Anna et al. 2004). Further work by Leshanksy and

Pinsmen argued that the fundamental formulation of this equation is not correct because it is based on the Rayleigh-Plateau instability which should be suppressed under the confinement of microchannels (Leshansky and Pismen 2009). Instead the authors developed a model based on the blockage of flow around the droplet as it is being split using lubrication analysis. They came up with a separate equation that has a similar overall profile to Link *et al.* Continued work by Jullien *et al.* revealed that splitting can be sub-divided into two other regimes depending on whether droplets obstruct or do not obstruct the flow during the process (Jullien, Ching et al. 2009). Numerical simulations by Carlson *et al.*, confirm similar arguments that splitting depends on the size of the droplet and Capillary number (Carlson, Do-Quang et al. 2010).

Asymmetric branch channels can be used to control the split ratio by modulating the division of flow to the two outlets (Adamson, Mustafi et al. 2006; Menetrier-Deremble and Tabeling 2006; Nie and Kennedy 2010). Control can also be achieved by adjusting the output pressures of the two branches (Yamada, Doi et al. 2008). One concern with breakup is the stability of the process over long time periods. If the two outlet branches are long, then the breakup of droplets changes the hydrodynamic resistance of the branches over time leading to oscillations in the split ratio. To overcome this problem, Nie and Kennedy used a loop design combined with a pressure equalizing bridge at the outlet (Nie and Kennedy 2010). The bridge allows for the droplets to exit via separate outlets once there split. Still when droplets were present in the loop the split ratio had a standard deviation of more than 5%.

Non-Splitting

If droplets do not split at the junction then they will sort into one of the outlets. The mechanism that governs sorting differs depending on the size of the droplets relative to the channel, which may be classified into three sub-regimes: external flow mediated, collision mediated and feedback mediated.

External Flow Mediated

In external flow mediated sorting, droplets do not significantly alter the flow field, and travel following the streamlines set up by the continuous phase. By creating diverting streamlines at the junction droplets can sorted based on size (Tan and Lee 2005; Tan, Ho et al. 2008; Mazutis and Griffiths 2009). When a droplet reaches the junction it may be influenced by one, or both diverting flows; the imbalance created on the droplet by viscous drag forces it towards one of the

exits. Generally, the application for this type of sorting is to separate smaller satellite droplets from larger droplets in order to purify the droplet stream.

Collision Mediated

At relatively low confinement ($L_{drop}<w_c$), and close droplet spacings, droplets may collide at the junction before they sort. Belloul *et al.* studied this phenomenon in an asymmetric branch design where droplets were small so that their hydrodynamic impact was minimal (Belloul, Engl et al. 2009). When droplet spacing was large, all of the droplets would sort into the short channel. As the spacing decreased, however, droplets began to sort into both channels even though they should still theoretically sort into the shorter channel. The reason for this behaviour is the collision of droplets at the junction. Small droplets enter the junction and stagnate for a short period of time before they choose one of the outlets. If a droplet has not left the junction before the next droplet enters there will be a collision. Once they collide, droplets are able to sort into both outlets. Belloul *et al.* found a limit for the collision regime related to the stagnation time, the asymmetry in the branch channels and the degree of confinement of the droplets (Belloul, Engl et al. 2009).

Feedback Mediated

Feedback mediated sorting covers the remaining regime between collision/external flow mediated sorting and splitting. Confinement is important, and droplets have a significant effect on the flow field by changing the hydrodynamic resistance of the channels. Sorting at the junction is governed by a simple rule: droplets always sort into the branch with the highest flow rate (Engl, Roche et al. 2005). This causes the droplets to distribute themselves between the two outlets in an attempt to balance the flow between the two outlets.

There are two operational modes for the junction: filtering or sorting (also termed repartition) (Engl, Roche et al. 2005; Jousse, Farr et al. 2006; Sessoms, Belloul et al. 2009). Filtering occurs when all the droplets sort into only one of the branches. This occurs at high dilution when the population of droplets in the filtering branch is not large enough to balance the two flow rates. At lower dilutions droplet divide between the two outlets. The transition between the two modes is defined by a critical spacing, λ_f, which may also be interpreted as the critical number of droplets required to increase the resistance of the smaller channel to match that of the larger channel.

As droplets continuously enter and exit the branches, flow rates may oscillate in either a periodic or aperiodic manner (Jousse, Farr et al. 2006; Fuerstman, Garstecki et al. 2007; Cybulski and Garstecki 2010; Sessoms, Amon et al. 2010). Fascinating sorting patterns can form where the sequence of choices made by the droplets repeats indefinitely. For example, defining a droplet as going into branch #1 as Up and branch #2 as Down, a sequence such as UDUUDUD can form. Once set in place, sequences are generally stable, being able to withstand most natural disturbances. Large disturbances can cause the specific pattern to change (i.e. UDUUDUD to UUUDDUD) but the overall pattern length, and composition (number of U-s and D-s) remains the same (Cybulski and Garstecki 2010). Hence the system is often said to exhibit ``memory``. Initial conditions influence the exact sequence that forms but have no effect on the overall pattern length or composition once steady state is reached (Cybulski and Garstecki 2010; Sessoms, Amon et al. 2010).

Once a droplet makes a decision it influences other droplets for the time that it remains in the channel. Therefore, each decision has a finite lifespan, or time-delay, for which it remains active. Hence, cyclic periods correspond to the residence times of droplets in the branches (Sessoms, Amon et al. 2010). Parametric studies have shown that the length and composition of the pattern depends on the incoming spacing compared to the channel lengths, and the droplet resistance to the channel resistance (Jousse, Farr et al. 2006; Cybulski and Garstecki 2010; Sessoms, Amon et al. 2010; Smith and Gaver 2010). Pattern complexity increases as the incoming spacing decreases since more droplets are present in the channel. Surrounding the islands of periodic order are regimes where the system is chaotic (no discernible pattern forms), yet the droplets still divide in proportions that minimize the flow imbalance. Alternatively, the two regimes may be classified as being reversible (periodic) and irreversible (chaotic) (Fuerstman, Garstecki et al. 2007; Behzad, Seyed-allaei et al. 2010). Rhythmic behaviour, bifurcations (chaotic, periodic behaviour) and multi-stability (several attractors for a set of parameters) are common properties of discrete time-delayed feedback systems; signalling dynamics of neurons being one of the most notable examples (Wu, Zhang et al. 2004). Droplet sorting may also be considered as a form of simple cellular automata (Schiff 2008).

Invaluable to the understanding of the sorting process has been the adaption of compact numerical modelling to the problem (Jousse, Farr et al. 2006; Fuerstman, Garstecki et al. 2007; Schindler and Ajdari 2008; Sessoms, Belloul et al. 2009; Behzad, Seyed-allaei et al. 2010; Cybulski and Garstecki 2010; Sessoms, Amon et al. 2010; Smith and Gaver 2010). This approach

takes a global look at the flow field treating droplets as a series of spatially moving resistors travelling along a network of fixed resistors which are the channels. Flow fields are calculated in a similar manner to the rules of electric circuits, where pressure replaces voltage, flow rate replaces current and hydraulic resistance replaces electrical resistance; combined with the rule that droplets sort into the channel with the highest flow rate when they enter the junction. Computational costs are reduced by using a highly variable explicit time-stepping scheme to march the simulation forward. Time steps are determined by the minimal interval to the next event that can change the resistances in the network. Examples include a new droplet being generated, a droplet exiting the domain or a droplet entering the sorting junction. Compact numerical modelling has served as an effective tool for revealing the behaviour of various droplet/flow field interaction devices (Schindler and Ajdari 2008).

The advantage of using numerical modelling is that many parameters can be probed using limited resources and tests may be performed which cannot be setup in the real world. In fact, although several studies involving droplet trafficking include experimental results, these are generally limited in size and scope, and only serve to provide a few validation points for the more comprehensive numerical and analytical models. The difficulty with performing experiments lies in creating a stable environment for sorting patterns to form. All sources of experimental noise must be suppressed. Droplet size and spacing must be consistent with very little variance, <2%, or patterns will degrade quickly. This requires effective design of the microfluidic network (Fuerstman, Garstecki et al. 2007; Fuerstman, Lai et al. 2007; Sessoms, Amon et al. 2010) or the use of specialized droplet generation systems (Cybulski and Garstecki 2010).

Initial approaches to model the sorting problem used a “mean-field” approximation to determine the distribution of droplets (Engl, Roche et al. 2005; Jousse, Lian et al. 2005; Sessoms, Belloul et al. 2009; Cybulski and Garstecki 2010). In this formulation droplets are treated as a continuous medium rather than as discrete elements. Such a macroscopic approach leads to “average” values for the various parameters and is valid when the concentration of droplets is high in the two outlets. Mean field models have shown good agreement with experimental (Engl, Roche et al. 2005; Sessoms, Belloul et al. 2009) and numerical results under these limits. However, continuum models were not able to predict the periodicity that occurs, nor the changes in periodic structure that evolve at low droplet concentrations, nor the bifurcation between order and chaos.

To date, only one study, performed by Sessoms *et al.*, has successfully developed a discrete model of the system (Sessoms, Amon et al. 2010). Sessoms *et al*. seminal work developed a set of "selection rules" that describe nearly all salient features of the sorting problem for loop-based designs with asymmetric branch lengths. To assist their understanding, Sessoms *et al.* studied the problem using an idealized numerical model that made the problem more tractable by removing the coupling between the flow field and the droplets, and replacing the sorting rule (i.e. branch with the highest flow rate in conventional models) with a resistance balance equation. They also introduced the concept of tracking "holes" left behind when a droplet sorts into an opposite branch. Thus each sorting event creates a droplet which sorts into one channel and a hole into the other. By tracking the number of holes and droplets, the authors observed that only a limited number of conditions occur where the total number of holes and droplets is either constant or oscillates by one. Additionally, they observed that the pattern length was always equal to the residence time of one of the branches (cycle times). From these observations they were able to derive analytically a set of rules to determine which cycle time of the two was possible, and thus were able to predict the pattern length, and when the pattern will change. The model agreed very well with full-model simulations and experiments. Their work represents the most comprehensive model on the sorting phenomenon.

In this Chapter the work of Sessoms *et al.* is further developed by expanding the degrees of asymmetry that are considered including geometric (branch lengths, cross-sectional areas), droplet (resistances) and flow (outlet pressures) asymmetries. Each type of asymmetry is discussed briefly below:

- Geometric asymmetries can be imposed by the design and fabrication of the network. Studies to date have focused only on changing the length of the branches while keeping the cross-sectional areas the same. Changes in cross-sectional area have a dual effect. First, the relative speed of the droplets changes between the two channels, and second, the resistance changes in a non-linear manner for both the channel and droplet.
- Droplet resistances in both branches may vary based on the geometry, or by external influences such as heating one branch to change the viscosity (Yap, Tan et al. 2009).
- Adjusting the outlet pressures changes the flow rates to the two branches and is thus simple means of regulating the distribution of droplets in the channels. A pressure imbalance can also occur naturally. For example, if the exits of the sorter are connected to a larger network, then changing flow conditions downstream can alter the pressures at the exits and the sorting outcome.

These encompass all the asymmetries that are probably to occur in a typical microfluidic junction. First, an analytical model is developed based on the continuum approximation. Next, numerical simulations (full-model and ideal-model) are used to gain an understanding of the sorting phenomena. From these observations, a new discrete model is developed that differs from the one presented by Sessoms *et al.* and is applicable to all types of asymmetries. Results are presented for the general case (all asymmetries), and then for the more simplified, and more practical case of only asymmetric branch lengths and pressures. In addition to predicting the pattern length, composition and bifurcations, the model also includes a basic stability analysis to determine whether a predicted pattern will revert to chaos. A method for determining all of the unique patterns that can occur from a given number of U-s and D-s is also presented. The predictive power of the model is quantified by comparing it to both numerical (ideal-model and full-model) and experimental results. The chapter concludes with a discussion of the practical implementation of sorting at a junction and design considerations for a "random droplet sampler".

7.2 Analytical Model: Continuum Based Approximation

In this section, an analytical model is developed based on the assumption that the droplets are not discrete elements but may be approximated as a continuous medium. Similar analyses have been performed on loop structures and asymmetric bifurcations by Sessoms *et al.*, Cybulski *et al.*, and Engl *et al.* to obtain mean field approximations of droplet trafficking (Engl, Roche et al. 2005; Sessoms, Belloul et al. 2009; Cybulski and Garstecki 2010). Here these works are adapted, and improved, to also include asymmetric pressures, channel cross-sectional areas and droplet resistances. As well, droplet spacing (Sessoms, Belloul et al. 2009) rather than frequency (Cybulski and Garstecki 2010) was chosen as the parameter characterizing sorting, since the former leads to a less ambiguous set of equations that are easier to interpret. A model is first developed for the general case (all asymmetries), which is then simplified to study the more practical circumstance of only asymmetric branch lengths and pressures. Note that in the following derivation dimensionless values are marked by an asterisk.

7.2.1 Conceptual Framework

Relevant variables describing the operation of the T-junction sorter are presented in Figure 7.2. Droplets enter the system from the main channel with an incoming spacing (λ) and frequency (f) and leave with spacings (λ_1, λ_2) and frequencies (f_1, f_2). The system is defined by two output branches of length (L_1, L_2), base hydrodynamic resistances ($R_{hyd}^{(1)}$, $R_{hyd}^{(2)}$), cross-sections ($w_1 \cdot h_1$, $w_2 \cdot h_2$) with applied exit pressures (P_1, P_2). Each channel may also have a unique droplet resistance ($R_{drop}^{(1)}$, $R_{drop}^{(2)}$). Because of decisions at the junction, the number of droplets in the two branches (n_1, n_2) changes dynamically as droplets sort or exit the system. The primary goal of the model is to predict the distribution of droplets between the two branches.

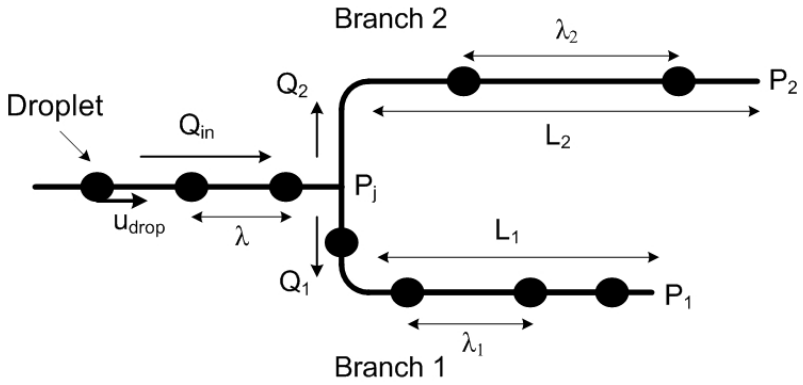

Figure 7.2 A diagram indicating the main variables relevant to sorting at a T-junction. Asymmetry may exist in the branch lengths, cross-sections, and applied pressures.

7.2.2 General Model of Sorting

The first task is to determine which of the two channels the droplets first filters into, and the critical point where droplets stop filtering and begin sorting into both channels. By default the shorter channel is not necessary the filtering channel since a pressure bias can cause it to have a larger effective resistance. The filtering channel is actually the one with the naturally higher flow rate in the absence of droplets, which can be determined by taking a ratio of the flow rates:

$$\frac{Q_1}{Q_2} = \frac{P_j - P_1}{R_{hyd}^{(1)}} \frac{R_{hyd}^{(2)}}{P_j - P_2} = \frac{R_{eff}^{(2)}}{R_{eff}^{(1)}} \tag{7.1}$$

Envisioning that the same pressure drop (P_j-P_1) was applied across both branches, an effective resistance can be defined that includes the pressure imbalance:

$$R_{eff}^{(1)} = R_{hyd}^{(1)}$$
$$R_{eff}^{(2)} = R_{hyd}^{(2)} \frac{P_j - P_1}{P_j - P_2} = \frac{R_{hyd}^{(2)}}{P^*} \tag{7.2}$$

where P^* is defined as the non-dimensional pressure skew between the two outlets. The hydrodynamic resistance of a rectangular microchannel is given by (Bruus 2007):

$$R_{hyd} = \frac{12\mu L}{wh^3}\left[1 - \frac{h}{w}\left(\frac{192}{\pi^5}\sum_{n=1,3,5}^{\infty}\frac{1}{n^5}\tanh\left(\frac{n\pi w}{2h}\right)\right)\right]^{-1} \tag{7.3}$$

where μ is the viscosity. Droplet resistance may also be defined as an equivalent added channel length in the form:

$$L_{drop} = \frac{R_{drop}}{R_{hyd}} L_{channel} \tag{7.4}$$

If $R_{eff}^{(2)} / R_{eff}^{(1)} \geq 1$, then branch 1 is the filtering channel, and if not it is branch #2 . From this point the filtering channel is designated with the subscript *a* and the sorting channel with *b*. This definition can be summarized in the following form:

If $R^{(2)}_{eff} >= R^{(1)}_{eff}$ *Then* subscript *1*→ *a*, and *2*→ *b*
Else *Then* subscript *2*→*a*, and *1*→ *b*

P^* is recalculated as $P^*=(P_J-P_b)/(P_J-P_a)$ and the effective lengths, hydrodynamic resistances, cross-sections, droplet resistances are re-designated as well. Droplets choose the channel with the highest flow rate when they enter the junction; this naturally forces the total flow rates ($Q^{(b)}_T$, $Q^{(b)}_T$) to be nearly equal over the long term (Engl, Roche et al. 2005; Schindler and Ajdari 2008; Sessoms, Belloul et al. 2009; Smith and Gaver 2010). Applying conservation of mass to the dispersed phase:

$$Q_d = Q_d^{(a)} + Q_d^{(b)} \tag{7.5}$$

where $Q_d=V_d f$, V_d is the droplet volume and f the frequency. Substitution reduces the previous equation to:

$$f_d = f_d^{(a)} + f_d^{(b)} \tag{7.6}$$

Frequency is related to the droplet speed and average spacing by $f=u_{drop}/\lambda$. Droplet velocities are calculated as: $u_{di}=Q_i\beta_i/A_i$, where Q_i is the total flow rate of both phases, A_i the cross-sectional area and β_i the slip factor (relative speed of the droplets to the average speed of flow). Assuming that incoming flow rate splits *equally* between the two channels then:

$$\frac{2\beta_{in}}{A_{in}\lambda}=\frac{\beta_a}{A_a\lambda_a}+\frac{\beta_b}{A_b\lambda_b} \tag{7.7}$$

where the subscript $_{in}$ refers to the incoming channel that leads to the T-junction. Spacing is related to the number of droplets in each branch by $n=L/\lambda$, resulting in the following equation:

$$\frac{2\beta_{in}}{A_m\lambda}=\left(n_a\frac{\beta_a}{A_aL_a}+n_b\frac{\beta_b}{A_bL_b}\right) \tag{7.8}$$

The question remains how to determine the number of droplets required in each channel to balance the flow rates. Using compact modelling of the flow, the flow rate in each branch is:

$$Q^{(a)}=\frac{P_j-P_a}{R_{hyd}^{(a)}+n_aR_{drop}^{(a)}} \qquad Q^{(b)}=\frac{P_j-P_b}{R_{hyd}^{(b)}+n_bR_{drop}^{(b)}} \tag{7.9}$$

where now the total hydrodynamic resistance of the channels is the sum of the base resistance and the resistance added by the droplets. On average the two flow rates are equal to each other, by rearranging the equations a relationship for n_b is found:

$$n_b=\frac{P^*}{R_{drop}^*}\left(-\frac{\left(R_{hyd}^*-P^*\right)}{P^*R_{drop}^{*(a)}}+n_a\right) \tag{7.10}$$

where the dimensionless terms have been included: $R_{drop}^*=R_{drop}^{(b)}/R_{drop}^{(a)}$, $R_{hyd}^*=R_{hyd}^{(b)}/R_{hyd}^{(a)}$ and $R_{drop}^{*(a)}=R_{drop}^{(a)}/R_{hyd}^{(a)}$. Filtering occurs when all of the incoming droplets sort pass through channel *a*. Therefore, equating the left side to zero and applying the spacing relationship, $\lambda_a=\lambda/2$, for perfectly divide flow rates, the condition for droplet sorting is found:

$$\frac{2}{\lambda_f^*}\geq\frac{\left(R_{hyd}^*-P^*\right)}{P^*R_{drop}^{*(a)}} \tag{7.11}$$

where the non-dimensional spacing $\lambda^*=\lambda/L_a$ has been introduced. Solving Eqn. 7.8 and Eqn. 7.10 then provides solutions for n_a and n_b:

$$n_a = \frac{1}{\left(\Lambda^* + \frac{P^*\beta^*}{R^*_{drop}A^*}\right)}\left(\frac{2}{\lambda^*}\frac{\Lambda^* A^{*(a)}}{\beta^{*(a)}} + \frac{\beta^*}{R^{*(a)}_{drop}R^*_{drop}A^*}\left(R^*_{hyd} - P^*\right)\right)$$

$$n_b = \frac{\frac{P^*}{R^*_{drop}}}{\left(\Lambda^* + \frac{P^*\beta^*}{R^*_{drop}A^*}\right)}\left(\frac{2}{\lambda^*}\frac{\Lambda^* A^{*(a)}}{\beta^{*(a)}} - \frac{1}{R^{*(a)}_{drop}R^*_{drop}A^*}\frac{\Lambda^* R^*_{drop}A^*}{P^*}\left(R^*_{hyd} - P^*\right)\right) \tag{7.12}$$

The total number of droplets in the two channels is $n_T = n_a + n_b$:

$$n_T = \frac{2}{\lambda^*}\frac{\Lambda^* A^{*(a)}}{\beta^{*(a)}}\frac{\left(1+\frac{P^*}{R^*_{drop}}\right)}{\left(\Lambda^* + \frac{P^*\beta^*}{R^*_{drop}A^*}\right)} - \frac{\left(R^*_{hyd} - P^*\right)}{R^{*(a)}_{drop}R^*_{drop}A^*}\frac{\left(\Lambda^* A^* - \beta^*\right)}{\left(\Lambda^* + \frac{P^*\beta^*}{R^*_{drop}A^*}\right)} \tag{7.13}$$

where the various non-dimensional factors are summarized as:

$$\lambda^* = \frac{\lambda}{L_a} \quad \Lambda^* = \frac{L_b}{L_a} \quad A^{*(a)} = \frac{A_a}{A_{in}} \quad A^* = \frac{A_b}{A_a} \quad \beta^{*(a)} = \frac{\beta_a}{\beta_{in}} \quad \beta^* = \frac{\beta_b}{\beta_a}$$

$$R^*_{drop} = \frac{R^{(b)}_{drop}}{R^{(a)}_{drop}} \quad R^{*(a)}_{drop} = \frac{R^{(a)}_{drop}}{R^{(a)}_{hyd}} \quad R^*_{hyd} = \frac{R^{(b)}_{hyd}}{R^{(a)}_{hyd}}$$

The equation shows that the total number of droplets is a linear function of $2/\lambda^*$ and the rest of the variables define the slope and intercept. The frequency of droplets entering a channel is related by, $A_a \lambda_a f_a = A \cdot \lambda \cdot f/2$, which can then be used to find the probability of a droplet entering a branch:

$$\text{Prob}_a = \frac{f_a}{f} = \frac{n_a \beta^{*(a)}}{\left(\frac{2}{\lambda^*}\right)A^{*(a)}} \tag{7.14}$$

$$\text{Prob}_b = 1 - \text{Prob}_a$$

Analysis by Sessoms *et al.* showed that the residence time in the two channels governs the sorting cycle (Sessoms, Belloul et al. 2009; Sessoms, Amon et al. 2010). Given that, $t = L/u_{drop}$, and that the flow splits equally, the dimensionless periods for the two branches may be calculated as:

$$t_a^* = t_a f = \left(\frac{2}{\lambda^*}\right)\frac{A^{*(a)}}{\beta^{*(a)}}$$
$$t_b^* = t_b f = \frac{\Lambda^* A^{*(a)} A^*}{\beta^{*(a)}\beta^*}\left(\frac{2}{\lambda^*}\right) \tag{7.15}$$

Again the term $2/\lambda^*$ appears as the governing parameter. Reconsidering the previous equations for n_a, n_b *and* n_T, they may be interpreted as being functions of the dimensionless period.

7.2.3 Model for Asymmetric Pressures and Branch Lengths

In this simplified model the only asymmetry between the channels is the applied pressures and the branch lengths. Under these conditions several terms drop out: $A^{*(a)} = 1$, $A^* = 1$, $\beta^{*(a)} = 1$, $\beta^* = 1$ $R^*_{drop} = 1$ and $R^*_{hyd} = \Lambda^*$. The reconstituted equations become:

$$n_a = \frac{1}{\left(\Lambda^* + P^*\right)}\left(\frac{2}{\lambda^*}\Lambda^* + \frac{1}{R^{*(a)}_{drop}}\left(\Lambda^* - P^*\right)\right)$$
$$n_b = \frac{P^*}{\left(\Lambda^* + P^*\right)}\left(\frac{2}{\lambda^*}\Lambda^* - \frac{1}{R^{*(a)}_{drop}}\frac{\Lambda^*}{P^*}\left(\Lambda^* - P^*\right)\right) \tag{7.16}$$
$$n_T = \frac{2}{\lambda^*}\Lambda^*\frac{\left(1 + P^*\right)}{\left(\Lambda^* + P^*\right)} - \frac{\left(\Lambda^* - P^*\right)}{\left(\Lambda^* + P^*\right)}\frac{\left(\Lambda^* - 1\right)}{R^{*(a)}_{drop}}$$

The new probabilities are:

$$\text{Prob}_a = \frac{f_a}{f} = \frac{n_a}{\left(\frac{2}{\lambda^*}\right)} \tag{7.17}$$
$$\text{Prob}_b = 1 - \text{Prob}_a$$

and dimensionless residence times:

$$t_a^* = t_a f = \left(\frac{2}{\lambda^*}\right)$$
$$t_b^* = t_b f = \Lambda^*\left(\frac{2}{\lambda^*}\right) \tag{7.18}$$

Two interesting limits occur for the total number of droplets. In the first case, the channels are symmetric while the pressures are not, and in the second the pressures are symmetric but the channels are not:

$$\begin{aligned} n_T\big|_{\Lambda^*=1} &= \frac{2}{\lambda^*} \\ n_T\big|_{P^*=1} &= \frac{4}{\lambda^*}\frac{\Lambda^*}{\left(\Lambda^*+1\right)} - \frac{1}{R_{drop}^{*(a)}}\frac{\left(\Lambda^*-1\right)^2}{\left(\Lambda^*+1\right)} \end{aligned} \tag{7.19}$$

Not intuitive at first, and somewhat surprising, in the first case, changes in pressure have no effect on the *total* number of droplets in the two branches, instead the distribution between the branches varies from 0 to n_T. For the second case the number of droplets depends on the relative size of the channels and the droplet resistance.

Recall that the basis of the model assumes a continuous medium of droplets, in reality droplets are discrete elements which is the source of the periodic behaviour of the system. The continuum model does not provide a method of determining what pattern will form, or when a pattern will transition into a new one, yet it is still very useful as it provides information on the relationship between various factors on the distribution of droplets, and provides a foundation for the development of a discrete model that can be used to predict the periodic behaviour. The derivation of the discrete model is remitted for the time being in favour of outlining the methodology used for the numerical simulations, as this will aid in the explanation of the discrete model.

7.3 Numerical Simulations of Trafficking

Performing an extensive experimental study that covers all of the parametric influences on the sorting process is not a practical enterprise. Numerical simulations can help to fill the knowledge gap by providing an idealized set of experimental data that makes the problem more manageable. As discussed by Smith and Gaver, modelling of droplets motion in a microfluidic network is an "agent based" simulation (Smith and Gaver 2010) as it satisfies the following criteria:

1. **Autonomy-Agents (droplets) operate without direct intervention.**

   Droplet motion is governed by predetermined governing equations that derive the droplets motion combined with the sorting rule at the junction.

2. **Social Ability-Agents interact via an agent-communication language.**

   In this case the language is the flow field and droplets communicate by changing the flow field by modifying the hydrodynamic resistance of the channel.

3. **Reactivity-Agents perceive their environment and respond to changes.**

   Droplets alter their speed according to the flow rate in the channel. As well, conditions in the two outlet branches define the sorting rule.

4. **Pro-activeness-Agents do not simply act in response to their environment; they are able to exhibit goal-directed behaviour.**

   The decision made at the junction acts to reduce the overall time for the droplets to pass through the network.

The algorithm developed for this study builds upon the work of Jousse *et al.*(Jousse, Farr et al. 2006), Schindler and Ajdari (Schindler and Ajdari 2008), Smith and Gaver (Smith and Gaver 2010) , Seesoms *et al.*(Sessoms, Belloul et al. 2009; Sessoms, Amon et al. 2010), and Cybulski and Garstecki (Cybulski and Garstecki 2010) and Behzad *et al.*(Behzad, Seyed-allaei et al. 2010). These works take a compact modelling approach where droplets are treated as point particles and the flow field can be reduced to 1-D pipe networks. Details on the numerical algorithm are provided below.

7.3.1 Droplet Trafficking Algorithm

Droplets travel along the branches of the network with a slip factor β, and hydrodynamic resistance L_d. These two terms are assumed to be constant throughout the network, thus any Ca, geometric or spacing dependence is omitted from this model but may be added in the future. Formation, sorting and associated events occur instantaneously without any delay. When a droplet enters the bifurcation it chooses the branch with the highest instantaneous flow rate no matter how small the difference may be. In this way droplets always try to balance the flow rates of the two bifurcation channels.

The position of each droplet throughout the network is recorded at all times. A highly variable explicit time stepping scheme is used to calculate the droplet distribution within the network

(Engl, Roche et al. 2005). The new time step is calculated by determining the shortest interval for one of three events to occur that may change the droplet distribution:

1. A new droplet is generated.
2. A droplet reaches the junction and needs to be sorted.
3. A droplet exits one of the two branch channels.

At each time step the total flow rates are calculated by applying compact 1D modelling methods that mirror Kirchoff's Rules for electrical circuits (Bruus 2007).This leads to a system of equations to describe the flow rates in each channel, $Q_{1\text{-}3}$, and internal pressure at the junction P_1, from the instantaneous resistance of the channels $R_{1\text{-}3}$. Droplet velocities are calculated as:

$$u_{di} = \frac{Q_i \beta_i}{A_i} \tag{7.20}$$

where Q_i is the total flow rate, and A_i the cross-sectional area of the *ith* channel. Subsequently, the time step is calculated as the minimal interval to the next event. This time step is then used to convect each droplet in the network according to their local velocity ($\Delta x_i = u_{di}\Delta t$). If a new droplet is formed it is added to the beginning of the inlet channel. If a sorting event occurs, a droplet is added to the beginning of the channel with the highest instantaneous flow rate and removed from the incoming channel. If a droplet leaves one of the two outlets it is simply removed from that channel.

Network dimensions are emulated from the experimental chip design (refer to Section 7.5). A wide range of incoming spacings is spanned for each configuration to produce different sorting patterns (channel dimensions, pressures, *etc.*). For each frequency setting, the sorting of at least 1000 droplets is recorded to ensure that the system reaches a steady state. Using the back half of the data, the average flow rate, number of droplets and junction pressure are recorded. The sorting pattern is extracted with the same algorithm applied to analyze the experimental data (refer to Section 7.5). The complete algorithm for the droplet trafficking is summarized in Figure 7.3 and was written in Matlab.

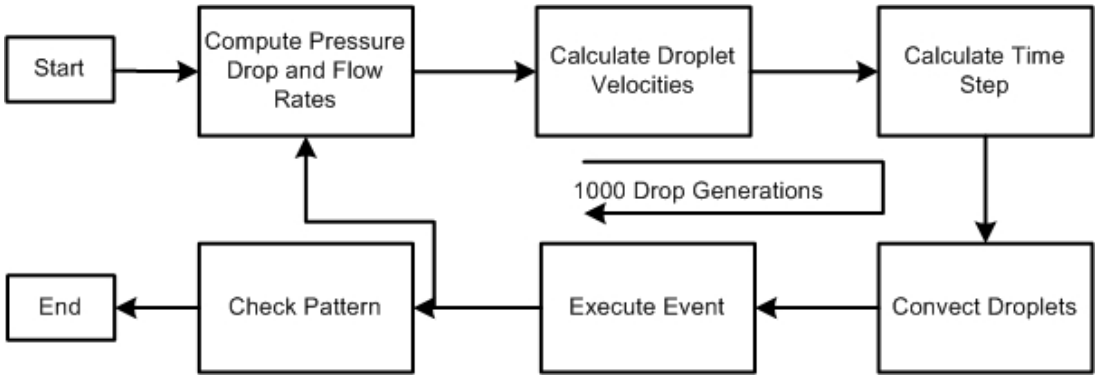

Figure 7.3 Flow chart of the trafficking algorithm for the numerical simulations.

7.3.2 Idealized Numerical Simulation of Droplet Trafficking

Developing a theoretical model based on the numerical results is an arduous task given the non-linear coupling between the number of droplets in the channel, the flow rates and the sorting rule. To make the problem more manageable, we follow the strategy taken by Sessoms *et al.* and develop an idealized numerical simulation of the trafficking problem (Sessoms, Amon et al. 2010). The primary assumption is that the flow rates are constant and thus always equal to one half the incoming flow rate ($Q_{a,b}=Q/2$). In reality, this assumption is valid when variations due to droplets entering or leaving the bifurcation channels are negligible*, ie.* $R_{drop}<<R_{hyd}+nR_{drop}$. This simplified numerical simulation provides an opportunity to investigate pattern formation caused by the discrete nature of the system and the feedback associated with the sorting rule. Only small changes are made to the original trafficking algorithm. Since the flow rates are fixed, the time step is also fixed at λ, and spatial locations of the droplets in the branches are constant and equal to multiples of $\lambda/2$. Thus only a finite number of droplet distributions exist, the system is completely deterministic, and periodic behaviour is expected for all incoming spacings.

Droplets sort in order to balance the flow between the two branches. When a droplet enters the bifurcation it chooses the branch with the highest flow rate at that moment, which is captured by the following function ψ_t that defines the expected difference in flow (Q_1-Q_2):

$$\psi_t = \frac{R_{hyd}^* - P^*}{R_{drop}^{*(1)} P^*} + R_{drop}^* \frac{n_2}{P^*} - n_1 \tag{7.21}$$

and for the simplified cased:

$$\psi_t = \frac{\Lambda^* - P^*}{R_{drop}^{*(1)} P^*} + \frac{n_2}{P^*} - n_1 \tag{7.22}$$

A positive value results in a droplet flowing into Branch *1* and a negative into Branch *2*. Sessoms *et al.* also came up with an ingenious scheme to help them understand the sorting phenomenon (Sessoms, Amon et al. 2010). In addition to tracking the droplets through the network, they also tracked the "holes" left behind by a droplet after it makes a decision. Every sorting event thus simultaneously creates a droplet that sorts into the appropriate channel as well as a "hole" that sorts into the other channel. By tracking both the droplets and holes the authors were able to derive a set of selection rules that determines the length of the emerging pattern. The current algorithm also employs this same idea. The computational sequence is as follows:

1. Before a droplet is injected the number of droplets in each channel is counted and the value of ψ_t is computed.
2. A droplet is added to the beginning of the appropriate channel and a hole to the other.
3. At this point the total number of droplets and holes in each channel is counted again and recorded. Designated as N_1 and N_2 for the droplets and N_{1H} and N_{2H} for the holes.
4. All holes and droplets are then moved by $\lambda/2$. If a droplet's or hole's position exceeds the length of the channel it is removed. More than one droplet or hole may be removed in a step.

A video of sorting from the ideal-model simulations is available in Appendix B.

7.4 Discrete Model of the Droplet Sorting

Extensive experiments were performed to understand the sorting process using the ideal-model numerical simulations. Many conditions were studied, and from extensive review of the outputs of the models, a set of "selection rules" were found that determine the pattern length and composition. This analysis is an extension of the work of Sessoms *et al.* and their study of sorting in asymmetric junctions (Sessoms, Amon et al. 2010), however, with a different approach that accounts for the larger amount of asymmetries in the system. The following discussion provides derivation of the rules.

Transitions from one periodic regime to another depends on the incoming spacing $2/\lambda^*$. The first transition occurs when the system switches from filtering to sorting. This occurs when the resistance of the filter branch becomes larger than the sorting branch, (refer to Eqn.7.11):

$$\frac{2}{\lambda^*} > \frac{\left(R_{hyd}^* - P^*\right)}{P^* R_{drop}^{*(a)}} \tag{7.23}$$

Considering the discrete nature of the system -that droplets numbers can only take on integer values -the critical transition from filtering to sorting occurs when:

$$\frac{2}{\lambda_f^*} = floor\left[\frac{\left(R_{hyd}^* - P^*\right)}{P^* R_{drop}^{*(a)}}\right] + 1 \tag{7.24}$$

where we define the number of droplets in branch *a* needed to balance the two channels as:

$$N_{bal} = 2/\lambda_f^* - 1 \tag{7.25}$$

Note that from now on capitalized *N* refers to droplet counts in the discrete model and small *n* for the continuum model. By increasing $2/\lambda^*$ further (decreasing the incoming spacing) droplets begin to sort into both branches. Based on the discretization of position, droplets in each channel now have a fixed retention time given by:

$$\begin{aligned} T_a^* &= ceil\left(\left(\frac{2}{\lambda^*}\right)\frac{A^{*(a)}}{\beta^{*(a)}}\right) \\ T_b^* &= ceil\left(\frac{\Lambda^* A^{*(a)} A^*}{\beta^{*(a)}\beta^*}\left(\frac{2}{\lambda^*}\right)\right) \end{aligned} \tag{7.26}$$

Sessoms *et al.* showed that subsequent transitions in the periodic sequence occur when the discrete residence times (T_a^*, T_b^*) change values (Sessoms, Amon et al. 2010). This happens for specific spacings in the general model, $2/\lambda_c^*(k)$:

$$\begin{aligned} \frac{2}{\lambda_c^*(k)} &= \frac{\beta^{*(a)}}{A^{*(a)}}\left(N_{bal} + k\right) \\ \frac{2}{\lambda_c^*(k)} &= \frac{\beta^{*(a)}\beta^*}{\Lambda^* A^{*(a)} A^*}\left(N_{bal} + k\right) \end{aligned} \tag{7.27}$$

where $k \in \mathbb{N}$. These critical spacings bracket regions where the length of the pattern remains the same. Crossing from one region into another means that the cycle time of one of the branches is different, and thus the pattern may change.

The sorting rule (Eqn. 7.21) forces the hydrodynamic resistance of the two channels to oscillate around the 0 point. Sessoms *et al.* developed a set of selection rules that define when the cycle time T_{cyc}^* will equate to either T_a^* or T_b^* for the case of asymmetric channel lengths (Sessoms, Amon et al. 2010). From personal correspondence with the authors, these rules were not created based on mathematical derivation; instead they were derived by observing a unique relationship between the number of holes and droplets in the two channels from their ideal-model numerical simulations (Sessoms 2010). Here we repeat their derivation of the selection rules and provide a mathematical foundation for their presence as reference. Afterwards, a modified set of selection rules are outlined for the general case based on new interpretation of the numerical simulations.

7.4.1 Selection Rules from Sessoms *et al.*

Through observation of the ideal-model simulations the authors found that three possible cases occur for sorting:

1. N_a and N_b are constant. The cycle has a period $\left|T_a^* - T_b^*\right|$, where typically this is a harmonic of one of the periods, T_b^*.
2. N_a is constant and N_b oscillates by 1. The cycle has a period of T_a^*.
3. N_b is constant and N_a oscillates by 1. The cycle has a period of T_b^*.

They also found an intriguing relationship between the number of droplets in channel *b*, N_b, and the number of holes in *a*, N_{Ha}:

$$N_b + N_{Ha} = M, M-1 \tag{7.28}$$

where $M = T_a^* - N_{bal}$ is define by the authors as the "remain number of droplets" that must be distributed between the two channels. For case 2, N_{Ha} is constant and N_b oscillates between $M - N_{Ha}$ for a time $T_a^* - t$ and $M - N_{Ha} - 1$ for a time $t \le T_a^*$. Over the entire cycle, the total number of holes and droplets must be conserved so that:

$$\left(T_a^* - t\right)\left(M - N_{Ha}\right) + t\left(M - N_{Ha} - 1\right) = T_b^* N_{Ha} \tag{7.29}$$

Performing a similar analysis for case 3, results in:

$$\left(T_b^* - t\right)\left(M - N_b\right) + t\left(M - N_b - 1\right) = T_a^* N_b \tag{7.30}$$

Which provides the following condition for i=a or b:

$$0 \le \frac{T_i^*}{T_a^* + T_b^*} M - n_i \le \frac{T_i^*}{T_a^* + T_b^*} \tag{7.31}$$

From this, the fractional parts ϵ_p and ϵ_q of the multiplication of pM, $p = T_a^* / \left(T_a^* + T_b^*\right)$, and qM $q = T_b^* / \left(T_a^* + T_b^*\right)$ are calculated. Four possible cases can occur, noting that ϵ_p+ϵ_q equals 0 or 1.

1. ϵ_p=ϵ_q=*0*
    - $pM = N_{Ha}$ and $qM = N_b$ where both are constant integers. The cycle time is a harmonic $T_{cyc}^* = \left|T_a^* - T_b^*\right|$ and $N_a = T_a^* - N_{Ha}$, $N_{Hb} = T_b^* - N_b$
2. ϵ_p=*p*, ϵ_q=*q*
    - Both N_{Ha} and N_b are constant and equal to the integers *p·(M-1)* and *q·(M-1)*. The cycle time is a harmonic $T_{cyc}^* = \left|T_a^* - T_b^*\right|$ and $N_a = T_a^* - N_{Ha}$, $N_{Hb} = T_b^* - N_b$
3. *0*<ϵ_p<*p, q*<ϵ_q<*1*
    - N_{Ha} is constant and equal to the integer part of pM. The cycle time is $T_{cyc}^* = T_a^*$ and $N_a = T_a^* - N_{Ha}$, $N_b = M - N_{Ha}, M - N_{Ha} - 1$ and $N_{Hb} = T_b^* - N_b$
4. *p*<ϵ_p<*1, 0*<ϵ_q<*q*
    - N_b is constant and equal to the integer part of qM. The cycle time is $T_{cyc}^* = T_b^*$ and $N_{Ha} = M - N_b, M - N_b - 1$ and $N_a = T_a^* - N_{Ha}$ and $N_{Hb} = T_b^* - N_b$

When these sorting rules are applied to the ideal numerical simulations with asymmetric channels they choose the right pattern length (T_{cyc}^*) with flawless accuracy. As mentioned previously, the derivation of these set of rules, and in particular the key relationship, Eqn. 7.28, was found from observation. As will be shown below, Eqn. 7.28 may be derived mathematically as well. First, defining relations for the number of droplets and holes in the two arms:

$$\begin{aligned} N_a + N_b &= N_T \\ N_a + N_{Ha} &= T_a^* \\ N_b + N_{Hb} &= T_b^* \end{aligned} \tag{7.32}$$

where N_T is the total number of droplets. Reconsidering the sorting rule (Eqn. 7.21) and substituting the relations above in, we recover Eqn. 7.28.

$$0 = \left(\frac{\Lambda^* - 1}{R_{drop}^{*(a)}} \right) + N_b - N_a$$

$$0 = \left(\frac{\Lambda^* - 1}{R_{drop}^{*(a)}} \right) + N_b - T_a^* + N_{Ha} \tag{7.33}$$

$$N_b + N_{Ha} = T_a^* - \left(\frac{\Lambda^* - 1}{R_{drop}^{*(a)}} \right) = M, M - 1$$

This shows that the observed relation is derived from the sorting rule- not an entirely surprising result.

7.4.2 New Set of Selection Rules based on N_T

At first attempts were made to modify the approach taken by Sessoms *et al.* and adapt it to the general case (Sessoms 2010). These, however, were unsuccessful because a similar relationship like the one in Eqn. 7.21 could not be identified from the numerical data. The reason is that the addition of pressures bias and droplet resistance difference creates an unequal weighting in the influence a single droplet has on the flow rate in each channel. When a droplet enters Branch b it may require more than one droplet in Branch a to rebalance the flow. Thus the number of droplets may fluctuate by more than 1 to compensate for the unequal weighting. Due to this fact, a consistent relationship like the one in Eqn 7.21 was not observed. Instead a new approach was taken to develop the "selection rules" using the continuum model as a basis.

General Case

Comparisons with numerical results shows that the continuum based model for predicting the total number of droplets is actually quite accurate (refer to Figure 7.14). The formulation of n_T naturally includes all of the constraints in the model and is therefore the best description of the overall conditions. Using this as a basis, a modified equation is developed that includes the discrete nature of the system and mimics the conditions set forth in the ideal-model numerical

simulations. Replacing $\Lambda^* = T_b^* \beta^* / \left(T_a^* A^*\right)$ and $\frac{2}{\lambda^*}\frac{A^{*(a)}}{\beta^{*(a)}} = T_a^*$, in the Eqn. 7.13, the new discrete calculation for the total number of droplets becomes:

$$N_T = ceil\left[T_a^* \Lambda_{dis}^* \frac{\left(1+\frac{P^*}{R_{drop}^*}\right)}{\left(\Lambda_{dis}^* + \frac{P^*\beta^*}{R_{drop}^* A^*}\right)} - \frac{\left(R_{hyd}^* - P^*\right)}{R_{drop}^{*(a)} R_{drop}^* A^*} \frac{\left(\Lambda_{dis}^* A^* - \beta^*\right)}{\left(\Lambda_{dis}^* + \frac{P^*\beta^*}{R_{drop}^* A^*}\right)} \right] \tag{7.34}$$

From the sorting rule (Eqn. 7.21), and the relation given in Eqn. 7.34, a base value for N_b can be estimated:

$$N_b = ceil\left[\frac{P^*}{P^* + R_{drop}^*} \left(N_T - \frac{\left(R_{hyd}^* - P^*\right)}{P^* R_{drop}^{*(a)}} \right) \right] \tag{7.35}$$

and by extension other base values become: $N_a = N_T - N_b$, and $N_{Ha} = T_a^* - N_a$, and $N_{Hb} = T_b^* - N_b$. Observation show that N_a+N_b can only take on certain values:

(i) N_a and N_b are both constant $T_{cyc}^* = \left|T_a^* - T_b^*\right|$

(ii) N_a is constant and N_b fluctuates by 1, ($N_a + N_b = N_T, N_T - 1$), $T_{cyc}^* = T_a^*$

(iii) N_b is constant and N_a fluctuates by 1 and ($N_a + N_b = N_T, N_T - 1$), $T_{cyc}^* = T_b^*$

(iv) N_b is constant and N_a fluctuates by more than 1 ($N_a + N_b = N_T, N_T - 1, N_T + 1$), $T_{cyc}^* = T_b^*$.

Only one of the four possible conditions can occur. To determine which one does, a series of tests are applied to confirm that the conditions satisfy (a) oscillations around the zero point in Eqn. 7.21 and (b) conservation of the total number of droplets in the two branches over the cycle time. Therefore, four separate scenarios can occur for the sorting function ψ:

$$\psi_1 = \frac{R^*_{hyd} - P^*}{R^{*(a)}_{drop} P^*} + R^*_{drop} \frac{N_b}{P^*} - N_a$$

$$\psi_2 = \frac{R^*_{hyd} - P^*}{R^{*(a)}_{drop} P^*} + R^*_{drop} \frac{N_b - 1}{P^*} - N_a$$

$$\psi_3 = \frac{R^*_{hyd} - P^*}{R^{*(a)}_{drop} P^*} + R^*_{drop} \frac{N_b - 1}{P^*} - N_a - 1 \qquad (7.36)$$

$$\psi_4 = \frac{R^*_{hyd} - P^*}{R^{*(a)}_{drop} P^*} + R^*_{drop} \frac{N_b}{P^*} - N_a - 1$$

For test (a) to be satisfied then ψ must switch between positive and negative values. Omitting case (i) for the moment, then a criteria for the three other cases (ii-iv) can be calculated through a series of ratios of $\psi_{1\text{-}4}$: case (ii) $Ch_1=\psi_1/\psi_2$, (iii) $Ch_2= \psi_2/\psi_3$, and (iv) $Ch_3= \psi_1/\psi_4$. A case is a possibility if the respective ratio ≤ 0 indicating that the sorting function switches signs. If a case passes the first test than the second test is to verify that it can be fulfilled within the cycle time. The analysis is similar to Eqns. 7.29 and 7.30, resulting in the following criteria for (ii) and (iii):

(ii) $$0 < N_b - \frac{T^*_b}{T^*_a} N_{Ha} < 1$$

(iii) $$0 < \frac{T^*_a}{T^*_b} \left(N_{Hb} + 1\right) - N_a < 1 \qquad (7.37)$$

If either condition equates to 0 or 1 then case (i) is active as the total number of droplet is constant. If the cycle time condition is not satisfied for (ii) then the only option left is the more complex case (iv).

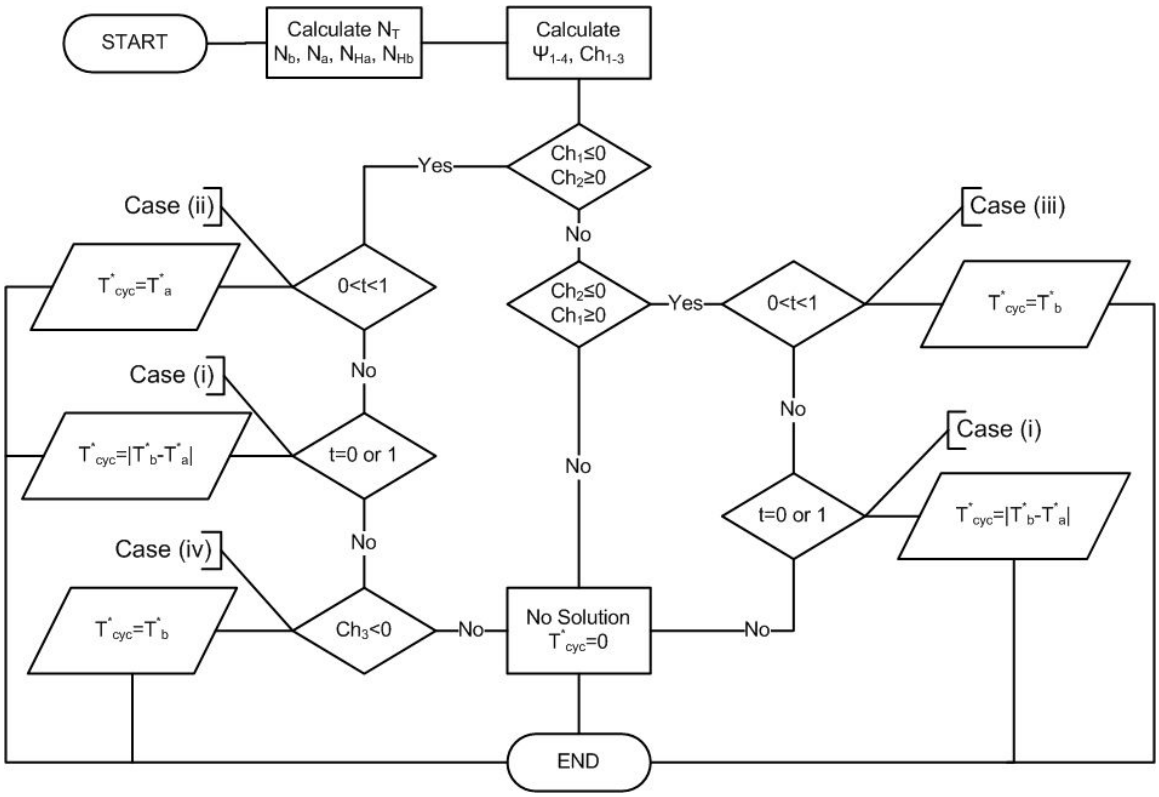

Figure 7.4 Flow chart of the selection rule algorithm for the new discrete model.

From this information the composition of the actual pattern can be determined. The total length of the pattern is given by $|\Omega| = T^*_{cyc}$, and the number of D-s and U-s in the pattern for the four cases are: (i) $N_D = N_{Ha}, N_U = T^*_{cyc} - N_D$ (ii) $N_D = N_{Ha}, N_U = T^*_{cyc} - N_D$ (iii) $N_D = N_b - 1$, $N_U = T^*_{cyc} - N_D$ (iv) $N_D = N_b$, $N_U = T^*_{cyc} - N_D$. Finally, the fraction of droplets sorting into each channel may be calculated:

$$\begin{aligned} \text{Prob}_a &= \frac{N_U}{|\Omega|} \\ \text{Prob}_b &= 1 - \text{Prob}_a \end{aligned} \tag{7.38}$$

The algorithm is summarized in the flow chart presented in Figure 7.4 and the outcome for each case is summarized in Table 7.1. To be clear the overall step by step process is outlined below:

(1) Calculate an estimate for N_T from Eqn. 7.34 and the base value for N_b from Eqn. 7.35.

(2) Calculate the 4 ψ.'s. in Eqn. 7.36

(3) Calculate Ch_{1-3} and then the cycle time inequality in Eqn. 7.37 if it applies.

(4) Follow the algorithm to determine the predicted case and obtain the results.

For the simplified case, the process is the same except that substitutions need to be made to remove the frivolous variables. In the following section a method for determining the number of unique sequences from a given pattern composition is presented.

Table 7.1 List of outcomes from the discrete model for the selection rules. Variables are calculated with respect to the base value.

Case	Condition	T^*_{cyc}	Branch A	Branch B	N_D
(i)	(ii) t=0	$\lvert T^*_b - T^*_a \rvert$	N_a N_{Ha}	N_b N_{Hb}	N_{Ha}
	(ii) t=1	$\lvert T^*_b - T^*_a \rvert$	N_a N_{Ha}	N_b-1 N_{Hb}+1	N_{Ha}
	(iii) t=0	$\lvert T^*_b - T^*_a \rvert$	N_a N_{Ha}	N_b-1 N_{Hb}+1	N_b-1
	(iii) t=1	$\lvert T^*_b - T^*_a \rvert$	N_a+1 N_{Ha}-1	N_b-1 N_{Hb}+1	N_b-1
(ii)	0<t<1	T^*_a	N_a N_{Ha}	N_b, N_b-1 N_{Hb}, N_{Hb}+1	N_{Ha}
(iii)	0<t<1	T^*_b	N_a, N_a+1 $N_{Ha,}$, $N_{Ha,}$-1	N_b-1 N_{Hb}+1	N_b-1
(iv)	(ii) t>0 or t>1	T^*_b	N_a-1, N_a+1 N_{Ha}+1, $N_{Ha,}$-1	N_b N_{Hb}	N_b

7.4.3 Available Sequences

Once the pattern length and the number of U-s and D-s are known, the number of possible sequences can be obtained from counting all permutations (Cybulski and Garstecki 2010):

$$\left|\Omega_{dis}\right| = \frac{T^*_{cyc}!}{N_U! N_D!} \tag{7.39}$$

However, this calculation does not eliminate the redundant cyclic shifts that occur. For example, UUUUDD may be shifted UUUDDU or UDDUUU and so on. For the case of 4 U-s and 2 D-s there are 15 possible distributions, each with 5 cyclic shifts: UUUUDD, UUUDUD, UUDUUD. As the pattern length increases, determining the number of unique sequences, $\left|\Omega_{seq}\right|$, becomes progressively more difficult. Fortunately, this type problem has been solved before, and is part of what is known as Group Theory in the field of Combinatorial Enumeration. Such problems can be solved using Póyla's Counting Method for Cyclic Groups (Davis 2006; Harris 2008; Weisstein

2011). To demonstrate the technique a short example for $T^*_{cyc}=6$ is presented. The first step is to calculate the Cyclic Index, $Z(C_p)$, for the Cyclic Group, C_p, which is given as:

$$Z(C_p)=\frac{1}{p}\sum_{k|p}\varphi(k)a_k^{p/k} \tag{7.40}$$

where k|p means k *divides* p for integers, and $\varphi(k)$ is Euler's Totient function which is defined as the total number of integers that are *relatively prime* to *k*. For $T^*_{cyc}=6$ the Cyclic group is:

$$Z(C_6)=\frac{1}{6}\left(a_1^6+a_2^3+2a_3^2+2a_6^1\right) \tag{7.41}$$

The notation $a_k^{p/k}$ refers to the cycle structure representation. In this case, the cycle structure consists of 2 unknowns (*U, D*) and has the form *(x+y)*, if there were 3 choices the structure is *(x+y+z)* and so on. Substitution results in the following terms: $a_1^6=(x+y)^6$, $a_2^3=(x^2+y^2)^3$, $a_3^2=(x^3+y^3)^2$, $a_6^1=(x^6+y^6)$, and upon substitution into Eqn. 7.41:

$$P=\frac{1}{6}\left((x+y)^6+(x^2+y^2)^3+2(x^3+y^3)^2+2(x^6+y^6)\right) \tag{7.42}$$

The number of unique patterns for a specific combination, say 4 U-s and 2 D-s is determined by calculating the coefficient for the term x^4y^2, where *x* corresponds to *U* and *y* to *D*. Likewise for 3 U-s and 3 D-s the coefficient for the term x^3y^3 is required. Expanding Eqn. 7.42 and grouping the terms can be tedious; instead the calculation may be expedited by using the formula for multinomial coefficients:

$$(x+y)^n=\sum_{\substack{i+j=n\\ i,j\geq 0}}\frac{n!}{i!\,j!}x^iy^j \tag{7.43}$$

For x^4y^2, only $(x+y)^6$ and $(x^2+y^2)^3$ can produce x^4y^2 and using Eqn. 7.43 the multinomial coefficients are $\frac{6!}{4!2!}$ and $\frac{3!}{2!1!}$, resulting in a total coefficient of $\frac{1}{6}\left(\frac{6!}{4!2!}+\frac{3!}{2!1!}\right)=3$. Thus there are a total of 3 unique patterns for 4 U-s 2 D-s, and likewise 4 for 3 U-s 3 D-s. Table 7.2 summarizes the calculation for pattern lengths 2 through 9, for $U\geq D$ and $D\geq 1$. As well, the table lists the specific sequences that can be obtained. As the pattern length increases the number of unique sequences increases rapidly and Póyla's method becomes more and more attractive. A pattern length of 10, for instance, has 5 unique patterns with 2 D-s, 22 with 3 D-s and 26 with 4 D-s.

Although we can identify the possible patterns that can form for a gives set of U-s and D-s some may not be physically attainable during sorting. Cybulski and Garsterki, as well as Sessoms *et al.,* both observed that the initial state of system influences the specific pattern that forms (Cybulski and Garstecki 2010; Sessoms, Amon et al. 2010). Large disturbances such as striking the tubing can also cause the system to switch to a new sequence. Cybulski and Garstecki noted that all possible sequences could usually be obtained; however, in certain narrow regions some sequences were absent. They surmise that in the space of all possible initial configurations for the system that patterns may have different measures of their basins of attraction-some even of zero-order and are thus impossible to attain. An example of a very likely low level sequence is UUUUDDDD for $T^*_{cyc}=8$ in a completely symmetric design. Since the design is symmetric we would expect something close to an alternating UDUDUDUD sequence to be the most favourable. For the UUUUDDDD sequence to form it would probably require that one of the channels is initially filled with at least 4 droplets that are closely spaced (DDDD), and that these droplets do not leave the branch before at least 4 new droplets are sorted (UUUU). In this example, the likelihood of a specific pattern forming was estimated through deductive reasoning; however, future extensions should take a more mathematical approach to tackle the problem.

7.4.4 Summary of Discrete Model

In the preceding sections a detailed model was presented to describe sorting at a junction with several asymmetries. This model, based on the modifying the continuum based model to produce integer values for the total number of droplets. With this model we are able to predict the cross-over from filter to sorting, the pattern length, bifurcations, the distribution of droplets, and the number of unique sequences that may form. The next section details the experimental methodology. The discussion focuses on the various problems that must be overcome to achieve stable pattern formation in practice.

Table 7.2 List of all unique sequences $\left|\Omega_{seq}\right|$ that are possible for T^{*}_{cyc}= *2 to 9* with the number of D-s in the sequence varying from 1-4.

T^{*}_{cyc}	$Z(C_p)$	$\left\|\Omega_{seq}\right\|$ **1 D-s**	$\left\|\Omega_{seq}\right\|$ **2 D-s**	$\left\|\Omega_{seq}\right\|$ **3 D-s**	$\left\|\Omega_{seq}\right\|$ **4 D-s**
2	$\frac{1}{2}\left(a_1^2 + a_2^1\right)$	1 [UD]	--	--	--
3	$\frac{1}{3}\left(a_1^3 + 2a_3^1\right)$	1 [UUD]	--	--	--
4	$\frac{1}{4}\left(a_1^4 + a_2^2 + 2a_4^1\right)$	1 [UUUD]	2 [UUDD] [UDUD]	--	--
5	$\frac{1}{5}\left(a_1^5 + 4a_5^1\right)$	1 [UUUUD]	2 [UUUDD] [UUDUD]	--	--
6	$\frac{1}{6}\left(a_1^6 + a_2^3 + 2a_3^2 + 2a_6^1\right)$	1 [UUUUUD]	3 [UUUUDD] [UUUDUD] [UUDUUD]	4 [UUUDDD] [UDUDUD] [UUDUDD] [UUDDUD]	--
7	$\frac{1}{7}\left(a_1^7 + 6a_7^1\right)$	1 [UUUUUUD]	3 [UUUUUDD] [UUUUDUD] [UUUDUUD]	5 [UUUUDDD] [UUDUDUD] [UUUDUDD] [UDUUUDD] [UUDUUDD]	--
8	$\frac{1}{8}\left(a_1^8 + a_2^4 + 2a_4^2 + 4a_8^1\right)$	1 [UUUUUUUD]	4 [UUUUUUDD] [UUUUUDUD] [UUUUDUUD] [UUUDUUUD]	7 [UUUUUDDD] [UUUDUDUD] [UUUUDUDD] [UUDUUDUD] [UUUDUUDD] [UUDUUUDD] [UDUUUUDD]	10 [UUUUDDDD] [UUDDUUDD] [UUUDUDDD] [UDDUUUDD] [UUDUUDDD] [UUDUDUDD] [UDUUUDDD] [UDUUDUDD] [UUUDDUDD] [UDUDUDUD]
9	$\frac{1}{9}\left(a_1^9 + 2a_3^3 + 6a_9^1\right)$	1 [UUUUUUUD]	4 [UUUUUUUDD] [UUUUUUDUD] [UUUUUDUUD] [UUUUDUUUD]	10 [UUUUUUDDD] [UDUUUUUDD] [UUUUUDUDD] [UUUUDUDUD] [UUUUDUUDD] [UUUDUUDUD] [UUUDUUUDD] [UUDUUUDUD] [UUDUUUUDD] [UUDUUDUUD]	14 [UUUUUDDDD] [UUUDUDUDD] [UUUUUDUDD] [UUDUDUUDD] [UUUUDUUDD] [UUDUUDUDD] [UUUDUUUDD] [UDUUUDUDD] [UUDUUUUDD] [UDUUDUUDD] [UUUUDDUDD] [UDUDUUUDD] [UUUDDUUDD] [UUDUDUDUD]

7.5 Experimental Design

Achieving repeatable droplet sorting patterns at a bifurcation is not easy to accomplish in practical terms. Although experimental results have been presented in literature, these are often only small test cases to qualitatively verify numerical results. Achieving stable sorting patterns requires near perfect experimental conditions. For example, often a sorting pattern will only repeat for a few cycles before degenerating and reverting back to chaos. The difficulty is caused by the stochastic noise in the system that can perturb the stable configuration. For instance, Cybulski and Garstecki found that striking the inlet tubing would cause the sequence to switch (i.e. UDUDUD to UUDUUD) (Cybulski and Garstecki 2010). The authors studied rather small pattern lengths ($n<10$) and found the system to be highly stable to natural disturbances caused by noise in the system (striking the tube being an unnatural and severe disturbance). Conversely, Sessoms *et al.* noted that the system would switch between different sequences by itself while the overall length of the pattern would remain the same (Sessoms, Amon et al. 2010) for longer sequence lengths ($n>20$). The authors attributed this problem to the variation in droplet spacing, which they measured as being ~2% in their experiments. The major effects that can lead to pattern degradation may be summarized as (Christopher, Bergstein et al. 2009; Cybulski and Garstecki 2010; Sessoms, Amon et al. 2010):

- Pressure fluctuations from droplets forming, sorting or exiting a channel.
- Variations in pressure at the source.
- Variation in droplet resistance (drop size and speed).
- Variation in droplet spacing which alters the sorting pattern.
- Delay in sorting at the junction due to stagnation of the droplet as it makes its decision.

The first four sources are all related to the design and operation of the droplet generator, the last is inherent to the sorting phenomenon. When performing trafficking experiments researchers have tackled these issues in a variety of ways. Previous studies on droplet generators demonstrated that, in order to achieve any degree of stability, high resistance inlet tubing leads are required to ensure that resistance changes within the microfluidic chip have negligible effect on the overall flow conditions (de Mas, Gunther et al. 2005; Gunther and Jensen 2006; Cybulski and Garstecki 2010). Similarly, in the design of experimental sorting chips, researchers have also used high resistance fore and aft channels to separate the sorting loop from the generator (Jousse, Farr et al. 2006; Fuerstman, Garstecki et al. 2007; Fuerstman, Lai et al. 2007; Sessoms, Amon et al. 2010).

Cybulski and Garstecki took this further and developed a novel drop on demand system for their experiments to overcome the problem of feedback associated with passive droplet generators (Cybulski and Garstecki 2010). In the current study, the problem is more complicated because the pressure at the outlets needs to be controlled in the experiments, unlike previous works which used a closed loop system to study the sorting phenomena. To overcome these problems, extensive efforts were made to optimize the design of the sorting chip and experimental setup to minimize the effect of noise on the sorting process. At the beginning of the design process spacing variation was as high as 10%, however, through continuous improvements to the design the variation was reduced to 1%. The process by which these substantial improvements were made are discussed below.

7.5.1 Overall Chip Design

A schematic of the final chip design is shown in Figure 7.5. The chip consists of three main components: (1) T-junction generator where droplets are formed which then connects to (2) the diluter that controls increases the spacing and speed of droplets by adding more oil to the flow and (3) the sorting branches and recombination loop. Two sorting channel configurations were tested in the experiments, a symmetric design (5, 5 mm) and an asymmetric design (4, 5mm).

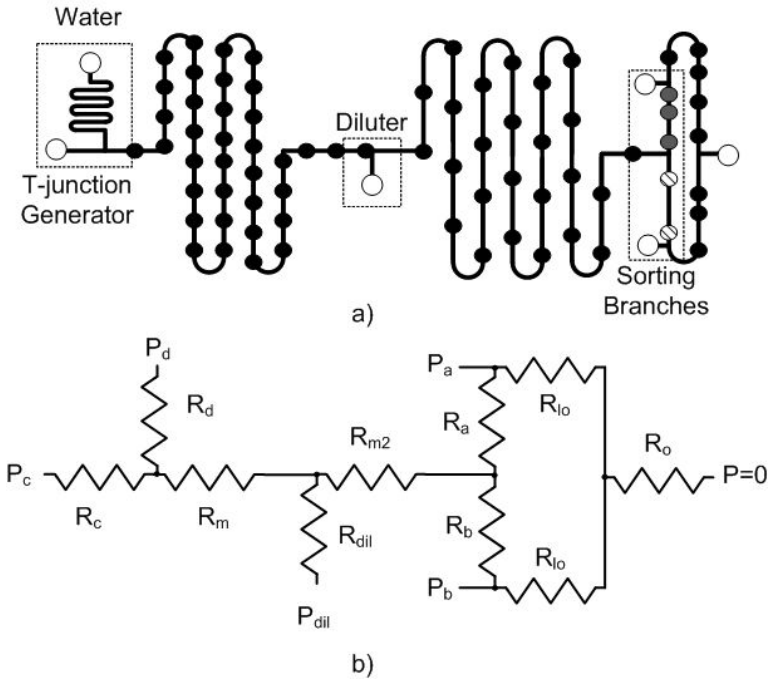

Figure 7.5 (a) Overall network architecture for the experimental sorting chip which consists of 3 main components: the T-junction generator, diluter and sorting branches. (b) The equivalent hydrodynamic representation of the network used for compact flow modelling.

Each part, as well as the integration of the parts, had to be carefully designed. Compact fluid flow modelling was used to design the overall network to suppress the influence of the noise factors discussed above. Figure 7.5b shows the equivalent compact model network used in the analysis. The final dimensions and optimum overall network design are summarized in Table 7.3. Overall the process was iterative as each time new and unexpected problems emerged that needed to be solved. These issues are discussed in detail in the following sections.

Table 7.3 Dimensions of the final chip design. Data includes the overall length of the channel and the approximate number of droplets for a typical spacing of 600 μm. The cross-sectional area of all the channels was 50x100μm.

Channel	Description	Length (mm)	Approx. # of Droplets	Notes
R_d	Dispersed Phase Inlet	5	--	
R_c	Continuous Phase Inlet	300	--	Long serpentine channel
R_m	Main outlet for T-junction	50	80	Serpentine radius 2mm
R_{m2}	Main outlet for Diluter	100	165	Serpentine radius 2mm
R_{dil}	Diluter Inlet	0.5	--	Very short
R_a	Sorting Branch a	4,5	15	Small exit to the outlet
R_b	Sorting Branch b	5	15	Small exit to the outlet
R_{lo}	Loop Branch	20	50	
R_o	Outlet of System	4	---	Special guided exit

7.5.2 T-junction Generator Design

As discussed in Chapter 6, stable operation of T-junction generators using pressure control requires careful design of the overall network configuration. As mentioned before, spacing is a far more sensitive to fluctuations in flow rates than droplet size. Therefore, achieving low fluctuations in spacing requires an order of magnitude reduction in variance of the flow rates.

Following the design rules outlined in Chapter 6, the overall dimensions of the three channels compromising the T-junction generator were chosen. The inlet of the continuous phase is short (L_c=5 mm) while the inlet of the dispersed phase is very long (L_d=300 mm) which is much longer than the main outlet of (L_m=100 mm). The long continuous phase channel was created by connecting another chip with a serpentine channel since space was limited on the sorting chip. A long main channel was necessary so that fluctuations in resistance caused by droplets entering or leaving the channel did not influence the performance of the generator. For a typical spacing of

0.6 mm, the main channel holds approximately 80 droplets. To minimize pressure fluctuations caused by the emerging interface a 1:1 T-junction design was used. As well, surfactant was added to reduce the surface tension as well as any other pressure fluctuations that may be caused the droplets deforming at the generator, diluter, sorting junction and exits.

For the first design a long serpentine channel with tight turns (~200μm radius) was used to reduce the overall footprint of the main channel. This was chosen without much concern at the time. However, during experiments an interesting phenomenon was observed when droplets passed through these tight turns: the spacing of a pair of droplets before they entered the turn and after changed by an astonishing 10%. The reason was thought to be related to a change in the resistance of the droplet as it goes around the turn. Along the outside wall of the turn the droplets contact length increases and along the inside it decreases. This reduces the overall resistance of the droplet causing it to speed up compared to the bulk flow (Muradoglu and Stone 2007). The problem is not just that the spacing changes as a pair goes around a turn, because the droplet resistance changes, and because there are several turns in the design, the main channel resistance can fluctuate significantly causing the production of droplets to vary (size, and output spacing). This discovery of droplet resistance changing in terms prompted a further investigation which has been continued by a fellow student. As for the current study, the serpentine was redesigned and the turn radius increased to 2 mm and no change in spacing was observed.

7.5.3 Diluter Design

The channel after the diluter was designed to be very long compared to the sorting branches so that oscillations in the resistance of the branches would have negligible influence on the dilution. The inlet of the diluter was extremely short to reduce pressure losses between the tubing and the microchannel. The width of the channel was narrower than the rest of the network (50 μm) to prevent droplets from intruding into the dilution reservoir by accident (refer to Fig. 7.6a). Finally, a 2 mm serpentine radius was used as well.

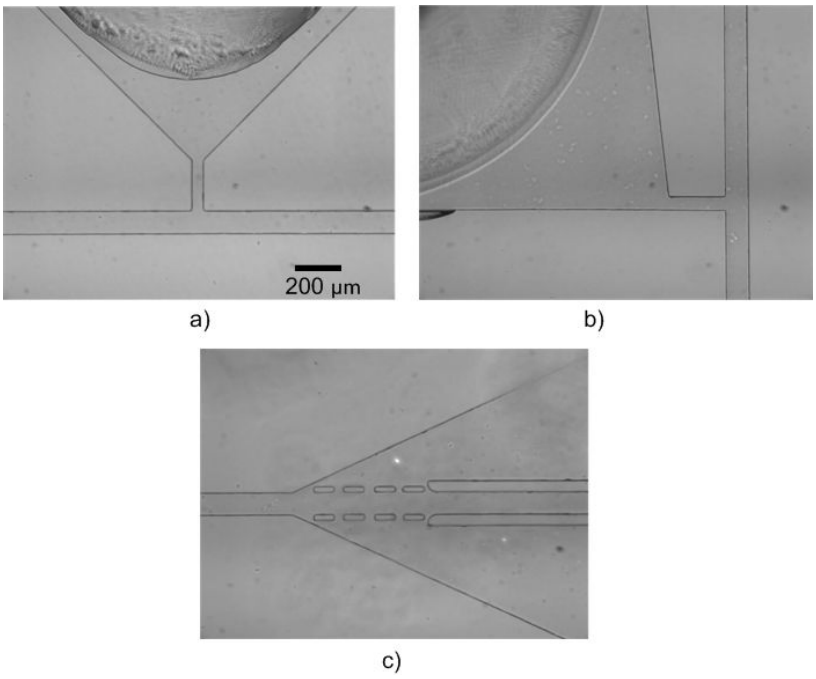

Figure 7.6 Micrographs of the chip near (a) the diluter inlet, (b) the outlet of the branches and (c) the exit of the chip. At each inlet drop of glue was added to the master to create a large reservoir that minimized pressure losses from the inlet tubing to the microchannel.

7.5.4 Sorting Branch Design

In the original design the recombination loop after the sorting branches was not included. Droplets would exit from the end of the sorting branches (P_a, P_b), however, this caused several problems with the sorting. As droplets exited the channels they would expand suddenly which caused large pressure fluctuations due to the changing Laplace pressure across the droplet. This would disturb the sorting at the junction and stable patterns could not form. Furthermore, as the droplets exit they became trapped in the expansion region and would occasionally block the exit causing further oscillations in the pressure field.

To overcome this problem the recombination loop was added and the exits were turned into diluters. Now as the droplets exit the branching channels additional oil from P_a and P_b increase the spacing of the droplets. The droplets than exit the network through one outlet which has a special designed "track" to prevent the droplets from expanding uncontrollably as they exit (refer to Fig.6c). Initially the outlet holes were punched close to the microchannel to reduce the pressure drop, however when the tubing was press fit into these holes it would deform the surrounding PDMS including the sorting branch channels. Since resistance depends on the height of the channels this deformation would change the sorting conditions unintentionally. This problem was

solved by punching the holes further away from the microchannels. To reduce any pressure losses created by the increased distance, a drop of UV curable glue was added to the SU-8 masters at the outlet locations to create large cavities with minimal hydrodynamic resistance. These large cavities can be seen in Figure 7.6.

7.5.5 Experimental Setup to Reduce Noise Contributions

As outlined before, one of the many contributions to noise are the pressure fluctuations coming from the supply, in this case the Fluigent system. Obviously the pressures applied at the inlets of the network must be consistent if droplet formation is to be stable. This required extensive optimization of the pressure system, fine tuning the setup to minimize fluctuations in droplet spacing and sorting.

The Fluigent system requires a pressure supply that is greater than the output pressures distributed to the chip. Originally the source of this input was a tank (20L) connected to an air compressor (max 100psi). The air compressor was set to automatically fill the tank if the pressure dropped below 80psi. Experiments would often run for several hours and the tank would be refilled every 20 minutes. Every time the tank refilled it disturbed the internal regulators within the Fluigent system which caused a fluctuation in the applied pressures. Careful observation of the droplet spacing over a long time showed that oscillations in spacing corresponded with the tank refilling. This issue was solved by connecting a dedicated line from the in-lab air supply, which provides a tightly regulated and stable source of air pressure.

Although now the Fluigent system had a stable source of air pressure, fluctuations could still exist from the internal regulators controlling the output pressures. The Fluigent system uses proprietary software to set the desired pressures. Within this software it uses a PID control loop to regulate the set pressure. The feedback coefficient can be controlled which allows for tuning the system to the specific experimental setup. Poor choice in the feedback coefficient results in long settling times and oscillations around the set point. Through extensive experimentation using the actual sorting chip the optimum feedback coefficient was 5. Lower values also produced good results but values over 25 resulted in oscillations around the pressure set point as measured internally by the Fluigent system. Still some oscillations are expected because of accuracy of the Fluigent system which is quoted as 0.5% of full scale by the manufacturer. To dampen out these fluctuations soft walled tubing was added to the inlets of the chip to increase the compliance of

the system. This tubing acts as a capacitor reducing fluctuations in the incoming pressure. To increase the accuracy of the Fluigent system it must pass through a heat up procedure before being used. This is an automated function that is set by the software. Afterwards the system is calibrated for zero point to make sure that the differential pressure applied (P_a, P_b) was accurate. This procedure was completed before every experiment.

Figure 7.7 shows the experimental results under the final design and experimental conditions. The figure presents the time trace spacing for four different measurements using the same chip. Measurements were made for approximately 80 pairs of droplets which is approximately one complete volume replacement of the main channel. Standard deviations for these results ranged from 1-1.5% of the mean value with min and max values of 2.5-3%. Reducing the variations further may be possible by improving the experimental setup, however there will always be some variation due to the stochastic nature of the formation process. Still the current experimental setup was considered to be sufficient as stable sorting patterns could be seen in the experiments.

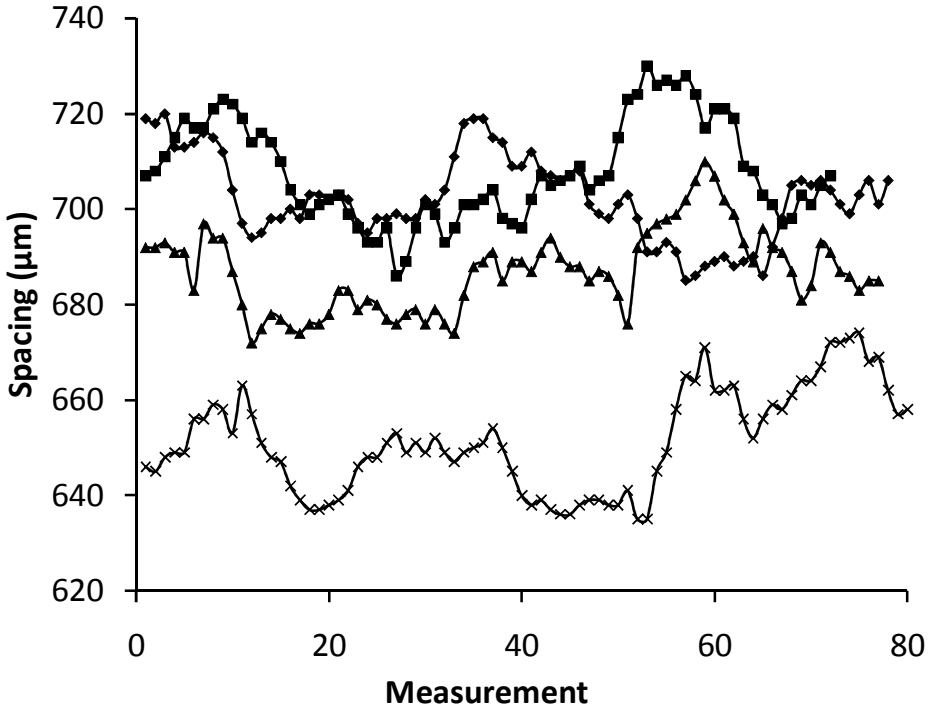

Figure 7.7 Droplet spacing measured over 80 droplets for 4 different cases using the same chip.

7.5.6 Chip Fabrication

PDMS chips were fabricated using standard soft lithography techniques as described in Chapter 3 Section 3. Briefly, two SU-8 masters were fabricated for the experiments with channel heights of 50μm for the L-1:1 and L-1:0.8 designs. PDMS molds 5:1 were made from these masters which were subsequently oxygen plasma bonded (500mTorr, 29.7W for 20s) to PDMS coated glass slides. A lower ratio of PDMS base to curing agent creates a stiffer material that is able to withstand swelling and bulging better. Completed chips were then heated overnight at 160˚C to allow the PDMS to revert back to its natural hydrophobic nature. Prior to beginning experiments, silicone oil was pumped through the network for 45min to allow the channels to swell completely. Afterwards, all open inlets were plugged and high pressure (1 bar) was used to dissolve any remaining air bubbles trapped within the chip. At this point the chip was ready to be used in the sorting experiments.

7.5.7 Video Experimental Setup

The experimental setup is similar to that presented for the T-junction generator. However, videos of the sorting process were taken with the low speed Retiga 200R Fast 1394 CCD camera rather than the high speed camera because the Retiga was easier to integrate into a custom Matlab program that provides real-time analysis of the sorting process. All fluids were controlled using the Fluigent system with pressure control provided to 5 different inlet streams.

7.5.8 Data Extraction from Videos

Videos captured by the camera are analyzed in real time to extract the sorting parameters. Figure 7.8 shows the typical image captured by the camera during the sorting experiments. Two detection boxes are drawn on top of the outlet channels and a passing interface is detected by a change in the overall intensity. Using the phase contrast on the microscope causes the rounded interface of the droplet to be significantly brighter than the surrounding oil which allows for straightforward detection of the droplets. However, the low frame rate of the camera (<30 f ps) means that the frequency of the incoming droplets is also limited to approximately <5Hz to guarantee that all droplets are detected in the outlet sorting channels.

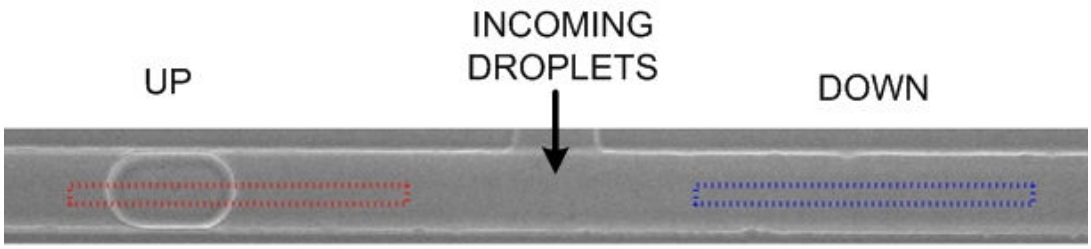

Figure 7.8 Snapshot from a video of the sorting process with the two interrogation boxes overlaid.

For each measurement at least 100 sorting events are analyzed and the trajectory of each droplet is recorded. A droplet trajectory is indicated by whether it chooses either the UP (U) or DOWN (D) outlet channel. The sequence of events is recorded as a string of characters, for example: UUDUDDUDUUDUDD. An algorithm adapted from Smith and Gaver is then applied to extract any periodicity if it exists (Smith and Gaver 2010). The algorithm creates a stencil of potential pattern length *n* from the first *n* events and compares it to the remaining sequence. If the stencil repeats for the entire sequence then the pattern is said to be converged. If not, then the stencil length is increased and the process repeats. If no pattern is found over the entire length of the sequence then the sorting is assumed to be chaotic. Note that this method finds the smallest pattern length, which may be a harmonic of a longer overall pattern. For example, the alternating sequence of UDUDUDUD, will result in a pattern length of 2 (UD) but the entire pattern is actually a multiple of this harmonic.

In addition to extracting the sorting pattern the incoming and outgoing frequency and spacing of the droplets are calculated. The speed and size of the droplets are measured beforehand by analyzing a high speed video of the incoming droplets. The incoming spacing is then calculated by the frequency of incoming droplets and the speed ($\lambda=u/f$). The fraction of droplets sorting into the two channels is determined as the portion of U and D events from the total sequence.

7.5.9 Experimental Procedure

Below a brief outline of the experimental procedure is provided for the reader's reference:

- Chips were fabricated and prepared.
- The Fluigent system is then warmed up and calibrated to zero point.
- The chip was connected to the pressure system and flushed with oil for 20 minutes, until all gas bubble were dissolved.

- Next the aqueous phase was connected and pressures were set to generate droplets for 30 minutes.
- The camera and microscope were then setup to take videos at the T-junction.
- Pressures were then adjusted to achieve the desired spacing and droplet speed. Once these were set the system was run for 15 minutes to achieve steady droplet sorting.
- First a high speed video of the droplets entering the T-junction was recorded. From this video the incoming speed and approximate spacing was calculated. This data was then inputted into the Matlab file that takes videos of the sorting process with the Retiga Camera.
- Next a video of the droplet sorting was recorded and analyzed to determine the pattern. All relevant data: spacing, speed, frequency, sorting pattern, number of droplets was outputted to an Excel file.
- For a new measurement the pressures were adjusted again and the video recording was repeated.
- This was repeated to get a wide range of droplet spacings and asymmetric pressures for the chip being tested.

7.6 Measuring Droplet Resistance Experimentally

Since the sorting phenomenon is caused by the feedback associated with the presence of a droplet in a channel, knowing the incremental increase in resistance caused by a droplet is important to understanding the sorting process. Several factors influence the hydrodynamic resistance of a droplet train including (a) the Laplace pressure drop across the front and back caps, (b) viscous dissipation in the thin film surrounding the droplets, (c) the continuous phase bypassing the droplets through the gutters (d) viscous dissipation from eddies created in the continuous phase and within the droplets (Adzima and Velankar 2006; Fuerstman, Lai et al. 2007; Labrot, Schindler et al. 2009; Vanapalli, Banpurkar et al. 2009; Baroud, Gallaire et al. 2010; Ody 2010). Several experimental studies have isolated the main factors at play which include the viscosity contrast between the two fluids, the Capillary number, the relative droplet size compared to the channel size and the spacing between droplets. However, the complex interaction between all of these parameters results in a non-trivial dependence that has not been fully explained to date (Baroud, Gallaire et al. 2010). Therefore the droplet resistance must be measured experimentally in order to obtain a reliable value.

A number of different techniques have been developed recently to measure droplet hydrodynamic resistance in microchannels. The most obvious method is to simply measure the pressure drop across a channel for a fixed flow rate with and without droplets present (Adzima and Velankar 2006; Labrot, Schindler et al. 2009). By comparing the two results, the additional resistance created by the droplets can be calculated as:

$$R_d = \frac{\Delta P^* - \Delta P}{nQ} \tag{7.44}$$

where ΔP^* is the pressure drop with droplets, ΔP without droplets, n is the total number of droplets and Q the total flow rate. However, for microfluidics the technique is limited since connecting the pressure sensor to the channel, typically be soft tubing, increases the dead volume and compliance of the system significantly. This results in extremely long settling times that are difficult to control (Labrot, Schindler et al. 2009).

Since it is difficult to incorporate a pressure sensor directly into the chip, other techniques have been developed that extract the droplet resistance through indirect measurements of the flow field. Vanapalli *et al.* used a highly sensitive microfluidic manometer to measure the resistance of individual droplets in a microchannel (Vanapalli, Banpurkar et al. 2009). The manometer is based on the deflection of an interface created by two streams of fluid that have passed through a "test" channel and an identical "comparator" channel which are in parallel (Abkarian, Faivre et al. 2006). One of the fluids is dyed so that the interface of the converged streams can be monitored using a camera. When a change occurs in the "test" channel, such as a droplet passing through, it causes an imbalance in the two streams which deflects the interface. From a calibration plot, the deflection can be correlated to a pressure imbalance and by association an increase in the hydrodynamic resistance. This technique produces highly accurate measurements with millisecond response times to hydrodynamic changes. However, it is also very time consuming and requires careful calibration of the interface deflection. As Vanapalli *et al.* pointed out, it is also difficult to incorporate a conventional T-junction droplet generator with the comparator because the two streams are never balanced during the formation cycle. To overcome this limitation, the authors developed a novel drop on demand system to perform their experiments. However, a choice was made to avoid this additional cost and use a different technique for measuring the droplet resistance.

The second technique proposed by Labrot *et al.* uses the same sorting phenomenon that is currently being studied. The design consists of a bifurcation T-junction that connects to a loop with asymmetric channel lengths. Drops entering the loop choose one of the two branches based on the difference in hydrodynamic resistance. By following the number of droplets in each of the two branches the effective droplet resistance can be estimated Labrot *et al.* vetted the loop based method by comparing results with the pressure sensor method; though the loop method produced significantly larger scatter in the calculated droplet resistance (~20%). Because this technique compliments the current study so well, it was chosen as the first method for measuring droplet resistance.

7.6.1 Loop Based Droplet Resistance Measurements

Experiments were performed using a slightly modified version of the loop based method using chip design is shown in Figure 7.9. In this method drops are continuously formed from the T-junction until they fill the entire loop network and steady state is reached. The high hydrodynamic resistance channel on the exit ensures that the dynamic resistance created in the loop does not affect the upstream T-junction generator. During this time the diluting stream indicated in Figure 7.9 is pressurized so that there is a positive flow from this channel and no droplets enter it. After steady state is reached the pressures are adjusted so that the there is no backflow in the storage area and the loop is flushed with oil until no droplets remain. The pressures are then readjusted so that the droplets stored in the serpentine enter the loop. As the droplets enter the loop they are monitored using the microscope. Droplet resistance is measured by counting the number of droplets that enter the short branch before the first droplet chooses the long branch.

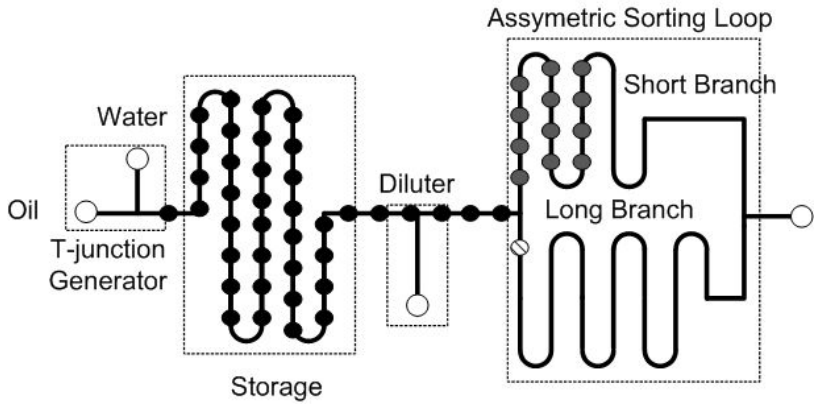

Figure 7.9 Chip design for measuring droplet resistance using sorting at an asymmetric loop. Droplets stored upstream in the storage area are transported to the loop sorting into the short branch to equate the resistances of the two branches. The experimental procedure consists of counting the number of droplets that sort to the short branch (grey dots) before the first droplet sorts into the long branch (stripped dot).

The droplet resistance is then calculated by equating the two resistances, which leads to an upper and lower limit:

$$\frac{R_b - R_a}{n-1} > R_d > \frac{R_b - R_a}{n} \tag{7.45}$$

where R_b is the resistance of the long channel, R_a the short channel and n the number of droplets entering the short channel.

Experiments were performed for several droplet sizes ranging from $L_d^* = 1.2 \rightarrow 2$ for viscosity contrasts $\eta = 1/10 \rightarrow 1$ using silicone oil and water/glycerol combinations with 1% SDS as the surfactant. Typically, 15-35 droplets were counted before one droplet entered the long channel which resulted in a tight range on the limits in Eqn. 7.45. However, the results from these experiments were unsatisfactory. Obtaining repeatable measurements was nearly impossible as there was large chip to chip variability (~50%), though some general trends could still be identified. First, droplet resistance increased proportionally with droplet length. Second, there seemed to be no dependence on the viscosity contrast in the range that was considered. Third, the hydrodynamic resistance of a single droplet was large, typically ~4-5times larger than the equivalent resistance of oil that it replaced. The reason for the large variability is unknown, but it is hypothesized that stopping and starting the droplet train leads to non-steady droplet speeds during the sorting process and hence non-steady droplet resistances due to the *Ca* dependence. As well, sharp turns were used in the design which may also have contributed to a non-uniform droplet resistance in the channels. To overcome these problems a different method was used to measure the droplet resistance where the droplets are continuously moving. The new technique is similar to the pressure sensor method, though with some modifications so that the experiments could be performed with the available equipment.

7.6.2 Pressure Method for Droplet Resistance Measurement

Experiments were performed using the same design as for the sorting experiments except that outlets B and C were plugged so that droplets formed upstream at the T-junction only exit outlet A (see Figure 7.10). The pressure drop across the outlet channel (from the diluting inlet to the exit) was measured by assuming that the pressure at the diluting inlet was the same as the pressure which was applied from the Fluigent system. The flow rate was measured using the flow sensor connected in series at the Outlet A. High speed videos were analyzed to measure the droplet size, spacing and speed. Before running the chip with the droplets, the channel resistance

without droplets was measured for 3 different pressures (500, 800, 1000 mbar) to quantify any bulging effects. Typically, the channel resistance would change by 10% from 500 to 1000 mbar. A curve fit was applied to the data in order to estimate the natural channel resistance at an applied pressure when performing the droplet resistance calculations.

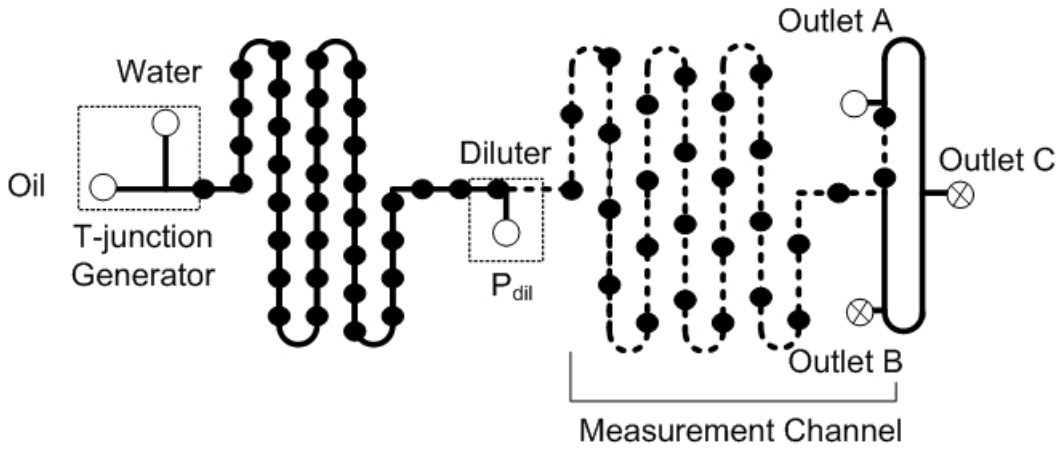

Figure 7.10 Modified chip design for the droplet measurement using the applied pressure at the diluter (P_{dil}) and the resistance of the measurement channel (dashed line). The flow sensor is connected to Outlet A, while Outlets B and C are plugged during the measurements. Droplet spacing and speed is measured at the bifurcation using the high speed camera.

Droplets of various size, spacing and speeds were generated using the T-junction generator and the pressure drop and flow rate were recorded, for various combinations of silicone oil and water/glycerol. The droplet resistance was calculated using the following equation:

$$R_{drop} = \frac{R^{+}_{hyd} - R_{hyd}}{n} \tag{7.46}$$

R^{+}_{hyd} is the hydrodynamic resistance of the channel with droplets, R_{hyd} without droplets, n is the total number of droplets in channel as measured from the spacing. Often the droplet resistance is quoted as the equivalent length of added channel resistance, which is given as:

$$L_{Rdrop} = \frac{R_{drop}}{R_{hyd}} L \tag{7.47}$$

Experiments were performed with two water/oil combinations: water/silicone oil 60%glycerol+water/silicone oil. Surfactants were present in both cases (1% SDS in the aqueous solution). Measurements were made for various droplet sizes (L_d/w_c=1.2~1.8) under typical flow conditions in the sorting experiments (*Ca~0.005*). Droplet spacing was $\lambda^{*}>6$ for all experiments so that co-operative effects from droplet proximity are not significant (Labrot, Schindler et al.

2009). The results are presented in Figure 7.11. In both cases, droplet resistance increased proportionally with droplet length in the measurement range. As well, the glycerol/water combination resulted in twice the droplet resistance for the same size. Based on this data, in the sorting experiments the water/glycerol combination was used because the larger droplet resistances would have a greater impact on the flow fields at the bifurcation.

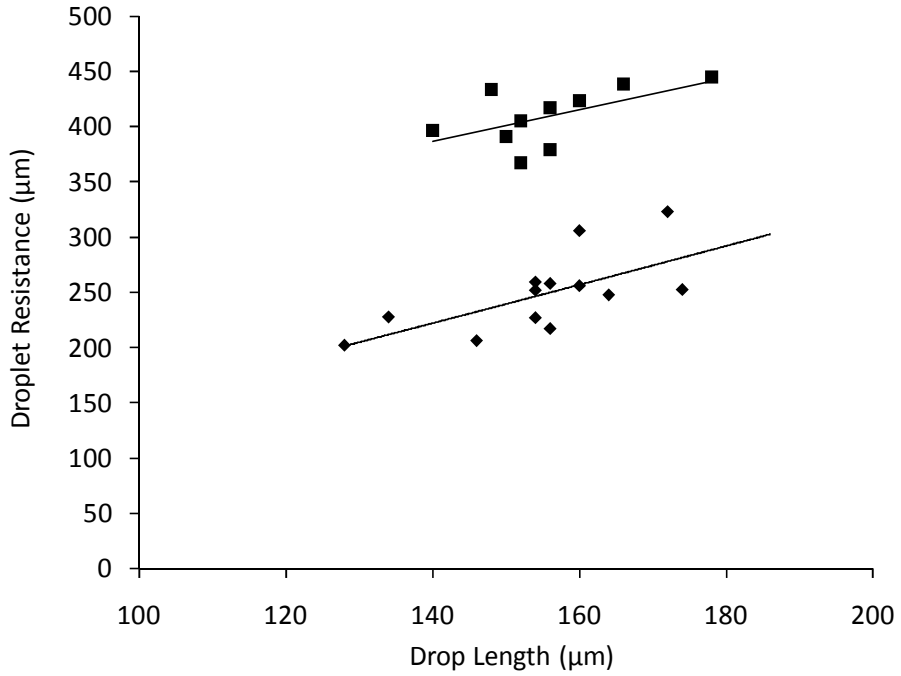

Figure 7.11 Equivalent droplet resistance L_{Rdrop} with respect to droplet length L_d for η=0.1 (♦) and η =1(■). Trend lines are linear fits to the data.

7.7 Model Validation

In this section both the continuum and discrete models are compared to the numerical and experimental results to validate the developed theories. First, results are compared for the idealized numerical simulations beginning with the general case solution and then followed by the simplified cases with only asymmetric pressures and branch lengths. The performance of the discrete model is validated by analyzing the predictive ability for both cycle time and droplet distribution. Afterwards, the model is tested against the full numerical simulations, which incorporates the non-ideality that flow rates fluctuate during the sorting process. This simple addition to the system creates regions of complete chaos. As part of this discussion a possible explanation is provided for when a pattern may be stable or not. Finally, the model is applied to

the real experimental data. Comments are then made on the practical application of the knowledge gained to the development of a random droplet sampler.

7.7.1 Ideal-Model General Case Studies

The general case involves all of the possible asymmetries that may appear including: asymmetry in lengths, cross-section area, pressures and droplet resistances. Most often only a few of these asymmetries may be present, however, testing against the entire gauntlet provides a means to analyze the performance of the model under extreme conditions. Idealized numerical simulations were performed for four case studies as summarized in Table 3.4. For each case the incoming droplet frequency was varied to achieve a large range of incoming droplet spacings and sorting patterns.

Table 7.4 Four case studies for the general numerical simulations. Parameters include the length of the two branches (L_1, L_2) [mm], pressures (P_1, P_2) [Pa], droplet equivalent lengths (L_{drop1}, L_{drop2}) [mm], widths and height (w,h) [μm]. The dimensionless variables are the area ratio A^*, droplet resistance ratio R^*_{drop}, branch length ratio Λ and pressure skew P^*. Pressure at the junction was set to 100 Pa.

Case	L_1	L_2	P_1	P_2	L_{drop1}	L_{drop2}	w,h_1	w,h_2	A^*	R^*_{drop}	Λ^*	P^*
1	5	4.5	10	0	0.5	0.5	100,50	80,50	0.8	1	0.9	1.11
2	5	4	0	10	0.5	1	100,50	80,50	0.8	2	0.8	0.9
3	5	5	0	20	0.5	0.25	100,50	80,50	0.8	0.5	1	0.8
4	5	5	0	10	0.5	0.25	100,50	100,50	1	0.5	1	0.9

Results for the pattern length (i.e. T^*_{cyc}) are presented in Figure 7.12, for the droplet distribution (n_a, n_b) in Figure 7.13, and for the probability of a droplet sorting into Branch b (P_b) in Figure 7.14. First, an explanation of the general presentation of the results is required, as the same format is used throughout this section. Data is plotted versus the incoming droplet spacing $2/\lambda^*$, which was identified in the analytical modelling as the critical variable that defines the sorting phenomenon. All data from the numerical results are plotted using markers such as circles (○) or triangles (Δ). Predictions made by the discrete model are plotted using solid lines of various colours. The vertical dashed lines on the left side of the plot are the prediction for the limit of the filtering regime as calculated by the continuum (– –) and discrete (·–) models. Alternating grey and white regions define the areas where the cycle time is expected to be the same as calculated by the bounds from Eqn. 7.27. Crossing from one region into another may cause the cycle time to change so we expect a possible change in the pattern length.

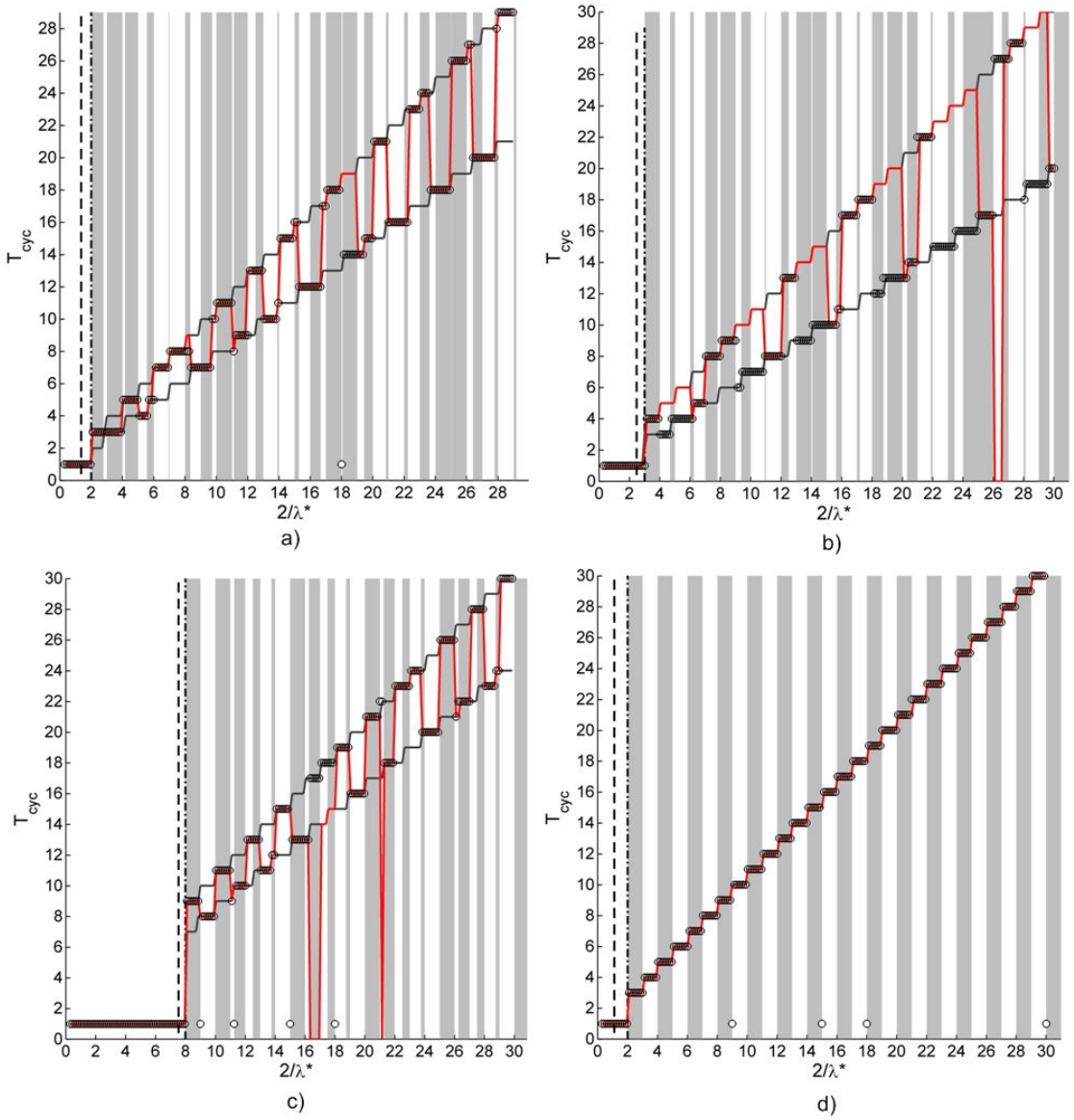

Figure 7.12 Idealized numerical simulation results for the pattern length (○). Overlaid are the predictions from the continuum and discrete models. Vertical dashed lines on the left represent the limits for the filtering regime as predicted by the continuum (--) and discrete models (·–). Grey and white regions define the regions where the cycle time is expected to remain unchanged. Black lines are the predictions for T^*_a and T^*_b from the discrete model. The red line corresponds to the selection rules derived in Section 3.3. Each plot corresponds to Case 1(a), Case2 (b), Case 3(c) and Case 4 (d).

Figure 7.12 shows the pattern length from the numerical simulations versus the prediction from the selection rules. The two black lines on the plots are the predicted cycle times for the two branches (T^*_a, T^*_b). The red line is the selection made by the model for the cycle time of the system (T^*_{cyc}). If the red line equals 0 it means that no selection was made from the rules. This problem occurs occasionally; the reason for this issue is discussed later.

For the most part, the model is able to capture most of the salient features of the numerical results. As expected, the sorting system oscillates between the two potential cycle times in a non-trivial manner. The discrete model is able to accurately predict the limit of the filtering regime and shows a significant improvement over the continuum model prediction. In these four cases, the numbers of droplets needed to balance the system (N_{bal}) are 2, 3, 8, and 2 respectively. As predicted, cycle times correspond either to T^*_a or T^*_b and transitions from one regime to another are accurately predicted by Eqn. 7.27. From the visual representation of the alternating grey and white regions, one can clearly see the striking complexity that can arise in the cyclic structure.

For case 4, where the lengths and cross sectional areas are the same, there is only one possible set of cycle times and the selection rules are completely accurate (see Figure 7.12d). In the other cases where the cycle times for the two branches are different errors do occur but in general the predictions are good. Over the 4 cases considered here the sequence length was predicted correctly 85.9% of the time. This result is skewed by the worst case, number 2, where the accuracy was only 56.4%. Poor predictions are typically caused by a poor estimation of N_T from Eqn. 7.34. Generally, Eqn. 7.34 slightly over predicts the value for N_T (refer to Figure 7.13d). This becomes a problem near whole numbers where a small over prediction causes the ceiling function in Eqn. 7.34 to set N_T to the wrong value (+1 of the actual) during the calculations. Upon inspection this is generally the source of all errors in the prediction including the situation when model returns a 0 value for the prediction.

In Fig. 7.13 the average total number of droplets in the two channels (○) over time and the specific number of droplets in channel A (Δ) and channel B (∇) at any point in time. The red line is the prediction from the discrete model for the average number of droplets (Eqn. 7.34). Looking closely at Case 2 (Fig. 13b) one can see that there is a systematic over prediction throughout the data that leads to the poor performance of the model that was just discussed.

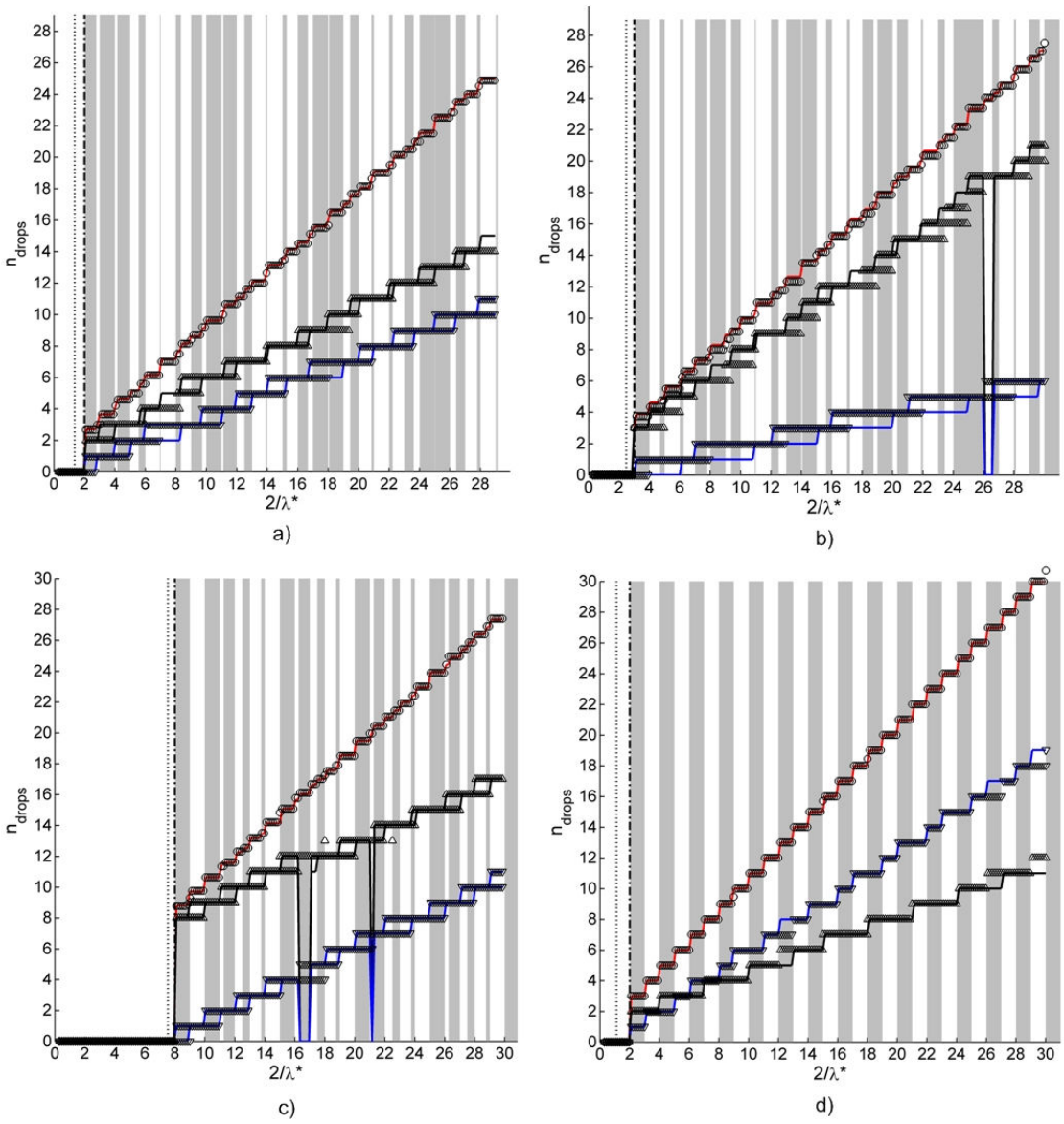

Figure 7.13 Idealized numerical simulation results for the average number of droplets (○) in the two branches over time and the specific number of droplets at any point in time for branch A (Δ) and B (∇). Red line corresponds to the discrete model prediction for the average number of droplets. Black and blue lines are for the number of droplets in branches A and B respectively.

Black and blue lines are the prediction for the number of droplets in branches *a* and *b*. Recall that as part of the derivation of the selection rules for the idealized numerical simulations it was identified that the number of droplets in a channel may be constant or oscillate by 1. In the figures this can be seen by looking at the number of markers for a single value of $2/\lambda^*$. For instance, in Figure 7.13a at $2/\lambda^*=14$ we see to the left that the number of droplets in the two channels remains constant at 7 (branch a) and 5 (branch b) in the period regime. This corresponds to case (i) in the selection rules. To the right there is a new periodic regime, and the number of droplets are

constant in branch A (8) and oscillating in branch B (5, 6) which corresponds to case (ii). In Figure 7.13d, there are actually no oscillating conditions throughout the entire range of $2/\lambda^*$. This is typical for cases when the cycle times of the two branches are identical. Generally, if the model is able to accurately predict N_T then it is also able to predict the number of droplets in the two branches.

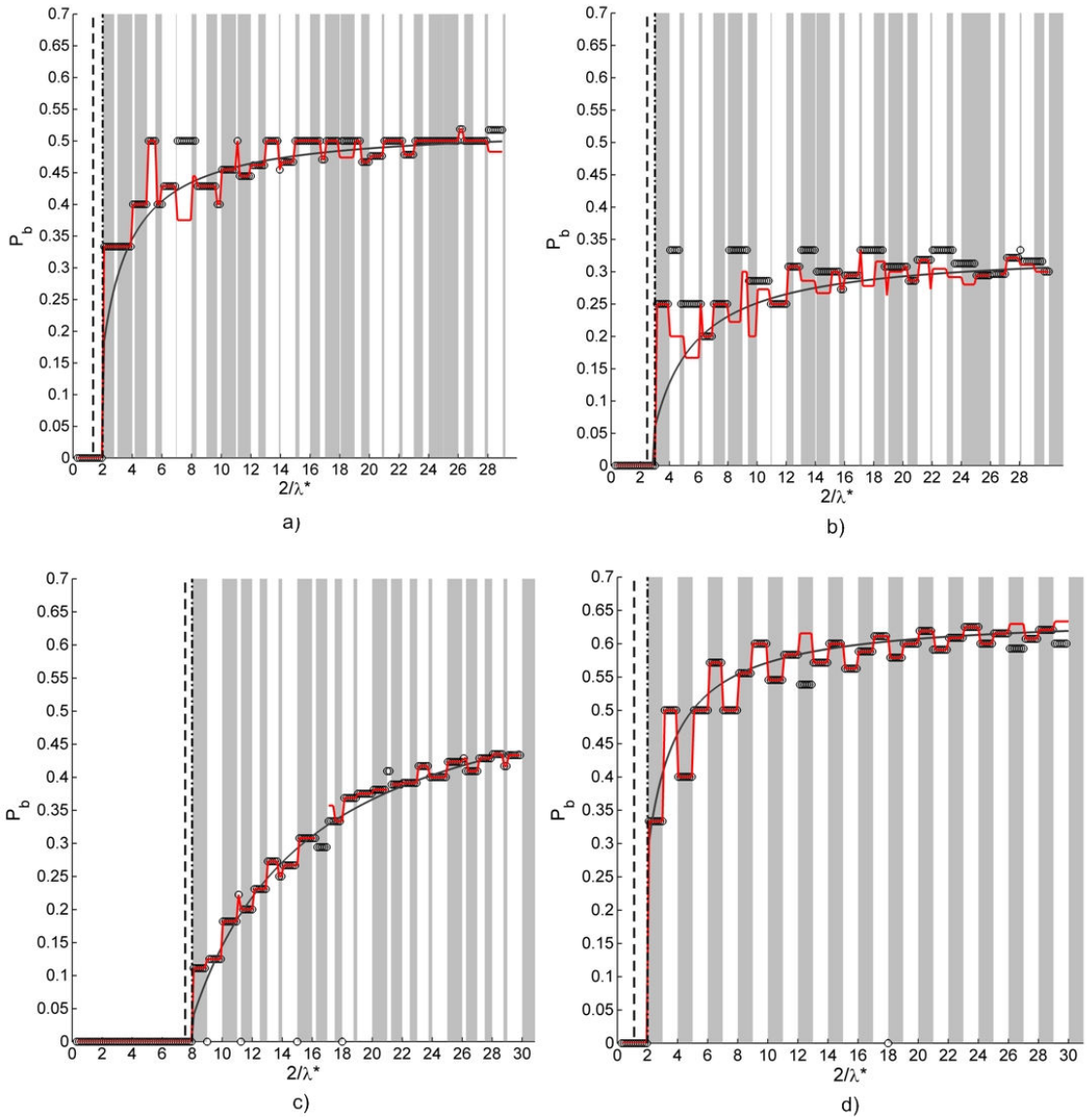

Figure 7.14 Fraction of droplets sorting into channel B ($Prob_b$) from the ideal-model simulations (○). The red line is the prediction by the discrete model and the solid black the continuum model.

Figure 7.14 shows the probability of a droplet entering branch B. The red line is the discrete model prediction and the solid black line the continuum model prediction. Overall the distribution of droplets into channel B increases, although not monotonically, and approaches an asymptote at higher values of $2/\lambda^*$. This limit extends to the continuum approximation as the population of droplets in the channels increases. The figures clearly show that the oscillations are well described by the discrete model predictions. Most of the plateaus are captured by the model as well as the discontinuous jumps in the distribution as periodic regimes are crossed. Additionally, the critical transition from filtering to sorting is accurately predicted.

Looking more closely, we see an odd state of affairs for Case 4 where the distribution of droplet in channel B reaches a limit greater than 50%. This seems to go against intuition because one would expect the filtering branch (channel A) to have the higher portion of droplets in all cases. There is however a clear explanation. In Case 4, the two branches have symmetric lengths and cross-sectional areas but asymmetric pressures and droplet resistances. Droplets originally filter into the channel with the lower resistance; in this situation Branch #1 because of the asymmetry in pressures. This sets Branch #1 as the filtering channel (channel A). However, once droplets begin to sort the distribution is governed by balancing the channel resistances. Droplet resistance in channel B is one half that of channel A. Therefore, more droplets are required in channel b to balance the system. This explains why the fraction of droplet entering channel b is greater than 50% once the droplets begin to sort.

In this section the predictive ability of the discrete model was tested against ideal-model simulations involving the full range of possible asymmetries. Both the continuum model and the discrete model are able to predict the performance quite well; although, the performance can be poor in some circumstances. This is due to the large number of variables combined with the problems of discretizing the calculations. In the following section the discrete model is compared to more practical conditions with only asymmetric pressures and branch lengths, whence the lower number of variables leads to improved accuracy.

7.7.2 Ideal-Model Simplified Case Studies

The simplified model was tested against nine different case studies that varied the droplet resistance, branch lengths and pressures as summarized in Table 7.5.

Table 7.5 Nine case studies used to test the simplified conditions. Parameters include the length of the two branches (L_1, L_2) [mm], pressures (P_1, P_2) [Pa], and droplet equivalent lengths (L_{drop1}, L_{drop2}) [mm]. The dimensionless variables branch length ratio Λ and pressure skew P^*. Junction pressure was set to 100 Pa.

Case	L_1	L_2	P_1	P_2	L_{drop}	Λ^*	P^*
1	5	5	0	0	0.25	1	1
2	5	4.5	10	0	0.5	0.9	0.9
3	5	4	20	0	1	0.8	0.8
4	5	5	0	10	1	1	0.9
5	5	4.5	0	20	0.25	1.11	0.8
6	5	4	0	0	0.5	0.8	1
7	5	5	20	0	0.5	1	0.8
8	5	4.5	0	0	1	0.9	1
9	5	4	0	10	0.25	0.8	1.11

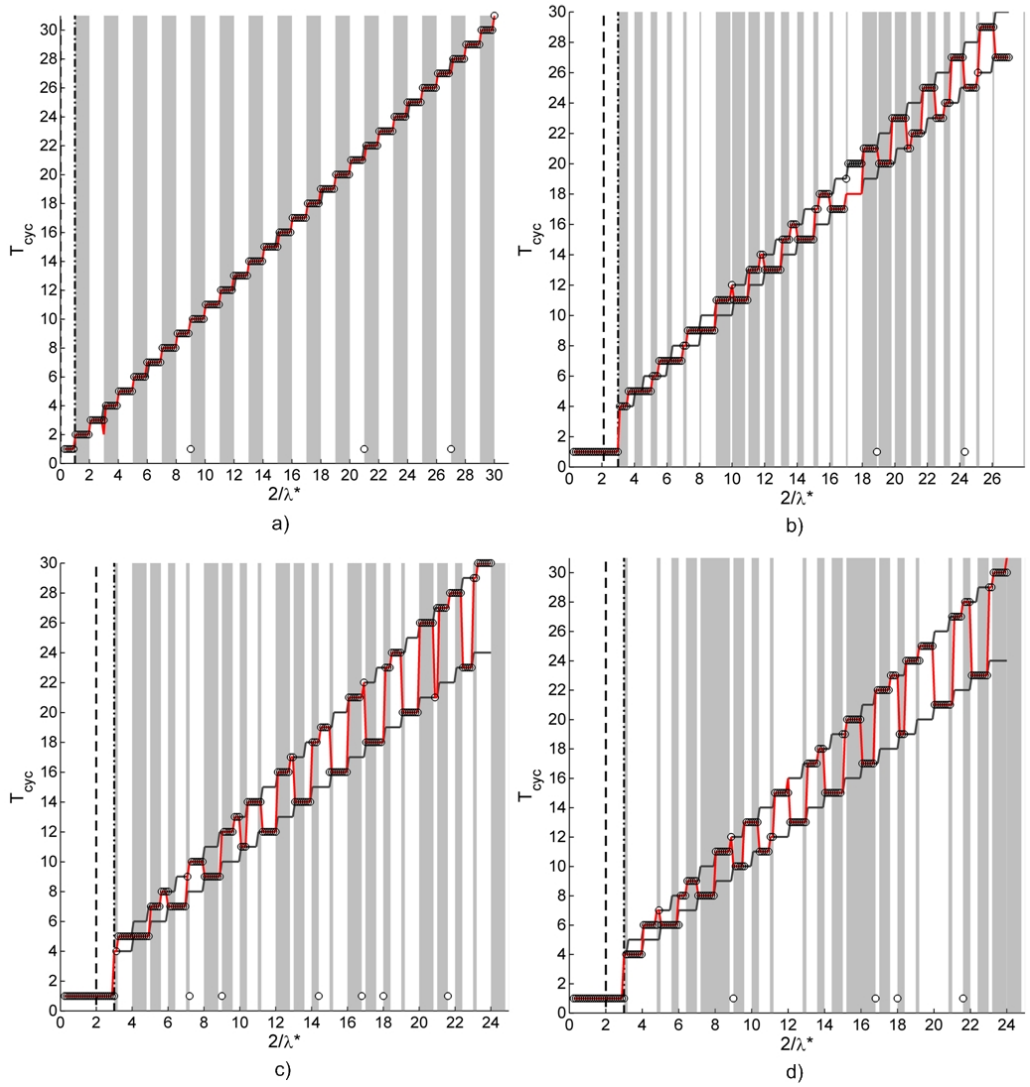

Figure 7.15 Ideal-model numerical simulation results for the pattern length (○) corresponding to test Case 1 (a), Case 2 (b), Case 6 (c), and Case 9 (d).

Figure 7.15 and 7.16 present the comparison for the pattern length and $Prob_b$ for four of these studies. Overall the same features are apparent as those already described for the general case studies. The cut-off for filtering, bifurcation between different periodic regimes, T^*_{cyc} and $Prob_b$ are all captured by the discrete model. In fact, overall the discrete model is more accurate in predicting the pattern length and droplet distribution for the simplified case studies. Across the 9 studies presented here, the model was correct in predicting the cycle time and droplet distribution 96.7% and 97.1% of time. Again mistakes in the prediction were caused by the slight over prediction of N_T near whole number values. Generally, this problem increased with greater asymmetry such as when both pressure and branch length asymmetry were combined together on the same branch. Still, the excellent accuracy of the model provides confirmation of the predictive power of the model.

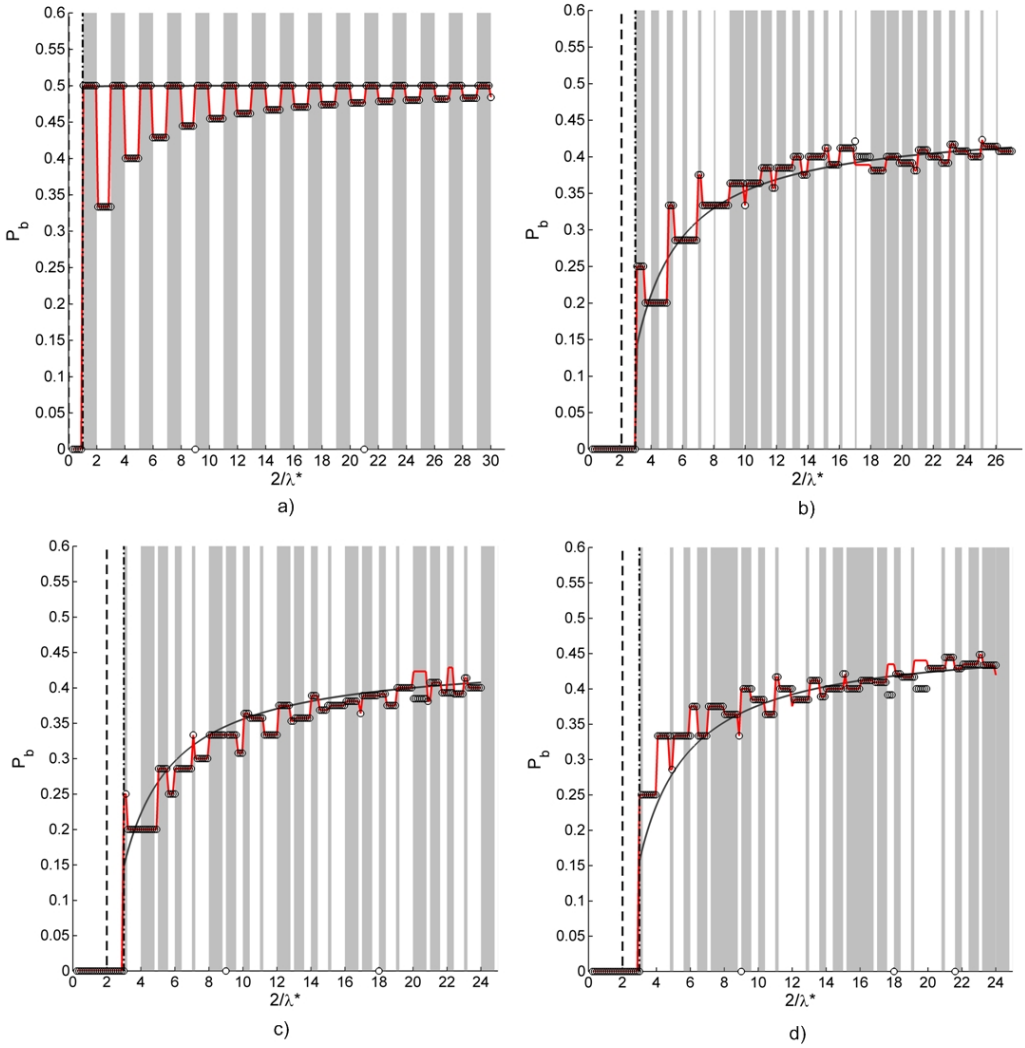

Figure 7.16 Ideal-model numerical simulation results for the $Prob_b$ (○) corresponding to test Case 1 (a), Case 2 (b), Case 6 (c), and Case 9 (d).

7.7.3 Full-Model Simplified Case Studies

In this section the discrete model is compared to the full-model numerical simulations. A total of 9 studies were performed as summarized in Table 7.6. Simulations were performed using the same geometry as the test chip from the diluter onwards (refer to Table 7.3), and under similar applied pressures as used in the experiments (refer to Section 7.5). These conditions are also close to those used to validate the discrete model against the ideal-model case studies (Table 7.5).

Table 7.6 Nine case studies used to test the full-model conditions. Parameters include the length of the two branches (L_1, L_2) [mm], pressures (P_1, P_2) [Pa], and droplet equivalent lengths (L_{drop1}, L_{drop2}) [mm]. The dimensionless variables branch length ratio Λ and pressure skew P^*. Simulations were performed including the main channel inlet with the same dimensions as the experimental chip design (100 mm). Pressure at the junction was approximately 228.5 Pa and the applied pressures at the outlet were set to a base of 215 Pa.

Case	L_1	L_2	P_1	P_2	L_{drop}	Λ^*	P^*
1	5	5	0	0	1	1	1
2	5	5	0	3	0.5	1	0.821
3	5	5	0	3	0.25	1	0.821
4	5	4.5	0	0	0.5	1.11	1
5	5	4.5	3	0	0.25	1.11	0.821
6	5	4.5	0	3	1	0.9	0.821
7	5	4	0	0	0.25	0.8	1
8	5	4	3	0	1	0.8	0.821
9	5	4	0	3	0.5	0.8	0.821

Recall that the only difference with the full-model case studies is that the flow rates are allowed to oscillate naturally. Although the discrete model does not consider these oscillations, all of the salient features are still captured when applied to the full-model studies, with the exception of additional chaotic regions appearing between two successive plateaus to the point where certain periodic regimes disappear entirely. The following discussion breaks down the results for a few specific cases.

Symmetric Channels, Symmetric Pressures

Figure 7.17 shows the results for Case 1 where both branch lengths and pressures are symmetric. Plots are in a similar format as before, except that when the simulation produces no discernible pattern or the pattern length is greater than twice the number of droplets in the channel then it is set to 0. These are the regions where the system is chaotic.

As can be seen in Figure 7.15b, these chaotic regimes are located near bifurcations from one plateau to another. The size of these regimes grows with increasing $2/\lambda^*$ to the point where odd numbered patterns eventually disappear. For this example, the last stable odd cycle is $T^*_{cyc}=5$.

Cybulski *et al.* observed a similar limit and found that the maximum odd cycle that could be observed was a function of the droplet resistance (Cybulski and Garstecki 2010). This was confirmed by repeating numerical simulations with droplet resistances of 0.5 and 0.25 mm, which produced maximum odd cycles of 11 and 19 respectively. Therefore, the trend appears to be that as the droplet resistance increases the stability of the system decreases. Note that even in the chaotic regimes, the distribution of droplets still appears to follow the correct trend as shown in Figure 7.17b.

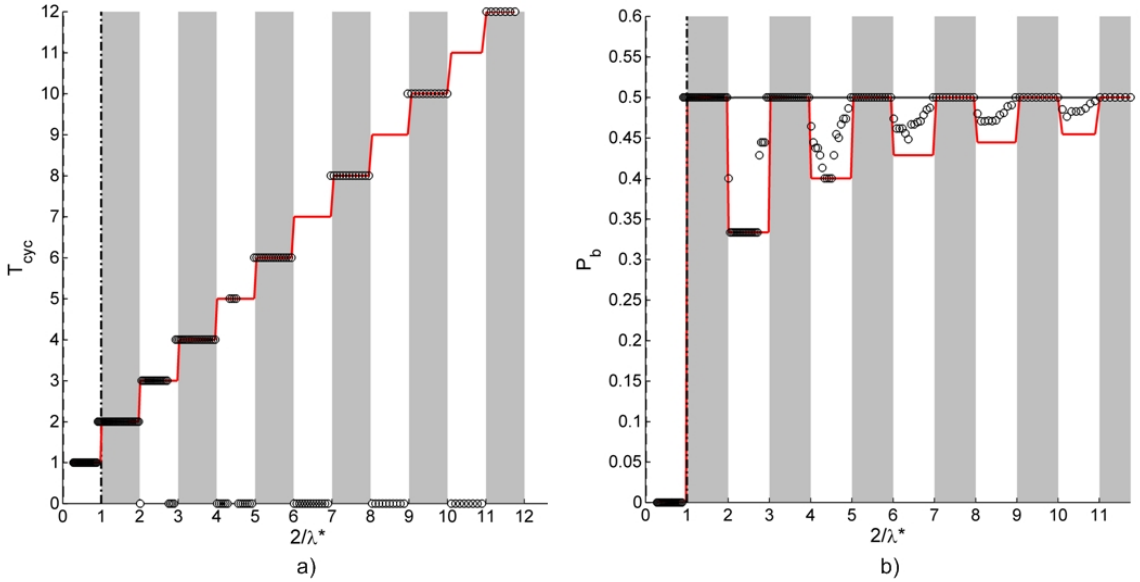

Figure 7.17 Full-model numerical simulation results for the T_{cyc}^{*} (a) and Prob_{b} (b) for Case 1.

Symmetric Channels, Asymmetric Pressures

A comparison can be made between Case 1 and 2, where the only difference is a shift in P^{*} and droplet resistance. The plots for Case 2 are provided in Figure 7.18. Both cases have the same general pattern because the channels are symmetric and therefore the cycle times are the same. Notable differences are a shift in the critical spacing for filter because of the pressure shift and a deviation in the distribution of droplets. Similar to Case 1, the size of the chaotic regimes increases with $2/\lambda^{*}$ and odd cyclical periods greater than 11 disappear.

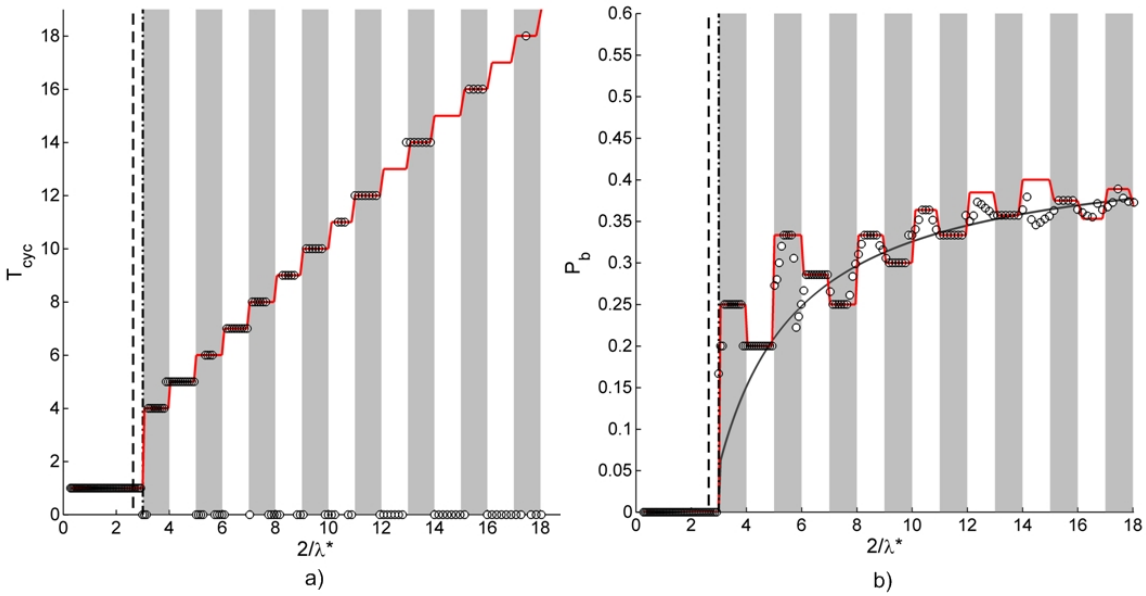

Figure 7.18 Full-model numerical simulation results for the T_{cyc}^{*} (a) and Prob_b (b) for Case 2.

Asymmetric Channels, Symmetric Pressures

Figure 7.19 shows the results for Case 7 where the channels are asymmetric but the pressure are not. In this example, however, it is the even numbered cycle times that disappear with the maximum stable period being 12.

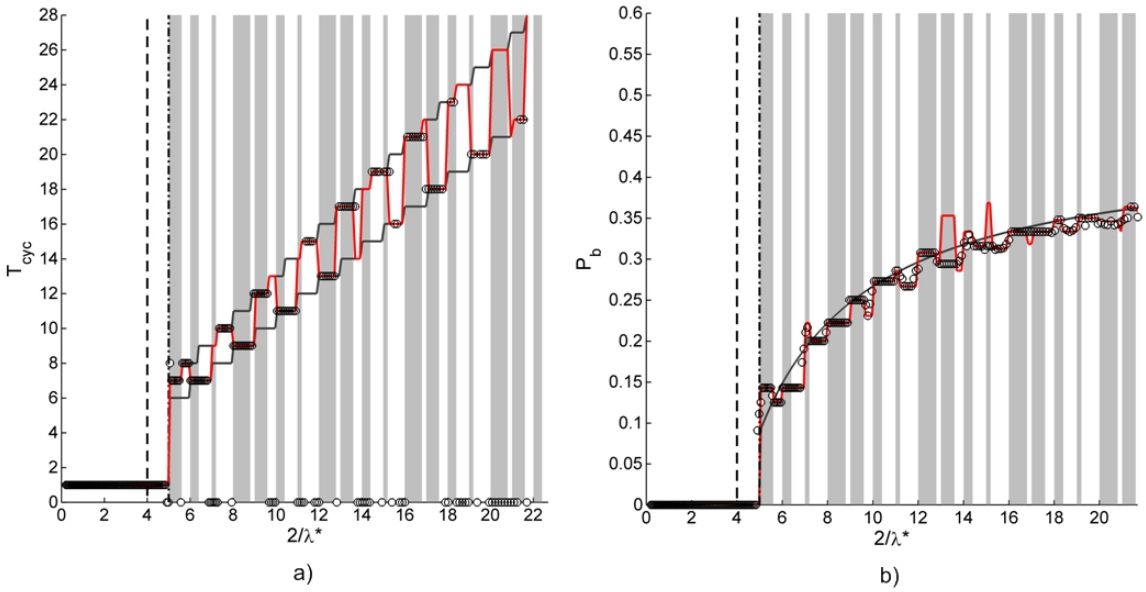

Figure 7.19 Full-model numerical simulation results for the T_{cyc}^{*} (a) and Prob_b (b) for Case 7.

Asymmetric Channels, Asymmetric Pressures

Figure 7.20 shows the results for Case 5 and 6 which have similar branch lengths but alternated pressures. In Case 5, the shorter channel is the filtering channel while it is the opposite for Case 6. Same as before chaotic regimes increase with $2/\lambda^*$. For Case 6 even numbered cycles greater than 4 disappear. While for Case 5 it is not clear whether odd or even cycles disappear as both are present at high $2/\lambda^*$.

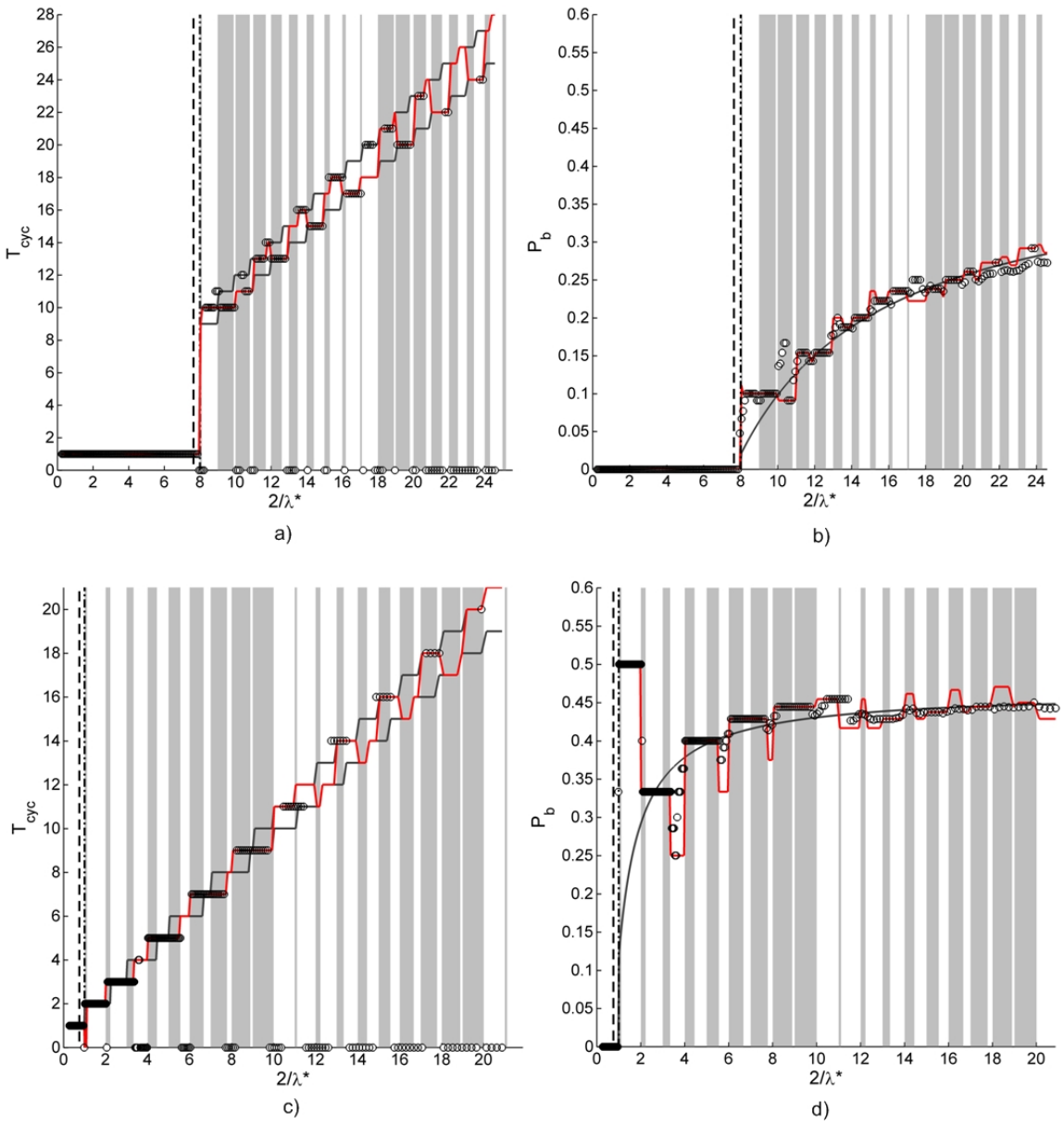

Figure 7.20 Full-model numerical simulation results for the T^*_{cyc} (a) and Prob_b (b) for Case 5 and T^*_{cyc} (c) and Prob_b (d) for Case 6.

7.8 Prediction of Stable and Chaotic Regimes

Closer inspection of the chaotic regimes reveals that they typically consist of very long patterns that contain fragments of the bracketing stable regimes. For example, if the two bracketing regimes are $T_{cyc}^{*} = 4{,}5$ with sequences of UDUD and UUUDD, then these may appear in the longer chaotic sequence such as dUUUDDuUDUDuduud. Similar observations were made by Cybulski and Garstecki in their experimental results in the chaotic regime (Cybulski and Garstecki 2010).This suggests that the system is switching between the two cycle periods.

One of the main facets of the continuum model is that the two flow rates are equal on average; however, this is not true if the sequence does not absolutely balance the two branches. Figure 7.21 shows the ratio Q_b/Q_a for a completely symmetric setup (Case 1 in Table 7.6). For odd sequences which are generally chaotic, the flow ratio is not equal and more fluid flows into branch A then B. The small imbalance means that the output spacings of the two branches are different than the ideal value ($\lambda_{a,b}=\lambda/2$). Thus a hypothesis may be suggested: *a predicted pattern is unstable if one of the cycle times accounting for the flow imbalance is different from the ideal case*. If the flow imbalance is not great enough to cause the cycle time to change then the pattern is stable, otherwise it is unstable. Below a simple calculation is developed for determining the stability of a pattern based on this hypothesis.

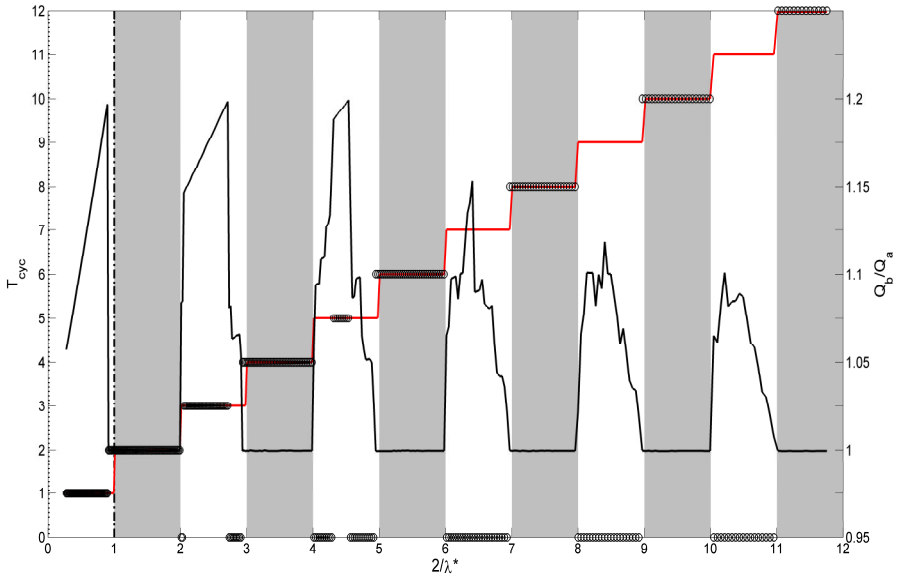

Figure 7.21 Full-model numerical simulation results for the T_{cyc}^{*} plotted on the left axis with the red line as the prediction and Q_b/Q_a plotted on the right axis as the solid black line.

7.8.1 Calculation of the Stability of a Pattern

Estimating the flow imbalance can be calculated by revisiting Eqn. 7.9, and using the number of U-s and D-s determined from the model:

$$\varphi^* = \frac{Q_b}{Q_a} = \frac{L_a + N_U L_{drop}}{\frac{1}{P^*}\left(L_b + N_D L_{drop}\right)}\kappa \tag{7.48}$$

This calculation represents the extreme case for the flow imbalance. Actually, during the complete cycle the average flow imbalance will be lower. Calculating the average is not straightforward because all of the calculations so far have been based on the assumption that the flow rates are equal. Instead, we adjust the calculation using a fitting parameter, $0<\kappa<1$, to correspond with the data. The shift in the flow imbalance, φ^*_{sh}, from the ideal case may be calculated as:

$$\varphi^*_{sh} = \left(\varphi^* - 1\right)\frac{1}{2} \tag{7.49}$$

where the distribution of flow in the two branches then becomes:

$$\begin{aligned} \varphi^*_a &= \frac{Q_a}{Q} = 0.5 - \varphi^*_{sh} \\ \varphi^*_b &= \frac{Q_a}{Q} = 0.5 + \varphi^*_{sh} \end{aligned} \tag{7.50}$$

Subsequently, modified cycle times can be predicted because of this adjustment in flow rates:

$$\begin{aligned} T^*_{a\,\mathrm{mod}} &= t_a f = ceil\left(\frac{1}{\lambda^* \varphi^*_a}\right) \\ T^*_{b\,\mathrm{mod}} &= t_b f = ceil\left(\Lambda^* \frac{1}{\lambda^* \varphi^*_b}\right) \end{aligned} \tag{7.51}$$

The hypothesis is that a pattern may be chaotic if one of the new cycle times is different than the ideal times. This may be captured with the following rule:

If $T^*_{a\,\mathrm{mod}} = T^*_a$ and $T^*_{b\,\mathrm{mod}} = T^*_b$	*Then* the sorting is stable.
Else	The sorting regime is unstable.

Figure 7.22 shows the predicted stable and unstable regions for a few selected cases. A red line distinguishes regions that are expected to be stable and a blue line those that are unstable. These two lines are offset from the numerical data to make the comparison clearer.

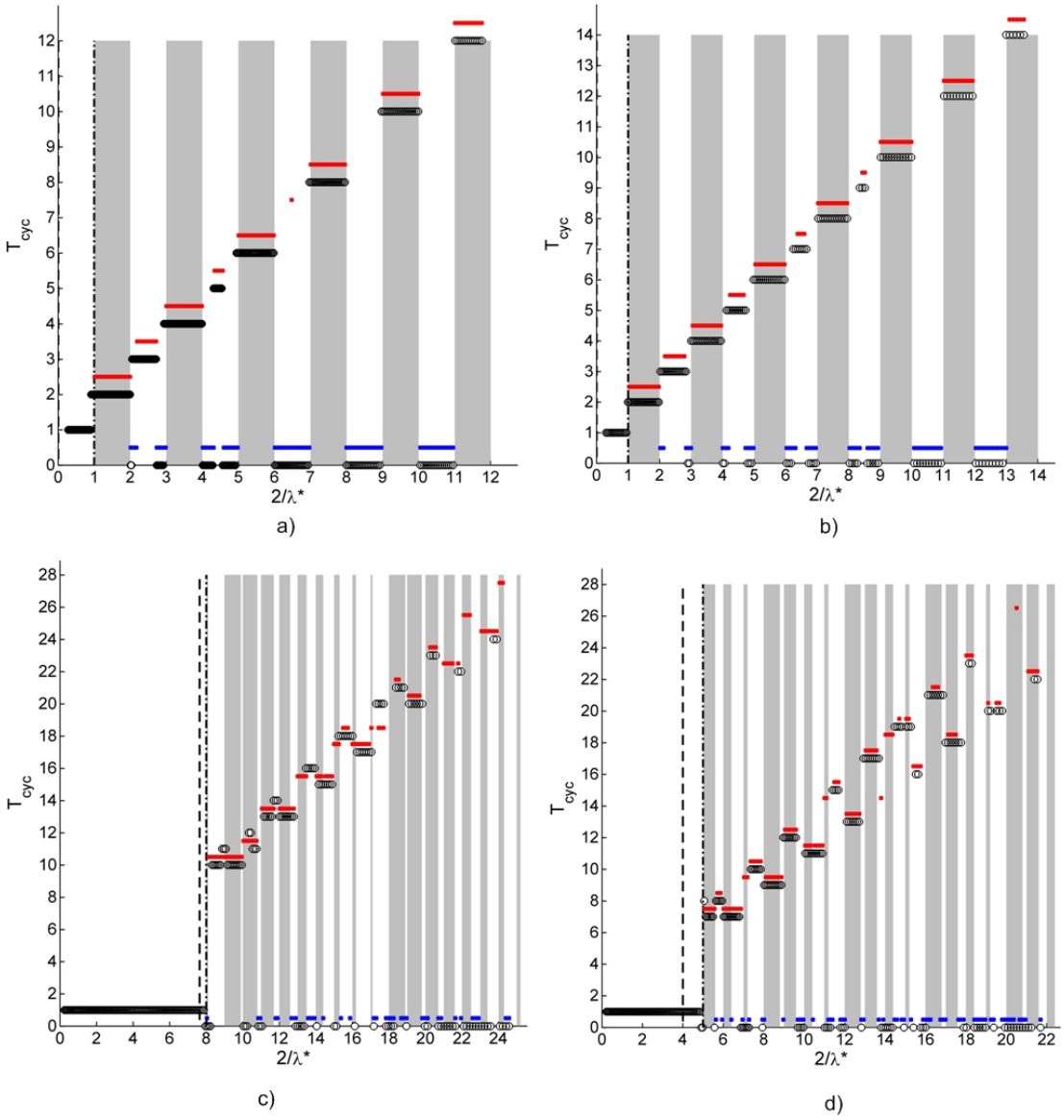

Figure 7.22 Full-model numerical simulation results for the T_{cyc}^{*} with the prediction for stable (red line) and chaotic regimes (blue line). Lines are offset slightly above the numerical results for clarity. Referring to Table 3.3 results are for (a) Case 1, $\kappa=3/4$, (b) Case 1 with $L_{drop}=0.5$, $\kappa=3/4$, (c) Case 5, $\kappa=1/6$ and (d) Case 7, $\kappa=1/3$.

Particularly good agreement is found for the symmetric cases (Figure 7.22 a,b). The gradual decay of higher ordered odd patterns is accurately captured by the calculation. The prediction of the asymmetric examples (Figure 7.22 c,d) is not as good, but still respectable. The poor

performance is most likely due to the uniform κ factor used throughout the calculations. In reality the average weighting will not be uniform across the entire spacing. Therefore, a future improvement on this calculation would be a more robust estimation of the average flow imbalance. Still, the overall qualitative agreement between the prediction and the simulations suggests that the foundation of the hypothesis is correct. Extensions of the model focusing on the stability of a pattern should thus be based around fluctuations in the cycle time.

7.9 Additional Non-idealities: Spacing Fluctuations

Additional non-idealities in the system, such as stochastic noise present in experiments, contribute to a decrease in the overall stability. The presence of noise is included by purposefully adding variance to the incoming droplet spacing. Simulations were run for the completely symmetric design (Case 1 with 0.25 L_{drop}) with the inclusion of spacing fluctuations of 1%, 3% and 5.5% standard deviations (σ). Overall the results were qualitatively similar to the original case; however the number and breadth of the chaotic regimes increased proportionally with variance in spacing. Originally, the last odd sequence that could be observed was 19, for the cases with added variance the maximum odd sequences were 15, 11, and 7 respectively. In the case of 5.5% variance, even numbered sequences were also eliminated above 8 so that the system was nearly chaotic over the entire range. Similar results were found when the droplet resistance fluctuated. Hence a conclusion may be drawn that the increase in noise in the system will decrease the likelihood that a stable sorting pattern will form. Additional noise contributions can be included in the stability calculation by simply substituting the extreme limits of the variable (e.g. 3 times σ) into the calculation of T^*_{amod} and T^*_{amod}.

7.10 Effect of Initial Conditions

Both Cybulski and Garstecki, and Sessoms *et al.* noted that initial conditions in the branches determine the specific pattern that forms (Cybulski and Garstecki 2010; Sessoms, Amon et al. 2010). Particularly, Cybulski and Garstecki observed in experiments that striking the inlet tubing created a significant disturbance that would cause the pattern to switch (i.e. UUUDDD to UDUDUD for example). In this manner Cybulski and Garstecki were able to conjure all possible combination of patterns for a given sequence length. Sessoms *et al.* witnessed confirming results with their numerical simulations when the system was started with different distribution of droplets in the two channels.

Along these lines simulations were performed with initial conditions where (a) there were no droplets present in any channel (b) 10 droplets were equally spaced in channel a (c) 10 droplets were equally spaced in channel b. The conditions were applied to the symmetric case (Case 1 Table 3.6). Results were in agreement with the other authors; different initial conditions resulted in different sequences, but the overall pattern length was the same. For example for $T_{cyc}^{*}=8$, patterns of (a) DUUDDUDU (b) UUDDUUDD and (c) UDUDUDUD were obtained for the three initial conditions. This suggests that the system exhibits multi-stability, where several attractors exist for a given set of parameters that lead to the same output, a common feature of time delayed systems.

7.11 Experimental Comparison

As further validation, experiments were performed to compare the discrete model to the real physical system. Details on the experimental procedure and setup were previously provided in Section 7.5. Experiments were performed with symmetric (5:5mm) and asymmetric (5:4 mm) branch designs with pressure biases as well. Droplets were spaced far apart to eliminate any interaction. From a single chip both the symmetric pressure and asymmetric pressure data was obtained. Data presented below is the summation of results over at least 5 different chips for one case study (branch length). At least 100 sorting events were monitored for each data point. Overall 120 data points were collected for verifying the model. Results are divided in Figure 7.23 and 24 as:

a) Symmetric branches, symmetric pressures: $\Lambda^{*}=1$, $P^{*}=1$
b) Symmetric branches, asymmetric pressures. $\Lambda^{*}=1$, $P^{*}=0.8$
c) Asymmetric branches, symmetric pressures $\Lambda^{*}=1.25$, $P^{*}=1$
d) Asymmetric branches, symmetric pressures. $\Lambda^{*}=0.8$, $P^{*}=0.76$

In the experiments the junction pressure was inferred by calculating the value from a compact model of the fluidic network. From these calculations, an average P^{*} was used in the discrete model to describe all of the experimental results. As well, in the calculations an equivalent droplet resistance of 0.45mm which was measured independently (refer to Section 7.6). Droplet speeds typically ranged from 2-5 mm/s (equivalent to Ca=0.002) and droplet length was approximately 1.5 times the width of the channel. An example of a sorting video is provided in Appendix C.

As can be seen from Figure 7.23 and 7.24 there is good quantitative agreement between the discrete model and the experimental results. Filtering cut off, cycling times, total number of droplets and droplet distribution are all well predicted by the models. Both regular and chaotic periodic regimes were obtained across the full spectrum, though there is a noticeable decrease in the size and number of stable periodic regimes as compared to the full-numerical simulations; the reason being the presence of additional non-idealities and fluctuations (e.g. spacing variance) in the real physical system as described in Section 7.3. Repeating patterns as large as 8 droplets were observed for the completely symmetric case. Higher patterns could not be observed because the spacing of droplets was too close to eliminate the prospect of droplet/droplet interaction. The results also show that the distribution of droplets can be controlled by adjusting the pressures. Comparing (a) with (b) for $2/\lambda^{*}=3\rightarrow4$ in Figure 7.17, the distribution of droplet is 50/50 for the symmetric case (a) and 75/25 when the asymmetric pressure is applied (b).

In summary, good qualitative and quantitative agreement was observed between the discrete model developed in comparison to ideal-model, full-model and experimental result. The model was able to accurately predict the sequence length and the distribution of droplets into the two branches. Furthermore, a preliminary methodology for identifying regions of stability and instability was also tested successfully.

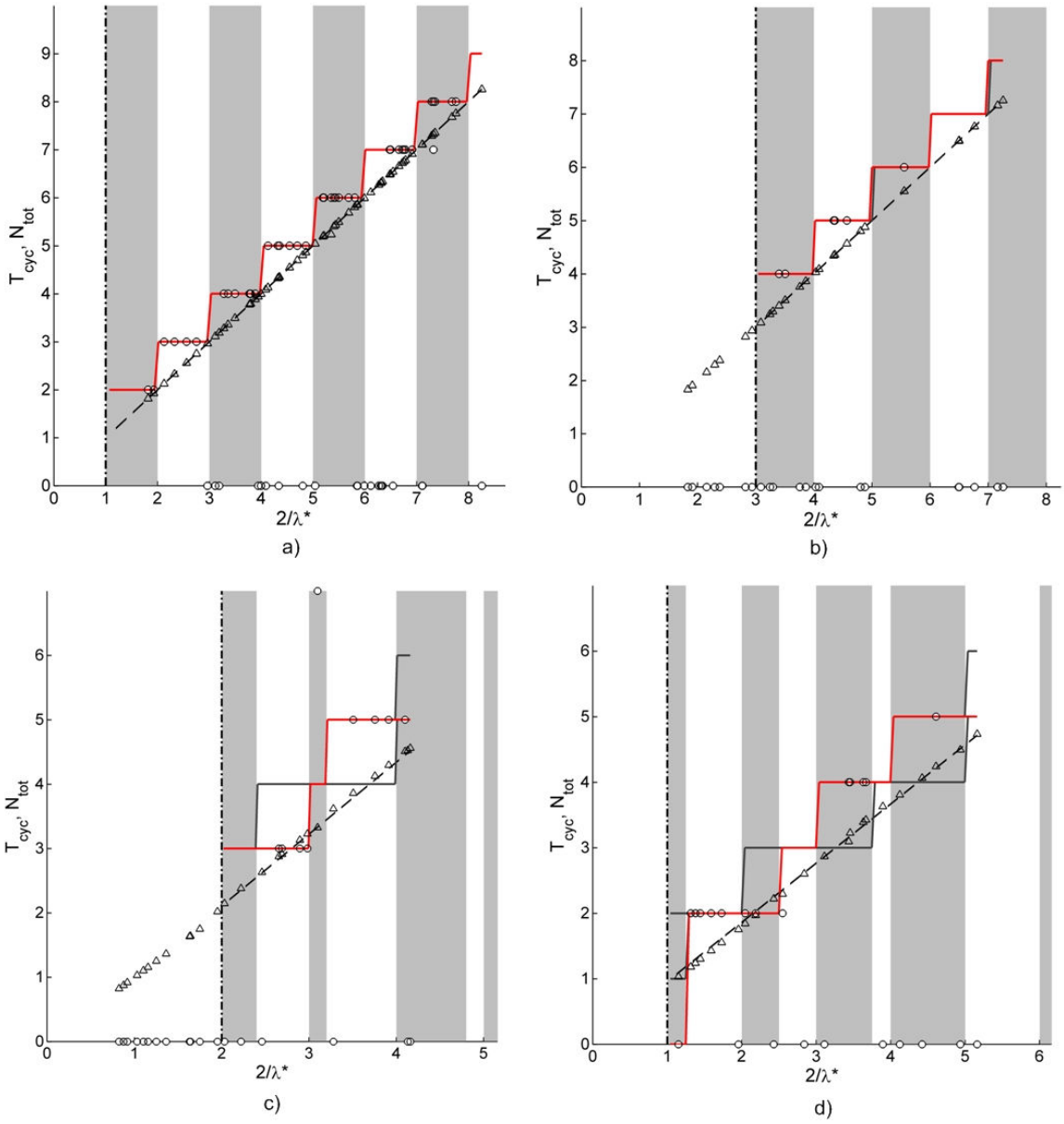

Figure 7.23 Experimental results for the T_{cyc}^{*} and n_T for (a) symmetric branches and pressures (b) symmetric branches and asymmetric pressures, (c) asymmetric branches and symmetric pressures (c) asymmetric branches and asymmetric pressures. Red line is the discrete model prediction for T_{cyc}^{*}, the solid black line is the prediction for T_a^{*} and T_b^{*} and the dashed line (--) is the continuum model prediction for the total number of droplets.

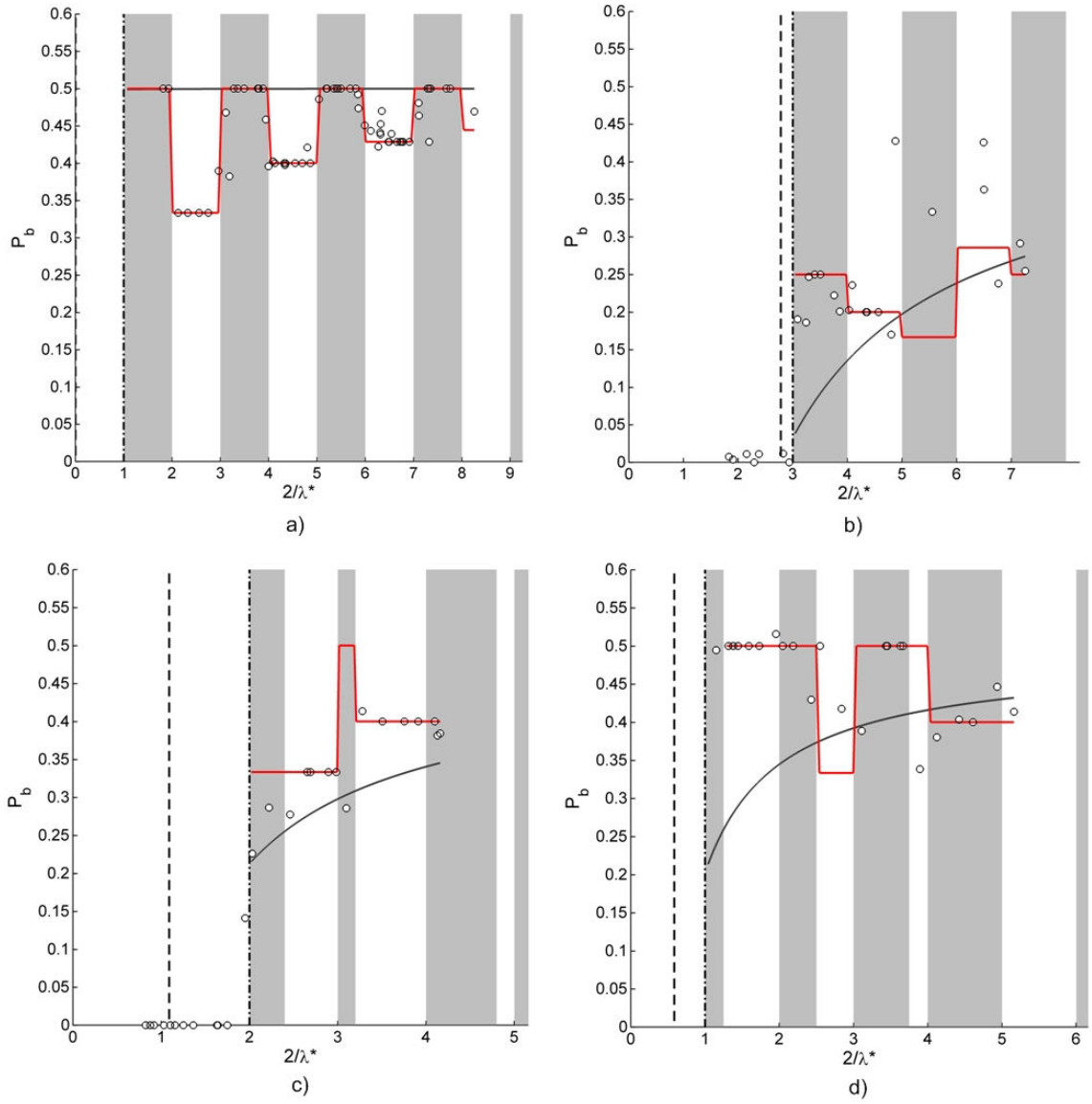

Figure 7.24 Experimental results for the $Prob_b$ for (a) symmetric branches and pressures (b) symmetric branches and asymmetric pressures, (c) asymmetric branches and symmetric pressures (c) asymmetric branches and asymmetric pressures. Red line is the discrete model prediction and the black the continuum model.

7.12 Suggests for Implementing Sorting in Practice

The obvious practical application of the sorting phenomena is to use it to split the population of droplets into two groups. Adjusting the pressure bias between the branches allows for control over the distribution of droplets. Figure 7.25 shows the full-model numerical results for $Prob_b$ as a function of P^* for symmetric and asymmetric branch designs. Note that the periodic behaviour creates plateaus in the distribution of the droplets. Here a few comments are made on the practical implementation of such a sorting module in a larger network design along with a few general design rules that have come to light from this study.

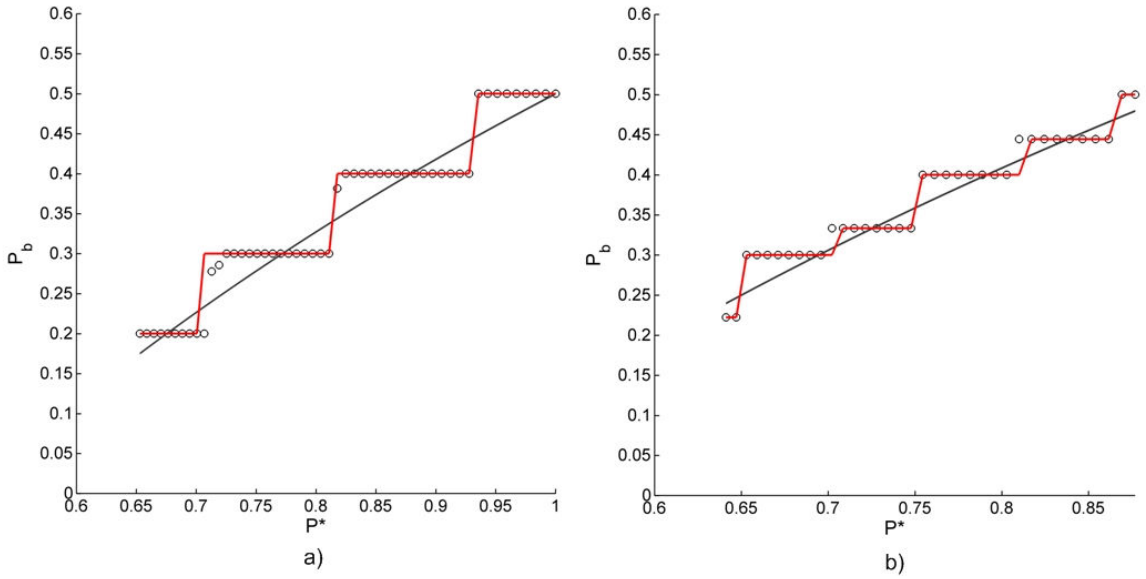

Figure 7.25 Ideal-model simulations of the effect of adjusting P^* on the distribution of droplets for (a) L=5:5, $L_{drop}=0.5$, and (b) $L=5:4.5$ $L_{drop}=0.5$. Base pattern length is 10.

There are two possible designs, the first with the intention of sorting specific droplets out of population say the 3rd and 5th droplet out of every 7, and the second with the intention of choosing a portion (2/7ths) of the droplets at random. The former is nearly impossible to achieve in practice. Even if the best care is taken when designing and operating the chip, it is still difficult to achieve stable sorting as evidenced in this study. Furthermore, choosing only the 3rd and 5th droplet would require that a specific sequence needs to repeat *ad infinitum* (i.e. UUDUDUU). We know, however that not all sequences are probably available at a given spacing and that the specific sequence that forms depends on the initial conditions which are difficult to control. One option would be to create a severe disturbance like Cybulski and Garstecki used to switch the system between sorting patterns. The different patterns can be cycled through until the right one is

reached. This of course will take some time and many droplets will sort to the wrong channel before the system is set up. There is also no guarantee that an unintentional disturbance somewhere else in the network might break the sequence.

A delicate balance is required across all of the parameters to achieve stable sorting. From the discussion on stability of patterns, one would conclude that a lower R_{drop} is more favourable. In reality, this may not be the case, since the system will also then be more susceptible to outside disturbances because the droplet resistance may not be the dominating factor influencing the flow between the two branches. Conversely, if R_{drop} is too high than the stable patterns which are available decreases. Thus an optimum R_{drop}/L_a most likely exists that maximizes the overall stability of the system. Further study into this concept is still required.

The design of a random droplet sampler is more straightforward. The goal should be to run the sorter in one of the chaotic regimes where there is no specific pattern. Generally, it seems best to operate the system at high values $2/\lambda^*$ since the system is more likely to be chaotic. Additionally, in this high range the distribution of droplets is closely approximated by the much simpler continuum model (refer to Figures 7.17-7.20). To avoid the chance of any pattern forming small disturbances can be added to the system such as oscillating the outlet pressures slightly, or purposefully varying the incoming spacing around an average value. At low $2/\lambda^*$ the distribution of droplets is discontinuous as seen in Figure 7.25 where there are only a fixed set of plateaus that can be reached. At high $2/\lambda^*$ the function will be smoother and more continuous allowing for a wider range of potential distributions. The full-model simulations indicate that generally the system follows the continuum model when $2/\lambda^* > 20$. Therefore, for a typical droplet spacing of 1 mm the corresponding branch length that is needed is 10 mm. This is a reasonable size that can fit into most chip designs. In terms of chip design, it is also important that the sampler is isolated from the upstream processes (refer to Section 7.5). This requires careful design of the global network to limit severe cross-coupling between the sorter, generator, diluter and other components.

7.13 Conclusions

In this chapter, a detailed study of the trafficking of droplets at a single network node was performed. Using compact numerical modelling we were able to develop a discrete model of the system that predicts several features including transitions between filtering and sorting,

bifurcation in the patterns, composition of the patterns, and estimates of the stability of a pattern. The non-trivial dependence on the various factors was well captured by the model in both numerical and experimental case studies. The complexity of flow produced form a simple junction emphasizes the challenge that remains for the design of large scale automated droplet networks.

Nomenclature

Acronyms:

1D	one dimensional
PDMS	poly(dimethyl)siloxane

Mathematical Symbols:

α	fitting constant for splitting
β	slip factor of droplet
ε_o	extension of the droplet during splitting
λ	inter-droplet spacing (m)
μ	dynamic viscosity of fluid (Pa s)
φ	ratio of flow to the two branches
ψ	sorting function at the junction, difference in flow between both branches
$\lvert\Omega\rvert$	length of sorting pattern
f	frequency (Hz)
h	channel height (m)
n	number of droplets
w	channel width (m)
t	time (s)
Ca	capillary number (dimensionless)
L	length (m)
N	number of droplets discrete model
$P_{1,2,j}$	pressure at exits and junction (Pa)
Prob_b	probability of a droplet entering a channel
Q	flow rate (m^3 s)
R_{hyd}	hydrodynamic resistance of channel (Pa s m^{-3})
R_{drop}	hydrodynamic resistance of droplet (Pa s m^{-3})

Chapter 8

Conclusions and Recommendations.

8.1 Contributions of this Thesis

Droplet based microfluidic devices have the ability to significantly improve the performance of biochemical assays. The potential benefits of droplet based devices are decreased processing times, increased functionality and reduction in cost due to lower reagent consumption. Such high throughput droplet devices will consist of many independent functions (generation, sorting, breakup, detection ect.) connected via complex microfluidic network with multiple input streams. Interaction through the network can result in coupling between the various processes, and therefore it is important to understand how to properly design such devices effectively. The hypothesis that guided this work was that stable and robust control of droplet generation and transport could be achieved with pressure driven flow. The investigation focused on the simplest microfluidic network consisting of a single T-junction generator and a single network node with the goal of understanding the mechanisms involved in the operation of both components.

The initial phase of research focused on the formation of liquid-liquid droplets in microfluidic T-junction generators within the squeezing-to-transition regime (Chapter 4). Considerable effort was put into a systematic study of the parameters influencing droplet production. Through video analysis of the formation process, three stages of droplet formation were identified, including the newly defined lag stage that appears at the beginning of the formation cycle once the interface pulls back after a droplet detaches. It was shown that the amount of pull back is related to the relative strength of the velocity of the fluid draining from the collapsing thread and the incoming fluid flow of the dispersed phase. The filling stage was defined by a force balance on the emerging interface which determines the degree of penetration into the main channel. To calculate the force balance an accurate model of the flow the through the gap was developed using an asymptotic semi-analytical model based on numerical simulations of the flow. The model for the gap flow includes additional factors that account for the 3D curvature of the droplet and the viscosity contrast between the two phases. Finally, the necking stage was modelled using a control volume approach combined with a modified pinch-off criteria. The complete model of droplet formation captured all dependencies observed in experiments including the influences of the intersection geometry, capillary number and flow ratio.

The next phase of research investigated the effects of surfactants on the formation process (Chapter 5). Experimental observations revealed that surfactant transport occurs on a timescale comparable to the production rate of droplets resulting in time-dependent interfacial coverage, even for small fast adsorbing surfactants such as SDS. This causes strong coupling between the mass transport of surfactant molecules and the interface shape. Neglecting these effects results in an under prediction of droplet size from the previous model developed in Chapter 4. Surfactant effects were characterized experimentally by measuring the dynamic interfacial tension through the force balance on the emerging interface (Chapter4). It was observed that the dynamic interfacial tension was influenced by the dilation rate of the interface which depends on the channel width ratio and the flow rate of the dispersed phase. Measurements showed significant deviation from the equilibrium interfacial tension for both fast and slow adsorbing surfactants at modest production rates (10-100 Hz). Under certain conditions the interfacial tension was closer to that of a bare interface than a fully covered interface. The addition of surfactants also results in longer necking times presumably due to Marangoni stresses reducing flow through the collapsing thread. A theoretical model was developed to estimate the jump in interfacial tension during the formation process for surfactant solutions above and below the CMC. The model accurately captured the influence of dispersed flow rate and T-junction intersection design on the dynamic interfacial tension. The adsorption kinetics model was then incorporated into the T-junction drop production model with good success following some small modifications to the necking criteria.

Next, the influence of global network architecture on the performance of a single T-junction generator operating under pressure driven flow was investigated. Feedback created by the formed droplets leads to intrinsic coupling between downstream processes and droplet generation causing fluctuations in droplet production. Reducing these variations is important to improving the fidelity of droplet based devices. It was found that fluctuations appear over a timescale associated with a single droplet formation cycle (short term) and several droplet formation cycles (long term). Short term fluctuations are associated with the changing interface curvature during the formation cycle which alters the Laplace pressure drop. Long term fluctuations are caused by the constantly changing hydrodynamic resistance of the output channel as droplets enter and leave the system. It was shown that these two types of fluctuations can be quantified by monitoring droplet velocity (short-term) and inter-droplet spacing (long term). Further analysis using compact numerical modelling of the T-junction generator demonstrated that long term oscillations have a periodicity that matches the residence time of droplets in the system. In addition, these long term oscillations appear to be ubiquitous as they are perpetuated by unavoidable stochastic noise in the

system. However, the magnitude of these oscillations could be suppressed through effective design of the network of microchannels. A simple analytical model was developed to account for the influence of T-junction geometry, droplet resistance and Laplace pressure on the stability of the system. It was shown that by following the design rules for the global network fluctuations in droplet spacing, size and velocity could be reduced to sub 1% levels.

The final phases of this thesis looked at the transport of droplets through a simple network node consisting of one inlet and two outlets under various conditions of asymmetry between the two output channels including channel length, output pressure and hydrodynamic resistance difference. Due to feedback, droplets interact with each other causing the decision of droplets that have already passed through the node to influence the decision of proceeding droplets. It was shown that droplets distribute themselves in order to equalize the flow to the two output branches. In some cases, the trajectory of droplets followed a highly ordered pattern, while under other conditions the system was chaotic but droplets still distributed themselves to equalize the flow to the two branches. A theoretical analysis showed that the length and composition of the patterns was a function of the non-dimensional residence time of the two branches. With the assistance of a compact numerical model of the sorting process, a discrete analytical model of the system was developed that accurately predicts transitions between filtering and sorting, bifurcation in the patterns, and composition of the patterns. In addition, chaotic regimes were shown to occur when the distribution of droplets in the two branches did not perfectly balance the two flows causing a change in the residence time from the ideal value. Finally, it was shown that such a simple bifurcation could be used to randomly sample a population of droplets under the right conditions.

The models developed in this thesis have broad application to the design of droplet microfluidic devices. To realize robust droplet based devices it will be necessary to combine different modular components together. The two models developed here for the T-junction generator and the trafficking of droplet through networks allow for such modular design. With these models the designer can select the appropriate geometry of the T-junction generator to produce droplets of the desired size and frequency with highly stable output over the long term.

In fact, a critical finding in this thesis is the importance of geometry on the operation of microfluidic droplet devices. A number of geometric parameters appeared in the analysis of the T-junction generator and the transport of droplets through a junction such as the height-to-width ratio, the dispersed-to-continuous inlet width ratio, and the branch length ratio for the

microfluidic network. This strong dependency on the geometric parameters leads to concerns with the manufacturability of such devices. In large scale production process small variance in the fabricated components is natural which will lead to slightly different performance between devices. Experiments performed in this thesis were done in triplicate using different chips each time. Prior to each experiment the geometric dimensions (height, width) were recorded and small variations (1-5% in width or height) between chips were seen using the soft-lithography fabrication process. When analyzing the data it was important to use the specific data for each chip in order to get good agreement with the models.

This leads to the question of the overall robustness of large network microfluidic devices. In the laboratory setting generally only a few devices are fabricated and each device is essentially "calibrated" during operation. Little effort is put into analyzing chip-to-chip variance on the performance of these devices. This fact represents the gap between the prototype mentality of the academic setting and the practicality required for commercialization. In terms of the development of high-level droplet based devices, the use of pressure driven flow will be necessary to improve the flow control of these devices as specified in this thesis; however, additional systems will most likely be needed to further improve robustness due to variance in device production. The solution to this problem will most likely come in the form of closed loop control systems that monitor droplet production and transport within the network in real time and make appropriate corrections to the input parameters using a feedback algorithm. Such a system will require a high-speed sensor to detect droplet size, speed and location and must also be remote so as not to cross-contaminate droplets. Optical or electric based sensors are the most likely candidates given their speed. However, the question will be how to integrate these sensors within the chip at an economical cost.

8.2 Recommendations for Extension of Work

Several avenues for additional research into the breakup of droplets in microfluidic T-junction generators still exist. For instance, comparisons between the force balance model and the experiments showed that there was a discrepancy in the penetration depth requiring a pre-factor of ½ for agreement. It was hypothesized that this error may be caused by the possible deformation of the interface in the out of plane direction, additional fluid bypassing the interface through the thin-films or a new force balance in the y-direction may be more appropriate. To resolve these questions it may be possible to device an experimental setup to accurately measure the force balance on the emerging interface. This would most likely require the use of confocal μ-PIV, or

nano-scale μ-PIV with total internal reflection fluorescence, to measure the flow fields within the top and bottom films and along the two-phase interface in order to reconstruct the complete shape of the interface. Additional effort is also needed to study the flow field at the final moments of neck collapse to develop an appropriate model for the pull-back of the interface after breakup. Along this same line of thought, analysis of the thinning of the neck is also required, both in the absence and presence of surfactants, to understand exactly the mechanisms involved during the final moments of collapse that lead to interface pull-back. Furthermore, the current model for the operation of the T-junction generator may be extended to include non-steady flow of the two phases with coupling between the changing interface shape (Laplace pressure fluctuations) and the presence of droplets in the output channel (hydrodynamic resistance fluctuations).

In terms of transport of droplets through nodes in a microfluidic network the discrete model developed herein can be further developed. Numerical simulations can be improved by including several aspects of the real physical system including: (a) treating the droplets as having a finite size (b) time delay created by the stagnation of droplets at the junction when sorting (c) droplet resistance based on Capillary number and (d) pressure pulses created by droplets exiting. Most of these factors are expected to degrade the sorting process in some way. Still it would be valuable to quantify these effects.

Theoretical considerations may also attempt to include the natural imbalance in the flows, rather than the automatic assumption of equal flow rates. This may lead to a better definition for regions of stability and instability. The most pertinent direction of study would be to determine whether all patterns derived from combinatorics are actually possible. An additional avenue for continued work is to extend the current model to study a cascading network of nodes where one branch enters directly into another. In this manner, the droplet population can be split into more than two sets. Since sorting creates unevenly spaced droplets at the outlets, determining the operation of the downstream node becomes much more difficult. In fact, even with one network node it would be interesting to see what happens when the incoming spacing is not uniform, but set to a specific pattern. For example, it may be possible to take an incoming sequence of droplets with different spacings, smooth out the deviations in spacing, and get a uniform spacing as the output. Therefore, there is still much that still needs to be accomplished from both theoretical and experimental approaches.

Appendix A

This appendix is a video of the generation of water in silicon oil droplets from a 1:3 T-junction generator with $h=35\mu m$. Video is taken at 1000fps.

The file name of this video file is “Droplet_generation_13_Tjunction.avi”.

Appendix B

This appendix is a video that shows the output of the numerical simulation for sorting of droplets with a repeating pattern that has a length of 13. The conditions are P^*=1, Λ^*=1, $R^*_{drop}=1$ and $R^{*(a)}_{drop}=0.05$.

The file name of this video file is
"Ideal_model_simulation_13Pattern_DUUDUDUUUDUDU.avi".

Appendix C

This appendix is a video that shows the sorting of droplets in experiments with a pattern length of eight. The sorting pattern is LLLRLRRR and repeats twice in the video. Sorting conditions correspond to Λ^*=1and P^*=1 and $2/\lambda^* = 7.69$

The file name of this video file is “Droplet_sorting_video_experiments.avi”.

References

Abate, A. R., M. B. Romanowsky, J. J. Agresti and D. A. Weitz (2009). "Valve-based flow focusing for drop formation." Applied Physics Letters 94(2): 023503.

Abbyad, P., R. Dangla, A. Alexandrou and C. N. Baroud (2011). "Rails and anchors: guiding and trapping droplet microreactors in two dimensions." Lab on a Chip 11(5): 813-821.

Abgrall, P. and A. M. Gue (2007). "Lab-on-chip technologies: making a microfluidic network and coupling it into a complete microsystem - a review." Journal of Micromechanics and Microengineering 17(5): R15-R49.

Abkarian, M., M. Faivre and H. A. Stone (2006). "High-speed microfluidic differential manometer for cellular-scale hydrodynamics." Proceedings of the National Academy of Sciences of the United States of America 103(3): 538-542.

Adamson, D. N., D. Mustafi, J. X. J. Zhang, B. Zheng and R. F. Ismagilov (2006). "Production of arrays of chemically distinct nanolitre plugs via repeated splitting in microfluidic devices." Lab on a Chip 6(9): 1178-1186.

Adzima, B. J. and S. S. Velankar (2006). "Pressure drops for droplet flows in microfluidic channels." Journal of Micromechanics and Microengineering 16(8): 1504-1510.

Ahn, K., C. Kerbage, T. P. Hunt, R. M. Westervelt, D. R. Link and D. A. Weitz (2006). "Dielectrophoretic manipulation of drops for high-speed microfluidic sorting devices." Applied Physics Letters 88(2): 024104.

Ajaev, V. S. and G. M. Homsy (2006). "Modeling shapes and dynamics of confined bubbles." Annual Review of Fluid Mechanics 38: 277-307.

Angeli, D., J. E. Ferrell and E. D. Sontag (2004). "Detection of multistability, bifurcations, and hysteresis in a large class of biological positive-feed back systems." Proceedings of the National Academy of Sciences of the United States of America 101(7): 1822-1827.

Anna, S. L., N. Bontoux and H. A. Stone (2003). "Formation of dispersions using "flow focusing" in microchannels." Applied Physics Letters 82(3): 364-366.

Anna, S. L. and H. C. Mayer (2006). "Microscale tipstreaming in a microfluidic flow focusing device." Physics of Fluids 18(12): 121512.

Atencia, J. and D. J. Beebe (2005). "Controlled microfluidic interfaces." Nature 437(7059): 648-655.

Ayorinde, F. O., S. V. Gelain, J. H. Johnson and L. W. Wan (2000). "Analysis of some commercial polysorbate formulations using matrix-assisted laser desorption/ionization time-of-flight mass spectrometry." Rapid Communications in Mass Spectrometry 14(22): 2116-2124.

Bales, B. L., L. Messina, A. Vidal, M. Peric and O. R. Nascimento (1998). "Precision relative aggregation number determinations of SDS micelles using a spin probe. A model of micelle surface hydration." Journal of Physical Chemistry B 102(50): 10347-10358.

Barbier, V., H. Willaime, P. Tabeling and F. Jousse (2006). "Producing droplets in parallel microfluidic systems." Physical Review E 74(4).

Baret, J. C. (2011). "Surfactants in droplet-based microfluidics." Lab on a Chip 12: 422-433.

Baret, J. C., F. Kleinschmidt, A. El Harrak and A. D. Griffiths (2009). "Kinetic Aspects of Emulsion Stabilization by Surfactants: A Microfluidic Analysis." Langmuir 25(11): 6088-6093.

Baret, J. C., O. J. Miller, V. Taly, M. Ryckelynck, A. El-Harrak, L. Frenz, C. Rick, M. L. Samuels, S. Hutchinson, J. J. Argesti, D. R. Link, D. A. Weitz and A. D. Griffiths (2009). "Fluorescence-activated droplet sorting (FADS): efficient microfluidic cell sorting based on enzymatic activity." Lab on a Chip 9(13): 1850-1858.

Baroud, C. N., M. R. de Saint Vincent and J. P. Delville (2007). "An optical toolbox for total control of droplet microfluidics." Lab on a Chip 7(8): 1029-1033.

Baroud, C. N., J. P. Delville, F. Gallaire and R. Wunenburger (2007). "Thermocapillary valve for droplet production and sorting." Physical Review E 75(4): 046302.

Baroud, C. N., F. Gallaire and R. Dangla (2010). "Dynamics of microfluidic droplets." Lab on a Chip 10(16): 2032-2045.

Baroud, C. N. and H. Willaime (2004). "Multiphase flows in microfluidics." Comptes Rendus Physique 5(5): 547-555.

Battersby, B. J., G. A. Lawrie, A. P. R. Johnston and M. Trau (2002). "Optical barcoding of colloidal suspensions: applications in genomics, proteomics and drug discovery." Chemical Communications(14): 1435-1441.

Beebe, D. J., G. A. Mensing and G. M. Walker (2002). "Physics and applications of microfluidics in biology." Annual Review of Biomedical Engineering 4: 261-286.

Beer, N. R., B. J. Hindson, E. K. Wheeler, S. B. Hall, K. A. Rose, I. M. Kennedy and B. W. Colston (2007). "On-chip, real-time, single-copy polymerase chain reaction in picoliter droplets." Analytical Chemistry 79(22): 8471-8475.

Beer, N. R., K. A. Rose and I. M. Kennedy (2009). "Observed velocity fluctuations in monodisperse droplet generators." Lab on a Chip 9(6): 838-840.

Behzad, M. D., H. Seyed-allaei and M. R. Ejtehadi (2010). "Simulation of droplet trains in microfluidic networks." Physical Review E 82(3): 037303.

Belder, D. (2005). "Microfluidics with droplets." Angewandte Chemie-International Edition 44(23): 3521-3522.

Belloul, M., W. Engl, A. Colin, P. Panizza and A. Ajdari (2009). "Competition between Local Collisions and Collective Hydrodynamic Feedback Controls Traffic Flows in Microfluidic Networks." Physical Review Letters 102(19): 194502

Bendure, R. L. (1971). "Dynamic surface tension determination with maximum bubble pressure method." Journal of Colloid and Interface Science 35(2): 238-&.

Bhattacharya, S., A. Datta, J. M. Berg and S. Gangopadhyay (2005). "Studies on surface wettability of poly(dimethyl) siloxane (PDMS) and glass under oxygen-plasma treatment and correlation with bond strength." Journal of Microelectromechanical Systems 14(3): 590-597.

Boukellal, H., S. Selimovic, Y. W. Jia, G. Cristobal and S. Fraden (2009). "Simple, robust storage of drops and fluids in a microfluidic device." Lab on a Chip 9(2): 331-338.

Bransky, A., N. Korin, M. Khoury and S. Levenberg (2009). "A microfluidic droplet generator based on a piezoelectric actuator." Lab on a Chip 9(4): 516-520.

Bremond, N., A. R. Thiam and J. Bibette (2008). "Decompressing emulsion droplets favors coalescence." Physical Review Letters 100(2): 024501.

Bretherton, F. P. (1961). "The Motion of Long Bubbles in Tubes." Journal of Fluid Mechanics 10(2): 166-188.

Bruus, H. (2007). Theoretical Microfluidics. New York, Oxford University Press.

Carlson, A., M. Do-Quang and G. Amberg (2010). "Droplet dynamics in a bifurcating channel." International Journal of Multiphase Flow 36(5): 397-405.

Carr, R. T. and M. Lacoin (2000). "Nonlinear dynamics of microvascular blood flow." Annals of Biomedical Engineering 28(6): 641-652.

Carroll, N. J., S. B. Rathod, E. Derbins, S. Mendez, D. A. Weitz and D. N. Petsev (2008). "Droplet-based microfluidics for emulsion and solvent evaporation synthesis of monodisperse mesoporous silica microspheres." Langmuir 24(3): 658-661.

Castell, O. K., C. J. Allender and D. A. Barrow (2009). "Liquid-liquid phase separation: characterisation of a novel device capable of separating particle carrying multiphase flows." Lab on a Chip 9(3): 388-396.

Chabert, M., K. D. Dorfman and J. L. Viovy (2005). "Droplet fusion by alternating current (AC) field electrocoalescence in microchannels." Electrophoresis 26(19): 3706-3715.

Charcosset, C., I. Limayem and H. Fessi (2004). "The membrane emulsification process - a review." Journal of Chemical Technology and Biotechnology 79(3): 209-218.

Chatterjee, A. N. and N. R. Aluru (2005). "Combined circuit/device modeling and simulation of integrated microfluidic systems." Journal of Microelectromechanical Systems 14(1): 81-95.

Chen, C. T. and G. B. Lee (2006). "Formation of microdroplets in liquids utilizing active pneumatic choppers on a microfluidic chip." Journal of Microelectromechanical Systems 15(6): 1492-1498.

Chen, D. L. L. and R. F. Ismagilov (2006). "Microfluidic cartridges preloaded with nanoliter plugs of reagents: an alternative to 96-well plates for screening." Current Opinion in Chemical Biology 10(3): 226-231.

Chen, D. L. L., L. Li, S. Reyes, D. N. Adamson and R. F. Ismagilov (2007). "Using three-phase flow of immiscible liquids to prevent coalescence of droplets in microfluidic channels: Criteria to identify the third liquid and validation with protein crystallization." Langmuir 23(4): 2255-2260.

Cheow, L. F., L. Yobas and D. L. Kwong (2007). "Digital microfluidics: Droplet based logic gates." Applied Physics Letters 90(5): 054107.

Chin, C. D., V. Linder and S. K. Sia (2007). "Lab-on-a-chip devices for global health: Past studies and future opportunities." Lab on a Chip 7(1): 41-57.

Christopher, G. F. and S. L. Anna (2007). "Microfluidic methods for generating continuous droplet streams." Journal of Physics D-Applied Physics 40(19): R319-R336.

Christopher, G. F. and S. L. Anna (2009). "Passive breakup of viscoelastic droplets and filament self-thinning at a microfluidic T-junction." Journal of Rheology 53(3): 663-683.

Christopher, G. F., J. Bergstein, N. B. End, M. Poon, C. Nguyen and S. L. Anna (2009). "Coalescence and splitting of confined droplets at microfluidic junctions." Lab on a Chip 9(8): 1102-1109.

Christopher, G. F., N. N. Noharuddin, J. A. Taylor and S. L. Anna (2008). "Experimental observations of the squeezing-to-dripping transition in T-shaped microfluidic junctions." Physical Review E 78(3): 036317.

Christov, N. C., K. D. Danov, P. A. Kralchevsky, K. P. Ananthapadmanabhan and A. Lips (2006). "Maximum bubble pressure method: Universal surface age and transport mechanisms in surfactant solutions." Langmuir 22(18): 7528-7542.

Clausell-Tormos, J., D. Lieber, J. C. Baret, A. El-Harrak, O. J. Miller, L. Frenz, J. Blouwolff, K. J. Humphry, S. Koster, H. Duan, C. Holtze, D. A. Weitz, A. D. Griffiths and C. A. Merten (2008). "Droplet-based microfluidic platforms for the encapsulation and screening of mammalian cells and multicellular organisms " Chemistry & Biology 15(8): 875-875.

Cordero, M. L., D. R. Burnham, C. N. Baroud and D. McGloin (2008). "Thermocapillary manipulation of droplets using holographic beam shaping: Microfluidic pin ball." Applied Physics Letters 93(3): 034107.

Cramer, C., P. Fischer and E. J. Windhab (2004). "Drop formation in a co-flowing ambient fluid." Chemical Engineering Science 59(15): 3045-3058.

Cristini, V., S. Guido, A. Alfani, J. Blawzdziewicz and M. Loewenberg (2003). "Drop breakup and fragment size distribution in shear flow." Journal of Rheology 47(5): 1283-1298.

Cristini, V. and Y. C. Tan (2004). "Theory and numerical simulation of droplet dynamics in complex flows - a review." Lab on a Chip 4(4): 257-264.

Cristobal, G., J. P. Benoit, M. Joanicot and A. Ajdari (2006). "Microfluidic bypass for efficient passive regulation of droplet traffic at a junction." Applied Physics Letters 89(3): 034104.

Cybulski, O. and P. Garstecki (2010). "Dynamic memory in a microfluidic system of droplets traveling through a simple network of microchannels." Lab on a Chip 10(4): 484-493.

Cybulski, O. and P. Garstecki (2010). "Transport of resistance through a long microfluidic channel." Physical Review E 82(5): 056301.

Dai, L., W. F. Cai and F. Xin (2009). "Numerical Study on Bubble Formation of a Gas-Liquid Flow in a T-Junction Microchannel." Chemical Engineering & Technology 32(12): 1984-1991.

Dangla, R., S. Lee and C. N. Baroud (2011). "Trapping microfluidic drops in wells of surface energy." Physical Review Letters 107(12): 124501.

Darhuber, A. A. and S. M. Troian (2005). "Principles of microfluidic actuation by modulation of surface stresses." Annual Review of Fluid Mechanics 37: 425-455.

Davis, T. (2006) "Polya's Counting Theory."

de Gennes, P. G., F. Brochard-Wyart and D. Quere (2003). Capillarity and wetting phenomena: drops, bubbles, pearls, waves. New York, Springer-Verlag.

de Jong, J., R. G. H. Lammertink and M. Wessling (2006). "Membranes and microfluidics: a review." Lab on a Chip 6(9): 1125-1139.

de Mas, N., A. Gunther, T. Kraus, M. A. Schmidt and K. F. Jensen (2005). "Scaled-out multilayer gas-liquid microreactor with integrated velocimetry sensors." Industrial & Engineering Chemistry Research 44(24): 8997-9013.

De Menech, M., P. Garstecki, F. Jousse and H. A. Stone (2008). "Transition from squeezing to dripping in a microfluidic T-shaped junction." Journal of Fluid Mechanics 595: 141-161.

Delville, J. P., M. R. de Saint Vincent, R. D. Schroll, H. Chraibi, B. Issenmann, R. Wunenburger, D. Lasseux, W. W. Zhang and E. Brasselet (2009). "Laser microfluidics: fluid actuation by light." Journal of Optics a-Pure and Applied Optics 11(3): 034015.

deMello, A. J. (2006). "Control and detection of chemical reactions in microfluidic systems." Nature 442(7101): 394-402.

Dendukuri, D., K. Tsoi, T. A. Hatton and P. S. Doyle (2005). "Controlled synthesis of nonspherical microparticles using microfluidics." Langmuir 21(6): 2113-2116.

Dittrich, P. S., K. Tachikawa and A. Manz (2006). "Micro total analysis systems. Latest advancements and trends." Analytical Chemistry 78(12): 3887-3907.

Dollet, B., W. van Hoeve, J. P. Raven, P. Marmottant and M. Versluis (2008). "Role of the channel geometry on the bubble pinch-off in flow-focusing devices." Physical Review Letters 100(3): 034504.

Dreyfus, R., P. Tabeling and H. Willaime (2003). "Ordered and disordered patterns in two-phase flows in microchannels." Physical Review Letters 90(14): 144505.

Duffy, D. C., J. C. McDonald, O. J. A. Schueller and G. M. Whitesides (1998). "Rapid prototyping of microfluidic systems in poly(dimethylsiloxane)." Analytical Chemistry 70(23): 4974-4984.

Duffy, D. C., O. J. A. Schueller, S. T. Brittain and G. M. Whitesides (1999). "Rapid prototyping of microfluidic switches in poly(dimethyl siloxane) and their actuation by electro-osmotic flow." Journal of Micromechanics and Microengineering 9(3): 211-217.

Earnshaw, J. C., E. G. Johnson, B. J. Carroll and P. J. Doyle (1996). "The drop volume method for interfacial tension determination: An error analysis." Journal of Colloid and Interface Science 177(1): 150-155.

Eastoe, J. and J. S. Dalton (2000). "Dynamic surface tension and adsorption mechanisms of surfactants at the air-water interface." Advances in Colloid and Interface Science 85(2-3): 103-144.

Eastoe, J., J. S. Dalton, P. G. A. Rogueda, E. R. Crooks, A. R. Pitt and E. A. Simister (1997). "Dynamic surface tensions of nonionic surfactant solutions." Journal of Colloid and Interface Science 188(2): 423-430.

Edd, J. F., D. Di Carlo, K. J. Humphry, S. Koster, D. Irimia, D. A. Weitz and M. Toner (2008). "Controlled encapsulation of single-cells into monodisperse picolitre drops." Lab on a Chip 8(8): 1262-1264.

Eggleton, C. D. and K. J. Stebe (1998). "An adsorption-desorption-controlled surfactant on a deforming droplet." Journal of Colloid and Interface Science 208(1): 68-80.

El-Ali, J., P. K. Sorger and K. F. Jensen (2006). "Cells on chips." Nature 442(7101): 403-411.

Engl, W., M. Roche, A. Colin, P. Panizza and A. Ajdari (2005). "Droplet traffic at a simple junction at low capillary numbers." Physical Review Letters 95(20): 208304.

Eow, J. S., M. Ghadiri, A. O. Sharif and T. J. Williams (2001). "Electrostatic enhancement of coalescence of water droplets in oil: a review of the current understanding." Chemical Engineering Journal 84(3): 173-192.

Erni, P. (2011). "Deformation modes of complex fluid interfaces." Soft Matter 7(17): 7586-7600.

Faghri, A. and Y. Zhang (2006). Transport Phenomena in Multiphase Systems, Academic Press.

Fainerman, V. B., D. Mobius and R. Miller (2001). Surfactants: Chemistry, Interfacial Properties, Applications. Amsterdam, Netherlands, Elsevier Science B.V.

Fainerman, V. B., V. D. Mys, A. V. Makievski, J. T. Petkov and R. Miller (2006). "Dynamic surface tension of micellar solutions in the millisecond and submillisecond time range." Journal of Colloid and Interface Science 302(1): 40-46.

Fair, R. B. (2007). "Digital microfluidics: is a true lab-on-a-chip possible?" Microfluidics and Nanofluidics 3(3): 245-281.

Fidalgo, L. M., C. Abell and W. T. S. Huck (2007). "Surface-induced droplet fusion in microfluidic devices." Lab on a Chip 7(8): 984-986.

Fidalgo, L. M., G. Whyte, D. Bratton, C. F. Kaminski, C. Abell and W. T. S. Huck (2008). "From microdroplets to microfluidics: Selective emulsion separation in microfluidic devices." Angewandte Chemie-International Edition 47(11): 2042-2045.

Fischer, P. and P. Erni (2007). "Emulsion drops in external flow fields - The role of liquid interfaces." Current Opinion in Colloid & Interface Science 12(4-5): 196-205.

Franke, T., A. R. Abate, D. A. Weitz and A. Wixforth (2009). "Surface acoustic wave (SAW) directed droplet flow in microfluidics for PDMS devices." Lab on a Chip 9(18): 2625-2627.

Frenz, L., K. Blank, E. Brouzes and A. D. Griffiths (2009). "Reliable Microfluidic Incubation of Droplets in Delay Lines." Lab on a Chip 9: 1344-1348.

Fries, D. and P. R. von Rohr (2009). "Impact of inlet design on mass transfer in gas-liquid rectangular microchannels." Microfluidics and Nanofluidics 6(1): 27-35.

Fu, T. T., Y. G. Ma, D. Funfschilling, C. Y. Zhu and H. Z. Li (2010). "Squeezing-to-dripping transition for bubble formation in a microfluidic T-junction." Chemical Engineering Science 65(12): 3739-3748.

Fuerstman, M. J., P. Garstecki and G. M. Whitesides (2007). "Coding/decoding and reversibility of droplet trains in microfluidic networks." Science 315(5813): 828-832.

Fuerstman, M. J., A. Lai, M. E. Thurlow, S. S. Shevkoplyas, H. A. Stone and G. M. Whitesides (2007). "The pressure drop along rectangular microchannels containing bubbles." Lab on a Chip 7(11): 1479-1489.

Funfak, A., A. Brosing, M. Brand and J. M. Kohler (2007). "Micro fluid segment technique for screening and development studies on Danio rerio embryos." Lab on a Chip 7(9): 1132-1138.

Funfak, A., J. L. Cao, O. Wolfbeis, K. Martin and J. Kohler (2009). "Monitoring cell cultivation in microfluidic segments by optical pH sensing with a micro flow-through fluorometer using dye-doped polymer particles." Microchimica Acta 164(3-4): 279-286.

Garstecki, P., M. J. Fuerstman, H. A. Stone and G. M. Whitesides (2006). "Formation of droplets and bubbles in a microfluidic T-junction - scaling and mechanism of break-up." Lab on a Chip 6(3): 437-446.

Garstecki, P., H. A. Stone and G. M. Whitesides (2005). "Mechanism for flow-rate controlled breakup in confined geometries: A route to monodisperse emulsions." Physical Review Letters 94(16): 164501.

Garstecki, P. and G. M. Whitesides (2006). "Flowing crystals: Nonequilibrium structure of foam." Physical Review Letters 97(2): 024503.

Geerken, M. J., R. G. H. Lammertink and M. Wessling (2007). "Interfacial aspects of water drop formation at micro-engineered orifices." Journal of Colloid and Interface Science 312(2): 460-469.

Ghiassiaan, S. M. (2007). Two-phase flow, boiling and condensation in conventional and miniature systems, Cambridge University Press.

Glatzel, T., C. Litterst, C. Cupelli, T. Lindemann, C. Moosmann, R. Niekrawletz, W. Streule, R. Zengerle and P. Koltay (2008). "Computational fluid dynamics (CFD) software tools for microfluidic applications - A case study." Computers & Fluids 37(3): 218-235.

Glawdel, T. (2008). Design, Fabrication and Characterization of Electrokinetically Pumped MIcrofluidic Chips for Cell Culture Applications. Mechanical and Mechatronics Engineering. Waterloo, University of Waterloo. M.A.Sc.

Gu, H., F. Malloggi, S. A. Vanapalli and F. Mugele (2008). "Electrowetting-enhanced microfluidic device for drop generation." Applied Physics Letters 93(18): 183507.

Guillot, P., A. Ajdari, J. Goyon, M. Joanicot and A. Colin (2009). "Droplets and jets in microfluidic devices." Comptes Rendus Chimie 12(1-2): 247-257.

Guillot, P., A. Colin, A. S. Utada and A. Ajdari (2007). "Stability of a jet in confined pressure-driven biphasic flows at low reynolds numbers." Physical Review Letters 99(10): 104502.

Gunther, A. and K. F. Jensen (2006). "Multiphase microfluidics: from flow characteristics to chemical and materials synthesis." Lab on a Chip 6(12): 1487-1503.

Gunther, A., M. Jhunjhunwala, M. Thalmann, M. A. Schmidt and K. F. Jensen (2005). "Micromixing of miscible liquids in segmented gas-liquid flow." Langmuir 21(4): 1547-1555.

Gunther, A., S. A. Khan, M. Thalmann, F. Trachsel and K. F. Jensen (2004). "Transport and reaction in microscale segmented gas-liquid flow." Lab on a Chip 4(4): 278-286.

Gupta, A. and R. Kumar (2010). "Effect of geometry on droplet formation in the squeezing regime in a microfluidic T-junction." Microfluidics and Nanofluidics 8(6): 799-812.

Gupta, A., S. M. S. Murshed and R. Kumar (2009). "Droplet formation and stability of flows in a microfluidic T-junction." Applied Physics Letters 94(16): 164107.

Haeberle, S. and R. Zengerle (2007). "Microfluidic platforms for lab-on-a-chip applications." Lab on a Chip 7(9): 1094-1110.

Harris, J. M. (2008). Combinatorics and Graph Theory. New York, Springer.

Harvie, D. J. E., J. J. Cooper-White and M. R. Davidson (2008). "Deformation of a viscoelastic droplet passing through a microfluidic contraction." Journal of Non-Newtonian Fluid Mechanics 155(1-2): 67-79.

Hashimoto, M., P. Garstecki and G. M. Whitesides (2007). "Synthesis of composite emulsions and complex foams with the use of microfluidic flow-focusing devices." Small 3(10): 1792-1802.

Hashimoto, M., S. S. Shevkoplyas, B. Zasonska, T. Szymborski, P. Garstecki and G. M. Whitesides (2008). "Formation of Bubbles and Droplets in Parallel, Coupled Flow-Focusing Geometries." Small 4(10): 1795-1805.

He, M., J. S. Kuo and D. T. Chiu (2006). "Effects of ultrasmall orifices on the electrogeneration of femtoliter-volume aqueous droplets." Langmuir 22(14): 6408-6413.

Hodges, S. R., O. E. Jensen and J. M. Rallison (2004). "The motion of a viscous drop through a cylindrical tube." Journal of Fluid Mechanics 501: 279-301.

Holden, M. A., S. Kumar, A. Beskok and P. S. Cremer (2003). "Microfluidic diffusion diluter: bulging of PDMS microchannels under pressure-driven flow." Journal of Micromechanics and Microengineering 13(3): 412-418.

Holtze, C., A. C. Rowat, J. J. Agresti, J. B. Hutchison, F. E. Angile, C. H. J. Schmitz, S. Koster, H. Duan, K. J. Humphry, R. A. Scanga, J. S. Johnson, D. Pisignano and D. A. Weitz (2008). "Biocompatible surfactants for water-in-fluorocarbon emulsions." Lab on a Chip 8(10): 1632-1639.

Hosokawa, K., T. Fujii and I. Endo (1999). "Handling of picoliter liquid samples in a poly(dimethylsiloxane)-based microfluidic device." Analytical Chemistry 71(20): 4781-4785.

Hu, X., P. E. Boukany, O. L. Hemminger and L. J. Lee (2011). "The Use of Microfluidics in Rheology." Macromolecular Materials and Engineering 296(3-4): 308-320.

Hudson, S. D., J. T. Cabral, W. J. Goodrum, K. L. Beers and E. J. Amis (2005). "Microfluidic interfacial tensiometry." Applied Physics Letters 87(8): 081905.

Huebner, A., D. Bratton, G. Whyte, M. Yang, A. J. deMello, C. Abell and F. Hollfelder (2009). "Static microdroplet arrays: a microfluidic device for droplet trapping, incubation and release for enzymatic and cell-based assays." Lab on a Chip 9(5): 692-698.

Huebner, A., L. F. Olguin, D. Bratton, G. Whyte, W. T. S. Huck, A. J. de Mello, J. B. Edel, C. Abell and F. Hollfelder (2008). "Development of quantitative cell-based enzyme assays in microdroplets." Analytical Chemistry 80(10): 3890-3896.

Huebner, A., M. Srisa-Art, D. Holt, C. Abell, F. Hollfelder, A. J. Demello and J. B. Edel (2007). "Quantitative detection of protein expression in single cells using droplet microfluidics." Chemical Communications(12): 1218-1220.

Humphry, K. J., A. Ajdari, A. Fernandez-Nieves, H. A. Stone and D. A. Weitz (2009). "Suppression of instabilities in multiphase flow by geometric confinement." Physical Review E 79(5): 056310.

Hung, L. H., K. M. Choi, W. Y. Tseng, Y. C. Tan, K. J. Shea and A. P. Lee (2006). "Alternating droplet generation and controlled dynamic droplet fusion in microfluidic device for CdS nanoparticle synthesis." Lab on a Chip 6(2): 174-178.

Husny, J. and J. J. Cooper-White (2006). "The effect of elasticity on drop creation in T-shaped microchannels." Journal of Non-Newtonian Fluid Mechanics 137(1-3): 121-136.

Hwang, D. K., D. Dendukuri and P. S. Doyle (2008). "Microfluidic-based synthesis of non-spherical magnetic hydrogel microparticles." Lab on a Chip 8(10): 1640-1647.

Jakiela, S., S. Makulska, P. M. Korczyk and P. Garstecki (2011). "Speed of flow of individual droplets in microfluidic channels as a function of the capillary number, volume of droplets and contrast of viscosities." Lab on a Chip 11(21): 3603-3608.

Janasek, D., J. Franzke and A. Manz (2006). "Scaling and the design of miniaturized chemical-analysis systems." Nature 442(7101): 374-380.

Jin, B. J., Y. W. Kim, Y. Lee and J. Y. Yoo (2010). "Droplet merging in a straight microchannel using droplet size or viscosity difference." Journal of Micromechanics and Microengineering 20(3): 035003.

Jin, F., R. Balasubramaniam and K. J. Stebe (2004). "Surfactant adsorption to spherical particles: The intrinsic length scale governing the shift from diffusion to kinetic-controlled mass transfer." Journal of Adhesion 80(9): 773-796.

Jin, F., N. R. Gupta and K. J. Stebe (2006). "The detachment of a viscous drop in a viscous solution in the presence of a soluble surfactant." Physics of Fluids 18(2): 022103.

Joos, P. (1999). Dynamic Surface Phenomena. Zeist, Netherlands, VSP BV.

Joos, P. and M. Vanuffelen (1993). "Adsorption-kinetics with surface dilation 1. Desorption of slightly soluble monolayers at constant surface pressure." Journal of Colloid and Interface Science 155(2): 271-282.

Joos, P. and M. Vanuffelen (1995). "Theory of the growing drop technique for measuring dynamic interfacial tensions." Journal of Colloid and Interface Science 171(2): 297-305.

Joscelyne, S. M. and G. Tragardh (2000). "Membrane emulsification - a literature review." Journal of Membrane Science 169(1): 107-117.

Jousse, F., R. Farr, D. R. Link, M. J. Fuerstman and P. Garstecki (2006). "Bifurcation of droplet flows within capillaries." Physical Review E 74(3): 036311.

Jousse, F., G. P. Lian, R. Janes and J. Melrose (2005). "Compact model for multi-phase liquid-liquid flows in micro-fluidic devices." Lab on a Chip 5(6): 646-656.

Jullien, M. C., M. Ching, C. Cohen, L. Menetrier and P. Tabeling (2009). "Droplet breakup in microfluidic T-junctions at small capillary numbers." Physics of Fluids 21(7): 072001.

Khan, S. A. and S. Duraiswany (2009). "Microfluidic emulsions with dynamic compound drops." Lab on a Chip 9(13): 1840-1842.

Kim, H., D. W. Luo, D. Link, D. A. Weitz, M. Marquez and Z. D. Cheng (2007). "Controlled production of emulsion drops using an electric field in a flow-focusing microfluidic device." Applied Physics Letters 91(13).

Kinoshita, H., S. Kaneda, T. Fujii and M. Oshima (2007). "Three-dimensional measurement and visualization of internal flow of a moving droplet using confocal micro-PIV." Lab on a Chip 7(3): 338-346.

Kline, T. R., M. K. Runyon, M. Pothiawala and R. F. Ismagilov (2008). "ABO, D blood typing and subtyping using plug-based microfluidics." Analytical Chemistry 80(16): 6190-6197.

Kloubek, J. (1972). "Measurement of dynamic surface-tension by maximum bubble pressure method 4. Surface-tension of aqueous-solutions of sodium dodecyl sulfate." Journal of Colloid and Interface Science 41(1): 1-17.

Kohler, J. M. and T. Henkel (2005). "Chip devices for miniaturized biotechnology." Applied Microbiology and Biotechnology 69(2): 113-125.

Korczyk, P. M., O. Cybulski, S. Makulska and P. Garstecki (2011). "Effects of unsteadiness of the rates of flow on the dynamics of formation of droplets in microfluidic systems." Lab on a Chip 11(1): 173-175.

Koster, S., F. E. Angile, H. Duan, J. J. Agresti, A. Wintner, C. Schmitz, A. C. Rowat, C. A. Merten, D. Pisignano, A. D. Griffiths and D. A. Weitz (2008). "Drop-based microfluidic devices for encapsulation of single cells." Lab on a Chip 8(7): 1110-1115.

Kralj, J. G., H. R. Sahoo and K. F. Jensen (2007). "Integrated continuous microfluidic liquid-liquid extraction." Lab on a Chip 7(2): 256-263.

Kumacheva, E. and P. Garstecki (2011). Microfluidic Reactors for Polymer Particles. Sussex, UK, Wiley.

Labrot, V., M. Schindler, P. Guillot, A. Colin and M. Joanicot (2009). "Extracting the hydrodynamic resistance of droplets from their behavior in microchannel networks." Biomicrofluidics: 012804.

Lai, A., N. Bremond and H. A. Stone (2009). "Separation-driven coalescence of droplets: an analytical criterion for the approach to contact." Journal of Fluid Mechanics 632: 97-107.

Laval, P., N. Lisai, J. B. Salmon and M. Joanicot (2007). "A microfluidic device based on droplet storage for screening solubility diagrams." Lab on a Chip 7(7): 829-834.

Lee, J. N., C. Park and G. M. Whitesides (2003). "Solvent compatibility of poly(dimethylsiloxane)-based microfluidic devices." Analytical Chemistry 75(23): 6544-6554.

Lee, W., L. M. Walker and S. L. Anna (2009). "Role of geometry and fluid properties in droplet and thread formation processes in planar flow focusing." Physics of Fluids 21(3): 032103.

Lee, W., L. M. Walker and S. L. Anna (2011). "Competition Between Viscoelasticity and Surfactant Dynamics in Flow Focusing Microfluidics." Macromolecular Materials and Engineering 296(3-4): 203-213.

Leng, J. and J. B. Salmon (2009). "Microfluidic crystallization." Lab on a Chip 9(1): 24-34.

Leshansky, A. M. and L. M. Pismen (2009). "Breakup of drops in a microfluidic T junction." Physics of Fluids 21(2): 023303.

Li, L., J. Q. Boedicker and R. F. Ismagilov (2007). "Using a multijunction microfluidic device to inject substrate into an array of preformed plugs without cross-contamination: Comparing theory and experiments." Analytical Chemistry 79(7): 2756-2761.

Li, W., E. W. K. Young, M. Seo, Z. Nie, P. Garstecki, C. A. Simmons and E. Kumacheva (2008). "Simultaneous generation of droplets with different dimensions in parallel integrated microfluidic droplet generators." Soft Matter 4(2): 258-262.

Liau, A., R. Karnik, A. Majumdar and J. H. D. Cate (2005). "Mixing crowded biological solutions in milliseconds." Analytical Chemistry 77(23): 7618-7625.

Link, D. R., S. L. Anna, D. A. Weitz and H. A. Stone (2004). "Geometrically mediated breakup of drops in microfluidic devices." Physical Review Letters 92(5): 054503.

Link, D. R., E. Grasland-Mongrain, A. Duri, F. Sarrazin, Z. D. Cheng, G. Cristobal, M. Marquez and D. A. Weitz (2006). "Electric control of droplets in microfluidic devices." Angewandte Chemie-International Edition 45(16): 2556-2560.

Lister, J. R. and H. A. Stone (1998). "Capillary breakup of a viscous thread surrounded by another viscous fluid." Physics of Fluids 10(11): 2758-2764.

Liu, H. H. and Y. H. Zhang (2009). "Droplet formation in a T-shaped microfluidic junction." Journal of Applied Physics 106(3): 034906.

Liu, J., Y. F. Yap and N. T. Nguyen (2009). "Motion of a droplet through microfluidic ratchets." Physical Review E 80(4): 046319.

Liu, S. J., Y. F. Gu, R. B. Le Roux, S. M. Matthews, D. Bratton, K. Yunus, A. C. Fisher and W. T. S. Huck (2008). "The electrochemical detection of droplets in microfluidic devices." Lab on a Chip 8(11): 1937-1942.

Lorenz, R. M., J. S. Edgar, G. D. M. Jeffries and D. T. Chiu (2006). "Microfluidic and optical systems for the on-demand generation and manipulation of single femtoliter-volume aqueous droplets." Analytical Chemistry 78(18): 6433-6439.

Lorenz, R. M., J. S. Edgar, G. D. M. Jeffries, Y. Q. Zhao, D. McGloin and D. T. Chiu (2007). "Vortex-trap-induced fusion of femtoliter-volume aqueous droplets." Analytical Chemistry 79(1): 224-228.

Luo, D. W., S. R. Pullela, M. Marquez and Z. D. Cheng (2007). "Cell encapsules with tunable transport and mechanical properties." Biomicrofluidics 1(3): 034102.

Macleod, C. A. and C. J. Radke (1993). "A growing drop technique for measuring dynamic interfacial-tension." Journal of Colloid and Interface Science 160(2): 435-448.

Mahler, H.-C., M. Printz, R. Kopf, R. Schuller and R. Mueller (2008). "Behaviour of polysorbate 20 during dialysis, concentration and filtration using membrane separation techniques." Journal of Pharmaceutical Sciences 97(2): 764-774.

Malloggi, F., S. A. Vanapalli, H. Gu, D. van den Ende and F. Mugele (2007). "Electrowetting-controlled droplet generation in a microfluidic flow-focusing device." Journal of Physics-Condensed Matter 19(46): 462101.

Malsch, D., N. Gleichmann, M. Kielpinski, G. Mayer, T. Henkel, D. Mueller, V. van Steijn, C. R. Kleijn and M. T. Kreutzer (2010). "Dynamics of droplet formation at T-shaped nozzles with elastic feed lines." Microfluidics and Nanofluidics 8(4): 497-507.

Malsch, D., M. Kielpinski, R. Merthan, J. Albert, G. Mayer, J. M. Kohler, H. Susse, M. Stahl and T. Henkel (2008). "mu PIV - Analysis of Taylor flow in micro channels." Chemical engineering Journal 135S: S166-S172.

Manz, A., C. S. Effenhauser, N. Burggraf, D. J. Harrison, K. Seiler and K. Fluri (1994). "Electroosmotic Pumping and Electrophoretic Separations for Miniaturized Chemical-Analysis Systems." Journal of Micromechanics and Microengineering 4(4): 257-265.

Mark, D., S. Haeberle, G. Roth, F. von Stetten and R. Zengerle (2010). "Microfluidic lab-on-a-chip platforms: requirements, characteristics and applications." Chemical Society Reviews 39(3): 1153-1182.

Martin, J. D. and S. D. Hudson (2009). "Mass transfer and interfacial properties in two-phase microchannel flows." New Journal of Physics 11: 115005.

Mazutis, L. and A. D. Griffiths (2009). "Preparation of monodisperse emulsions by hydrodynamic size fractionation." Applied Physics Letters 95(20): 204103.

McDonald, J. C., D. C. Duffy, J. R. Anderson, D. T. Chiu, H. K. Wu, O. J. A. Schueller and G. M. Whitesides (2000). "Fabrication of microfluidic systems in poly(dimethylsiloxane)." Electrophoresis 21(1): 27-40.

McDonald, J. C. and G. M. Whitesides (2002). "Poly(dimethylsiloxane) as a material for fabricating microfluidic devices." Accounts of Chemical Research 35(7): 491-499.

Melin, J. and S. R. Quake (2007). "Microfluidic large-scale integration: The evolution of design rules for biological automation." Annual Review of Biophysics and Biomolecular Structure 36: 213-231.

Menetrier-Deremble, L. and P. Tabeling (2006). "Droplet breakup in microfluidic junctions of arbitrary angles." Physical Review E 74(3): 035303.

Meyer, R. F. and J. C. Crocker (2009). "Universal Dripping and Jetting in a Transverse Shear Flow." Physical Review Letters 102(19): 194501.

Mikati, N. and S. Wall (1993). "Diffusion of sodium dodecyl-sulfate studied by a steady-state technique." Langmuir 9(1): 113-116.

Miller, E. M. and A. R. Wheeler (2009). "Digital bioanalysis." Analytical and Bioanalytical Chemistry 393(2): 419-426.

Miller, R., M. Bree and V. B. Fainerman (1998). "Hydrodynamic effects in measurements with the drop volume technique at small drop times - 3. Surface tensions of viscous liquids." Colloids and Surfaces a-Physicochemical and Engineering Aspects 142(2-3): 237-242.

Miller, R., S. A. Zholob, A. V. Makievski, P. Joos and V. B. Fainerman (1997). "Remarks on the interpretation of data from the dynamic drop volume method." Langmuir 13(21): 5663-5668.

Mugele, F. and J. C. Baret (2005). "Electrowetting: From basics to applications." Journal of Physics-Condensed Matter 17(28): R705-R774.

Muradoglu, M. and H. A. Stone (2005). "Mixing in a drop moving through a serpentine channel: A computational study." Physics of Fluids 17(7): 073305.

Muradoglu, M. and H. A. Stone (2007). "Motion of large bubbles in curved channels." Journal of Fluid Mechanics 570: 455-466.

Nagel, K. (1996). "Particle hopping models and traffic flow theory." Physical Review E 53(5): 4655-4672.

Nagy, P. T. and G. P. Neitzel (2008). "Optical levitation and transport of microdroplets: Proof of concept." Physics of Fluids 20: 101703.

Nahra, H. K. and Y. Kamotani (2000). "Bubble formation from wall orifice in liquid cross-flow under low gravity." Chemical Engineering Science 55(20): 4653-4665.

Nguyen, N.-T., S. Lassemono, F. A. Chollet and C. Yang (2007). "Interfacial tension measurement with an optofluidic sensor." Ieee Sensors Journal 7(5-6): 692-697.

Nguyen, N. T., S. Lassemono and F. A. Chollet (2006). "Optical detection for droplet size control in microfluidic droplet-based analysis systems." Sensors and Actuators B-Chemical 117: 431-436.

Nguyen, N. T., K. M. Ng and X. Y. Huang (2006). "Manipulation of ferrofluid droplets using planar coils." Applied Physics Letters 89(5): 052509.

Nguyen, N. T. and S. T. Wereley (2006). Fundamentals and Applications of Microfluidics, Artech House Publishers.

Nie, J. and R. T. Kennedy (2010). "Sampling from Nanoliter Plugs via Asymmetrical Splitting of Segmented Flow." Analytical Chemistry 82(18): 7852-7856.

Nino, R. R. and J. M. R. Patino (1998). "Surface tension of bovine serum albumin and tween 20 at the air-aqueous interface." Journal of the American Oil Chemists Society 75(10): 1241-1248.

Nisisako, T. (2008). "Microstructured devices for preparing controlled multiple emulsions." Chemical Engineering & Technology 31(8): 1091-1098.

Nisisako, T., S. Okushima and T. Torii (2005). "Controlled formulation of monodisperse double emulsions in a multiple-phase microfluidic system." Soft Matter 1(1): 23-27.

Niu, X., S. Gulati, J. B. Edel and A. J. deMello (2008). "Pillar-induced droplet merging in microfluidic circuits." Lab on a Chip 8(11): 1837-1841.

Niu, X. Z., M. Y. Zhang, S. L. Peng, W. J. Wen and P. Sheng (2007). "Real-time detection, control, and sorting of microfluidic droplets." Biomicrofluidics 1(4): 044101.

Niu, X. Z., M. Y. Zhang, J. B. Wu, W. J. Wen and P. Sheng (2009). "Generation and manipulation of "smart" droplets." Soft Matter 5(3): 576-581.

Noskov, B. A. (2002). "Kinetics of adsorption from micellar solutions." Advances in Colloid and Interface Science 95(2-3): 237-293.

Ody, C. P. (2010). "Capillary contributions to the dynamics of discrete slugs in microchannels." Microfluidics and Nanofluidics 9(2-3): 397-410.

Ody, C. P., C. N. Baroud and E. de Langre (2007). "Transport of wetting liquid plugs in bifurcating microfluidic channels." Journal of Colloid and Interface Science 308(1): 231-238.

Okushima, S., T. Nisisako, T. Torii and T. Higuchi (2004). "Controlled production of monodisperse double emulsions by two-step droplet breakup in microfluidic devices." Langmuir 20(23): 9905-9908.

Ong, W. L., J. S. Hua, B. L. Zhang, T. Y. Teo, J. L. Zhuo, N. T. Nguyen, N. Ranganathan and L. Yobas (2007). "Experimental and computational analysis of droplet formation in a high-performance flow-focusing geometry." Sensors and Actuators a-Physical 138(1): 203-212.

Papageorgiou, D. T. (1995). "Analytical description of the breakup of liquid jets." Journal of Fluid Mechanics 301: 109-132.

Pennathur, S. (2008). "Flow control in microfluidics: are the workhorse flows adequate?" Lab on a Chip 8(3): 383-387.

Pipe, C. J. and G. H. McKinley (2009). "Microfluidic rheometry." Mechanics Research Communications 36(1): 110-120.

Prakash, M. and N. Gershenfeld (2007). "Microfluidic bubble logic." Science 315(5813): 832-835.

Pregibon, D. C., M. Toner and P. S. Doyle (2007). "Multifunctional encoded particles for high-throughput biomolecule analysis." Science 315(5817): 1393-1396.

Priest, C., S. Herminghaus and R. Seemann (2006). "Controlled electrocoalescence in microfluidics: Targeting a single lamella." Applied Physics Letters 89(13): 134101.

Priest, C., S. Herminghaus and R. Seemann (2006). "Generation of monodisperse gel emulsions in a microfluidic device." Applied Physics Letters 88(2): 024106.

Prosperetti, A. and G. Tryggvason (2007). Computational Methods for Two-Phase Flow, Cambridge University Press.

Qiao, R. and N. R. Aluru (2002). "A compact model for electroosmotic flows in microfluidic devices." Journal of Micromechanics and Microengineering 12(5): 625-635.

Quevedo, E., J. Steinbacher and D. T. McQuade (2005). "Interfacial polymerization within a simplified microfluidic device: Capturing capsules." Journal of the American Chemical Society 127(30): 10498-10499.

Ransohoff, T. C. and C. J. Radke (1988). "Laminar-flow of a wetting liquid along the corners of a predominantly gas-occupied noncircular pore." Journal of Colloid and Interface Science 121(2): 392-401.

Raven, J. P. and P. Marmottant (2006). "Periodic microfluidic bubbling oscillator: Insight into the stability of two-phase microflows." Physical Review Letters 97(15): 154501.

Raven, J. P. and P. Marmottant (2009). "Microfluidic Crystals: Dynamic Interplay between Rearrangement Waves and Flow." Physical Review Letters 102(8): 084501.

Rayleigh, J. W. S. (1879). "On the instability of jets." Proceedings of the London Mathematical Society: 4-13.

Rayner, M., G. Tragardh and C. Tragardh (2005). "The impact of mass transfer and interfacial expansion rate on droplet size in membrane emulsification processes." Colloids and Surfaces a-Physicochemical and Engineering Aspects 266(1-3): 1-17.

Roach, L. S., H. Song and R. F. Ismagilov (2005). "Controlling nonspecific protein adsorption in a plug-based microfluidic system by controlling interfacial chemistry using fluorous-phase surfactants." Analytical Chemistry 77(3): 785-796.

Roman, G. T., M. Wang, K. N. Shultz, C. Jennings and R. T. Kennedy (2008). "Sampling and Electrophoretic Analysis of Segmented Flow Streams Using Virtual Walls in a Microfluidic Device." Analytical Chemistry 80(21): 8231-8238.

Rosen, M. (1989). Surfactants and Interfacial Phenomena, Wiley-Interscience.

Ross, P. J. (1995). Taguchi Techniques for Quality Engineering, McGraw-Hill Professional.

Saeki, D., S. Sugiura, T. Kanamori, S. Sato, S. Mukataka and S. Ichikawa (2008). "Highly Productive Droplet Formation by Anisotropic Elongation of a Thread Flow in a Microchannel." Langmuir 24(23): 13809-13813.

Sang, L., Y. P. Hong and F. J. Wang (2009). "Investigation of viscosity effect on droplet formation in T-shaped microchannels by numerical and analytical methods." Microfluidics and Nanofluidics 6(5): 621-635.

Santiago, J. G., S. T. Wereley, C. D. Meinhart, D. J. Beebe and R. J. Adrian (1998). "A particle image velocimetry system for microfluidics." Experiments in Fluids 25(4): 316-319.

Schaerli, Y. and F. Hollfelder (2009). "The potential of microfluidic water-in-oil droplets in experimental biology." Molecular Biosystems 5(12): 1392-1404.

Schiff, J. L. (2008). Cellular automata: a discrete view of the world. Hoboken, NJ, Wiley-Interscience.

Schindler, M. and A. Ajdari (2008). "Droplet traffic in microfluidic networks: A simple model for understanding and designing." Physical Review Letters 100(4): 044501.

Schmitz, C. H. J., A. C. Rowat, S. Koster and D. A. Weitz (2009). "Dropspots: a picoliter array in a microfluidic device." Lab on a Chip 9(1): 44-49.

Schroder, V., O. Behrend and H. Schubert (1998). "Effect of dynamic interfacial tension on the emulsification process using microporous, ceramic membranes." Journal of Colloid and Interface Science 202(2): 334-340.

Schultz, K. M. and E. M. Furst (2011). "High-throughput rheology in a microfluidic device." Lab on a Chip 11(22): 3802-3809.

Seo, M., Z. H. Nie, S. Q. Xu, M. Mok, P. C. Lewis, R. Graham and E. Kumacheva (2005). "Continuous microfluidic reactors for polymer particles." Langmuir 21(25): 11614-11622.

Seo, M., C. Paquet, Z. H. Nie, S. Q. Xu and E. Kumacheva (2007). "Microfluidic consecutive flow-focusing droplet generators." Soft Matter 3(8): 986-992.

Sessoms, D. A. (2010). T. Glawdel. 12/8/2010, E-mail.

Sessoms, D. A., A. Amon, L. Courbin and P. Panizza (2010). "Complex Dynamics of Droplet Traffic in a Bifurcating Microfluidic Channel: Periodicity, Multistability, and Selection Rules." Physical Review Letters 105(15): 154501.

Sessoms, D. A., M. Belloul, W. Engl, M. Roche, L. Courbin and P. Panizza (2009). "Droplet motion in microfluidic networks: Hydrodynamic interactions and pressure-drop measurements." Physical Review E 80(1): 016317.

Sgro, A. E., P. B. Allen and D. T. Chiu (2007). "Thermoelectric manipulation of aqueous droplets in microfluidic devices." Analytical Chemistry 79(13): 4845-4851.

Shepherd, R. F., J. C. Conrad, S. K. Rhodes, D. R. Link, M. Marquez, D. A. Weitz and J. A. Lewis (2006). "Microfluidic assembly of homogeneous and janus colloid-filled hydrogel granules." Langmuir 22(21): 8618-8622.

Shestopalov, I., J. D. Tice and R. F. Ismagilov (2004). "Multi-step synthesis of nanoparticles performed on millisecond time scale in a microfluidic droplet-based system." Lab on a Chip 4(4): 316-321.

Shi, W. W., J. H. Qin, N. N. Ye and B. C. Lin (2008). "Droplet-based microfluidic system for individual Caenorhabditis elegans assay." Lab on a Chip 8(9): 1432-1435.

Shim, J. U., G. Cristobal, D. R. Link, T. Thorsen, Y. W. Jia, K. Piattelli and S. Fraden (2007). "Control and measurement of the phase behavior of aqueous solutions using microfluidics." Journal of the American Chemical Society 129(28): 8825-8835.

Shintaku, H., T. Kuwabara, S. Kawano, T. Suzuki, I. Kanno and H. Kotera (2007). "Micro cell encapsulation and its hydrogel-beads production using microfluidic device." Microsystem Technologies 13: 951-958.

Shui, L., J. C. T. Eijkel and A. van den Berg (2007). "Multiphase flow in microfluidic systems - Control and applications of droplets and interfaces." Advances in Colloid and Interface Science 133(1): 35-49.

Sierou, A. and J. R. Lister (2003). "Self-similar solutions for viscous capillary pinch-off." Journal of Fluid Mechanics 497: 381-403.

Smith, B. J. and D. P. Gaver (2010). "Agent-based simulations of complex droplet pattern formation in a two-branch microfluidic network." Lab on a Chip 10(3): 303-312.

Song, H., M. R. Bringer, J. D. Tice, C. J. Gerdts and R. F. Ismagilov (2003). "Experimental test of scaling of mixing by chaotic advection in droplets moving through microfluidic channels." Applied Physics Letters 83(22): 4664-4666.

Song, H., D. L. Chen and R. F. Ismagilov (2006). "Reactions in droplets in microflulidic channels." Angewandte Chemie-International Edition 45(44): 7336-7356.

Song, H. and R. F. Ismagilov (2003). "Millisecond kinetics on a microfluidic chip using nanoliters of reagents." Journal of the American Chemical Society 125(47): 14613-14619.

Song, H., H. W. Li, M. S. Munson, T. G. Van Ha and R. F. Ismagilov (2006). "On-chip titration of an anticoagulant argatroban and determination of the clotting time within whole blood or plasma using a plug-based microfluidic system." Analytical Chemistry 78(14): 4839-4849.

Song, H., J. D. Tice and R. F. Ismagilov (2003). "A microfluidic system for controlling reaction networks in time." Angewandte Chemie-International Edition 42(7): 768-772.

Squires, T. M. and S. R. Quake (2005). "Microfluidics: Fluid physics at the nanoliter scale." Reviews of Modern Physics 77(3): 977-1026.

Stan, C. A., S. K. Y. Tang and G. M. Whitesides (2009). "Independent Control of Drop Size and Velocity in Microfluidic Flow-Focusing Generators Using Variable Temperature and Flow Rate." Analytical Chemistry 81(6): 2399-2402.

Stebe, K. J., S. Y. Lin and C. Maldarelli (1991). "Remobilizing surfactant retarded fluid particle interfaces 1. Stress-free conditions at the interfaces of micellar solutions of surfactants with fast sorption kinetics." Physics of Fluids a-Fluid Dynamics 3(1): 3-20.

Stebe, K. J. and C. Maldarelli (1994). "Removilizing surfactant retarded fluid particle interfaces 2. Controlling the surface mobility at interfaces of solutions containing surface-active components." Journal of Colloid and Interface Science 163(1): 177-189.

Steegmans, M. L. J., C. Schroen and R. M. Boom (2009). "Generalised insights in droplet formation at T-junctions through statistical analysis." Chemical Engineering Science 64(13): 3042-3050.

Steegmans, M. L. J., K. Schroen and R. M. Boom (2009). "Characterization of Emulsification at Flat Microchannel Y Junctions." Langmuir 25(6): 3396-3401.

Steegmans, M. L. J., A. Warmerdam, K. Schroen and R. M. Boom (2009). "Dynamic Interfacial Tension Measurements with Microfluidic Y-Junctions." Langmuir 25(17): 9751-9758.

Stone, H. A. (1994). "Dynamics of drop deformation and breakup in viscous fluids." Annual Review of Fluid Mechanics 26: 65-102.

Stone, H. A. (2005). "On lubrication flows in geometries with zero local curvature." Chemical Engineering Science 60(17): 4838-4845.

Stone, H. A. (2010). "Interfaces: in fluid mechanics and across disciplines." Journal of Fluid Mechanics 645: 1-25.

Sugiura, S., M. Nakajima, T. Oda, M. Satake and M. Seki (2004). "Effect of interfacial tension on the dynamic behavior of droplet formation during microchannel emulsification." Journal of Colloid and Interface Science 269(1): 178-185.

Sullivan, M. T. and H. A. Stone (2008). "The role of feedback in microfluidic flow-focusing devices." Philosophical Transactions of the Royal Society a-Mathematical Physical and Engineering Sciences 366(1873): 2131-2143.

Surenjav, E., S. Herminghaus, C. Priest and R. Seemann (2009). "Discrete microfluidics: Reorganizing droplet arrays at a bend." Applied Physics Letters 95(15): 154104.

Surenjav, E., C. Priest, S. Herminghaus and R. Seemann (2009). "Manipulation of gel emulsions by variable microchannel geometry." Lab on a Chip 9(2): 325-330.

Tan, S. H., S. M. S. Murshed, N. T. Nguyen, T. N. Wong and L. Yobas (2008). "Thermally controlled droplet formation in flow focusing geometry: formation regimes and effect of nanoparticle suspension." Journal of Physics D-Applied Physics 41(16): 165501.

Tan, S. H., N. T. Nguyen, L. Yobas and T. G. Kang (2010). "Formation and manipulation of ferrofluid droplets at a microfluidic T-junction." Journal of Micromechanics and Microengineering 20(4): 045004.

Tan, W. H. and S. Takeuchi (2006). "Timing controllable electrofusion device for aqueous droplet-based microreactors." Lab on a Chip 6(6): 757-763.

Tan, Y. C., V. Cristini and A. P. Lee (2006). "Monodispersed microfluidic droplet generation by shear focusing microfluidic device." Sensors and Actuators B-Chemical 114(1): 350-356.

Tan, Y. C., J. S. Fisher, A. I. Lee, V. Cristini and A. P. Lee (2004). "Design of microfluidic channel geometries for the control of droplet volume, chemical concentration, and sorting." Lab on a Chip 4(4): 292-298.

Tan, Y. C., K. Hettiarachchi, M. Siu and Y. P. Pan (2006). "Controlled microfluidic encapsulation of cells, proteins, and microbeads in lipid vesicles." Journal of the American Chemical Society 128(17): 5656-5658.

Tan, Y. C., Y. L. Ho and A. P. Lee (2007). "Droplet coalescence by geometrically mediated flow in microfluidic channels." Microfluidics and Nanofluidics 3(4): 495-499.

Tan, Y. C., Y. L. Ho and A. P. Lee (2008). "Microfluidic sorting of droplets by size." Microfluidics and Nanofluidics 4(4): 343-348.

Tan, Y. C. and A. P. Lee (2005). "Microfluidic separation of satellite droplets as the basis of a monodispersed micron and submicron emulsification system." Lab on a Chip 5(10): 1178-1183.

Taylor, G. (1964). "DISINTEGRATION OF WATER DROPS IN ELECTRIC FIELD." Proceedings of the Royal Society of London Series a-Mathematical and Physical Sciences 280(138): 383-&.

Taylor, G. I. (1932). "The viscosity of a fluid containing small drops of another fluid." Proceedings of the Royal Society of London Series a-Containing Papers of a Mathematical and Physical Character 138(834): 41-48.

Tchikanda, S. W., R. H. Nilson and S. K. Griffiths (2004). "Modeling of pressure and shear-driven flows in open rectangular microchannels." International Journal of Heat and Mass Transfer 47(3): 527-538.

Teh, S. Y., R. Lin, L. H. Hung and A. P. Lee (2008). "Droplet microfluidics." Lab on a Chip 8(2): 198-220.

Tetradis-Meris, G., D. Rossetti, C. P. de Torres, R. Cao, G. P. Lian and R. Janes (2009). "Novel Parallel Integration of Microfluidic Device Network for Emulsion Formation." Industrial & Engineering Chemistry Research 48(19): 8881-8889.

Theodorakakos, A., T. Ous, A. Gavaises, J. M. Nouri, N. Nikolopoulos and H. Yanagihara (2006). "Dynamics of water droplets detached from porous surfaces of relevance to PEM fuel cells." Journal of Colloid and Interface Science 300(2): 673-687.

Thoroddsen, S. T., T. G. Etoh and K. Takehara (2008). "High-speed imaging of drops and bubbles." Annual Review of Fluid Mechanics 40: 257-285.

Thorsen, T., R. W. Roberts, F. H. Arnold and S. R. Quake (2001). "Dynamic pattern formation in a vesicle-generating microfluidic device." Physical Review Letters 86(18): 4163-4166.

Tice, J. D., A. D. Lyon and R. F. Ismagilov (2004). "Effects of viscosity on droplet formation and mixing in microfluidic channels." Analytica Chimica Acta 507(1): 73-77.

Tice, J. D., H. Song, A. D. Lyon and R. F. Ismagilov (2003). "Formation of droplets and mixing in multiphase microfluidics at low values of the Reynolds and the capillary numbers." Langmuir 19(22): 9127-9133.

Tiefenbach, K. J., H. Durchschlag and R. Jaenicke (1999). Spectroscopic and hydrodynamic investigations of nonionic and zwitterionic detergents. Analytical Ultracentrifugation V. H. Colfen. 113**:** 135-141.

Timgren, A., G. Tragardh and C. Tragardh (2008). "Application of the PIV technique to measurements around and inside a forming drop in a liquid-liquid system." Experiments in Fluids 44(4): 565-575.

Um, E. and J. K. Park (2009). "A microfluidic abacus channel for controlling the addition of droplets." Lab on a Chip 9(2): 207-212.

Umbanhowar, P. B., V. Prasad and D. A. Weitz (2000). "Monodisperse emulsion generation via drop break off in a coflowing stream." Langmuir 16(2): 347-351.

Unger, M. A., H. P. Chou, T. Thorsen, A. Scherer and S. R. Quake (2000). "Monolithic microfabricated valves and pumps by multilayer soft lithography." Science 288(5463): 113-116.

van der Graaf, S., T. Nisisako, C. Schroen, R. G. M. van der Sman and R. M. Boom (2006). "Lattice Boltzmann simulations of droplet formation in a T-shaped microchannel." Langmuir 22(9): 4144-4152.

van der Graaf, S., C. Schroen, R. G. M. van der Sman and R. M. Boom (2004). "Influence of dynamic interfacial tension on droplet formation during membrane emulsification." Journal of Colloid and Interface Science 277(2): 456-463.

van der Graaf, S., M. L. J. Steegmans, R. G. M. van der Sman, C. Schroen and R. M. Boom (2005). "Droplet formation in a T-shaped microchannel junction: A model system for membrane emulsification." Colloids and Surfaces a-Physicochemical and Engineering Aspects 266: 106-116.

van der Sman, R. G. M. and S. van der Graaf (2006). "Diffuse interface model of surfactant adsorption onto flat and droplet interfaces." Rheologica Acta 46(1): 3-11.

van Steijn, V. (2010). Formation and Transport of Bubbles in Microfluidic Systems. Delft, Netherlands, Delft University of Technology.

van Steijn, V., C. R. Kleijn and M. T. Kreutzer (2009). "Flows around Confined Bubbles and Their Importance in Triggering Pinch-Off." Physical Review Letters 103(21): 214501.

van Steijn, V., C. R. Kleijn and M. T. Kreutzer (2010). "Predictive model for the size of bubbles and droplets created in microfluidic T-junctions." Lab on a Chip 10(19): 2513-2518.

van Steijn, V., M. T. Kreutzer and C. R. Kleijn (2007). "mu-PIV study of the formation of segmented flow in microfluidic T-junctions." Chemical Engineering Science: 7505-7514.

van Steijn, V., M. T. Kreutzer and C. R. Kleijn (2008). "Velocity fluctuations of segmented flow in microchannels." Chemical Engineering Journal 135: S159-S165.

Vanapalli, S. A., A. G. Banpurkar, D. van den Ende, M. H. G. Duits and F. Mugele (2009). "Hydrodynamic resistance of single confined moving drops in rectangular microchannels." Lab on a Chip 9(7): 982-990.

Vanuffelen, M. and P. Joos (1993). "Adsorption-kinetics with surface dilation 2. The steady-state dynamic surface-tension by compressing an adsorbed soluble monolayer with a constant dilation rate." Journal of Colloid and Interface Science 158(2): 452-459.

Waldbaur, A., H. Rapp, K. Laenge and B. E. Rapp (2011). "Let there be chip-towards rapid prototyping of microfluidic devices: one-step manufacturing processes." Analytical Methods 3(12): 2681-2716.

Walsh, E., Y. Muzychka, P. Walsh, V. Egan and J. Punch (2009). "Pressure drop in two phase slug/bubble flows in mini scale capillaries." International Journal of Multiphase Flow 35(10): 879-884.

Wan, L. S. C. and P. F. S. Lee (1974). "CMC OF POLYSORBATES." Journal of Pharmaceutical Sciences 63(1): 136-137.

Wang, A.-B., I. C. Lin, Y.-W. Hsieh, W.-P. Shih and G.-W. Wu (2011). "Effective pressure and bubble generation in a microfluidic T-junction." Lab on a Chip 11(20): 3499-3507.

Wang, C., N. T. Nguyen and T. N. Wong (2007). "Optical measurement of flow field and concentration field inside a moving nanoliter droplet." Sensors and Actuators a-Physical 133: 317-322.

Wang, K., Y. C. Lu, J. H. Xu and G. S. Luo (2009). "Determination of Dynamic Interfacial Tension and Its Effect on Droplet Formation in the T-Shaped Microdispersion Process." Langmuir 25(4): 2153-2158.

Wang, K., Y. C. Lu, J. H. Xu, J. Tan and G. S. Luo (2009). "Liquid-liquid micro-dispersion in a double-pore T-shaped microfluidic device." Microfluidics and Nanofluidics 6(4): 557-564.

Wang, L., L. A. Flanagan, N. L. Jeon, E. Monuki and A. P. Lee (2007). "Dielectrophoresis switching with vertical sidewall electrodes for microfluidic flow cytometry." Lab on a Chip 7(9): 1114-1120.

Wang, W., C. Yang and C. M. Li (2009). "On-demand microfluidic droplet trapping and fusion for on-chip static droplet assays." Lab on a Chip 9(11): 1504-1506.

Wang, Y., A. S. Bedekar, S. Krishnamoorthy, S. S. Siddhaye and S. Sundaram (2007). "System-level modeling and simulation of biochemical assays in lab-on-a-chip devices." Microfluidics and Nanofluidics 3(3): 307-322.

Wang, Y., Q. Lin and T. Mukherjee (2006). "Composable behavioral models and schematic-based simulation of electrokinetic lab-on-a-chip systems." Ieee Transactions on Computer-Aided Design of Integrated Circuits and Systems 25(2): 258-273.

Ward, A. F. H. and L. Tordai (1946). "Time-dependence of boundary tensions of solutions 1. The role of diffusion in time-effects." Journal of Chemical Physics 14(7): 453-461.

Ward, T., M. Faivre, M. Abkarian and H. A. Stone (2005). "Microfluidic flow focusing: Drop size and scaling in pressure versus flow-rate-driven pumping." Electrophoresis 26(19): 3716-3724.

Weisstein, E. W. (2010). "Circular Segment." Retrieved 10/01/2010 http://mathworld.wolfram.com/CircularSegment.html.

Weisstein, E. W. (2011). "Cyclic Group." Retrieved 2/17/11 http://mathworld.wolfram.com/CyclicGroup.html.

Whitesides, G. M. (2006). "The origins and the future of microfluidics." Nature 442(7101): 368-373.

Wong, H., S. Morris and C. J. Radke (1992). "3-dimensional menisci in polygonal capillaries." Journal of Colloid and Interface Science 148(2): 317-336.

Wong, H., C. J. Radke and S. Morris (1995). "The motion of long bubbles in polygonal capillaries 1. Thin-films." Journal of Fluid Mechanics 292: 71-94.

Wong, H., C. J. Radke and S. Morris (1995). "The motion of long bubbles in polygonal capillaries 2. Drag, fluid, pressure and fluid-flow." Journal of Fluid Mechanics 292: 95-110.

Wu, D., G. Y. Xu, J. Liu and Y. M. Li (2006). "Investigation on adsorption dynamics of protein/Tween-20 mixture at the surface of solution by surface pressure measurement." Journal of Dispersion Science and Technology 27(4): 523-526.

Wu, J. H., R. Y. Zhang and X. F. Zou (2004). "Multiple periodic patterns via discrete neural nets with delayed feedback loops." International Journal of Bifurcation and Chaos 14(8): 2915-2923.

Xia, Y. N. and G. M. Whitesides (1998). "Soft lithography." Annual Review of Materials Science 28: 153-184.

Xu, J. H., S. W. Li, W. J. Lan and G. S. Luo (2008). "Microfluidic approach for rapid interfacial tension measurement." Langmuir 24(19): 11287-11292.

Xu, J. H., S. W. Li, J. Tan and G. S. Luo (2008). "Correlations of droplet formation in T-junction microfluidic devices: from squeezing to dripping." Microfluidics and Nanofluidics 5(6): 711-717.

Xu, J. H., G. S. Luo, G. G. Chen and J. D. Wang (2005). "Experimental and theoretical approaches on droplet formation from a micrometer screen hole." Journal of Membrane Science 266(1-2): 121-131.

Yamada, M., S. Doi, H. Maenaka, M. Yasuda and M. Seki (2008). "Hydrodynamic control of droplet division in bifurcating microchannel and its application to particle synthesis." Journal of Colloid and Interface Science 321(2): 401-407.

Yap, Y. F., S. H. Tan, N. T. Nguyen, S. M. S. Murshed, T. N. Wong and L. Yobas (2009). "Thermally mediated control of liquid microdroplets at a bifurcation." Journal of Physics D-Applied Physics 42(6): 065503.

Yeo, L. Y. and J. R. Friend (2009). "Ultrafast microfluidics using surface acoustic waves." Biomicrofluidics 3(1): 12002.

Yi, C. Q., C. W. Li, S. L. Ji and M. S. Yang (2006). "Microfluidics technology for manipulation and analysis of biological cells." Analytica Chimica Acta 560(1-2): 1-23.

Young, T. (1804). "An Essay on the Coehesion of Fluids." Philosophical Transactions of the Royal Society of London Series a-Mathematical Physical and Engineering Sciences 95: 65-87.

Zagnoni, M., J. Anderson and J. M. Cooper (2010). "Hysteresis in Multiphase Microfluidics at a T-Junction." Langmuir 26(12): 9416-9422.

Zhang, M., X. Gong and W. Wen (2009). "Manipulation of microfluidic droplets by electrorheological fluid." Electrophoresis 30(18): 3116-3123.

Zhang, M. Y., J. B. Wu, X. Z. Niu, W. J. Wen and P. Sheng (2008). "Manipulations of microfluidic droplets using electrorheological carrier fluid." Physical Review E 78(6): 066305.

Zhang, X. G., M. T. Harris and O. A. Basaran (1994). "Measurement of dynamic surface-tension by a growing drop technique." Journal of Colloid and Interface Science 168(1): 47-60.

Zhang, Y. X. and L. Q. Wang (2009). "Experimental investigation of bubble formation in a microfluidic T-shaped junction." Nanoscale and Microscale Thermophysical Engineering 13(4): 228-242.

Zhao, C.-X. and A. P. J. Middelberg (2011). "Two-phase microfluidic flows." Chemical Engineering Science 66(7): 1394-1411.

Zheng, B. and R. F. Ismagilov (2005). "A microfluidic approach for screening submicroliter volumes against multiple reagents by using preformed arrays of nanoliter plugs in a three-phase liquid/liquid/gas flow." Angewandte Chemie-International Edition 44(17): 2520-2523.

Zheng, B., L. S. Roach and R. F. Ismagilov (2003). "Screening of protein crystallization conditions on a microfluidic chip using nanoliter-size droplets." Journal of the American Chemical Society 125(37): 11170-11171.

Zheng, B., J. D. Tice and R. F. Ismagilov (2004). "Formation of droplets of in microfluidic channels alternating composition and applications to indexing of concentrations in droplet-based assays." Analytical Chemistry 76(17): 4977-4982.

Zhou, C. F., P. T. Yue and J. J. Feng (2006). "Formation of simple and compound drops in microfluidic devices." Physics of Fluids 18(9): 092105.

Zuev, Y. F., R. K. Kurbanov, B. Z. Idiyatullin and O. G. Us'yarov (2007). "Sodium dodecyl sulfate self-diffusion in premicellar and low-concentrated micellar solutions in the presence of a background electrolyte." Colloid Journal 69(4): 444-449.